A SPATIOTEMPORAL METHODOLOGY FOR PAVEMENT RUT CHARACTERIZATION AND DETERIORATION ANALYSIS USING LONG-TERM 3D PAVEMENT DATA

A Dissertation
Presented to
The Academic Faculty

By

Chieh Wang

In Partial Fulfillment
of the Requirements for the Degree
Doctor of Philosophy in the
School of Civil and Environmental

Georgia Institute of Technology

May 2017

A SPATIOTEMPORAL METHODOLOGY FOR PAVEMENT RUT CHARACTERIZATION AND DETERIORATION ANALYSIS USING LONG-TERM 3D PAVEMENT DATA

Approved by:

Dr. Yi-Chang (James) Tsai
School of Civil and Environmental Engineering
Georgia Institute of Technology

Dr. James Lai
School of Civil and Environmental Engineering
Georgia Institute of Technology

Dr. Adjo Amekudzi-Kennedy
School of Civil and Environmental Engineering
Georgia Institute of Technology

Dr. Zhaohua Wang
Center for Geographic Information Systems
Georgia Institute of Technology

Dr. Elliot Moore II
School of Electrical and Computer Engineering
Georgia Institute of Technology

Dr. Michael D. Meyer
Senior Advisor
WSP | Parsons Brinckerhoff

Date Approved: Nov. 21st, 2016

To Pei-Yin

ACKNOWLEDGEMENTS

I am indebted to many people for their support, encouragement, and companion that have made the completion of this dissertation possible. I am particularly grateful to my advisor, Dr. James Tsai, for his continued support and guidance throughout the entire journey. He provided great opportunities for me to explore different research topics, develop various technical skills, and strengthen my engineering communications and teaching capabilities. Most importantly, he always encourages and challenges me to be a researcher and educator better than I thought I could, and I sincerely appreciate it.

I would like to express my deep appreciation to the members of my dissertation committee for their invaluable guidance and feedback that helped shape my abstract ideas into concrete results. Being a world-renowned pavement expert, Dr. Lai brought his experience and knowledge into this research and helped me get into the substance of pavement studies. Continued leadership and guidance from Dr. Wang made my experience as a GRA much more enjoyable. Encouragement and genuine care I received from Dr. Amekudzi-Kennedy inspired me to be a more caring person. Enlightenment and inspiration I received from Dr. Meyer throughout the years have encouraged to continue my pursuit of excellence. Dr. Moore's expertise in signal processing allowed me to see the problem from different perspectives, which have made this research more complete. It has been a true privilege and delightful experience working with each of them.

The students and colleagues at Georgia Tech are one the greatest sources of support, be it personal and/or technical, that one can ever hope for in the times of struggle and frustration. I am fortunate to have an extremely talented research group and I would like to especially thank Chengbo Ai, Chenglong Jiang, Yiching Wu, Feng Li, April Gadsby, Vincent Cartillier, Geoffrey Price, Anirban Chatterjee, Georgene Geary, Thibaud Toullier, Zachary Lewis, and others for many forms of help they provided that have made the completion of this dissertation possible. Many people I encountered at all stages of this graduate program

have become lifelong friends. I would like to specifically thank Ronald Boodhoo, Aditi Misra, Shrivatsa Ravikumar, Richard Boadi, Popa Pratyaksa, and Ana Catalina Restrepo-Fraundorf for their friendship.

My experience at Georgia Tech was made richer because of many organizations that not only helped me become a better leader and team player but also provided great financial support to me and my family. I would like to acknowledge the support I received from the Ministry of Education of Taiwan, the International Road Federation, the Georgia Institute of Transportation Engineers, the Intelligent Transportation Society of Georgia, and the Georgia Chapter of the American Society of Highway Engineers, for making this journey possible. I would also like to thank the organizations, including the USDOT and the GDOT, for supporting the research.

This dissertation is dedicated to my wife Pei-Yin, whom I would like to thank for her unconditional love, companion, and understanding from the very first day I thought about studying abroad until now. I thank my parents and my in-laws for their unreserved support and love. I would like to thank my son Jayson for being the joy of my life. You are a great reminder of the purpose of this life.

To God be the glory, honor, and praise.

TABLE OF CONTENTS

LIST OF TABLES

LIST OF FIGURES

SUMMARY

Pavement rutting, defined as the permanent longitudinal deformation in the wheelpaths of the road, is an important type of pavement distress that is required to be monitored by the Highway Performance Monitoring System (HPMS) and the Moving Ahead for Progress in the 21st Century Act (MAP-21). Traditionally, performance of ruts has been measured by rut depth, a 1D indicator that is insufficient to characterize the 3D shape of rutting and its deterioration, which are essential for identifying causes and determine adequate and timely treatment methods.

With the advancement in sensing technology, continuous 3D pavement surface can now be accurately measured at 1 mm intervals, which are equivalent to more than 4,000 points instead of the traditional 3 or 5 points. This technology provides a great opportunity for characterizing 3D rut shape and its deterioration behaviors in the real-world environment. Although preliminary calibration and validation of 3D sensing technology have been undertaken, there is a lack of methods to utilize multi-timestamp 3D data for characterizing and studying 3D rutting and its deterioration. Therefore, the objective of this dissertation is to develop a methodology to utilize 3D sensing technology for characterizing 3D rut shape and analyzing its deterioration behavior.

The proposed methodology includes (1) a boundary-based 3D data registration method for matching multi-timestamp 3D transverse profiles in 3D space; (2) visualization of 3D rut shape and its deterioration over time; and (3) characterization of 3D rut shape and quantification of rut deterioration behavior. A sensitivity analysis is performed through an iterative static sampling simulation to assess the effect of different data sampling intervals on the spatial and temporal characteristics of rutting. The proposed methodology is further applied to develop a rut classification field study that utilizes the characteristics of 3D rut shape and its deterioration behavior to classify the causes of rutting. Case studies, using 3D pavement data collected between 2012 and 2016 on State Route 26, State Route

275, and Interstate Highway 95, are conducted to demonstrate the capability of the proposed methodology in characterizing and studying deterioration behaviors of rutting under different roadway and traffic characteristics.

Results of the case study show that the proposed boundary-based registration method can accurately register multi-timestamp 3D pavement data in the 3D space. Visualization of the registered data demonstrates that the proposed methodology is capable of reflecting the detailed 3D rut shape and quantifying its deterioration over time. The multi-scale deterioration analysis demonstrates that the proposed methodology not only can be utilized to support state DOTs' routine pavement performance evaluation and monitoring practices, but also enables the analysis of detailed rut shape and its deterioration down to the individual rut level. The sensitivity analysis on sampling intervals can significantly reduce data storage and processing needs and help state DOTs utilize 3D sensing technology effectively. The rut classification study shows promising results that permit the application of the proposed methodology to identify causes of rutting.

The proposed methodology is one of the first efforts that utilize long-term 3D pavement data to characterize 3D rutting and quantify its deterioration. Results of this dissertation will play a key role in advancing state DOTs' utilization of sensing technology for enhanced pavement evaluation and monitoring practices. Methods of this dissertation will serve as a cornerstone for future 3D pavement deterioration and classification research that can lead to improved pavement design, performance modeling, and maintenance decisions.

CHAPTER 1
INTRODUCTION

1.1 Background

Pavement ruts, defined as the permanent longitudinal deformation in the wheelpaths of the pavement, are one of the most common pavement surface distresses. Ruts are caused by insufficient compaction during construction, excessive asphalt in the pavement surface layer, as well as insufficient structural support. If ruts are not adequately treated in a timely manner, they can result in severe safety, rideability, and structural integrity problems. Consequently, the importance of pavement ruts has been recognized by federal and state agencies. At the federal level, the Moving Ahead for Progress in the 21st Century (MAP-21) Act has required performance measurements to be defined by state departments of transportation (DOTs) to monitor rutting. The recently passed Fixing Americas Surface Transportation (FAST) Act has called attention to studying the impact of pavement rutting on highway efficiency, in terms of road conditions and road repairs. At the state level, rut depth has been a required data item to be measured and reported by state DOTs in the Highway Performance Monitoring System (HPMS), which is a federal level information system that monitors administrative, extent, and condition information of all public roads since 1978. According to a National Cooperative Highway Research Program (NCHRP) survey, 100% of the fifty-five responding North American transportation agencies (e.g., state DOTs in the United States and ministries of transportation in Canada) stated that they monitor pavement rutting on a regular basis (Flintsch and McGhee, 2009).

Rut depth has been the primary rut measurement used to evaluate and monitor the conditions of ruts since the American Association of State Highway Officials (AASHO) Road Test in the late 1950s. Traditionally, rut depths had been measured manually according

to the straightedge method (ASTM E1703) (ASTM International, 2011). Currently, most transportation agencies have used rut bar systems to collect and calculate rut depths automatically (McGhee, 2004; American Association of State Highway and Transportation Officials, 2014c). However, rut depth, a 1D rut parameter, is insufficient to characterize the 3D rut shape and its deterioration behavior (Gramling et al., 1991; Lenngren, 1988), which are essential for identifying causes and determining adequate and timely treatment methods.

Acknowledging the importance of 3D rutting, many researchers have studied 3D rut characteristics, including rut depth, width, positive area, negative area, total area, and positive to negative area ratio (Simpson, 1999; White et al., 2002; Fang et al., 2004). The American Association of State Highway and Transportation Officials (AASHTO) has also defined a set of 3D rut parameters, including cross slope, percent deformation, rut depth, rut cross-sectional area, and potential water entrapment depth to characterize 3D rutting (American Association of State Highway and Transportation Officials, 2014a). However, it is difficult to accurately and reliably obtain these 3D rut characteristics, including rut depth, using the current 3-point and 5-point rut bar systems.

With the advancement in sensing technology, more and more automated data collection means with higher data resolution has been developed. These new devices, such as 3D line laser imaging systems, have shown to improve the accuracy of rut depth measurements (Tsai et al., 2011). Moreover, with a resolution down to 1 mm in the transverse direction, which is equivalent to 4,000 points instead of the traditional 3 or 5 points, the complete 3D shape of the pavement surface can be captured. Consequently, in recent years, 3D sensing technology has gained much attention and will soon become the mainstream technology for pavement data collection and analysis, as 22 state DOTs have partnered with the Federal Highway Administration (FHWA) and supported the TPF-5(299) pooled-fund study to improve the quality of pavement surface distress and transverse profile data collection and analysis. Studies have been conducted under this pooled fund to calibrate and validate the

use of 3D sensing technology in support of pavement data collection and analysis (Tsai and Wang, 2015b).

New developments, however, come with new challenges. Despite the promising features 3D sensing technology can bring, the following challenges have hindered state DOTs from fully utilizing 3D pavement data in their routine pavement management decisions. First, there is a lack of methods to register multi-timestamp 3D data for characterizing and studying 3D rutting and its deterioration. Second, there is limited understanding of the importance and relevance of existing and newly defined 3D rut parameters with regard to their ability to quantify 3D rut characteristics over time and infer the causes. Third, the amount of data can be immense, and there is no adequate sampling strategy in place to effectively process 3D pavement data. Therefore, there is a need to develop a methodology that explores and addresses these issues so that state DOTs and researchers can not only collect more accurate data, but also gain useful and effective information that can lead to better pavement management decisions.

1.2 Objectives

The primary objective of this dissertation is to develop a methodology to register long-term 3D pavement data spatially and temporally, and utilize the registered data for characterizing 3D rut shape and quantifying its deterioration in support of data-driven pavement management decisions. Specifically, the tasks of this dissertation are as follows:

- **To register multi-timestamp 3D pavement data.** A boundary-based 3D data registration method is proposed to identify the lane boundaries in 3D data, register and correct inter-sensor geometries, transform 3D data onto the same reference plane, and spatially map multi-timestamp 3D data so that they can be directly compared. This proposed method is an essential step that ensures the reliability of the subsequent rut characterization and deterioration analysis.

- **To visualize 3D rutting and its deterioration.** The registered multi-timestamp 3D pavement data and the temporal changes of 3D rut shapes are then plotted in the 3D space to visualize 3D rut shape and its deterioration.

- **To characterize 3D rut shape and its deterioration behavior.** Spatial and temporal rut parameters, including transverse profile-based parameters, longitudinal parameters, and temporal parameters are defined to characterize 3D rut shapes. Among them, the temporal parameters are the first attempt to incorporate temporal features to evaluate and monitor ruts. A multi-scale deterioration analysis is performed to study the deterioration of rutting at the entire project, 1-mile segment, and individual rut levels.

- **To classify the cause of rutting using spatial and temporal 3D rut characteristics.** A rut classification study was conducted on State Route 26 near Savannah, Georgia. Field pavement evaluation and testing was conducted to determine the cause of rutting at nine different test sites. A correlation-based feature selection method was used to select a subset of key rut features that can best inform the causes. A support vector machine classification model was further constructed to classify the cause of rutting.

- **To assess the effect of different data sampling intervals on the accuracy of rut parameters.** A sensitivity analysis is conducted to assess the effect of different static data sampling intervals on the accuracy of spatial and temporal rut parameters. Results of the sensitivity analysis are further used to develop a dynamic data sampling strategy to effectively reduce the amount of data required to be stored and processed while maintaining the accuracy of rut measurements. The proposed strategy addresses one of state DOTs major concerns on 3D data and helps them better utilize 3D data in support of their routine pavement evaluation and monitoring practices.

1.3 Contributions

The proposed methodology is one of the initial efforts that utilize long-term 3D pavement data for rutting studies. Contributions of this dissertation are fundamentally symmetrical to the objectives, and they are summarized as follows:

- The data registration method, to the best of the authors knowledge, is the first attempt to register multi-timestamp 3D pavement data for 3D rut characterization and deterioration analysis. A 6-mile case study on SR26 shows that the proposed method is able to accurately register data collected at multiple timestamps, improving the root-mean-square error between two datasets from 11.74 mm to 1.49 mm. The accurate registration results also indicate that the proposed method has the potential to be applied to study deterioration of other types of pavement distress, such as cracking, in addition to rutting.

- The visualizations of 3D rut shape and its change over time provides an objective and accurate means for engineers and researchers to directly see the 3D characteristics of rutting and quantify their change over time.

- Spatial and temporal rut parameters defined in this study allow the comprehensive and quantitative characterization of 3D rutting and its deterioration behaviors.

- The rut classification study examines the correlations among spatial and temporal rut parameters and the causes of ruts. The key parameters identified in this study can serve as the primary features to be collected by state DOTs on a routine basis for better identifying rut causes in support of data-driven maintenance decisions.

- The sensitivity analysis provides state DOTs a means to determine best sampling strategies for collecting data in support of their pavement evaluation and monitoring practices. The proposed dynamic data sampling strategy suggests a practice-ready

solution for state DOTs to utilize 3D pavement data without the concern of "drowning in data."

Results of this study will play a key role in advancing state DOTs utilization of emerging technology for enhanced pavement evaluation and monitoring practices. Methods proposed in this study will serve as the cornerstone for future pavement rut deterioration and classification research that can lead to improved pavement design, performance modeling, and maintenance decisions.

1.4 Dissertation Structure

This dissertation consists of eight chapters. Chapter 2 summarizes the current practices and related work in pavement rut data collection, characterization, deterioration analysis, and classification, and identifies research needs. Chapter 3 presents the proposed spatiotemporal methodology that outlines the components of this dissertation and their interactions. Descriptions of the data collection system and the long-term 3D data used in this study are also summarized. Chapter 4 describes the proposed boundary-based 3D pavement data registration method. A case study is performed in this chapter to demonstrate the capability of the proposed method. 2D and 3D visualization of 3D rutting and its deterioration is also presented in this chapter to demonstrate the use of the method. Chapter 5 contains the characterization of 3D rutting and its deterioration at multiple scales using case studies on SR26, SR275, and I95. Chapter 6 presents a rut classification study in which a correlation-based feature selection algorithm is applied to select a key subset of rut parameters, and a support vector machine is constructed to classify causes of rutting. Chapter 7 contains a sensitivity analysis on data sampling intervals and a proposed dynamic data sampling strategy that state DOTs can implement to reduce data storage and processing burdens while deriving meaningful and accurate information for rut performance evaluation and monitoring. Chapter 8 concludes the dissertation with the key findings and contributions of the study and provides recommendations for future research.

CHAPTER 2
LITERATURE REVIEW

In this chapter, pavement rutting and its mechanisms are first defined in Section 2.1. Pavement rutting condition evaluation practices, including data collection techniques (Section 2.2) and sources of error and variation (Section 2.3), are then reviewed. In addition, key concepts and literature in rut characterization, deterioration, and classification are summarized in Sections 2.4, 2.5, and 2.6. Finally, key findings and identified challenges and opportunities are summarized in Section 2.7.

2.1 Definition and Mechanisms of Rutting

Pavement rutting, also referred to as permanent deformation, is a "contiguous longitudinal depression deviating from a surface plane defined by transverse cross slope and longitudinal profile" (ASTM International, 2015). It is a "permanent or unrecoverable traffic-associated deformation within pavement layers" (Paterson, 1987). It can arise because of the densification effect from repetitive traffic loading; it can also be caused by design or structural failure of the surface and/or supporting layers of the pavement, or by construction quality issues.

The specific definition of rutting, in terms of dimensions, may vary significantly from agency to agency. For example, the Road Assessment and Maintenance Management (RAMM) system specifies that rutting be defined as the length of wheelpath where rut depth exceeds 30 mm (20 mm on state highways) (Transfund New Zealand, 1997), whereas the American Association of State Highway and Transportation Officials (AASHTO) defines rutting as "a broad longitudinal depression in the wheelpath of the pavement surface with a depth of at least 2 mm (0.080 in), a width of at least 0.3 m (1.0 ft), and with a longitudinal length of at least 30 m (100 ft)" (American Association of State Highway and Transporta-

tion Officials, 2014a). Moreover, as summarized in the review conducted by Fwa et al. (2012), many transportation agencies define a low severity rut to be at least 3 mm (1/8 in) or 6 mm (1/4 in) in depth.

Ruts can be categorized into different classifications by their mechanisms. Different treatment techniques can be applied to remedy different types of rut. For example, for ruts in the surface asphalt concrete (AC) layer, a standard mill and overlay can effectively correct the rutting; however, the same treatment may not be as effective for treating ruts in the subgrade.

In the literature, it is generally accepted that there are three primary types of rutting: densification due to repetitive traffic loading after initial compaction, plastic movement due to shear, and mechanical deformation due to insufficient structural capacity (Paterson, 1987; Morosiuk et al., 2004; Simpson, 2001b; Oteng-Seifah and Manke G, 1976; Onyango, 2009; Suh and Cho, 2013; White et al., 2002; Bandini and Pham, 2010; Kandhal and Cooley, 2003). Densification is typically a small amount of deformation after the initial compaction during construction. It is basically a further traffic-induced compaction of the hot mix asphalt (HMA) layer, and it slows down when the density of the HMA layer gets higher.

Plastic movement, also known as lateral distortion, typically takes place in the surface AC layer and is caused by an excessive amount of asphalt in the AC layer. Too much asphalt makes the AC layer unstable, which leads to lateral distortion in the AC layer when exposed to traffic. As shown in Figure 2.1, since this type of rutting is caused by the plastic flow of surface materials, materials in wheel paths are pushed laterally by the shear force of traffic loading, causing thinner pavement in the wheel paths and thicker pavement on both sides of wheel paths. This type of rutting is usually obvious and can progress much faster than the other types. Shoving and bleeding effects can also appear due to the excessive asphalt (Morosiuk et al., 2004).

Mechanical deformation is a result of insufficient structural capacity. It can occur in

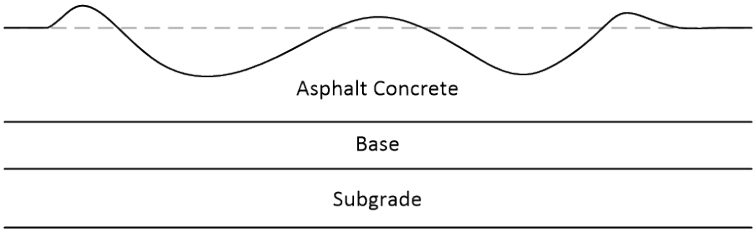

Figure 2.1: Illustration of Rutting due to Lateral Distortion

one or multiple layers of a pavement. Figure 2.2 illustrates rutting occurring in different pavement layers. If rutting occurs in a single layer due to failure or insufficient design, the thickness of the layer become thinner in the wheel paths, and the thickness of any other layer remains the same (Morosiuk et al., 2004; Simpson, 2001b). For example, if the base layer is defective, as shown in Figure 2.2b, the thickness of the base layer becomes thinner in both wheel paths; however, since the AC layer is still structurally sound, the thickness of the AC layer remains the same across the lane. Similarly, when failure occurs in multiple layers, as shown in Figure 2.2d, each defective layer becomes thinner in the wheel paths.

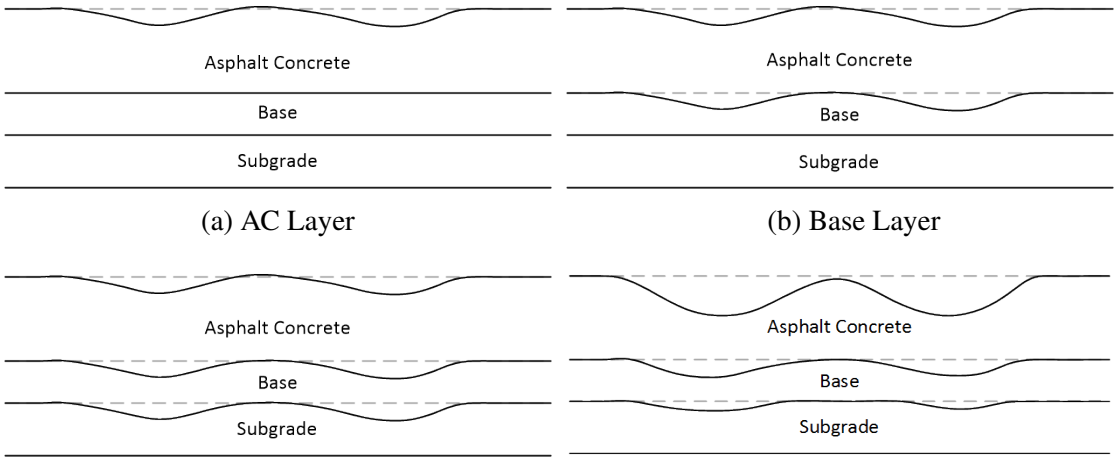

Figure 2.2: Illustration of Mechanical Deformation in One or Multiple Layers

2.2 Development of Data Acquisition Techniques

Numerous methods and techniques have been utilized to collect pavement rutting data. These methods can be generally divided into three major categories: direct measurement,

discrete transverse profiling, and continuous transverse profiling. Direct measurement techniques directly measure rut parameters, such as the rut depth or the rut width, with a ruler or a gauge. The two latter categories are considered indirect measurement techniques because transverse profiles of the pavement are collected and used for calculating rut parameters. In this study, as inspired by Serigos et al. (2015) and the requirements in the AASHTO provisional standard PP70 (American Association of State Highway and Transportation Officials, 2014b), we further categorized indirect measurement techniques into discrete transverse profiling and continuous transverse profiling. In this research, a transverse profile is considered continuous when its transverse resolution (i.e., separation between any two data points along the transverse direction) is 10 mm (0.4 in) or better, which is the data requirement for transverse profiles specified in the AASHTO PP70 provisional standard (American Association of State Highway and Transportation Officials, 2014b). Table 2.1 summarizes commonly recognized and practiced techniques for collecting pavement rutting data, their categories (direct, discrete profiling, or continuous profiling), and their types (manual or automatic). In the following subsections, each of these techniques is discussed.

2.2.1 Direct Measurement

Straightedge

Straightedge had been one of the most recognized methods to measure rut depth before the advent of automatic data collection methods, and it is still used by some transportation agencies (Li, 2012). This method involves laying a straightedge centered on the wheel path of the pavement in the transverse direction (perpendicular to the direction of traveling) and directly measuring depth and/or width of the rut. The length of the straightedge varied throughout the years from approximately 4 ft in the early years to above 6 ft as preferred by the ASTM standard test E1703/E1703M (ASTM International, 2011). Figure 2.3 shows the setup and field implementation of the ASTM standard test for measuring rut depth using a straightedge and a gauge.

Table 2.1: Summary of Pavement Rutting Data Acquisition Techniques

Category	Technique	Type	Description
Direct Measurement	Straightedge	Manual	Place a straightedge (>6 ft) on the pavement perpendicular to the direction of traveling and measure the maximum distance from the bottom of the straightedge to the pavement wheelpath surface using a gauge.
	Stringline	Manual	Stretch a wire (3.7 m) on the pavement surface along the transverse direction from one edge of the lane to the other and gauge the maximum distance from pavement surface in the wheelpath to the string line.
Discrete Transverse Profiling (Transverse Resolution >10 mm)	Rod and Level Survey	Manual	Measure elevation of pavement surface along a line using rod and level survey procedures, typically at 300-mm intervals.
	Dipstick	Manual	A portable inclinometer that collects discrete profiles by measuring relative elevation of the pavement surface along the transverse direction at 304.8-mm intervals (i.e., spacing between two feet of the Dipstick).
	Shadow Line	Automatic	Project illumination on a straight line and capture the shadow of it on the pavement surface (profile), distances between the shadow profile and the physical line are normally measured at 300-mm intervals.
	Point-based Rut Bar	Automatic	Vehicle-mounted downward sensors that measure the distance between each sensor itself and the surface directly below. Sensors are aligned in the transverse direction (rut bar). Measurements by all sensors at the same time form a discrete transverse profile. Number of sensors ranges from 3 to 37.
Continuous Transverse Profiling (Transverse Resolution <= 10 mm)	Transverse Profilograph	Manual	A portable 3.9 m (13 ft) straightedge horizontally placed on pavement surface in transverse direction. Manually plot the elevation across the width of the lane.
	Point Laser	Automatic	A vehicle-mounted point laser that scans the elevation of pavement surface in transverse direction by rotating the sensors.
	Line Laser	Automatic	Project a laser line onto the pavement; then apply photography and basic triangulation principles to calculate the vertical distance between the reference plane of the sensor and the pavement surface. Up to 1-mm resolution transversely.

One limitation of using the straightedge method is that the measured depths of the same rut may be different if lengths of the straightedges used are different. For example, if a subgrade rutting forms a 12-ft wide depression in the lane without an obvious hump, using any straightedge shorter than 12 ft will result in underestimation in the measured rut

depth.

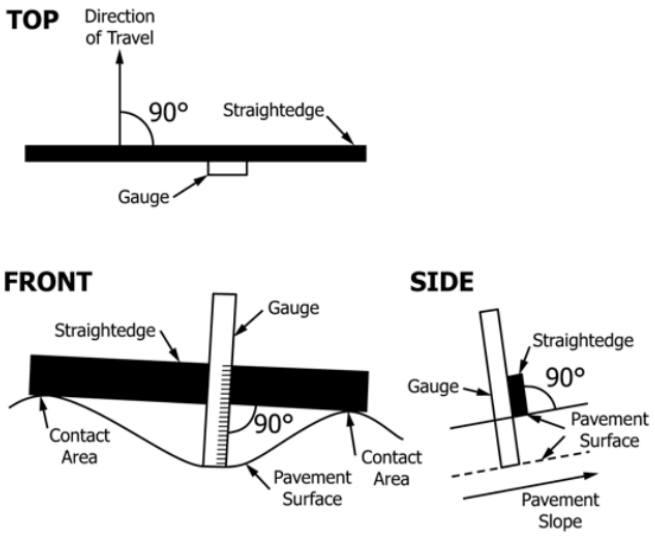

Figure 2.3: Measuring Rut Depth Using the Straightedge Method (ASTM International, 2011)

Stringline

To eliminate the possible underestimated rut depth from a straightedge, the stringline method has also been used. A stringline method stretches a wire (usually approximately 3.7-meter long) along the transverse direction from one edge of the lane to the other. The wire runs through to the two edges of the lane and may bend at the hump between the wheel paths if it is higher than the average elevation of both edges. For manual measurement, rut depth can be measured by gauging the maximum distance from the pavement surface in the wheel-path to the stringline, and rut width can be measured as the distance between two end points on both sides of the rut where the string line touches the pavement surface. Note that although stringline can be done manually, as discussed later in the automated data collection methods section, this technique has primarily been simulated as an imaginary string line in computer programs for calculating the depth and the width of a rut from a transverse profile.

Figure 2.4: Measuring Rut Depth Using the Stringline Method (White et al., 2002)

2.2.2 Discrete Transverse Profiling

Rod and Level Survey

One of the most straightforward methods to measure the deformation or the profile of a pavement is with precision road and level surveys (Haas et al., 1994). The rod and level survey can measure the relative elevation of any specific point of the pavement surface one at a time. A series of surveys can be carried out, and a profile of the pavement (either in the longitudinal or transverse direction) can be collected. This technique is usually used as ground truth data to be compared with data collected using other means. For example, Simpson collected elevation data using rod and level surveys at a 152 mm transverse interval and compared it with data collected by point-based rut bar systems, Dipstick profiler, and straightedge (Simpson, 2001b). Note that even though it may be possible to collect transverse profiles with high resolution (10 mm transverse interval between two data points), it is impractical to collect data with such intensity at the project or network level; therefore, profiles collected using the rod and level techniques are usually at an interval of 0.3m (Perera et al., 2008), which has been considered discrete profiles in this study.

The rod and level survey is a manual technique that typically involves more than one operator. Although this method can produce very accurate pavement profiles with high pre-

cision, it requires a lot of time and effort and has not been frequently used by transportation agencies for collecting pavement rutting data.

Dipstick Profiler

Originally developed to measure the evenness of building slabs, the Dipstick profiler has been used by transportation agencies to collect pavement profiles. The Dipstick profiler is a portable inclinometer that measures the elevation difference of the pavement surface between locations where its two feet rest. By manually walking (i.e., a series of pivoting on the front foot and rotating 180 degrees) the Dipstick profiler along the transverse direction of a lane, the transverse profile can be collected (Haas et al., 1994). The Dipstick profiler has been used by transportation agencies as part of the LTPP program data collection effort. In addition to transverse profiles, the Dipstick can also be used to collect longitudinal profile, superelevation, and cross slope data. However, cumulative systematic errors may affect the accuracy of the measurements collected by the Dipstick (Perera et al., 2008).

Figure 2.5: FACE Dipstick® (Chen et al., 2001)

Shadow Line

The shadow line technique is one of the first automated methods for collecting pavement profiles. The mechanism of this technique is to project a hairline onto the pavement at a

specific angle and photograph this projection using a fixed camera. Any deviation from a straight line reflects the unevenness of the pavement surface. The actual measurements of the pavement deformation are proportional to the measurements in the captured image and can be calculated using basic mathematics and trigonometry. The LTPP program used this technique to collect transverse profiles. A device named the PASCO Road Recon was used to record the projection of the hair line at 50-ft intervals in the driving direction. For each collected projection, the distance between the projection and the physical line was calculated at every 0.3 m (12 in) across the lane in the transverse direction, and these measurements together form the transverse profile (Simpson et al., 1995).

Point-based Rut Bar Systems

The point-based rut bar system is, perhaps, the most commonly used automated systems for collecting transverse profiles. As shown in Figure 2.6, a rut bar system typically consists of 3 to 37 downward sensors mounted at the front or the back of a vehicle, and each sensor of the system measures the distance between the sensor itself and the pavement surface directly beneath. The measurements of the points on a single transverse path then form a discrete transverse profile. For a rut bar system with less than 5 sensors, direct elevation differences among the measurements are used to calculate rut depth; for a rut bar system with at least 5 sensors, the stringline technique can be simulated for calculating rut parameters.

Typical technologies used for the point-based rut bar system include audible, ultrasonic, and point laser. This type of system has been the one most utilized among state transportation agencies. In an NCHRP study, 40 out of 43 participating state transportation agencies used point-based rut bar systems. Among these 40 states, 16 states used a 3-point system, 13 states used a 5-point system, and 11 states used rut bar systems with more than 5 points (5 of which use a 37-point rut bar) (McGhee, 2004).

Figure 2.6: Point-based Rut Bar System (Serigos et al., 2012)

2.2.3 Continuous Transverse Profiling

Transverse Profilograph

The transverse profilograph is a portable 3.9 m (13 ft) device horizontally placed on a pavement surface in the transverse direction. The straightedge component of the transverse profilograph serves as a guide rail to which a rolling component is attached. The rolling component has a drawing mechanism that translates pavement elevations beneath the straightedge to the transverse profile drawn on paper when pushing the rolling component across the width of the lane (Mehta et al., 2001).

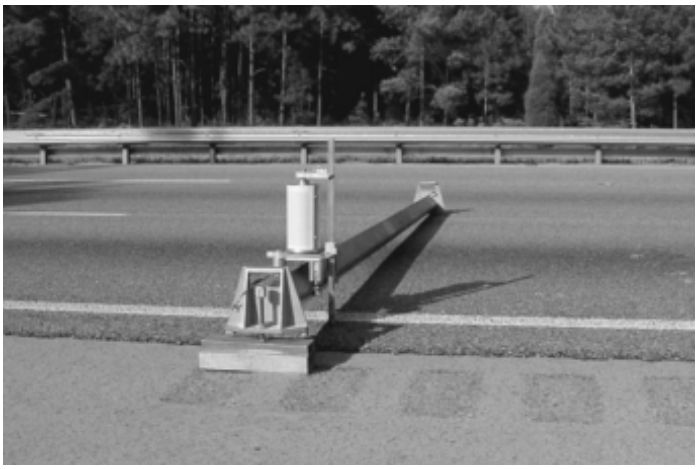

Figure 2.7: Transverse Profilograph (Mehta et al., 2001)

Point Laser Systems

This type of system applies one or more point lasers that, instead of shooting vertically down, scan the surface by shooting the laser at a rotating polygon scanner. The Pavement Profile Scanner (PPS) system developed by the Phoenix Scientific Inc. utilizes a phase measurement laser radar (Ladar) with a rotating polygon that scans across the lane at 1,000 profiles per second or 1 profile per 2.8 cm at 100 km/hr. A transverse profile of the PPS usually consists of 944 data points. The transverse resolution, because of the rotating nature of this type of system, is higher (3.8 mm) at the center of the profile and gets lower (7.2 mm) toward both ends (Phoenix Scientific Inc., 2016).

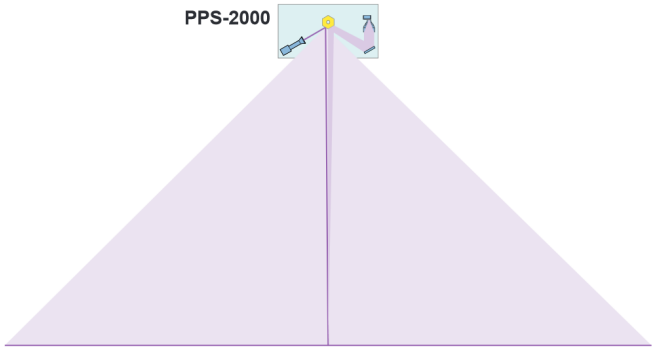

Figure 2.8: Mechanism of a Typical Point Laser System (Phoenix Scientific Inc., 2016)

Line Laser Systems

Another example of automated transverse profile collection techniques is the line laser system. This type of system projects a laser line onto the pavement; then, similar to the shadow line method, it applies photography and basic triangulation principles to calculate the vertical distance between the reference plane of the sensor and the specific point on the pavement surface. The line laser system is also known as the scanning laser system (White et al., 2002) or the 3D imaging system (Li, 2012) in the literature.

As shown in Table 2.2, examples of 3D imaging systems used for pavement data collection include INO/Pavemetric's LCMS (Pavemetrics Systems Inc., 2016), WayLink's

Table 2.2: Examples of 3D Imaging Systems

Manufacturer/ Product	Number of Sensors	Points Per Profile	Transverse Resolution (mm)	Longitudinal Resolution (mm)	Vertical Resolution (mm)
Pavemetrics/LCMS 2	2	4,160	1	1	0.1
WayLink/PaveVision3D Ultra	2	4,096	1	1	0.3
Pathway	up to 4	up to 6,000	1–2	≤ 25.4	≤ 0.5
AMES Engineering	1	2,048	1.95	2.5	0.65
TxDOT/VRUT	1	1,536	2.78	25.4	0.75

PaveVision3D Ultra (Wang et al., 2015), Pathway's 3D Data Acquisition System (Pathway Services Inc., 2016), AMES Engineering's Laser Image & Measurement System (AMES Engineering, 2016), and TxDOT's VRUT (Huang et al., 2011). These devices meet the data collection requirements specified in the AASHTO PP70 provisional standard, including a transverse resolution less than or equal to 10 mm, a longitudinal resolution less than 0.5 m (for project-level), and a vertical resolution less than or equal to 1 mm (American Association of State Highway and Transportation Officials, 2014b). Because of the high-resolution in transverse direction, these 3D imaging systems are also referred to as a continuous automated system (CAS), whereas point-based rut bar systems are referred to as discrete automated systems (DAS) (Serigos et al., 2015). Similar to point-based rut bar systems, straightedge and stringline methods can be simulated to calculate rut depths from these continuous profiles (Li, 2012; Simpson, 2001b). In addition to capturing rutting, most of these systems are capable of detecting and measuring other pavement surface distresses, such as cracking, pothole, and raveling.

2.3 Sources of Error and Variation

Variability may be introduced into the data during the data collection and/or the computation process. The variability can affect quality of the data collected, which may further affect the decisions made. All potential sources of error and variation should be idenfieid, and if possible, minimized for better quality (Flintsch and McGhee, 2009).

2.3.1 Data Collection Methods Used

Pavement rut data collected using different methods may result in very different results. For example, the rut depth measured using the straightedge technique can be different from the rut depth measured by the stringline technique (Austroads, 2011; Simpson, 1999). As shown in Figure 2.9, for the same transverse profile, rut depth and width measured by a 1.8-m straightedge can be drastically different from those measured by a 3.7-m stringline. This difference exists not only in manual data collection methods but also in automated ones because most automated pavement rut data collection methods in fact simulate either the straightedge or the stringline techniques.

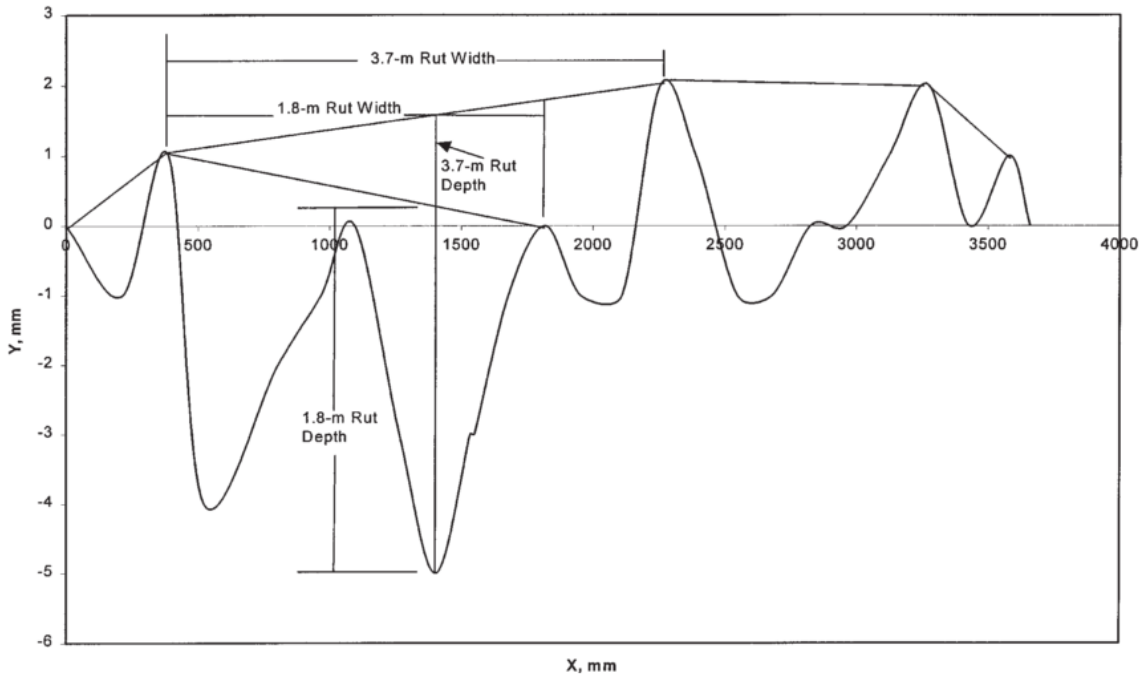

Figure 2.9: Measuring Rut with a 1.8-m Straightedge and a 3.7-m Stringline (Simpson, 1999)

2.3.2 Inherent Variability and Limitations

Inherent System Variability (Repeatability)

A typical variability in data collection is inherent from the equipment (for automated methods) and the inspector (for manual methods). For example, with the same data collection method, data collected by properly trained inspectors can be different. Inter-rater and intra-rater variability in manual data collection has been discussed in the literature (Bianchini et al., 2010; Bogus et al., 2010). Similarly, automated data collection methods, such as sensor-based and image-based technologies, may also have inherent variability in the data collected (Capuruço et al., 2006; Chang-Albitres et al., 2007; Lee and Kim, 2006; McGhee, 2004; Mraz et al., 2006; Wang et al., 2011).

System Limitations (Accuracy)

Manual data collection methods, such as the straightedge, can induce variability from the length of the straightedge. For example, as discussed in the literature, insufficient length of the level may result in a smaller measured rut depth and width (Chen et al., 2001; McQueen and Timm, 2005).

Automated data collection methods, on the other hand, also have certain limitations. For example, the accuracy of vehicle-mounted devices, such as most of the point laser and line laser systems, can be affected by the angles of the vehicles. As shown in Figure 2.10, the angle and location of the laser line changes with the yaw, pitch, and roll rotations of the vehicle (Li, 2012). The difference in the angle and location of the laser line results in different measurement values.

System Resolution

As briefly discussed above, resolution of the system (e.g., the number of data points in a transverse profile) can have profound impact on the calculated rut parameters. For example,

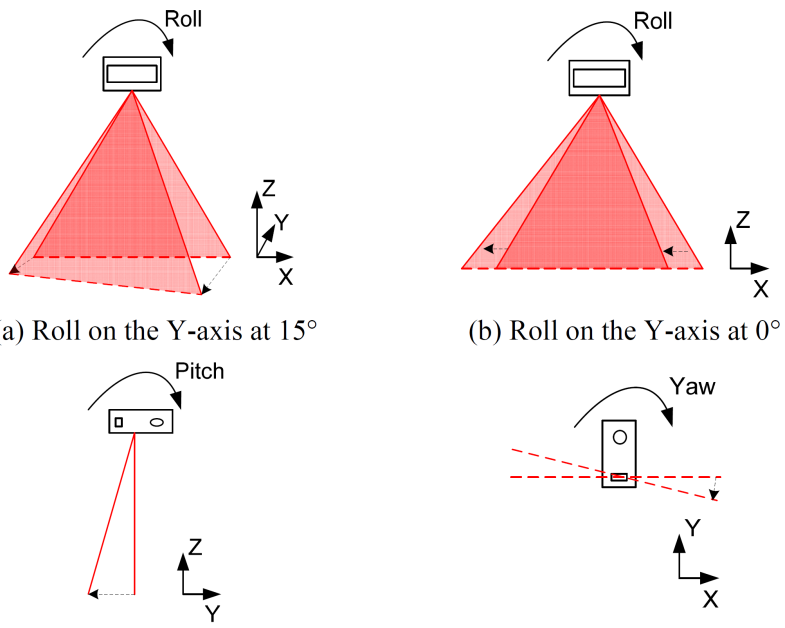

(a) Roll on the Y-axis at 15°

(b) Roll on the Y-axis at 0°

(c) Pitch on the X-axis

(d) Yaw on the Z-axis

Figure 2.10: Effect of Vehicle Rotations on Laser Line Locations (Li, 2012)

as shown in Figures 2.13 and 2.14, rut depth derived from a 3-point laser bar system can be very different from rut depth measured by a 5-point laser bar system; similarly, rut characteristics derived from a point-based rut bar system can also be fairly different from those derived from a line laser system. Simpson recommended that the minimum number of measurements should be at least 9 points in the transverse direction (Simpson, 2001b). In general, the more data points (higher resolution) the system collects in one transverse profile, the more accurately rut parameters can be derived (Chen and Li, 2008; Li, 2012; Tsai et al., 2015).

2.3.3 System Operations

Operations of the equipment and operator skills are also possible sources of variation in the collected data, which, in turn, affect the rut parameters derived. For example, Bogus et al. pointed out that experienced raters (e.g., DOT engineers) tend to be more consistent among multiple runs of rut depth data collection on the same pavement sections than student raters

(Bogus et al., 2010).

Another example, as depicted in Figure 2.11, is vehicle wander, which can lead to inconsistent lateral displacements in the data collected and, consequently, affect the pavement distress data derived (Li, 2012; Mehta et al., 2001; Qiu et al., 2015; Serigos et al., 2015). This source of variation exists in both point-based rut bar and line laser systems. Note that studies have attempted to address this issue by simulating lateral displacements (shifting lane boundaries) on the original profiles (Qiu et al., 2015; Serigos et al., 2015). In other words, these studies assumed profiles were perpendicular to the lane markings and ignored the fact that these transverse profiles would rotate with the wander of the vehicle, which is a source of variation as discussed in the previous subsection.

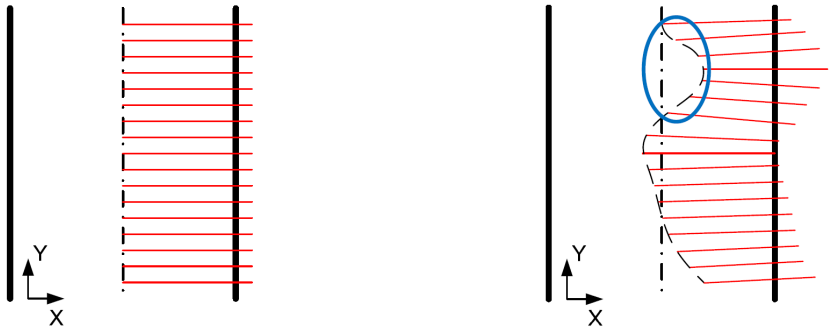

Figure 2.11: Illustration of the Effect of Vehicle Wander on Data Collection (Li, 2012)

2.3.4 Data Processing Methods

Indirect measurement techniques, such as line laser systems, require certain steps of data processing to retrieve the desired measurements. These steps of processing can also induce variability. For example, a typical process undertaken is the smoothing of raw profiles. Different smoothing methods may lead to different smoothed profiles, which then result in different values of measurement (Li, 2012). Another important step when calculating rut parameters according to the AASHTO PP69 standard is determining the locations of the lane markings. Inaccurately identified lane marking locations can lead to drastically different rutting results (Qiu et al., 2015).

2.3.5 Others

Other external factors, such as the data collection environment, can also contribute to variability in data (Li, 2012; McGhee, 2004). Examples of these factors are climatic factors (e.g., temperature, wind, humidity, lighting, and moisture), objects on pavement (e.g., debris, animals, traffic control devices, and data collection equipment), and existence of pavement surface distresses (e.g., raveling, cracking, and potholes).

2.4 Literature Review on Rut Characterization

Existing practices of state DOTs use rut depth as the primary rut parameter for pavement rut evaluation and monitoring purposes (Fwa et al., 2012). However, as discussed in the literature, rut depth itself is merely an indicator that may have its own variation and does not reveal the cause of ruts (Lenngren, 1988; Villiers et al., 2006; Simpson, 2001a). Consequently, many rut parameters have been developed by researchers and practitioners to characterize ruts. One of the most current set of rut parameters was defined by AASHTO in the PP69 provisional standard (American Association of State Highway and Transportation Officials, 2014a). Since many of the parameters discussed in this section were defined in PP69, we briefly summarized the basic procedure of PP69 here.

As shown in Figure 2.12, five key spots of the transverse profile are first identified. These key spots, denoted by black dots, include one lane center spot (Spot 1), two lane edge spots (Spot 3 and Spot 5), and two wheelpath spots (Spot 2 and Spot 4). Before deriving any data from the transverse profile, it is first leveled by rotating the profile by the cross slope angle. The profile is then shifted so that the value of Spot 3 (the inside edge elevation) is zero (shown as the black line), as shown in Figure 2.12a. For deriving parameters for the inside (i.e., left) wheelpath, as depicted in Figure 2.12b, the profile above is rotated about Spot 3 until the value of Spot 1 is zero. Similarly, for calculating parameters for the outside (i.e., right) wheelpath, as depicted in Figure 2.12c, the profile is first shifted so that

the value of Spot 5 is zero; then the profile is rotated about Spot 5 until the value of Spot 1 is zero.

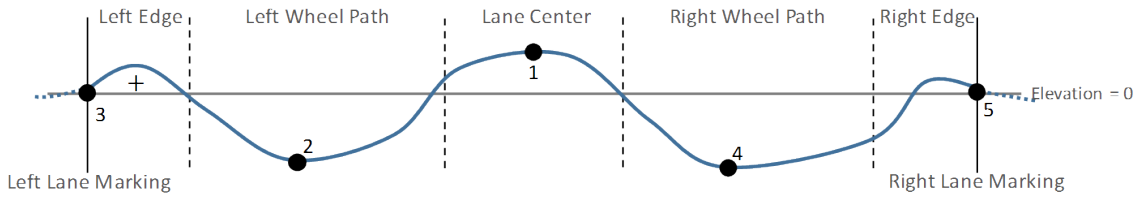

(a) Leveled Profile

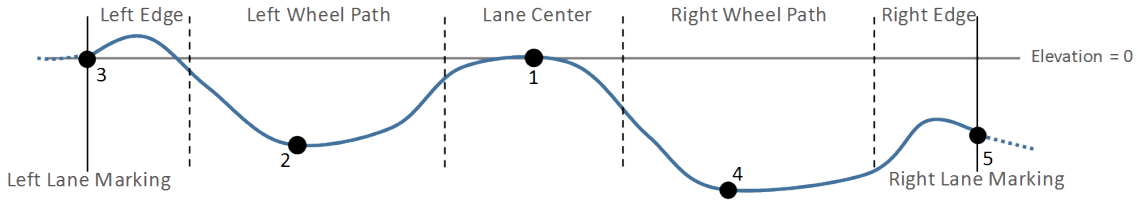

(b) Rotated Profile for Calculating Left-wheelpath Rut Parameters

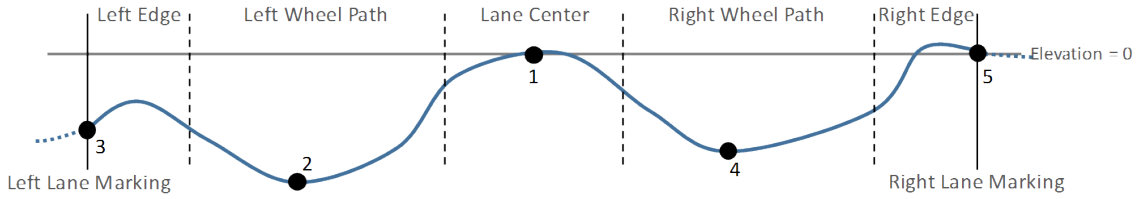

(c) Rotated Profile for Calculating Right-wheelpath Rut Parameters

Figure 2.12: AASHTO PP69 Rut Parameter Calculation Fundamentals

2.4.1 1D Parameters

Rut Depth

Rut depth is the most commonly used and reported rut parameter defined as "the maximum measured perpendicular distance between the bottom surface of the straightedge and the contact area of the gauge with the pavement surface at a specific location" (ASTM International, 2011). It can be directly measured using the straightedge and stringline techniques; it can also be calculated from transverse profiles collected by other techniques.

ASTM standard test E1703/E1703M, as depicted in Figure 2.3, measures rut depth by

setting a straightedge on top of two high points of a rut (perpendicular to the direction of travel) and records the maximum distance from the pavement surface to the bottom of the straightedge using a gauge that is perpendicular to the straightedge (ASTM International, 2011).

To calculate rut depth from a transverse profile, several different methods can be used. First, as illustrated in Figure 2.13, for discrete transverse profiles collected by a 3-point rut bar system, rut depth can be calculated by subtracting the wheelpath elevation from the lane center elevation. For example, the left wheelpath rut depth in Figure 2.13 can be calculated by subtracting D1 from D2.

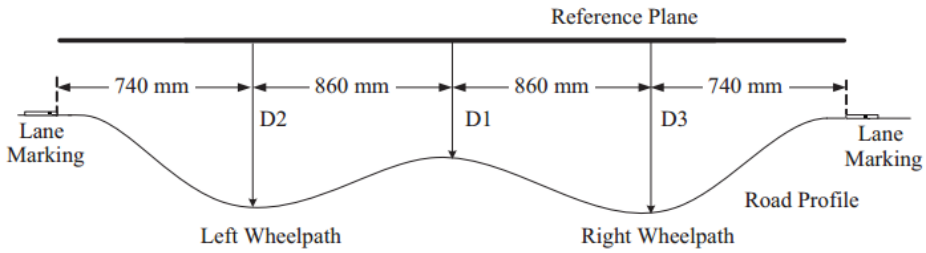

Figure 2.13: Illustration of a 3-Point Rut Bar System (Tsai et al., 2015)

Second, for transverse profiles that have at least 5 measurements, straightedge and stringline techniques can be simulated in the computer for calculating rut depth. AASHTO published a standard practice for determining rut depth in pavements (R48-10) in which the stringline technique is simulated to calculate rut depth from measurements collected by a 5-point rut bar system (American Association of State Highway and Transportation Officials, 2014c). As depicted in Figure 2.14, rut depths in the left and right wheelpaths can be estimated using the following equations:

$$RD_L = D_4 - \frac{D_5 - M}{2} \tag{2.1}$$

$$RD_R = D_2 - \frac{D_1 - M}{2} \tag{2.2}$$

where

M = $\frac{D_1+D_5}{2}$ or D_3, whichever is smaller;

RD_L = estimated rut depth in the left wheelpath, mm;

RD_R = estimated rut depth in the right wheelpath, mm;

$D_1, D_2, ..., D_5$ = distance measured as shown in Figure 2.14, mm.

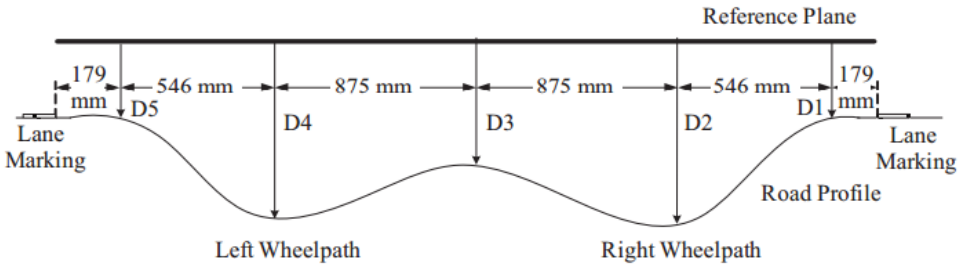

Figure 2.14: Illustration of a 5-Point Rut Bar System (Tsai et al., 2015)

For continuous transverse profiles, automated rut depth calculation methods have been developed (INO, 2010; Laurent et al., 1997; Li, 2012). For example, Pavemetrics Systems Inc. developed a method to simulate a 1.8-m straightedge technique for measuring rut depth. As shown in Figure 2.15, the pavement profile is first smoothed using a median filter. The smoothed profile is then approximated using multiple linear segments (approximately 100 segments for 4,000 points) for easier search of rut support points. Then, the support points of the pavement are located by finding the longest line that can connect any two joints of these segments without intersecting the profile (e.g., dashed line 2 in Figure 2.15a). Once the two support points of a rut are identified, rut depth can be measured according to the ASTM E1703/E1703M standard test. Note that the width of the gauge can be also specified in the algorithm to simulate the real-world situation (Figure 2.15b).

A Georgia Tech research team also developed a method to simulate the straightedge technique (Li, 2012). They enhanced the smoothing process using discrete cosine transform (DCT) and stepwise linear interpolation to obtain the smoothed profile (see Figure 2.16). From the smoothed profile, the team found the highest points from both ends and set a 1.8-m straight edge on these two points to measure the rut depth according to ASTM

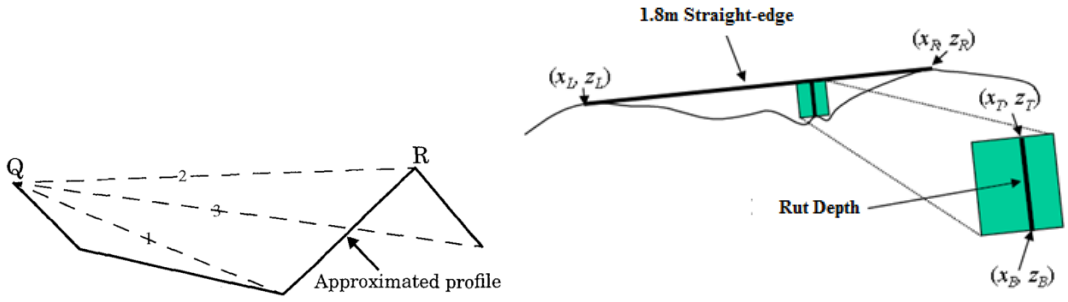

(a) (b)

Figure 2.15: Simulated Straightedge for Rut Depth Calculation (INO, 2010; Laurent et al., 1997)

E1703/E1703M (Li, 2012).

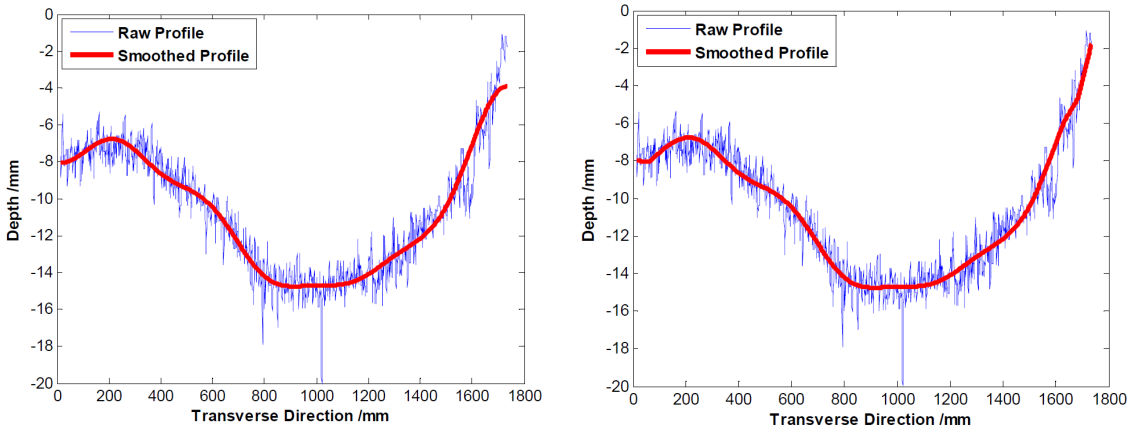

(a) DCT (b) Enhanced DCT

Figure 2.16: Transverse Profile Smoothing Method Developed by Georgia Tech (Li, 2012)

AASHTO PP69 also defines how to calculate rut depth from a transverse profile. As shown in Figure 2.17a, to calculate the left rut depth, the profile is rotated about Spot 3 until Spot 1 reaches the same elevation as Spot 3. The absolute elevation value of Spot 2 is the left rut depth. Similarly, from the previous step, the profile is rotated about Spot 1 until Spot 5 reaches the same elevation as Spot 1. The absolute elevation value of Spot 2 is the right rut depth.

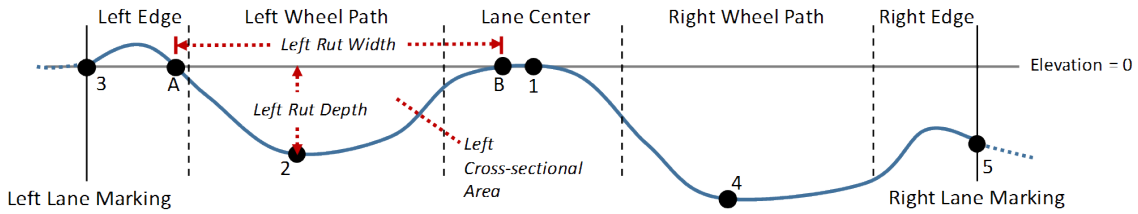

(a) Left Wheelpath

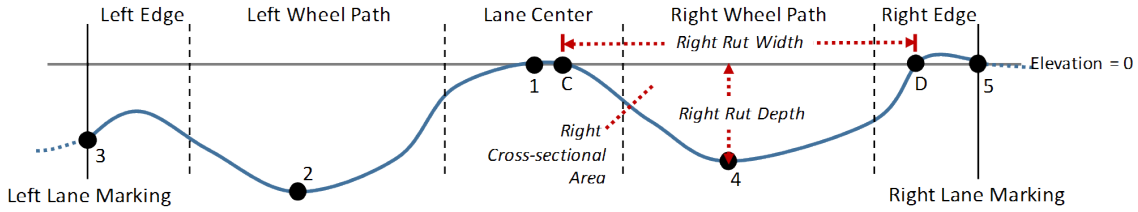

(b) Right Wheelpath

Figure 2.17: AASHTO PP69 Defined Rut Depth, Width, and Cross-sectional Area

Rut Width

To the best of our knowledge, there is no standard procedure for measuring rut width except for the AASHTO PP69 provisional standard. Rut width (RW) can be defined as the distance between two support points of a rut. Rut widths can be measured or computed using the aforementioned straightedge and stringline methods. As shown in Figure 2.9, rut widths are calculated as the horizontal distance between the two peaks of the pavement surface (Simpson, 1999).

Some other studies and research, instead of using the horizontal width as the rut width, use the actual distance between the two supporting points. For example, as shown in the following equation, Pavemetrics Systems Inc. calculates the Euclidean distance between the two support points.

$$RW = \sqrt{(x_L - x_R)^2 - (z_L - z_R)^2} \tag{2.3}$$

where

RW = rut width, mm;

x_L = lateral position of the left support point, mm;

x_R = lateral position of the right support point, mm;

z_L = vertical elevation of the left support point, mm; and

z_R = vertical elevation of the right support point, mm.

Rut Length

Similar to rut width, there has not been a specific definition of the rut length. Intuitively, it can be defined as the longitudinal extension of an individual rut, measured in distance units such as ft or m. The AASHTO PP69 standard practice indicates that a pavement longitudinal depression has to be longer than 30 m to be considered as a rut (American Association of State Highway and Transportation Officials, 2014a). Rut length has also been used by other transportation agencies as a measure to record. For example, the Transfund New Zealand defines rutting as the length of a wheelpath where the rut depth exceeds 30 mm (Transfund New Zealand, 1997). In the study conducted by Lenngren (1988), the author suggests that rut length, rut depth, rut width, and time are the four dimensions that can provide useful information for understanding the causes of rutting and, therefore, yield feasible guidelines for further maintenance strategies (Lenngren, 1988). Li used rut length to identify isolated rutting on roadways (Li, 2012).

2.4.2 2D Parameters

Area-based measurements, such as positive and negative areas (Simpson, 1999; White et al., 2002; Li et al., 2015), fill areas (Simpson, 1999), cross-sectional areas (American Association of State Highway and Transportation Officials, 2014a), and the absolute ratio of positive to negative areas (Simpson, 1999; White et al., 2002; Fang et al., 2004), have been proposed by various studies.

Positive-Negative Areas

As shown in Figure 2.18, the positive and negative areas are determined by drawing a straight line connecting two end points of the profile; any areas above this line are the positive areas, and any areas below this line are negative areas (Simpson, 1999). These areas are sometimes defined as the areas between the original (unloaded) profile and the deformed profile, as defined by White et al. (2002).

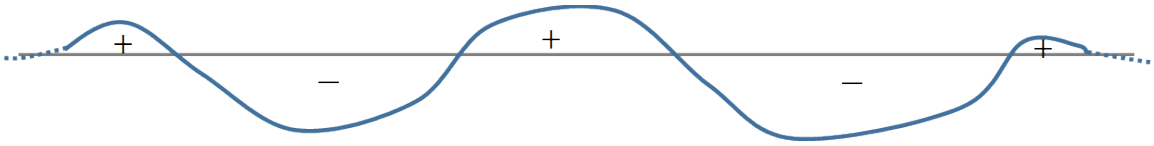

Figure 2.18: Illustration of Positive-Negative Areas

Two typical parameters are usually derived from the calculated positive and negative areas: the total distortion and the distortion ratio (Simpson et al., 1995; White et al., 2002; Fang et al., 2004). The total distortion (TD) is calculated as the sum of all positive areas subtracted by the sum of all negative areas. If the total positive area and the total negative area of a profile is the same, TD is zero. Similarly, if the positive area is greater than the negative area, TD is greater than zero. The distortion ratio (DR) is calculated as the ratio of the total positive area to the total negative area. These two parameters have been used as criteria for classifying the causes of pavement rutting (Simpson et al., 1995; White et al., 2002; Fang et al., 2004).

Cross-sectional Area

AASHTO PP69 defines the cross-sectional area (CA) in a similar fashion as the fill area. PP69 acknowledges that a transverse profile usually has cross slope and is less likely to be horizontal, such as the one shown in Figure 2.18. Therefore, as depicted in Figure 2.17a, for the left wheelpath cross-sectional area (LCA), PP69 rotates the entire profile about Spot 3 until the lane center (Spot 1) reaches the same elevation as Spot 3. The area enclosed by the horizontal line where elevation is zero, and the rotated profile is defined as the left

wheelpath cross-sectional area. Similarly, the area enclosed by the horizontal line and the rotated profile is the right wheelpath cross-sectional area (RCA) (American Association of State Highway and Transportation Officials, 2014a).

Fill Area

The fill area, as defined by Simpson (1999), is the area enclosed by the surface profile and a stringline that connects all peaks of the profile.

2.4.3 Other Parameters or Attributes

Cross Slope

Cross slope is defined as "the average transverse slope of the pavement surface expressed in percent" (American Association of State Highway and Transportation Officials, 2014a).

Percent Deformation

A unique parameter defined in the AASHTO PP69 is the percent deformation (PD), which is defined as "the difference between the straight-line length and the profile length of a section of pavement divided by the straight-line length multiplied by 100" (American Association of State Highway and Transportation Officials, 2014a).

Rut Volume

As indicated in most studies in the literature, a rut filled with water would lead to potential hydroplaning hazards (Fwa et al., 2012; Start et al., 2015). However, almost all studies in the literature considered only rut parameters that can be derived from single transverse profile for any rutting mechanistic and safety studies. To the best of our knowledge, by far, longitudinal parameters, such as rut volume, have only been explored as a means to assess the variation of automated data collection equipment (Li, 2012).

2.4.4 Issues of Existing Rut Characterization Practices

A fair number of rut parameters have been defined in the literature. With the advancement in sensing technology, it is now possible to collect and calculate these parameters with high accuracy. However, the usefulness of all parameters and their correlations still remain unclear. Although rut depth reveals the fundamental structural deformation behavior (i.e., strain), it does not provide a holistic representation of true rut characteristics. Moreover, while other rut parameters provide additional information to characterize ruts, they also bring information that is redundant and less relevant. There is a need, therefore, to critically assess the effectiveness of existing and new rut parameters for representing the characteristics of ruts so that they can be used effectively by state DOTs and researchers to evaluate and monitor rut conditions and derive adequate treatment decisions.

2.5 Literature Review on Rut Deterioration

Deterioration of pavement rutting has been extensively studied in the literature, mainly for pavement design purposes. Existing models predict the growth of rut depth over time and cumulative traffic loading, either empirically by correlating field observations (e.g., traffic configuration, weather conditions, other surface distresses) with the progression of rutting, or mechanistically by deriving theoretical pavement layer responses using structural analysis means and laboratory tests (Paterson, 1987). In this section, key literature in rut deterioration modeling is summarized.

2.5.1 Empirical Models

One of the earliest developments of a rut prediction model is the Brazilian model. This model was included in the World Banks Highway Development and Management (HDM-III) (Paterson, 1987). As shown in Equation 2.4, the mean rut depth is modeled using the age of pavements (AGE), the structural number of pavements (SNC), the compaction in-

dex (COMP), cumulative number of equivalent 80 kN standard axels (ESALs), and other effects, such as rehabilitation history (RH), precipitation (MMP), and the existence of pavement cracking (CRX):

$$RD_{mean} = AGE^{0.166} SNC^{-0.502} COMP^{-2.30} NE_4^{ERM} \tag{2.4}$$

where

RD_{mean}	=	mean rut depth (mm)
AGE	=	age of pavements since last intervention (years)
SNC	=	modified structural number of pavement
$COMP$	=	compaction index
NE_4	=	cumulative number of equivalent 80kN standard axles (ESALs)
ERM	=	$0.09 + 0.384DEF - 0.0009RH + 0.00158MMP \times CRX$
DEF	=	mean Benkelman beam deflection under 80kN standard axles (mm)
RH	=	rehabilitation factor (1 with overlay; 0 otherwise)
MMP	=	mean monthly precipitation (mm/month)
CRX	=	area of indexed cracking (%)

Figure 2.19 illustrates the predicted mean rut depth using this model. Under the annual traffic of 0.5 million ESALs, rutting in pavements with weaker structural numbers (SNC = 2) tend to progress much faster than stronger pavements (SNC = 6). Moreover, rutting in pavements with cracking grows more rapidly than pavements without cracking (Paterson, 1987).

The newer version of the Highway Development and Management publication (HDM-4) developed a series of even more sophisticated models for rut prediction (Morosiuk et al., 2004). The HDM-4 model was developed under the premise that there are several stages and sources of rutting, including the initial densification (RDO), the structural deformation (RDST), the plastic deformation (RDPD), and the wear from studded tires (RDW). For each of these sources, a model was developed, and they are shown in equations below.

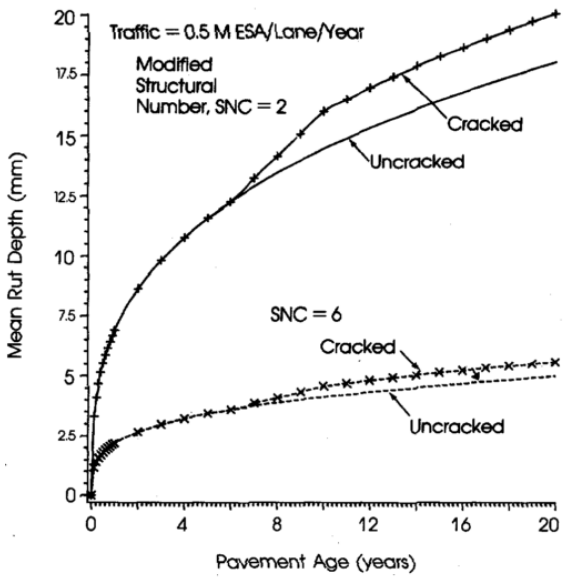

Figure 2.19: Predicted Mean Rut Depth (Paterson, 1987)

The total predicted rut depth, as shown in Equation 2.9, is defined the sum of predicted rut depths from of four sources (Morosiuk et al., 2004).

$$RDO = K_{rid} \times 51740(YE4 \times 10^6)^{0.09+0.0384DEF} SNP^{-0.502} COMP^{-2.3} \tag{2.5}$$

$$\Delta RDST = \begin{cases} 44950 K_{rst} \times SNP^{-1.14} YE4^{0.11} COMP^{-2.3}, \text{ without cracks} \\ 2.48 K_{rst} \times 10^{-5} SNP^{-0.84} YE4^{0.14} MMP^{1.07} ACX_a^{1.11}, \text{ cracks} \end{cases} \tag{2.6}$$

$$\Delta RDPD = 0.3 K_{rpd} CDS^{3.27} Sh^{-0.75} HS^{0.71} YE4 \tag{2.7}$$

$$\Delta RDW = 2.48 \times 10^{-5} PASS^{1.0} W^{-0.46} S^{1.22} SALT^{0.32} \tag{2.8}$$

$$RD_{total} = RDO + \Delta RDST + \Delta RDPD + \Delta RDW \tag{2.9}$$

where

ROD	=	rutting due to initial densification (mm);
$YE4$	=	annual number of ESALs, (millions/lane);
DEF	=	average annual Benkelman beam deflection (mm);
SNP	=	average annual adjusted modified structural number of pavement;
$COMP$	=	relative compaction (%);
$\Delta RDST$	=	incremental rut depth in structural deformation in analysis year (mm);
MMP	=	mean monthly precipitation (mm/month);
ACX_a	=	area of indexed cracking at the beginning of analysis year (%);
$\Delta RDPD$	=	incremental rut depth in plastic deformation in analysis year (mm);
CDS	=	construction defects indicator for bituminous surfacing;
Sh	=	heavy vehicle speed (km/h);
HS	=	total thickness of bituminous surface (mm);
ΔRDW	=	incremental rut depth due to studded tires in analysis year (mm);
$PASS$	=	annual number of vehicles passed with studded tires (1000);
S	=	average traffic speed (km/h);
$SALT$	=	variable for salted or unsalted roads (2 = salted; 1 = unsalted);
W	=	road width (m);
RD_{total}	=	total rut depth (mm);
$K_{rid}, K_{rst}, K_{rpd}$	=	calibration factors.

2.5.2 Mechanistic-Empirical Models

Most studies in the literature predict rut depths using the mechanistic-empirical approach. This type of model takes into consideration the mechanistic theory that deformation (strain) is a result of repetitive loading (stress) and then correlates the deformation with other factors from empirical settings. One example is the AASHTO Mechanistic-Empirical Pavement Design Guide (MEPDG) (ARA, Inc., 2004), as shown in the following equations (factors taken into account for predicting rut depths are measured strain, layer temperature, and number of load repetition):

$$RD_{total} = RD_{AC} + RD_{Base} + RD_{Subgrade} \tag{2.10}$$

$$RD_{total} = H_{AC} \times \varepsilon_{p_{AC}} + H_{Base} \times \varepsilon_{p_{Base}} + H_{Subgrade} \times \varepsilon_{p_{Subgrade}} \tag{2.11}$$

$$\varepsilon_p = \varepsilon_r K_Z \beta_{r1} 10^{K_{r1}} T^{K_{r2}\beta_{r2}} N^{K_{r3}\beta_{r3}} \tag{2.12}$$

where

H	=	layer thickness (mm);
ε_p	=	plastic (inelastic) vertical strain;
ε_r	=	resilient strain;
T	=	layer temperature (°F);
N	=	number of load repetition;
$\beta_{r1}, \beta_{r2}, \beta_{r3}$	=	local calibration coefficients;
k_{r1}, k_{r2}, k_{r3}	=	plastic deformation factors; and
K_Z	=	depth function factor.

Another M-E model was developed using data collected from the WesTrack experiment (Deacon et al., 2002). As shown in the following equations, this model takes into account the measured strain, stress, and load cycles to predict rut depths.

$$\gamma_p = a \exp(b\tau)\gamma_e n^c \tag{2.13}$$

$$RD_{AC,j} = Ka \left[\left(\frac{\gamma_{p,j-1}}{a_j} \right)^{1/c} + \Delta N_j \right]^c \tag{2.14}$$

$$RD_j = d_j \left[\left(\frac{RD_{j-1}}{d_j} \right)^{1/e} + \Delta N_j \right]^e, d = \frac{f}{(1.05 \times 10^{-9} \varepsilon^{-4.48})^e} \tag{2.15}$$

where

γ_p	=	plastic (inelastic) shear strain;
γ_e	=	corresponding elastic strain;
τ	=	corresponding elastic shear stress;
N	=	number of load cycles;
j	=	jth hour of trafficking;
ε_v	=	compressive strain on top of subgrade; and
a, b, c, d, e, f	=	coefficients.

2.5.3 Issues of Rut Deterioration Models

Although extensive studies have been conducted to predict pavement rutting progression using empirical and mechanistic approaches, most existing models have been designed or used as means of pavement design. The performance of these models, however, can have high variation. For example, an NCHRP study compared field-measured rut depths with model-predicted rut depths (Quintus et al., 2012), and their results, as depicted in Figure 2.20, indicate that these existing models cannot accurately predict rut depth development.

One common feature of existing rut deterioration analysis and models is that they all use rut depth as the sole indicator. However, as discussed previously, rut depth itself cannot represent the true 3D rut shape and its deterioration behavior. With the advancements in sensing technology, high resolution 3D pavement data can be collected at multiple timestamps. Deterioration of 3D rut shape, nevertheless, has not been studied. There is a need,

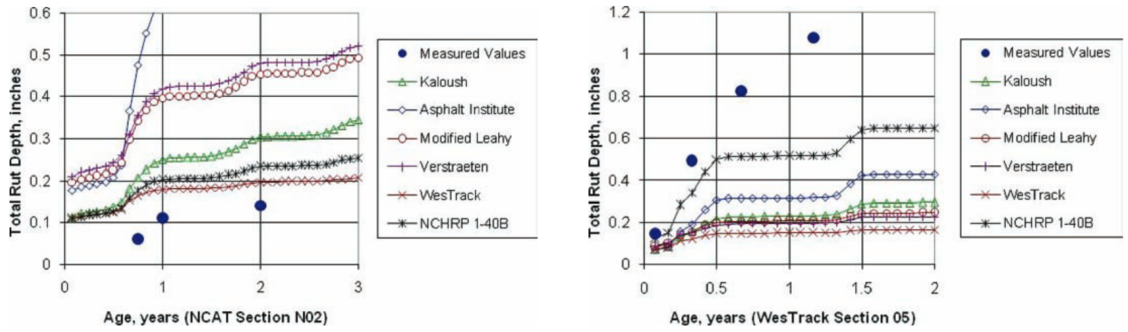

(a) Predicted rut depths for the NCAT Test Section N02.

(b) Predicted rut depths for WesTrack Test Section 05.

Figure 2.20: Observed and Predicted Rut Depths (Quintus et al., 2012)

therefore, to develop a methodology that enables the use of long-term 3D pavement data to better characterize and quantify the deterioration of 3D rutting.

2.6 Literature Review on Rut Classification

To determine the actual cause of rutting, many have argued that a trench cut is the only approach. However, taking a trench cut eliminates the possibility of doing preventive maintenance and minor rehabilitation; it is not a feasible solution at the transportation agencys expense in most cases unless the pavement is scheduled to be rehabilitated. As a result, methods have been developed to use various rut parameters, such as the positive and negative areas defined above, to help characterize the condition of ruts and inform possible cause. These studies were summarized below.

2.6.1 Rut Classification Methods

Most literature has used different features of transverse profiles as a means to pinpoint different rutting mechanisms (Fang et al., 2004; Morosiuk et al., 2004; Simpson et al., 1995; Villiers et al., 2006; White et al., 2002). Simpson et al. categorized transverse profiles into the four categories shown in Figure 2.21 based on the linear elastic theory (Simpson et al., 1995). In order to determine and differentiate rut mechanisms, the authors first identify the areas enclosed by the profile and the straight line that connects two end points of the

profile. Among the identified areas, those above the straight line are considered positive areas and those below are considered negative areas. Using these areas, two parameters, total distortion and distortion ratio, were used for determining the causes of rutting. Total distortion is calculated by subtracting the sum of negative areas from the sum of positive areas, and distortion ratio is the ratio of the sum of positive areas to the sum of negative areas. Using these two parameters, Table 2.3 summarizes the corresponding criteria for different types of rutting (Simpson et al., 1995).

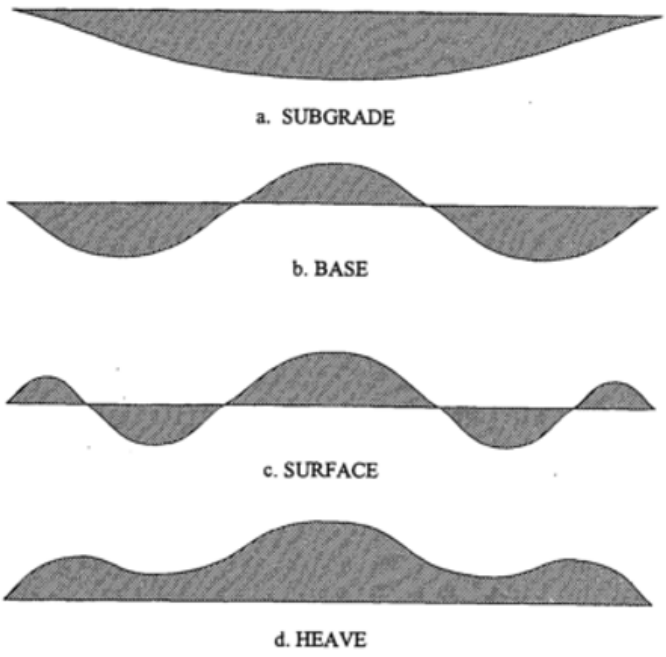

Figure 2.21: Illustration of Rut Types (Simpson et al., 1995)

Table 2.3: Criteria for Determining Rut Types (Simpson et al., 1995)

Type	Total Distortion (mm^2)	Distortion Ratio	Number of Sections
Surface	700 <x <5000	1.25 <x <3.0	15
Base	-4500 <x <700	0.4 <x <1.25	24
Subgrade	<-4500	<0.4	61
Heave	>5000	>3.0	28

White et al. extended the study conducted by Simpson et al. by changing the fundamental assumption instead of using linear elastic theory; they conducted a series of

finite element analyses (FEA) using nonlinear viscoelastic theory (White et al., 2002). Five rutting failure modes, including rutting due to failures in hot-mix asphalt, base, subbase, and subgrade, as well as heave, were analyzed and the results are shown in Figure 2.22. They modified the sorting criteria Simpson et al. proposed, also using total distortion and distortion ratio, and the results are shown in Table 2.4.

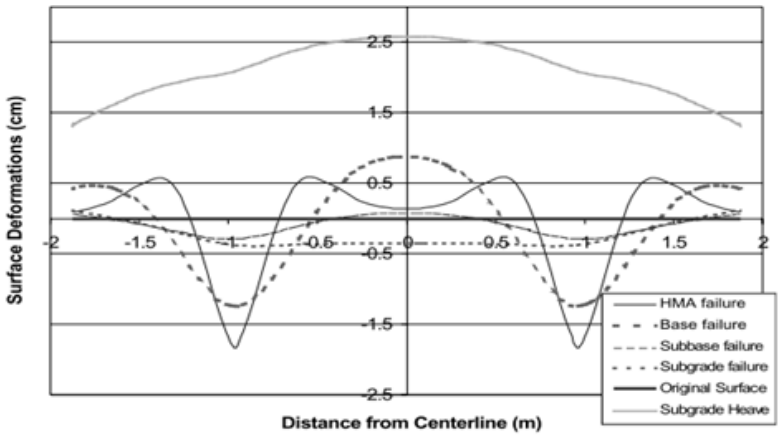

Figure 2.22: Profiles Derived from Different Rut Types (White et al., 2002)

Table 2.4: Criteria for Determining Rut Types (White et al., 2002)

Type	Total Distortion (mm^2)	Distortion Ratio	Other Conditions
Surface	-7500 $<$x $<$0	0.3 $<$x $<$0.8	Curvature reversal between wheelpaths
Base	-7500 $<$x $<$5000	0.4 $<$x $<$3.0	No curvature reversal between wheelpaths
Subbase/ Subgrade	$<$-2000	$<$0.5	N/A
Heave	$>$5000	0	N/A

The same parameters (total distortion and distortion ratio) were also used by Fang et al. (2004). In addition to these two features, Fang et al. incorporated rut depth as the third parameter to be considered. Nevertheless, instead of directly using these three parameters for determining rutting causes, Fang et al. first used rut depths and total distortion areas obtained from FEA simulation results to establish simple linear models to predict total distortion areas of different rut types from rut depths. These predicted total distortions were then used with the distortion ratio, the total distortion, and the reversal curvature

feature for determining rut types, as shown in Figure 2.23 (Fang et al., 2004).

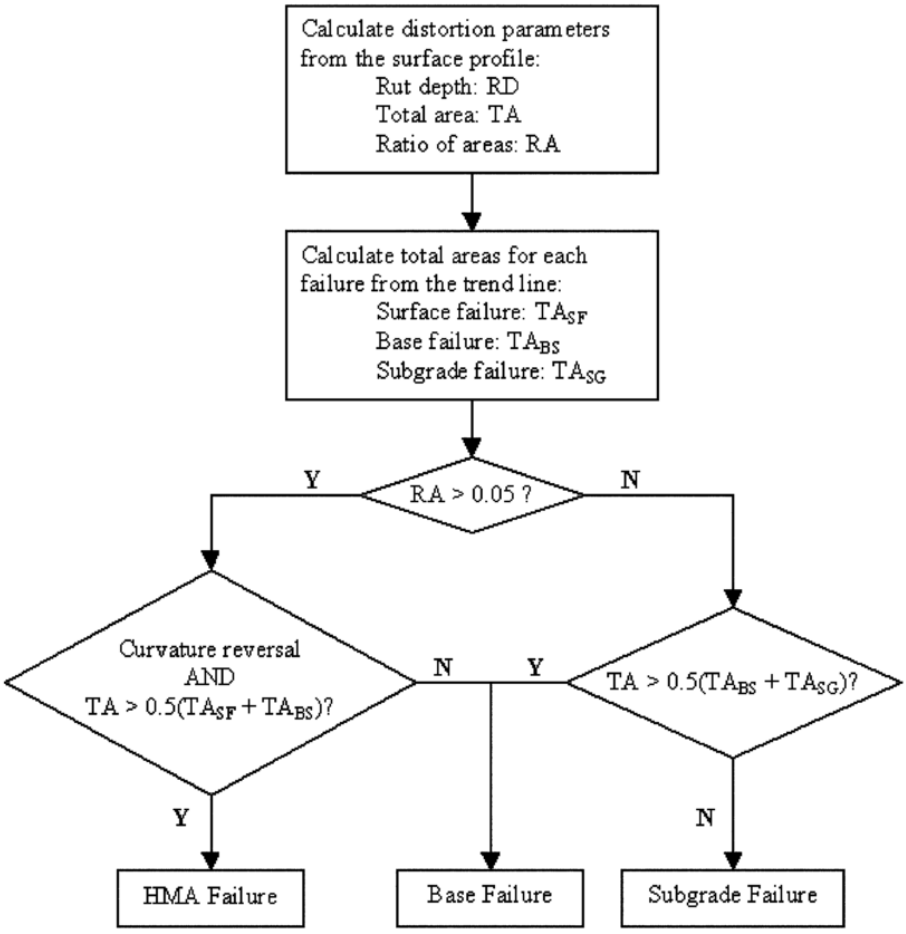

Figure 2.23: Decision Flowchart for Determining Pavement Layer Failure (Fang et al., 2004)

In addition to parameters derived from transverse profiles of pavement surfaces, other studies used additional physical features of different pavement layers, such as air voids in the AC layer, base layer moduli, and the shape of the base layer, to help categorize rutting (Villiers et al., 2006). Figure 2.24 shows the use of surface profiles, layer modulus, layer thickness, and air voids for determining rut types (Villiers et al., 2006).

Through discussions with senior pavement engineers of GDOT and review of some studies, it is identified that the length of rutting and the change of rut shape along time can also be important parameters for identifying the causes of rutting (Lenngren, 1988). For example, if rutting occurs along a long pavement section, it is more likely to be caused by

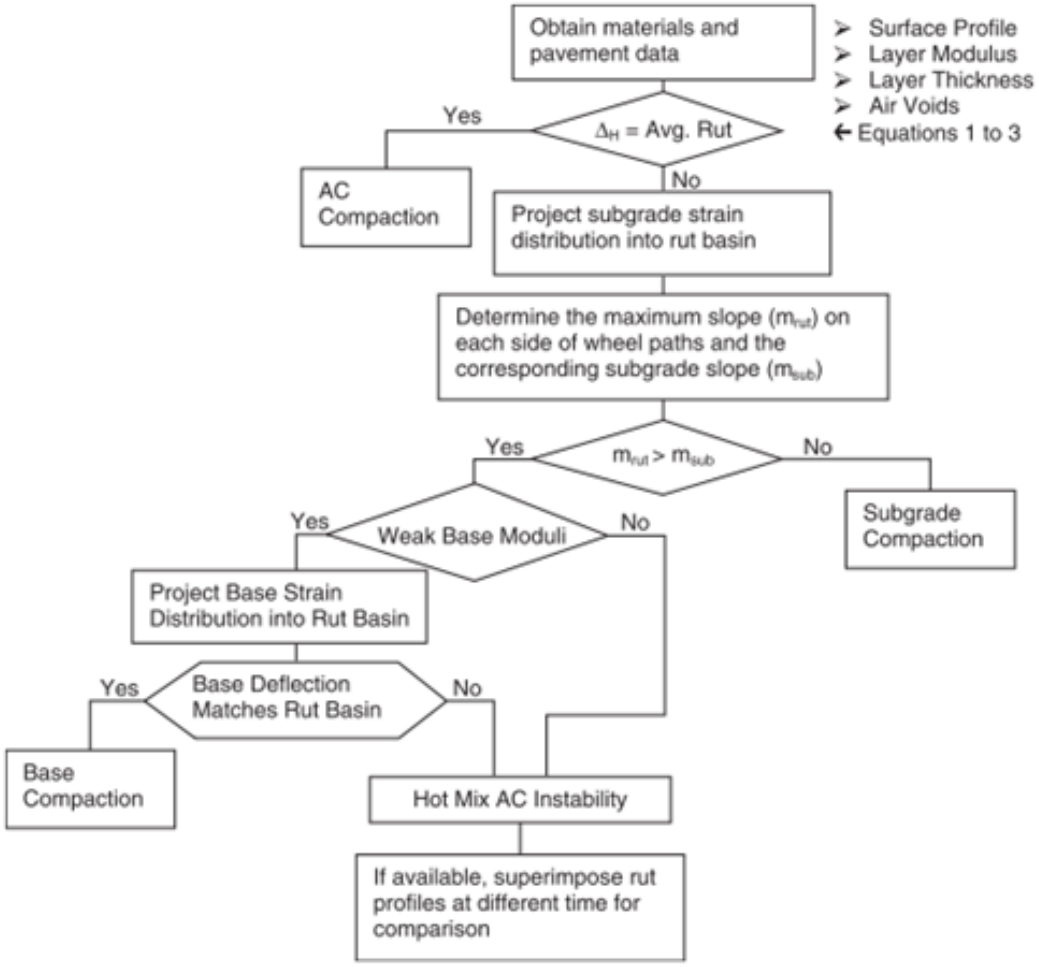

Figure 2.24: Decision Flowchart for Determining Cause of Rutting (Villiers et al., 2006)

issues during construction (e.g., too much asphalt in the surface layer mix); however, if rutting occurs only in a short segment of the pavement, it is more likely caused by issues within that locality (e.g., existence of other distresses or failure in the supporting layers). Time can also play an important role in determining the causes of rutting. For example, if rutting progresses quickly in the first years after construction, it is more likely to be caused by lateral distortion issues; slow progressing rutting is more likely caused by the densification of pavement in wheelpaths due to the air voids (Villiers et al., 2006).

2.6.2 Issues of Existing Rut Classification Methods

Although several studies in the literature have attempted to correlate the cause of rutting to the shape of transverse profiles, it remains challenging and an open question. Some challenges and gaps have been identified through the review presented, and they are summarized below:

- Lack of sufficient data made the selection of rut parameters for rut classification challenging. Existing methods use rut depth, total distortion, and distortion ratio to classify ruts; however, the effectiveness of these selected parameters with regard to predicting classifications of rut need to be further verified. With the advancement in sensing technology, more comprehensive 3D rut features can be calculated and derived; there is a need to explore how these 3D parameters can enhance the classification of rutting.
- In addition to existing rut parameters, change of rut shape over time can potentially provide useful information for understanding the deterioration and differentiating the cause of ruts. However, limited studies have attempted to utilize temporal features of rutting for the aforementioned purposes. There is a need, therefore, to develop a methodology to derive temporal characteristics of 3D rutting and use them to quantify rut deterioration and further support rut classification.

2.7 Summary

In this chapter, studies on the data collection, characterization, deterioration, and classification of ruts have been reviewed and summarized. Review of the literature and current practices indicates that several challenges may hinder state DOTs from effectively utilizing 3D pavement data and benefiting from the promising features of sensing technology. The following are some key findings of the literature review:

- There is a lack of methods to register multi-timestamp 3D data for characterizing

and studying 3D rutting and its deterioration. Sources of error and data variation make it unreliable to directly compare pavement conditions at larger scales (e.g., project-level) using 3D pavement data collected at different timestamps. In fact, existing studies that attempted to study the progression of pavement distresses using 3D pavement data have been done at a small scale (e.g., 100-ft section) with limited data (e.g., 2 timestamps). There is a need to develop a robust data registration method that registers multi-timestamp pavement data in the 3D space in support of 3D rut characterization and deterioration analysis.

- Current practices use rut depth as the primary parameter as a means of pavement rut evaluation, monitoring, and deterioration modeling. However, rut depth itself may not be able to fully characterize the conditions and deterioration of ruts. With the advancement in sensing technology, detailed 3D shape of rutting and its deterioration can be accurately captured. Therefore, there is a need to evaluate and characterize the 3D rut shape and quantify its deterioration using long-term 3D pavement data.
- Existing rut classification literature uses a limited number of rut parameters to identify the cause of rutting. With newly available spatial and temporal 3D rut characteristics, there is a need to examine the correlations among rut parameters and rut classes, identify key rut parameters that can best reveal rut causes, and develop enhanced rut classification models.
- With the advancement in sensing technology, more and more high-resolution 3D data can be available to state DOTs. However, the amount of data may far exceed the storage and processing capacity of these agencies. There is a need to develop effective sampling strategies to distill critical and useful information from these data while minimizing the amount of data to be processed.

CHAPTER 3
METHODOLOGY

In this chapter, a spatiotemporal methodology (see Figure 3.1) is proposed to register multi-timestamp 3D pavement data. The registered data are used to characterize 3D rut shape and quantify its deterioration. The derived spatial and temporal characteristics of ruts are further applied to classify the causes. Moreover, an iterative static sampling simulation is performed to examine the sensitivity of the distribution of rut parameters under different data sampling intervals. A dynamic sampling strategy is proposed for state DOTs to effectively acquire useful information from 3D pavement data. The following sections summarize the proposed methodology.

3.1 Long-term 3D Pavement Data Collection

3.1.1 Data Collection System

The LCMS system, consisting of two line laser sensors, is mounted on the Georgia Tech Sensing Vehicle (GTSV; see Figure 3.2) to collect long-term 3D pavement data in this research. The GTSV, sponsored by the United States DOT, is a sensing vehicle equipped with and integrates emerging sensing technologies, including 2D imaging, 3D laser imaging (LCMS), 3D light detection and range (LiDAR), the global positioning system (GPS), and an inertial measurement unit (IMU) (Tsai and Wang, 2014). Overall setup of the system is depicted in Figure 3.3. The two laser units that are mounted approximately 2 meters apart and 2.25 meters off the ground. The sensors are installed at a yaw angle of 10° to avoid signal crosstalk. A 50-mm overlap between the coverage of the two sensors is designed to ensure complete coverage of the lane.

Resolution of the system is approximately 1 mm in the transverse direction (x-axis), 5

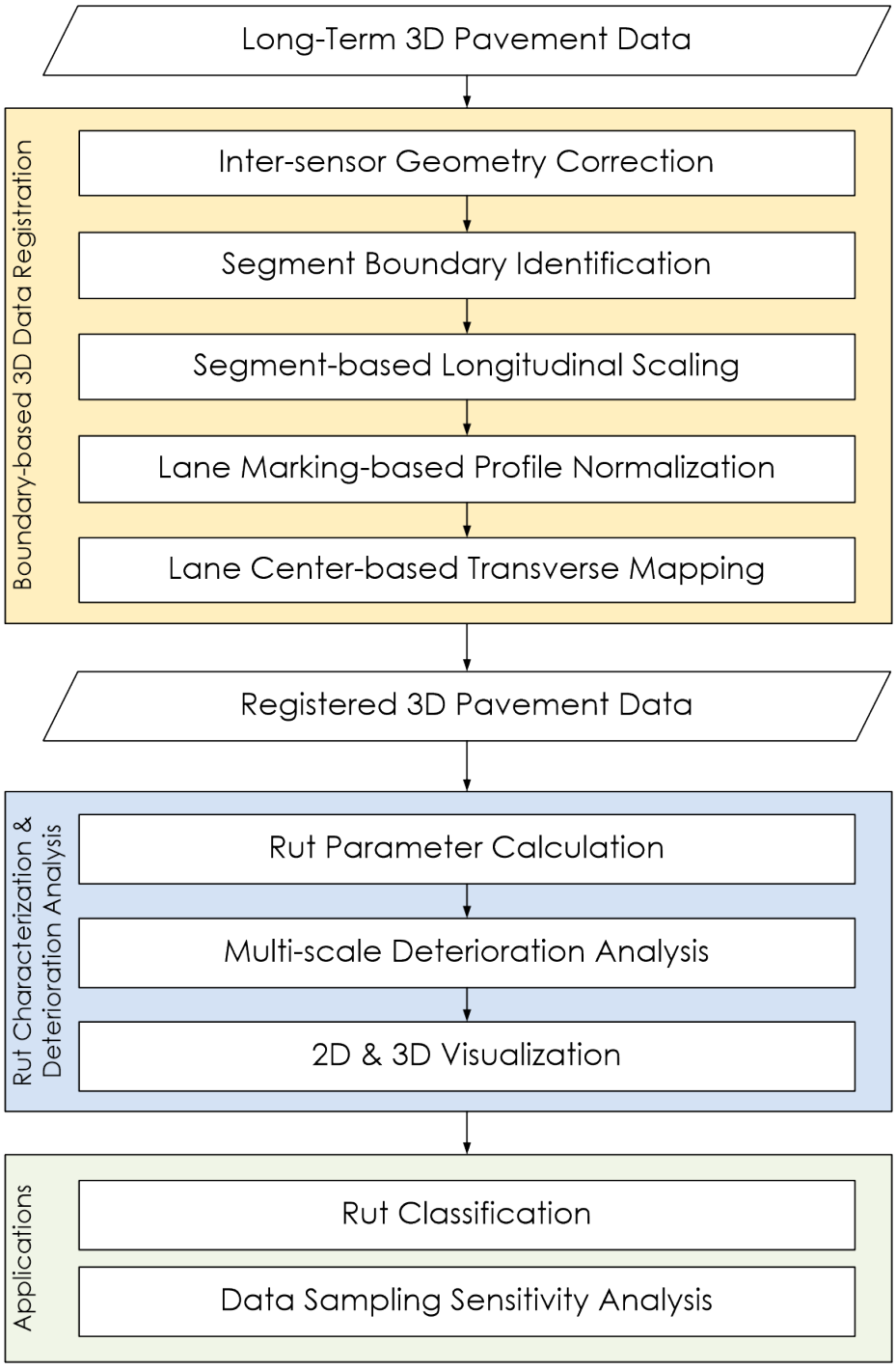

Figure 3.1: A Spatiotemporal Methodology for Registering Long-Term 3D Pavement Data for Characterizing 3D Rut Shape and Quantifying Rut Deterioration Behaviors

Figure 3.2: Georgia Tech Sensing Vehicle

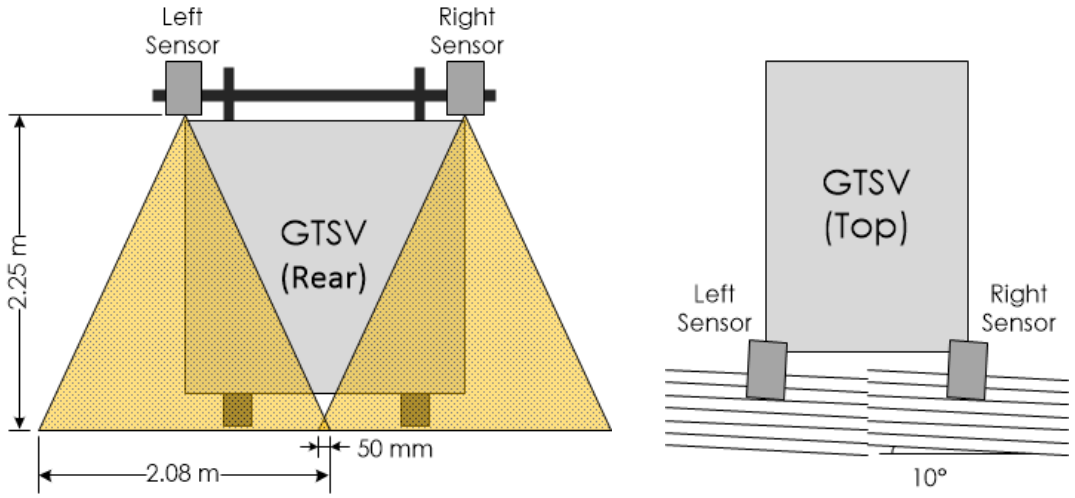

(a) Rear View

(b) Top View

Figure 3.3: Illustration of Laser Scanning System Setup on GTSV (Adapted from Li (2012))

mm in the longitudinal direction (y-axis), and 0.5 mm in the elevation direction (z-axis). With this setup, the system acquires 4,160 3D measurements per profile (2,080 per laser unit), which covers approximately 4-m across the lane. The system stores every 1,000 profiles into a file that contains both intensity and range data, as shown in Figure 3.4. The intensity data in Figure 3.4a shows the gray-scale information of the pavement appearance, and the range data in Figure 3.4b shows the depth information of the pavement surface in which the darker the pixel, the deeper and farther the pavement is from the sensor. The width of these images is 4,160 pixels, and each pixel corresponds to one 3D measurement

(i.e., 1-mm resolution). The height of these images is 5,000 pixels, and every 5 pixels along the vertical direction correspond to one 3D measurement (i.e., 5-mm resolution).

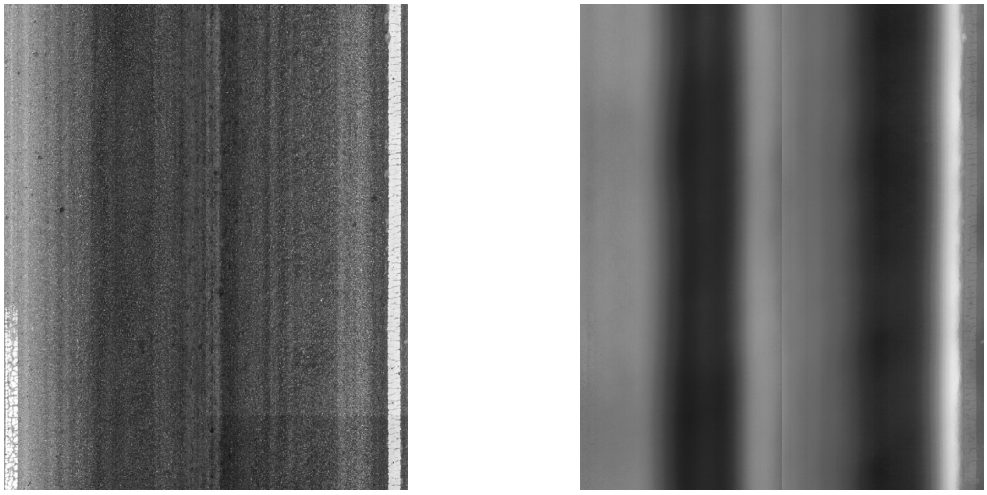

(a) Intensity Data (b) Range Data

Figure 3.4: Illustrations of 3D Pavement Data Collected by GTSV

3.1.2 Description of Long-Term 3D Pavement Data

Long-term 3D pavement data used in this research have been collected using the GTSV over the past five years on several selected routes and locations. The collected data are used to support the characterization and deterioration analysis of ruts in this research. As shown in Table 3.1, three routes with a variety of traffic characteristics have been selected. The 3D pavement data have been collected on each route at multiple timestamps that span from March 2012 to February 2016 (see Table 3.2).

Table 3.1: Long-Term 3D Pavement Data Descriptions

Route	Direction	Mileposts	ADT (Truck%)	Description
SR26	EB&WB	5.5-11.5	24,020 (11.94%)	A 4-lane major urban principal arterial road close to Savannah Port
SR275	NB	0-1	3,080 (N/A)	An undivided 2-lane rural collector
I95	SB	101-100	71,181 (12.65%)	A high-volume interstate highway

Table 3.2: Data Collection Dates for Long-Term 3D Pavement Data on Selected Routes

Timestamp	SR26	SR275	I95
1	03/21/2012	03/21/2012	03/21/2012
2	07/13/2012	07/13/2012	07/13/2012
3	03/20/2013	03/20/2013	03/20/2013
4	12/07/2013	12/07/2013	12/07/2013
5	07/18/2014	07/18/2014	07/18/2014
6	06/15/2015	06/15/2015	06/15/2015
7	02/17/2016	02/19/2016	02/19/2016

The GTSV and the long-term 3D data described in Tables 3.1 and 3.2 have been used for automatic crack detection and classification (Tsai et al., 2012a; Tsai and Li, 2012; Tsai et al., 2014a; Tsai et al., 2014c; Jiang and Tsai, 2016; Jiang, 2015), crack deterioration (Jiang et al., 2016), rut measurements validation (Li, 2012; Tsai et al., 2015; Tsai et al., 2013), raveling (Tsai and Wang, 2015a),and other pavement condition evaluation studies (Tsai et al., 2012c; Tsai et al., 2012b; Tsai et al., 2014b).

This dissertation uses this dataset to (1) register multiple timestamps of 3D data (Wang and Tsai, 2017c), (2) study 3D rut shapes and their deterioration behaviors (Wang and Tsai, 2017b), and (3) classify the causes of rutting (Wang and Tsai, 2017a).

3.2 Boundary-based Data Registration

In order to characterize 3D rut shape and quantify its true deterioration behavior, there is a need to develop a method that registers multi-timestamp 3D pavement data. In this study, 3D data registration refers to the process of matching two sets of 3D data so that registered data points in the two datasets correspond to the same physical points on a pavement surface in the real world environment. The proposed method, which uses segment boundaries as control points to register 3D pavement data, consists of the following steps:

- **Inter-sensor geometry correction**: A 3D pavement data pre-processing step that identifies possible inter-sensor geometry differences and corrects them. In this re-

search, inter-sensor geometries, including relative slopes and relative altitudes, are corrected and two profiles collected by the two sensors are stitched into a single profile.

- **Segment boundary identification**: Another pre-processing step that identifies the boundary features of a pavement segment (typically $\leq$ 1 mile) in 3D datasets. The boundaries identified in this research are the left and right lane markings, as well as the beginning and ending milepost locations in the intensity and range images (Figure 3.4). An automated lane marking detection algorithm is developed. Results of automated lane marking detection are then manually validated to ensure accurate data registration. Beginning and ending milepost locations are also manually identified using a graphical user interface developed in this study.

- **Segment-based longitudinal scaling**: For each segment, all timestamps of data are then scaled in the longitudinal direction (y-axis) so that they have the same data length. Herein, data length refers to the number of transverse profiles along the longitudinal direction.

- **Lane marking-based profile normalization**: While the first step addresses inter-sensor geometry differences and stitched half profiles into single profiles, this step accounts for the vehicle-pavement dynamics, such as the cross slope between the stitched profiles and the pavement surface. All transverse profiles are vertically transformed so that the elevations at both side boundaries of the lane (i.e., lane markings) are at zero.

- **Lane center-based transverse mapping**: Each normalized profile is then transversely translated (i.e., mapped) so that the x-coordinate of the lane center (i.e., middle point between left and right lane markings) is at 0 in the transverse direction (x-axis).

Long-term 3D pavement data collected at multiple timestamps can now be spatially and temporally registered using the proposed method. With the registered data, 2D and 3D visualizations are first generated to visualize the change of 3D rut shapes in the time dimension. Image subtraction is further implemented to show the exact change of 3D rut shapes between two timestamps. The visualization can help pavement engineers and researchers directly see how pavement surface changes over time. Locations with higher rut deterioration rates, in terms of change in depth, length, and volume, can also easily be identified to support cost-effective and timely treatment decisions.

3.3 3D Rut Characterization and Deterioration Analysis

The 3D rut shape and its deterioration behavior are further characterized and analyzed using case studies on SR26, SR275, and I95. The following describe the methods and procedures of the rut characterization and deterioration analysis:

- **Rut characterization**:
  - **Spatial rut parameters**: Spatial parameters are those that can be calculated using data collected at an individual timestamp. The majority of the existing rut parameters in the literature are spatial rut parameters. They include the following:
    - Transverse profile-based parameters, such as rut depth, rut width, cross-sectional area, positive and negative areas and their combinations
    - Longitudinal parameters, such as rut length and rut volume
  - **Temporal rut parameters**: Temporal parameters, including the mean elevated and depressed distances and the total elevated and depressed areas, are those that can only be calculated when comparing 3D pavement data from two or more timestamps. These parameters are calculated and presented in the rate of change per year.

- **Multi-scale deterioration analysis**: Rut deterioration is analyzed using descriptive statistics of rut parameters, such as boxplots that show the distribution, quartiles, and range of data, for all timestamps and assessing the trends of each rut parameter. 2D and 3D visualization is also used to visualize the exact deterioration of ruts at individual level.

3.4 Applications

The derived spatial and temporal rut parameters are further applied to (1) construct a classification model that categorizes causes of rutting based on the derived rut parameters of selected test sites; and (2) develop a sensitivity analysis study that assesses the effect of different data sampling intervals on the variability of rut parameters. These applications are further summarized below.

3.4.1 Rut Classification

Ruts can be caused by excessive asphalt in the HMA layer and insufficient structural support in one or more pavement layers. Different causes can be reflected by the shape of rutting in terms of the characteristics of its transverse profiles, they can also be associated with different lengths and volumes. A supervised classification model is constructed to identify the causes of rutting of nine selected test sites. Specifically, the following steps were conducted:

- Rut features: In addition to the spatial and temporal rut parameters discussed above, rut zonal parameters, including the maximum, minimum, average, standard deviation, and coefficients of a fitted quadratic function within each profile zones (e.g., wheel paths, lane center, and lane edge zones) are further defined and calculated.

- Experimental procedures: Four scenarios are designed to test the classification results using different combinations of parameters: (1) rut parameters based on the lit-

erature review; (2) all rut parameters, including spatial parameters considering both transverse and longitudinal directions and temporal parameters; (3) all but temporal parameters; (4) all but zonal parameters.

- Feature selection: A correlation-based feature selection algorithm is applied to select a subset of rut parameters as the key features that can better distinguish rut types and are less correlated with other parameters.

- Support vector machine (SVM): SVM models are constructed to classify rutting based on its cause. Two-thirds of the data are used as the training subset and one-third as the testing subset. Cross-validation is conducted using a 5-fold cross-validation.

3.4.2 Data Sampling Sensitivity Analysis

An iterative static sampling simulation is conducted to simulate different static data sampling intervals and assess their effect on the accuracy (e.g., mean and distribution) of rut parameters. A dynamic sampling strategy is proposed to sample data at varying intervals based on the sensitivity analysis results.

3.5 Summary

Detailed methods and results of the proposed methodology are summarized in the following chapters. Chapter 4 presents the proposed boundary-based data registration method and validation. Chapter 5 characterizes 3D rut shape, quantifies its deterioration using various spatial and temporal rut parameters. Chapter 6 presents the development and results of the rut classification application. Chapter 7 contains the sensitivity analysis of data sampling and proposes a dynamic sampling strategy for processing 3D pavement data.

CHAPTER 4
REGISTERING MULTI-TIMESTAMP 3D PAVEMENT DATA – A SEMI-AUTOMATED METHOD

In this chapter, a 3D pavement data registration method is proposed to enable the use of multi-timestamp 3D data in support of rut deterioration analysis. Although long-term network and project-level pavement rut conditions can be monitored using descriptive statistics of rut depth and other parameters, these statistics do not reveal the granularity of 3D rut shapes and their deterioration behaviors. With the full coverage and high-resolution 3D data being available, it is now possible to use 3D pavement data to study the true deterioration of ruts. However, as discussed previously in the literature review, various sources of error and data variability make it challenging to directly use raw 3D data for accurate deterioration studies. In fact, to the best of our knowledge, no methods have been proposed to attempt to register 3D pavement data among multiple timestamps to reveal 3D rut shapes and their deterioration using 3D sensing technology.

In this study, pavement data registration is defined as the process of matching two sets of 3D pavement data so that corresponding points in the two datasets correspond to the same physical points on the pavement in real-world environment. This definition is adapted from the definition of image registration by Fonseca and Manjunath (1996): "Image registration is the process of matching two images so that corresponding coordinate points in the two images correspond to the same physical region of the scene being imaged."

Image registration has been extensively studied in the literature (Brown, 1992). Numerous studies and applications have been developed in fields such as computer vision and pattern recognition (Lucas and Kanade, 1981; Lowe, 1999; Tsai et al., 2010), medical imaging (Friston et al., 1995; Freeborough et al., 1996), and remote sensing (Fonseca and Manjunath, 1996; Dawn et al., 2010). A general registration procedure consists of (1) fea-

ture identification; (2) feature matching; (3) spatial transformation; and (4) interpolation (Fonseca and Manjunath, 1996).

In a similar manner, the proposed method consists of a series of 3D data processing steps to register multiple timestamps of data. These steps, addressing some of the most common issues discussed in the literature, are as follows: (1) The inter-sensor geometry correction serves as a 3D data preprocessing step that corrects potential error in data; (2) The lane boundary identification step identifies the features of the datasets to be matched; (3) The longitudinal scaling step maps the data along the driving direction; (4) The profile transformation step transform data spatially to the same reference plane; and (5) The transverse mapping step maps the transformed profiles transversely.

A case study using 6 miles of 3D pavement data collected at two timestamps was conducted to validate the proposed method. With an overall root-mean-square-error of 1.49 mm, results of the case study show that the proposed method can effectively register multi-timestamp data in support of accurate rut deterioration analysis. The proposed method was also applied to register 8 timestamps of data on a 6-mile section on SR 26 westbound, results of this demonstration show promising features that lead to the subsequent analysis in this dissertation.

In the following sections, possible issues of unregistered data, detailed steps of the proposed method, as well as the case study are summarized.

4.1 Issues of Unregistered Data

In this section, several commonly observed and potential issues of the raw 3D pavement data, including inter-sensor geometries, vehicle-pavement geometries, and other random and systematic errors, are discussed. Note that inter-sensor geometries only exist in multi-sensor systems and do not apply to single-sensor systems. All other issues discussed in this section, on the other hand, are general to all automated data collection systems.

4.1.1 Inter-sensor Geometries

One of the first observed issues of the unregistered data is the variability introduced by the differences in inter-sensor geometries. This type of issues should be addressed for any two-sensor systems. For example, as shown in Figure 4.1, a typical two-sensor system is designed to have two parallel sensors that are mounted at the same altitude (i.e., $z_1 = z_2$) from the pavement horizon. Parallel herein refer to have the exact same pitch, roll, and yaw angles (i.e., $\theta_1 = \theta_2$, $\phi_1 = \phi_2$, and $\psi_1 = \psi_2$). However, in reality, it is unlikely that the two sensors would have the exact sensor angles and altitude.

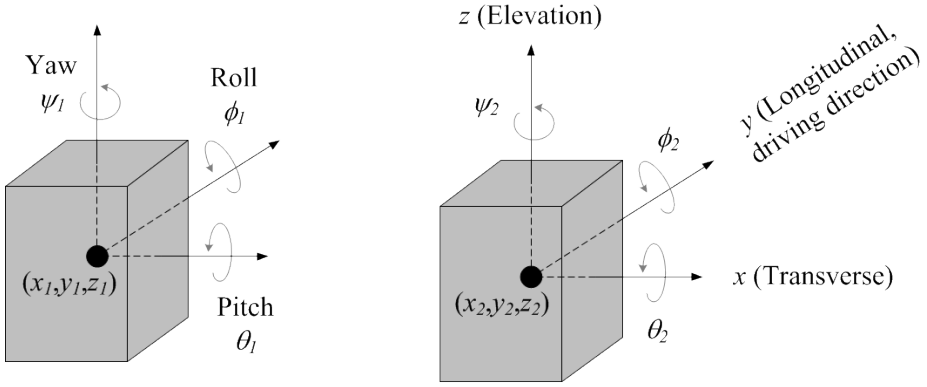

Figure 4.1: Geometries of Two Sensors

Inter-sensor geometries, defined as the difference in each type of sensor geometry between two sensors, can affect the accurate representation of the collected data. For example, as illustrated in Figure 4.2, with a -0.3° difference in the roll angles between the two sensors ($\phi_2 - \phi_1 = -0.3^\circ$), the combined profile (in orange) can significantly differ from the combined profile (in blue) from the parallel sensors.

Another observed issue is the possible elevation difference in the profiles collected by different sensors. As depicted in Figure 4.3, the two collected profiles, when put side by side, have an elevation gap between them. Several inter-sensor geometries can lead to this elevation gap. For example, inter-sensor roll angle, as discussed above, can result in artificially transformed profiles that result in elevation difference. In addition, inter-sensor altitude difference (i.e., $z_2 - z_1 \neq 0$) can also directly cause the observed elevation

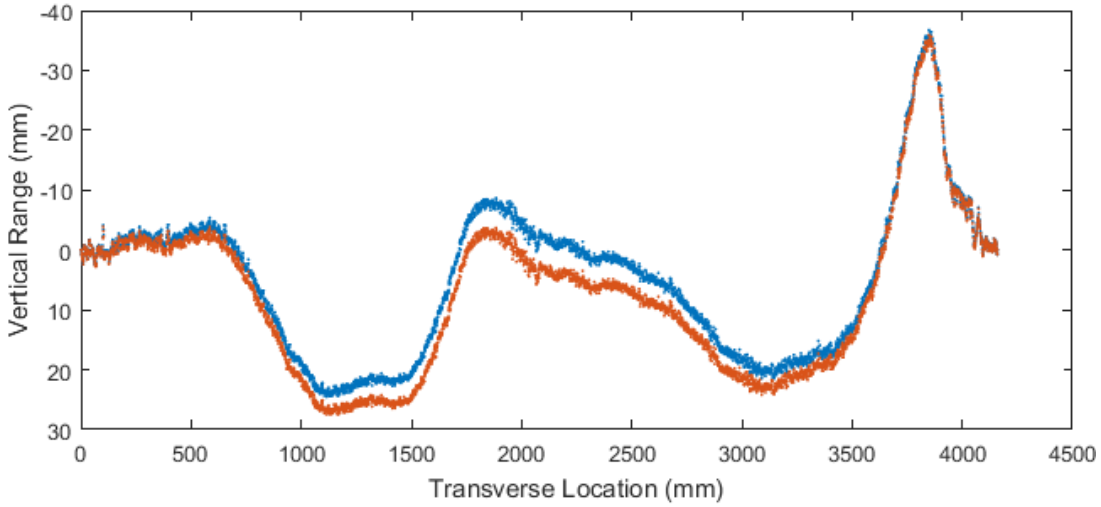

Figure 4.2: Illustration of the Effect of Inter-sensor Slope (Roll Angle) on Profiles

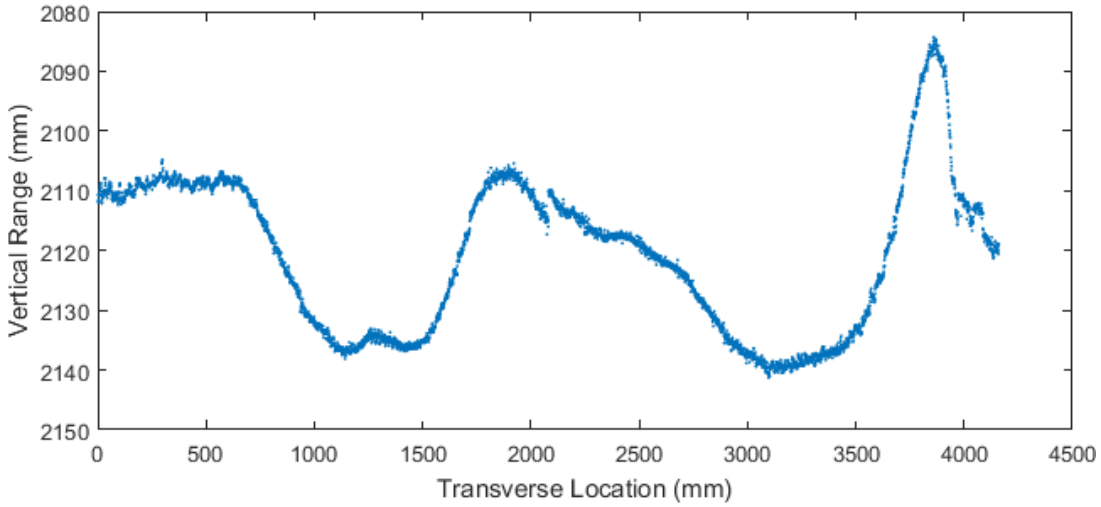

Figure 4.3: Illustration of the Effect of Inter-sensor Altitude on Profiles

difference.

Since one of the premises for deriving several rut parameters (e.g., positive and negative areas) in the literature is that a transverse profile across the entire lane is available, inter-sensor geometry differences need be accounted for in order to derive these rut parameters on a consistent basis. Among the four possible inter-sensor geometries, nevertheless, relative pitch and yaw angles may not have as significant effect as the differences in sensor roll angles and altitudes. For the pitch angle, if the two sensors have slightly different pitch angles, the profiles they collect would be shifted apart along the y-axis. For the yaw

angle, a difference in yaw angles would result in different orientations of the laser lines on the xy plane. Under the assumption that the shape of ruts does not change sharply over several meters along the longitudinal direction, the effect of the inter-sensor pitch and yaw angles can be negligible when these angles are small. The effect of inter-sensor roll angle and altitude, however, as depicted in Figures 4.3 and 4.2, can have significant impact on shape captured by the sensors and on the quantitative measurements. Therefore, these two inter-sensor geometries will be accounted for in the proposed method section.

4.1.2 Vehicle-Pavement Geometries

In addition to inter-sensor geometry issues, as depicted in Figure 4.4, geometry between vehicle and the road, i.e., vehicle pitch, roll, and yaw angles, as well as sensor altitude, may also cause variability in data. As shown in Figure 4.5, the two profiles were collected in two separate runs at the same location three days apart. Assuming the change in pavement surface shape was negligible between the two runs, these two profiles showed significant difference in their cross slopes. This difference can be the result of vehicle vibration, vehicle lateral displacement, and other possible factors. Difference in cross slope therefore hindered the applicability of two sets of data for direct comparison. In this study, a profile normalization process was proposed as part of the registration method to address this issue.

4.1.3 Other Potential Issues

Furthermore, due to varying tire pressure, pavement surface conditions, vehicle trajectories, resolution of the data collection triggering device, and other operational and systematic variation, differences in 3D pavement data collected at different timestamps are unavoidable. For example, although the GTSV is constructed and calibrated to collect transverse profiles at 5-mm intervals, the actual number of profiles collected over the same pavement sections at different timestamps may vary significantly, as shown in Table 4.1. This type of data variability can be introduced by systematic and operational errors. First, the line

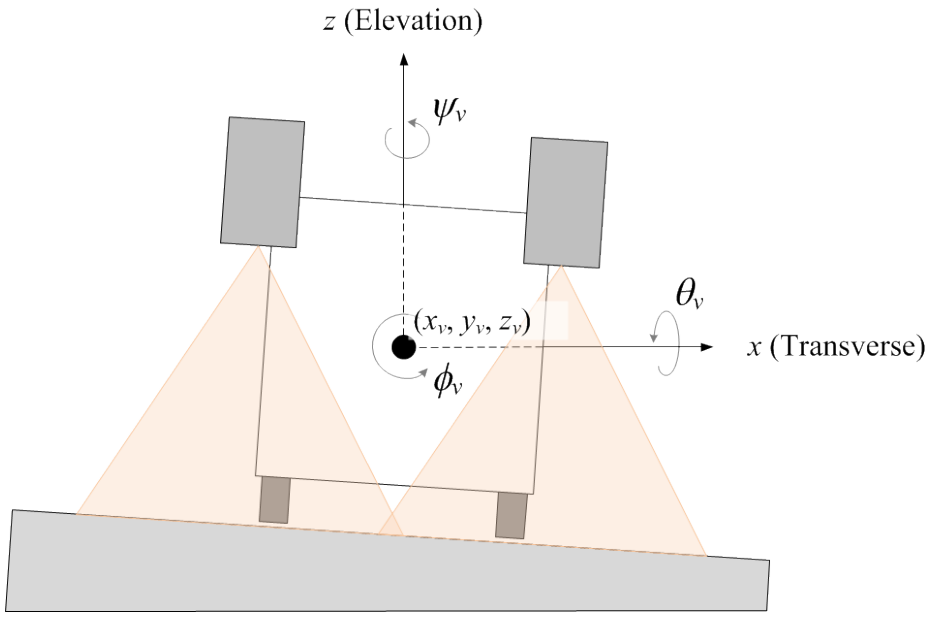

Figure 4.4: Vehicle-Pavement Geometries

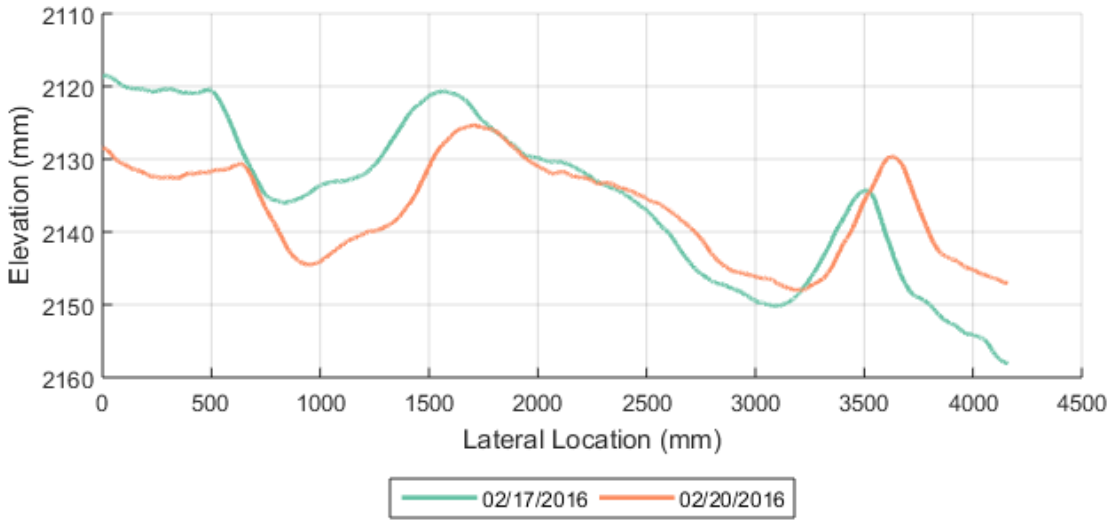

Figure 4.5: Profiles Collected at Same Location Show Different Cross Slopes

laser sensors are triggered by the distance measuring instrument (DMI) mounted on the right rear wheel of the GTSV. The DMI measures the rotation of the wheel and translates the rotation angle into the actual distance travelled. This can be affected by the actual tire pressure at the time of data collection, which can be influenced by temperature, pavement distresses, and the number of passengers in the van, etc. Second, the actual trajectory on

which the vehicle travels also affects the actual number of profiles collected. Even if the triggering distance of the DMI is fully calibrated, the number of transverse profiles collected is expected to be different because it is practically impossible to collect two runs of data along the exact trajectory without any lateral displacement. These systematic and operational errors, including the longitudinal and transverse data discrepancies discussed above, are further accounted for in the proposed method.

Table 4.1: Number of Profiles Collected for All Routes at Different Timestamps

Timestamp	SR26 EB	SR26 WB	SR275	I95
1	1,905,978	1,928,640	321,199	315,168
2	1,904,813	1,930,198	321,511	314,928
3	1,905,319	1,930,466	321,214	314,927
4	1,908,144	1,931,741	321,284	315,317
5	1,900,548	1,923,572	320,493	313,328
6	1,906,100	1,930,411	321,427	314,799
7	1,917,875	1,941,890	323,313	317,459

4.2 Methodology

To address possible issues discussed above and ensure fair comparison among data collected at different timestamps, a semi-automated data registration method was proposed. The proposed method consists of a series of data processing procedures, including inter-sensor geometry correction, segment boundary identification, segment-based longitudinal scaling, lane marking-based profile normalization, and lane center-based transverse mapping. Note that while this method was developed to register data collected by the GTSV, it should also be applicable to register other types of 3D pavement data collected in a similar manner. Data registration was implemented in Matlab R2015a with an Intel Core i7-4770 CPU @ 3.40GHz and 32GB RAM. Detailed steps of the proposed method are summarized in the following sections.

4.2.1 Inter-sensor Geometry Correction

As discussed in the previous section, inter-sensor geometries, including relative roll angle and relative altitude, were addressed in this study. The following subsections describe the detailed steps and formulation of the proposed method to correct inter-sensor geometries. Hereafter, we use slope interchangeably with roll angle.

Inter-sensor Slope Correction

To identify the inter-sensor slope, a calibration data was collected on a flat surface. As shown in Figure 4.6, the calibration data was collected in a garage with a flat concrete floor. For each sensor, 3D data within a region of interest (ROI), marked as the rectangle in Figure 4.6, was extracted.

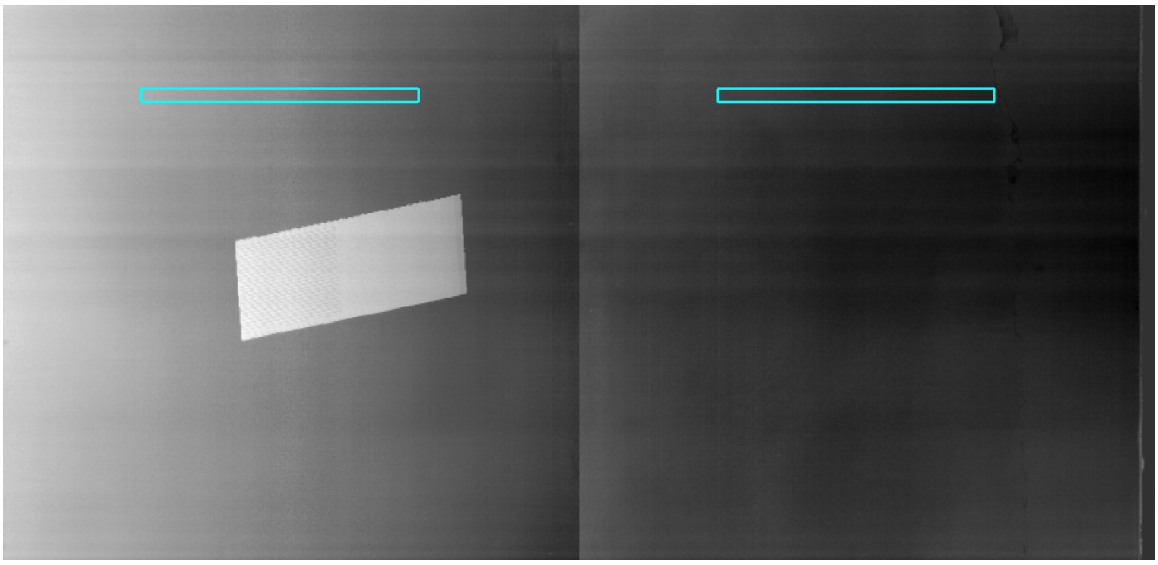

Figure 4.6: Regions of Interest for Deriving Inter-sensor Slope Using Calibration Data

The slope of each sensor was then calculated by fitting the data points in the corresponding ROI using a simple linear regression model as shown in Equation 4.1. As shown in Figure 4.7, two linear models were then fitted for the ROIs of Figure 4.6. The corresponding slopes for the left and the right ROIs were 0.0241 and 0.0100. With these slopes calculated, the inter-sensor slope, denoted as $\Delta\beta$, can be calculated using Equation 4.2.

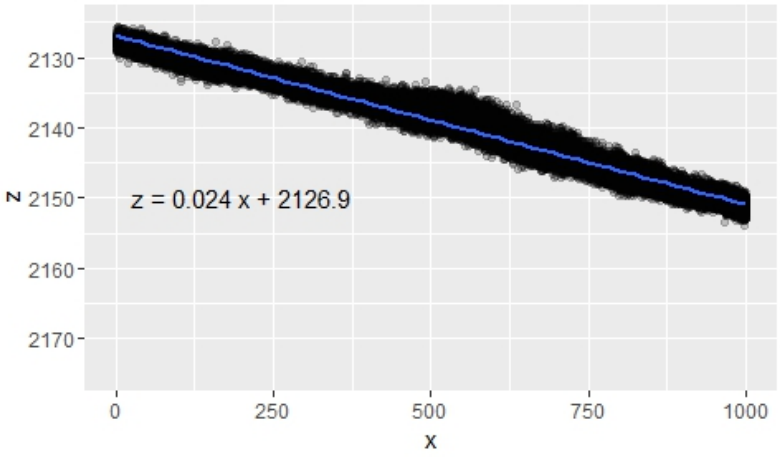

(a) Left ROI

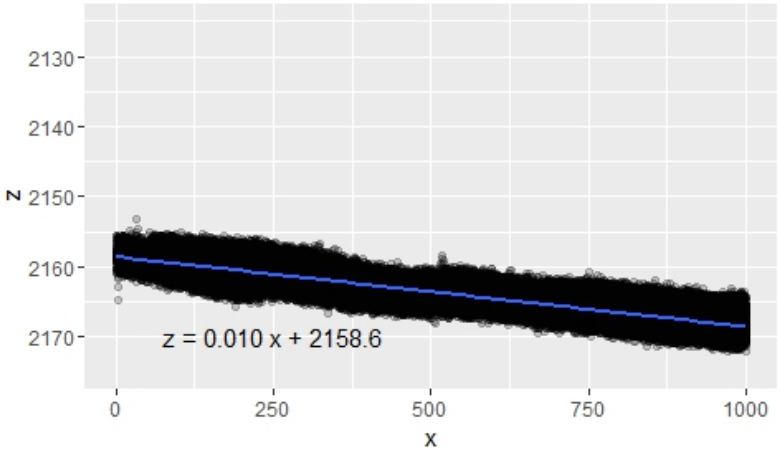

(b) Right ROI

Figure 4.7: Simple Linear Regression Models for ROI Data Points

$$\mathbf{z_i} = \alpha_i + \beta_i \mathbf{x_i} \tag{4.1}$$

$$\Delta\beta = \beta_2 - \beta_1 \tag{4.2}$$

where

$\mathbf{z_i}$ = data point elevation within ROI i;

$\mathbf{x_i}$ = data point location within ROI i along transverse direction;

$\Delta\beta$ = inter-sensor slope;

i = 1 for left ROI; and 2 for right ROI; and

α_i, β_i = linear model coefficients for ROI i.

To correct the inter-sensor slope, the profile collected by each sensor was transformed by half of the slope difference (i.e., $\Delta\beta/2$). For instance, in the above example, the inter-sensor slope was -0.0141, so each profile was transformed by a slope of 0.00705. In this case, shear transformation was used to transform a profile to the corrected slope. As depicted in Figure 4.8, the difference between shear transform and rotation is that shear transformation is transform along a single dimension (i.e., z-axis in this case), whereas rotation transforms the shape in both dimensions (i.e., xz plane). From a machine vision stand-point, when the view of sensor is top-down, it is deemed to be more accurate to use shear transformation than rotation, although the difference between the two can be negligible when the angle θ is small. Mathematically, to shear the green profile to the blue profile in Figure 4.8b, Equation 4.3 was applied.

$$\begin{bmatrix} \mathbf{x}' \\ \mathbf{z}' \end{bmatrix} = \begin{bmatrix} \mathbf{x} \\ \mathbf{x}m + \mathbf{z} \end{bmatrix} = \begin{bmatrix} 1 & 0 \\ m & 1 \end{bmatrix} \begin{bmatrix} \mathbf{x} \\ \mathbf{z} \end{bmatrix} \tag{4.3}$$

where

$\mathbf{z}, \mathbf{x}$ = coordinates of the original profile;

$\mathbf{z}', \mathbf{x}'$ = coordinates of the transformed profile; and

m = the correction slope.

For historical 3D pavement data that were collected without calibration data as discussed above, a similar approach can be applied to identify inter-sensor slopes. This post-processing technique involves the following steps: (1) finding a common flat rigid surface (e.g., a concrete slab or a bridge deck) that is collected in all previous timestamps; (2) col-

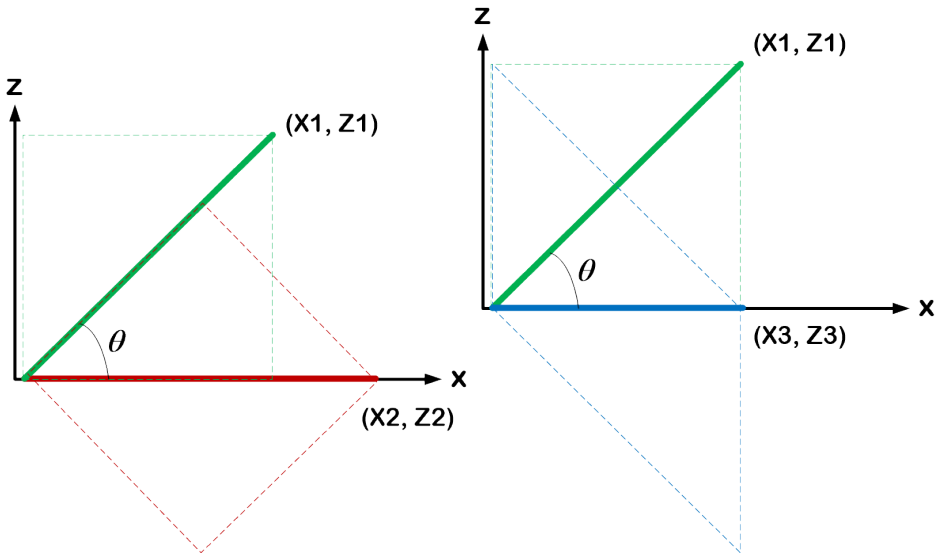

(a) Rotation (b) Shear Transformation

Figure 4.8: Illustration of Geometric Transformation Techniques

lecting data on this surface again (field data); (3) collecting calibration surface data; (4) extracting historical data and calculating the relative inter-sensor slope of each timestamp, (5) correcting the newest collected data using the calibration results in Steps 2 and 3; (6) correcting the rest of the timestamps of data using the relative inter-sensor slope calculated in Step 4; and (7) correcting the slopes of the rest of the timestamps.

Inter-sensor Altitude Correction

After the correction of the inter-sensor sensor slope, as a process of correcting the possible altitude difference between the sensors, two profiles are stitched together by translating the right profile along the z axis so that the elevation offset is eliminated.

The actual distance of this translation is the difference between the average elevations of the 20-mm data closest to lane center from both sensors. As defined in Equation 4.4 and illustrated in Figure 4.9, the right profile elevations were adjusted by adding the difference in the average elevations of last twenty measurements of the left profile and the first twenty measurements of the right profile.

$$\mathbf{z_r} = \mathbf{z_r} + (\bar{z}_{l_{20}} - \bar{z}_{r_{20}}) \tag{4.4}$$

where

$\mathbf{z_r}$ = right profile;

$\bar{z}_{l_{20}}$ = mean elevation of the last 20-mm of the left profile; and

$\bar{z}_{r_{20}}$ = mean elevation of the first 20-mm of the right profile.

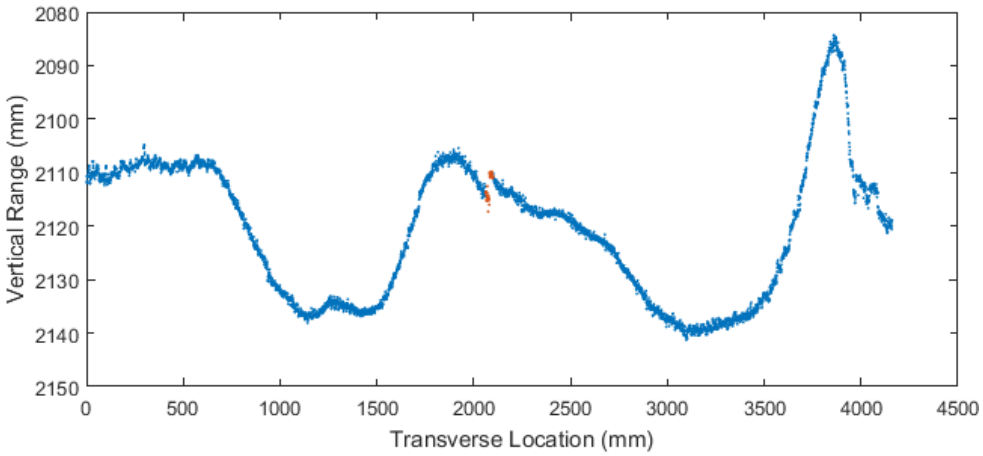

(a) Before Stitching

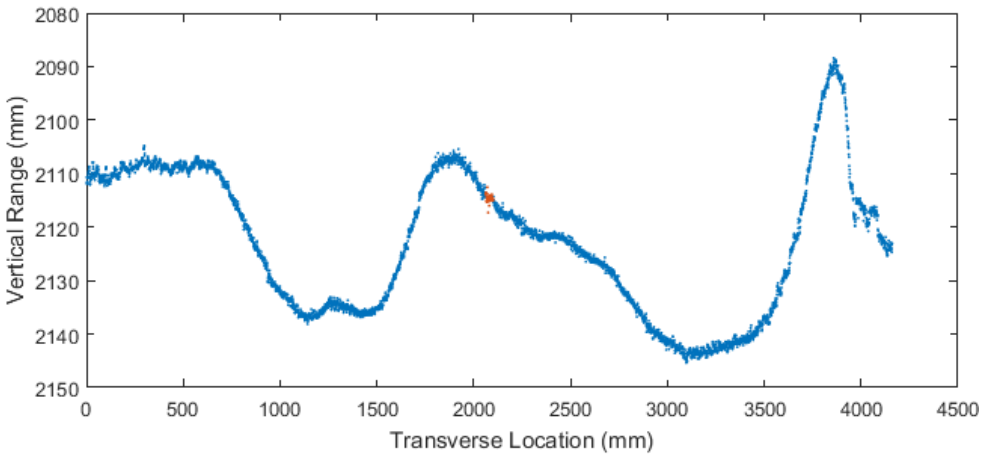

(b) After Stitching

Figure 4.9: Profile Stitching for Inter-sensor Altitude Correction

For pavement rutting analysis, high data resolution is not as needed as much as for the analysis of other pavement distresses, such as cracking or raveling. Therefore, to remove possible noise in the data, a 50 mm by 50 mm simple moving average window was used to

filter the stitched data; an example of a smoothed profile is shown in Figure 4.10.

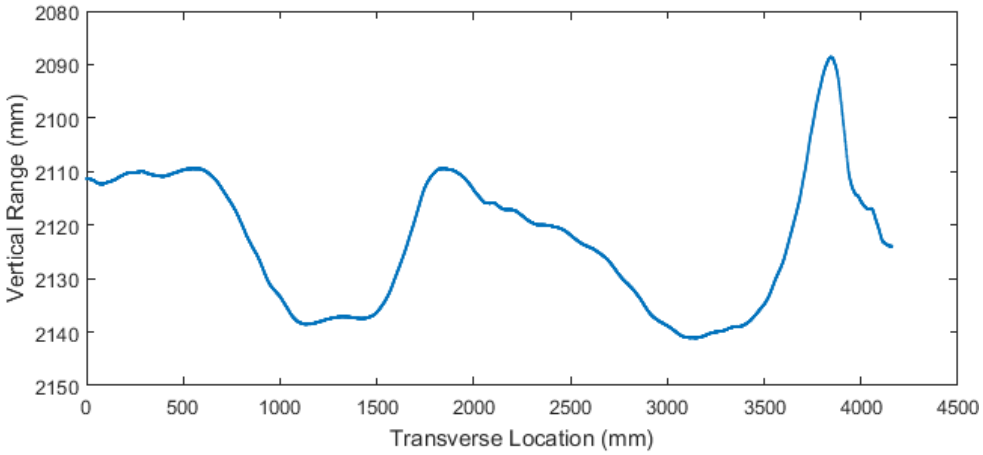

Figure 4.10: Inter-sensor Geometry Corrected Profile after Smoothing

4.2.2 Segment Boundary Identification

Similar to most image registration methods, features need to be identified in the datasets so that they can be cross-referenced. 3D pavement surface data, however, may not always have distinct features (e.g., edges and cracks) in the images as do many other image registration applications. One unique feature for most paved roads that state DOTs routinely monitor is the lane markings that defines the lane boundaries. Therefore, in this study, as depicted in Figure 4.11, it is assumed that lane marking locations do not change over time, and we use lane marking as the boundaries of the lane in the transverse direction (x-axis). In addition, for the longitudinal direction (y-axis), the beginning and ending mileposts of each segment are used as the longitudinal boundaries. The following sections describe the methods and procedures proposed to identify the boundaries of each segment at different timestamps.

Automatic Lane Marking Detection

Because of the nature of mobile data collection, i.e., lateral meandering, the data collected by the GTSV do not have fixed lateral coverage within the lane. In order to facilitate multi-year data overlay and other feature extraction functions, it is deemed necessary to detect

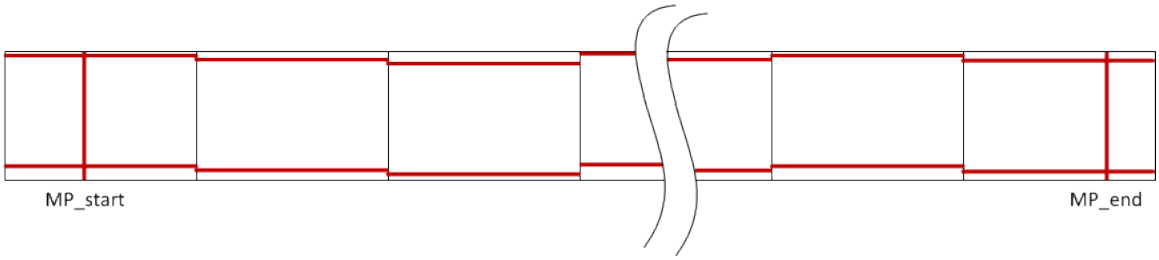

(a) Timestamp #1

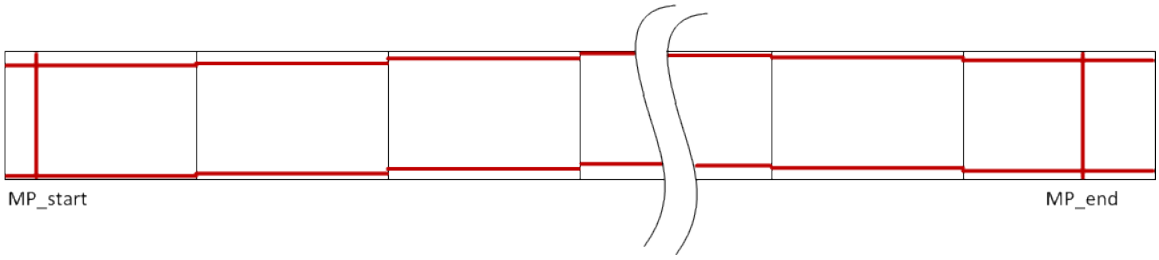

(b) Timestamp #2

Figure 4.11: Illustration of Segment Boundary Identification

lane marking locations in the data. Lane marking detection has been extensively studied in literature and is a fairly mature technology that has been used in autonomous vehicles and driver assistance warning systems (Bertozzi and Broggi, 1998; McCall and Trivedi, 2004; Chang et al., 2008; Wu et al., 2006). Using Figure 4.12 as an example, the following steps are used to automatically detect lane marking locations in the intensity images collected by the GTSV.

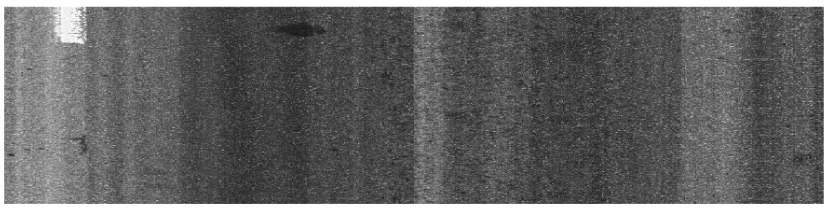

Figure 4.12: A 2D Intensity Image for Lane Marking Detection Illustration

- **Step 1: Dynamic Multiple Thresholding**

  In 2D intensity (grayscale) images, lane marking pixels usually are brighter than their surrounding pixels. Therefore, a thresholding method may be an effective way to identify lane markings within the image. However, because the composition of

intensity pixels within each image may vary significantly, using an absolute intensity value as the threshold may not yield good results. One alternative is to use a unique relative thresholding value for each image based on the distribution of the intensity values of the pixels. Otsu proposed a dynamic thresholding method that uses a dynamic (relative) threshold determined by analyzing the variable of the histogram of the image pixel values (Otsu, 1979), and it is applied separately to the left and right 2D images in this study to yield possible lane marking locations. Shown as the binary image in Figure 4.13, pixels above the dynamic threshold determined using the Otsus method are assigned a value of 1 (white pixels) and the rest of the pixels are assigned a value of 0 (black pixels).

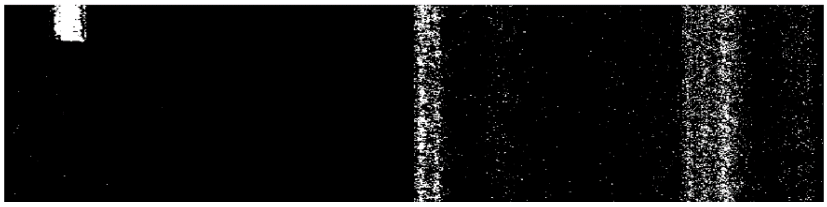

Figure 4.13: Intermediate Results after Dynamic Thresholding

- **Step 2: Erosion**

  Erosion is a common image processing technique for noise removal. For each pixel, its output value is the minimum value of all its neighboring pixels. For example, if a pixel has a value of 1 but one of its neighboring pixels has a value of 0, its value then becomes 0. The intermediate results after erosion are shown in Figure 4.14.

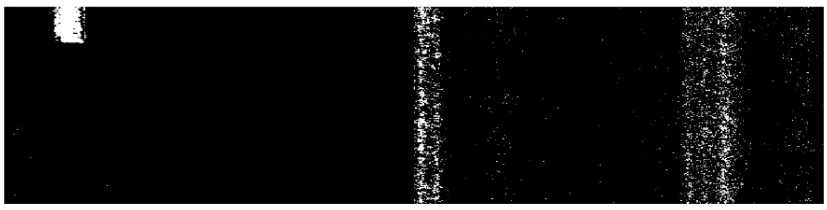

Figure 4.14: Intermediate Results after Erosion

- **Step 3: Connected Component Analysis**

  A connected component algorithm identifies connected white pixels and groups them

into one connected component. For any white pixel, if one or more of its 8 neighboring pixels are also white, these white pixels are determined to be connected. The algorithm searches the entire image and groups all connected white pixels into connected components. In this step, we heuristically eliminate any connected components that have fewer than 1000 pixels because they are more likely to be noise pixels instead of lane marking pixels. Figure 4.15 shows the intermediate results after the connected component analysis.

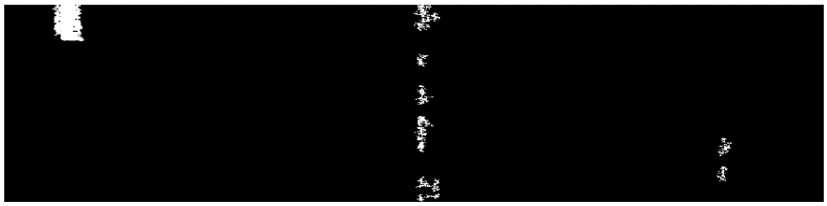

Figure 4.15: Intermediate Results after Connected Component Analysis

- **Step 4: Orientation Analysis**

  For the remaining connected components, their orientation is calculated using a function provided in Matlab (see Figure 4.16). Since lane markings are expected to be expanding in the longitudinal direction (i.e., approximately 90 degrees), any connected components with an orientation smaller than 50 degrees were removed from the detection results. Figure 4.17 shows the intermediate results after the orientation analysis.

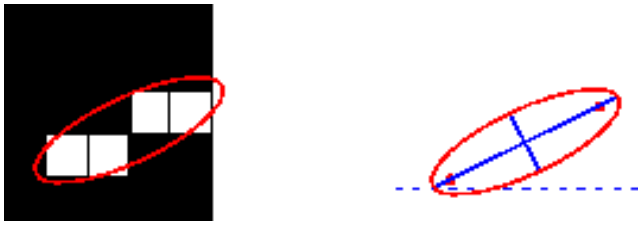

Figure 4.16: Connected Component Orientation (Source: matworks.com)

- **Step 5: Detected Region Location and Size Confirmation**

  The location and size of the bounding box of each remaining connected component

Figure 4.17: Intermediate Results after Orientation Analysis

is then checked using engineering judgment. First, if the bounding box is within the middle 1,200 vertical columns (middle of the image), it is considered a false detection because this region is most likely within the center of a lane, and no lane lines should appear in this region. In addition, if the bounding box of a connected component is larger than the expected size of a lane line, it is likely a false detection, such as pedestrian crossing markings, arrows, or other symbols. In this study, any connected component with a bounding box that has an area larger than 185,000 pixels is removed from the results. Figure 4.18 shows the immediate results after the location and size confirmation.

Figure 4.18: Intermediate Results after Detected Region Location and Size Check

- **Step 6: White Pixel Ratio Confirmation**

  The last step of the proposed lane marking detection algorithm is to check the ratio of the number of white pixels versus the number of black pixels within each bounding box. The idea behind this checkpoint is that any bounding box with sparse white pixels can very possibly be a false detection. In this study, if the number of white pixels is less than the number of black pixels (i.e., white pixel ratio less than 50%) within a bounding box, the corresponding connected component is removed from the results. Figure 4.19 shows the intermediate results after the white pixel ratio

confirmation.

Figure 4.19: Intermediate Results after Detected Region White Pixel Ratio Check

- **Step 7: Lane Marking Location Determination**

  In the final detected results, the image is again treated as the left half and the right half images. The rightmost column with at least one detected pixel in the left image is identified as the left lane boundary; similarly, the left most column with at least one detected pixel in the right half image is identified as the right lane boundary. Figure 4.20 shows the final detected lane boundary results overlaid on top of the original 2D intensity image.

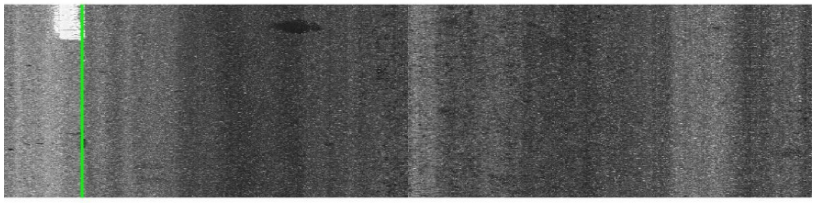

Figure 4.20: Final Lane Marking Detection Result

The following figures show some additional results of the proposed lane marking detection algorithm.

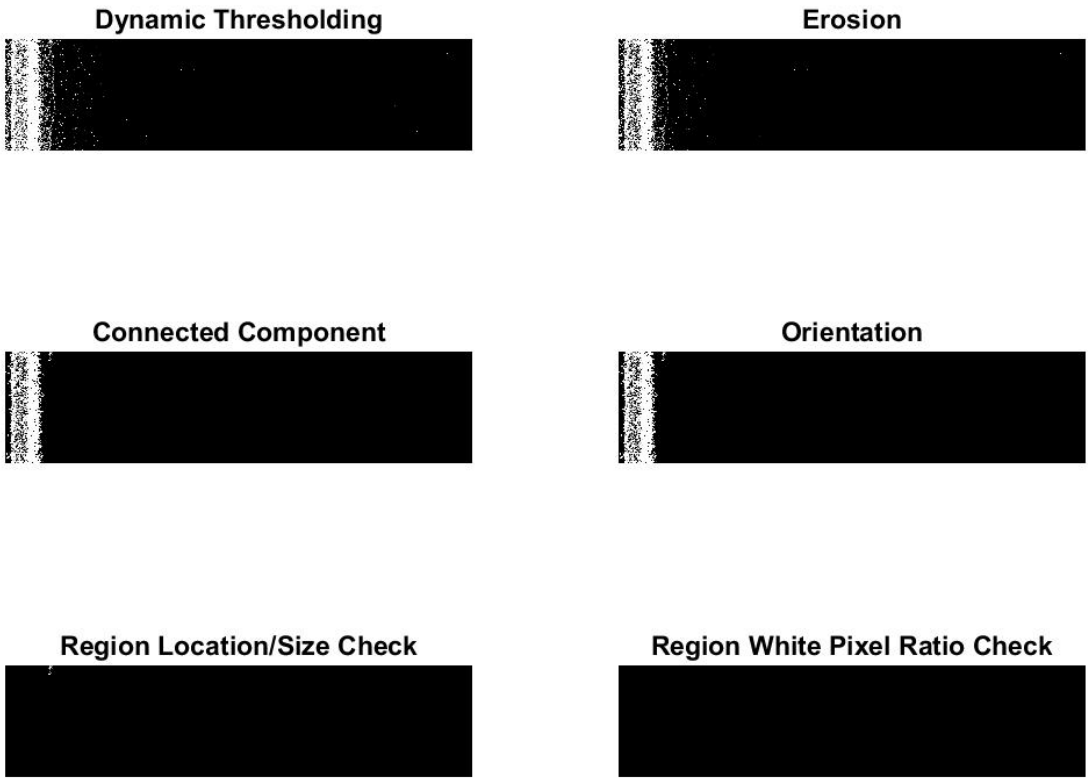

(a) Intermediate Results

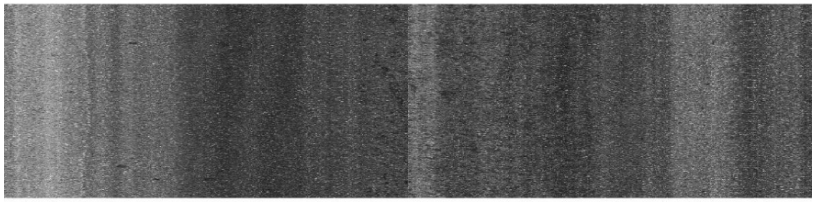

(b) Detection Results

Figure 4.21: Lane Marking Detection Example Results #2

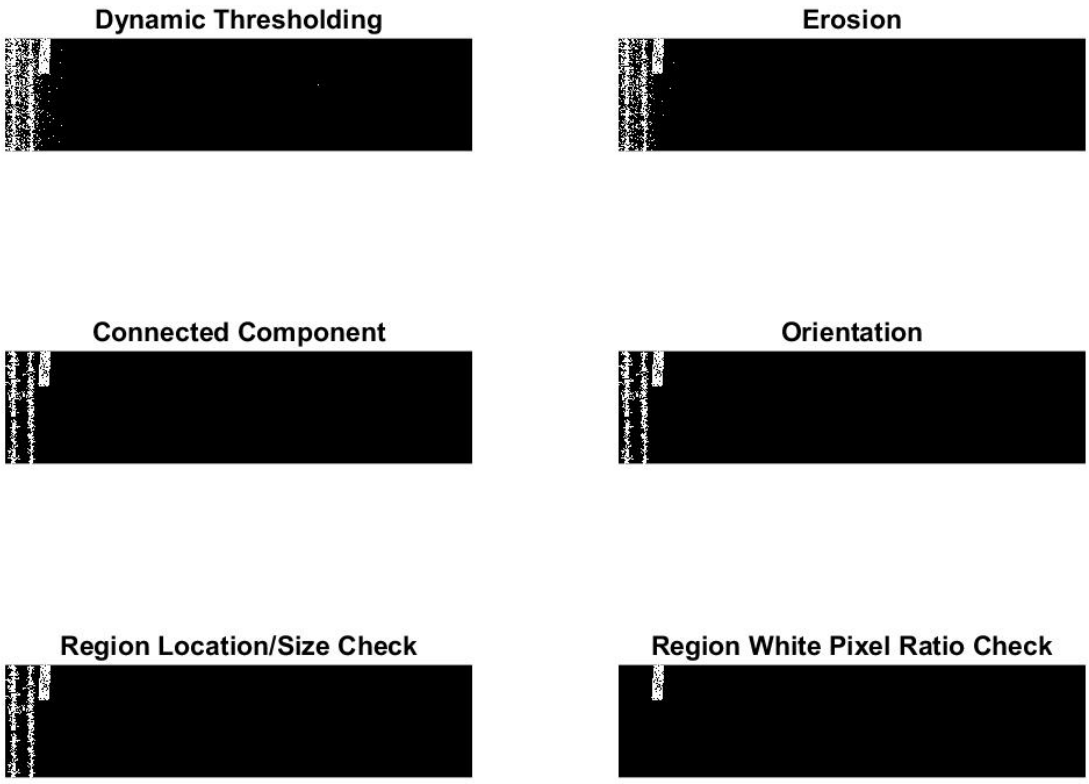

(a) Intermediate Results

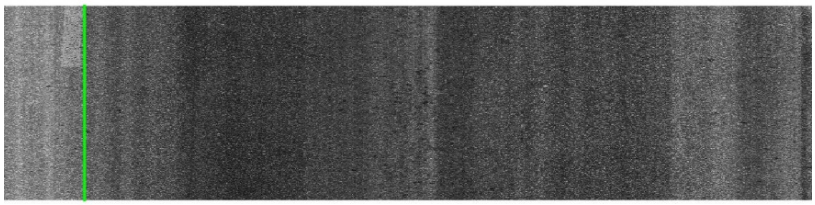

(b) Detection Results

Figure 4.22: Lane Marking Detection Example Results #3

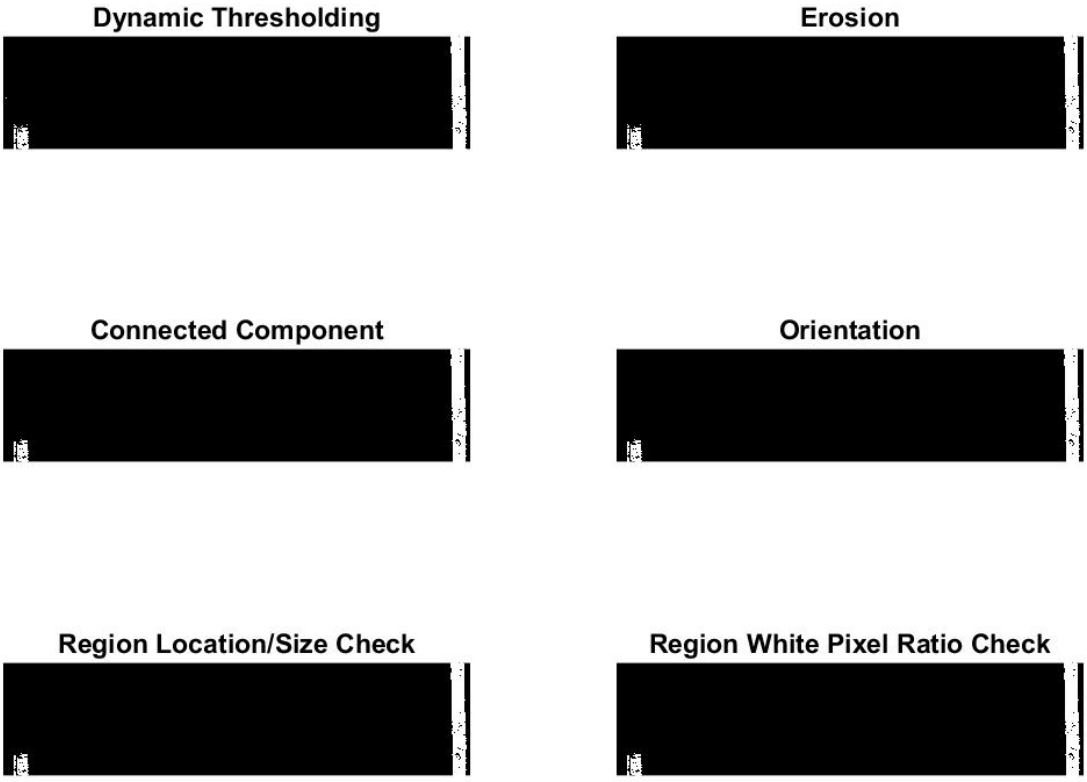

(a) Intermediate Results

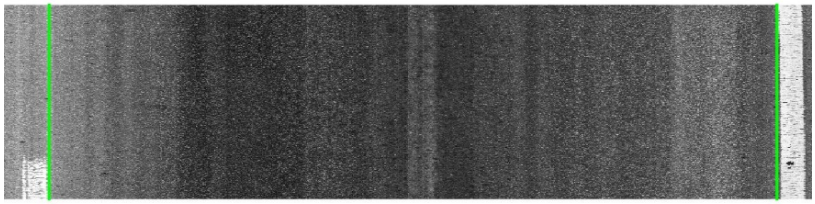

(b) Detection Results

Figure 4.23: Lane Marking Detection Example Results #4

Lane Marking Detection Validation

To ensure the accuracy of data registration, results of automatic lane marking detection were further manually validated using a graphic user interface (Figure 4.24) developed in this study. Any false detections and missed detections were corrected during this process.

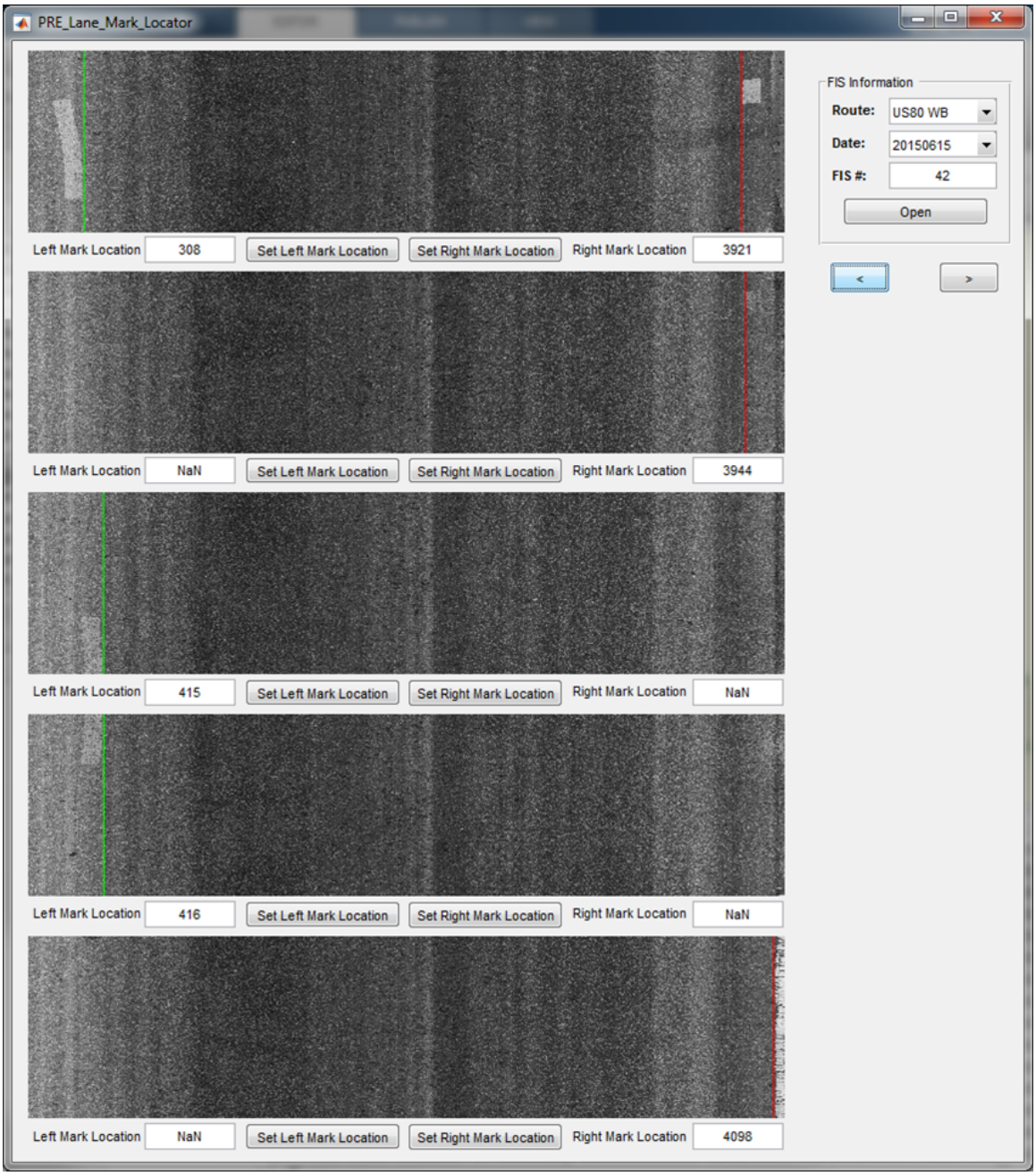

Figure 4.24: Lane Marking Detection Validation GUI

Milepost Identification

While lane marking locations determine the lateral boundaries of the pavement segment, locations of beginning and ending mileposts for each segment are manually identified using another graphic user interface (GUI) developed in this study. As shown in Figure 4.25, the milepost location identification GUI consists of a file selection function that loads the beginning or ending image of each segment. The image viewer can be switched between intensity and range images so that both intensity features (e.g., lane markings) and range features (e.g., cracks) can be identified and used as common references among all timestamps. The common physical features in the images of the same milepost are then set as the longitudinal boundary of the segment.

4.2.3 Segment-based Longitudinal Scaling

To address the issue of the varying number of transverse profiles collected at different timestamps, a simple longitudinal scaling method is proposed. The fundamental assumption of this proposed method is that the effect of the factors that caused these differences, be they tire pressure, pavement surface conditions, vehicle meandering, rounding error of the DMI (e.g., the sensor triggering device), etc., are uniformly distributed along the driving direction throughout each data collection process. Under this assumption, instead of viewing the interval between any two consecutive profiles as 5 mm, each run's data were mapped to the entire section and equal distance intervals were assumed. As depicted in Figure 4.26, assuming after data collection, Run 1 and Run 2 resulted in a difference of three transverse profiles (30 profiles in Run 1 and 27 profiles in Run 2). To ensure fair comparison between these two runs, Run 2 was longitudinally scaled so that the first and last profiles were aligned with Run 1, and the rest of the profiles of Run 2 were equally spaced throughout the scaled section. In other words, the distance between any two profiles in Run 2 was no longer 5 mm but 5.56 mm.

In the real-world scenario, this step is performed by scaling multiple timestamps of data

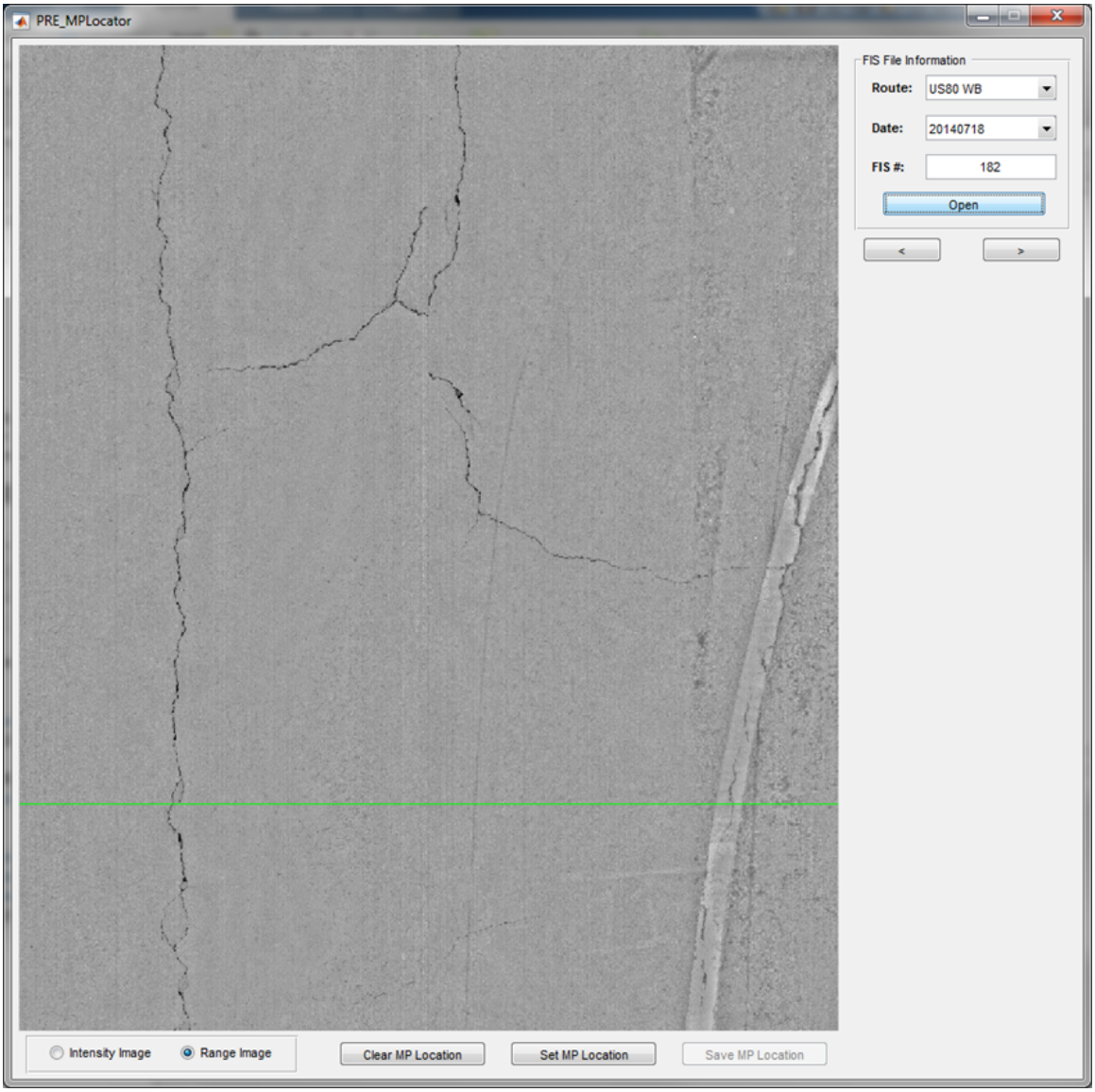

Figure 4.25: Milepost Identification GUI

collected in a segment according to the identified milepost locations described in the previous section. To enable profiles from different timestamps to be compared in a one-to-one manner after the scaling, the profile at the closest location can be directly used. Mathematically, the largest difference between two sets of profiles would be less than 2.5 mm, which is a negligible distance for the rut shape to significantly change. An alternative to enable one-to-one relationship between two timestamps of data is to interpolate the profiles at the desired locations.

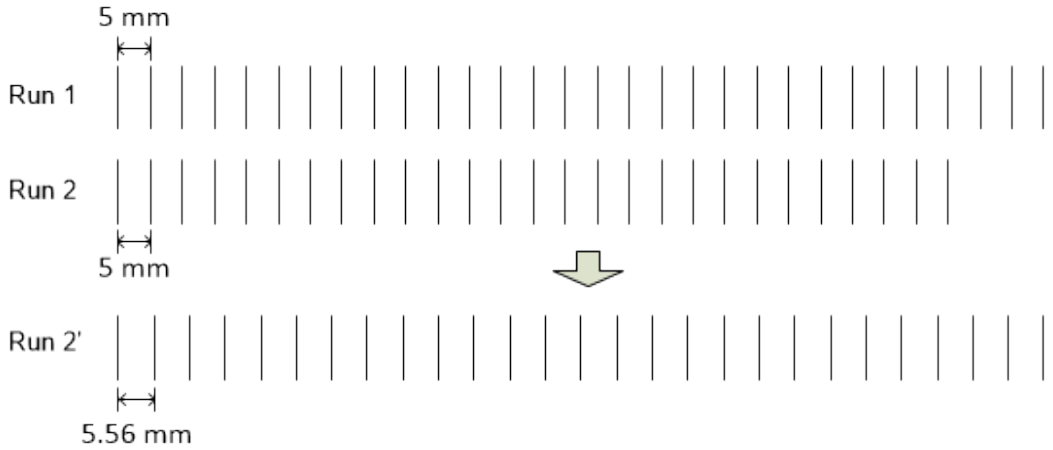

Figure 4.26: Longitudinal Scaling Maps Two Runs of Data on the Same Section

4.2.4 Lane Marking-based Profile Normalization

To address the issues caused by vehicle-pavement dynamics, including the altitude, pitch, roll, and yaw angles, a data normalization step is proposed in this section. Data normalization herein refers to the process of transforming 3D data so that they are rearranged on the same reference for direct comparison. In this study, it is assumed that the elevation of pavement surface at both edges of the lane (i.e., at lane marking locations) does not change over time. Under this assumption, if the edges of the lane were identified in the collected data, one can easily move all profiles onto the same reference plane through mathematical geometry transformation.

Profiles collected at the same location at different timestamps may have quite different cross slopes, as shown in Figure 4.5 above. Under the assumption that the elevation of pavement surface near lane marking locations does not change over time, the profiles are translated and transformed vertically so that they can be compared on the same reference plane. In this study, the profiles were first translated vertically so that the profile elevation just inside of the left lane marking was at zero. The translated profiles were then shear transformed on the xz plane so that the profile elevation just inside of the right lane marking was at zero (see Figure 4.27).

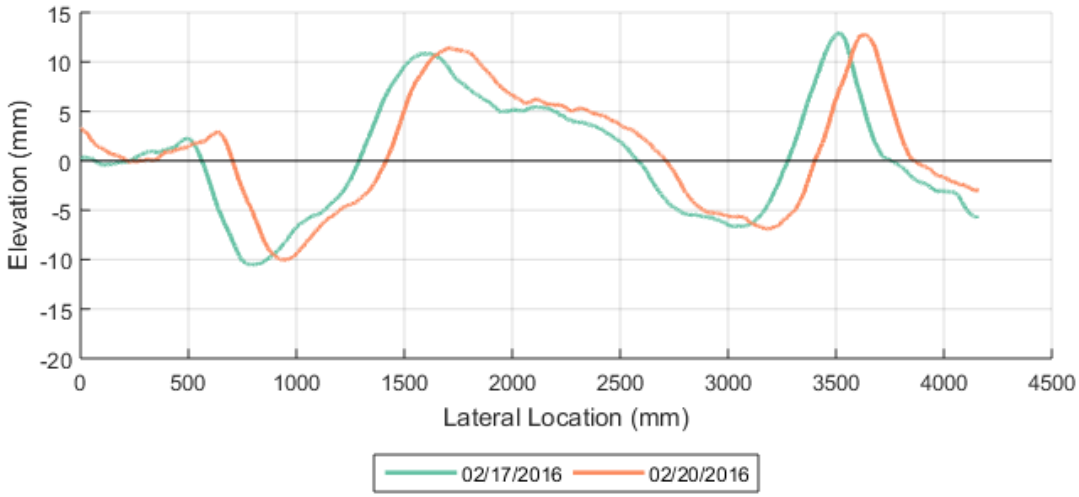

Figure 4.27: Vertically Translated and Transformed Profiles

4.2.5 Lane Center-based Transverse Mapping

The result of vertical translation and transformation showed that the two profiles were re-arranged on the same reference plane (i.e., the horizon). It is noted that the two profiles had an obvious transverse offset, which was likely caused by the lateral displacement of the vehicle during the two runs of data collection. To correct this, both profiles were transversely translated so that they were aligned at the lane center location, which was defined as the origin of the x axis. The distance of transverse translation for each profile can be determined by comparing the relative lane center location, which is essentially the vehicle driving trajectory. After this step, the profiles were fully registered and the results are shown in Figure 4.28.

4.2.6 Validation

To evaluate the proposed data registration method and quantify the difference between two sets of 3D pavement data, the root-mean-square error (RMSE) was used. Higher RMSEs indicate larger differences between two datasets, and an RMSE close to zero indicates that

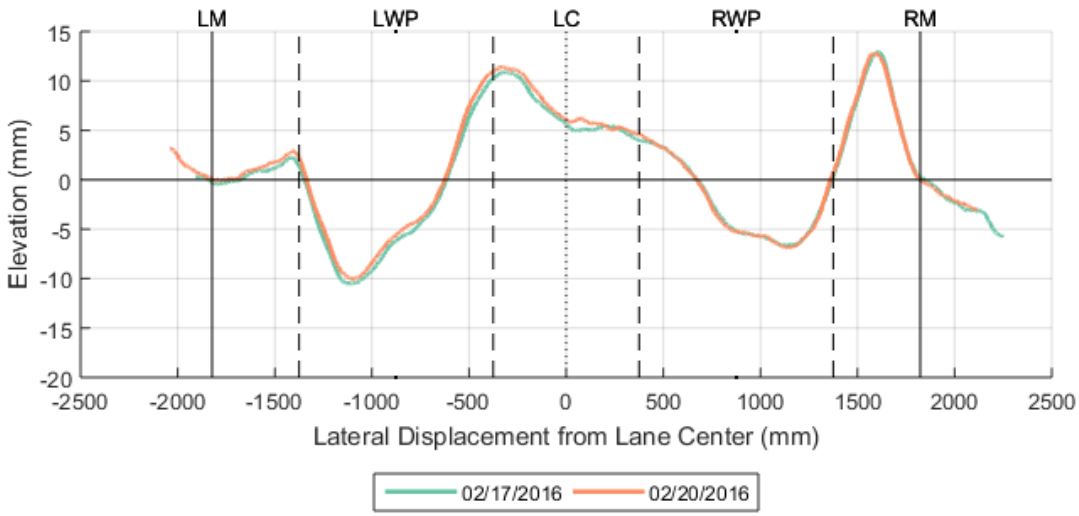

Figure 4.28: An Example of Final Registered Profiles

the two datasets have almost identical measurements.

$$RMSE = \sqrt{\frac{\sum_{i=1}^{n}\sum_{j=1}^{m}\left(z_{2_{ij}} - z_{1_{ij}}\right)^2}{m \times n}} \tag{4.5}$$

where

$z_{1_{ij}}$ = elevation of point ij in dataset 1;

$z_{2_{ij}}$ = elevation of point ij in dataset 2;

m = total number of points per transverse profile; and

n = total number of points per longitudinal profile.

4.3 A Case Study on SR 26

A case study was conducted using 3D pavement data collected between Mileposts 11.5 and 5.5 on Georgia State Route 26. The proposed method was applied to register two sets of 3D pavement data collected on February 17 and 20, 2016. Since the two sets of data were collected merely three days apart, it was assumed that the pavement should have the very similar conditions (if not the same) and the change of its shape could be negligible.

Step-by-step data registration results of these two datasets were then compared against

each other using the RMSE and they are summarized in Table 4.2. From the results, it is noted that the root-mean-square error was approximately 12 mm, indicating that significant differences existed between the two sets of data. The RMSE was significantly improved when the data were normalized, demonstrating that arranging data on the same reference plane was a crucial step. The 2.98-mm RMSE, in fact, was primarily caused by the lateral displacement between the two runs of data collection. The final registered data showed an RMSE of 1.49 mm, which was a significant improvement from the RMSE of the raw data.

Table 4.2: Data Registration Validation

Data Registration Step	Root-Mean-Square Error
Raw Data	11.74 mm
Inter-sensor Geometry Correction	12.15 mm
Longitudinal Scaling	12.02 mm
Profile Normalization	2.98 mm
Transverse Mapping*	1.49 mm

* RMSEs were calculated using only data within the lane

4.3.1 Examples of Data Registration Results

The following figures demonstrate the results of step-by-step registration of a short section (approximately 175 ft) on SR 26. In these figures, the light-yellow color indicates the elevation of the corresponding data points was approximately zero, which is the same as the reference plane defined by the lane boundaries. The green color indicates the elevation was positive, and the red color denotes the elevation was negative. The greener the color, the higher the elevation. Similarly, the redder the color, the deeper the elevation.

Figure 4.29 shows two runs of raw data of this section. It was noted that an elevation gap could clearly be seen between the sensors. Moreover, the elevation of corresponding points between the two datasets were not consistent. The elevation gap observed in Figure 4.29 was eliminated through the inter-sensor geometry correction, as shown in Figure 4.30. The elevation inconsistency between the two datasets, however, remained an issue. Results

of longitudinal scaling, as depicted in Figure 4.31, did not make a significant difference from the results shown in Figure 4.30. This finding was also reflected in the RMSE results shown in Table 4.2 between the inter-sensor geometry correction and longitudinal scaling steps. This is because although longitudinal scaling was done to map the data longitudinally throughout the section, the actual distance before and after mapping between the profiles would not exceed 2.5 mm; therefore, its impact on reducing the error was not significant. Data transformation results are shown in Figure 4.32. It is noted that the two runs of data, in terms of the elevations of all data points, were much more consistent when compared with the above results. Higher elevations were observed in similar locations in both datasets. Lower elevation locations were matching in a similar manner. This result reflected the significantly lower RMSE observed after data transformation.

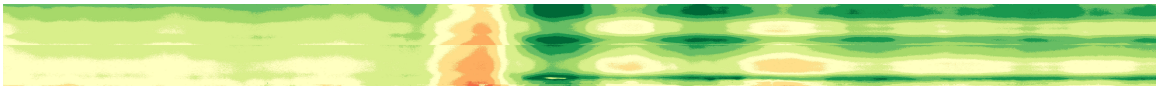

(a) 2/17/2016

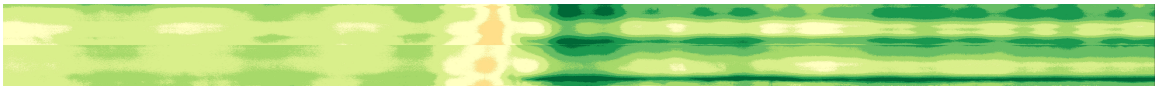

(b) 2/20/2016

Figure 4.29: Visualization of Raw 3D Pavement Data

(a) 2/17/2016

(b) 2/20/2016

Figure 4.30: Visualization of Data after Inter-sensor Geometry Correction

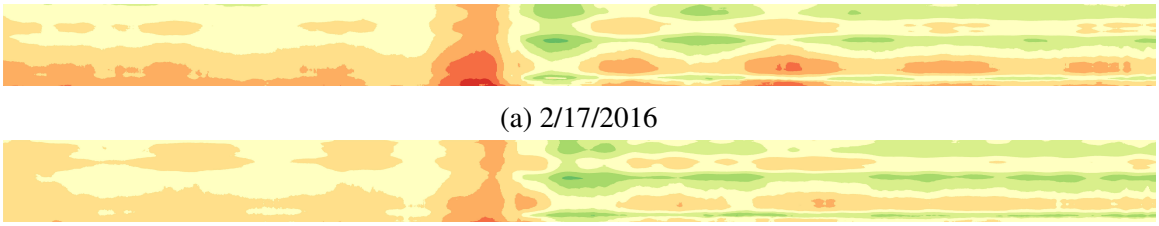

(a) 2/17/2016

(b) 2/20/2016

Figure 4.31: Visualization of Data after Longitudinal Scaling

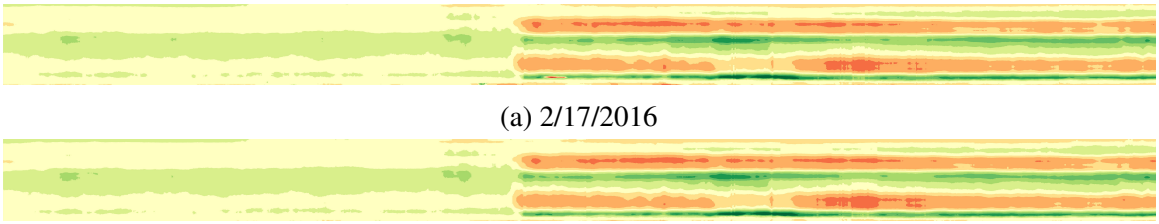

(a) 2/17/2016

(b) 2/20/2016

Figure 4.32: Visualization of Data after Data Normalization

4.4 Exploratory 2D and 3D Rut Deterioration Visualization Using Registered Data

4.4.1 Visualizing 3D Rut Deterioration in 2D Color Maps

The proposed method was further applied to register 3D pavement data collected on the same section at the available timestamps (see Table 3.2). The before-and-after results of these timestamps were visualized in the following two examples to demonstrate how the proposed method could support the subsequent rut deterioration analysis.

Figure 4.33 shows a 175-ft section on SR 26 westbound starting from Milepost 11.5. On May 3, 2012, a deep patching pavement rehabilitation was done to fix the severe rutting in this section. As a result, among the 7 timestamps shown, the first timestamp showed severe rutting throughout this section; the surface was not as severely rutted at the following six timestamps. It is noted, however, that rutting started to grow back in a certain location, such as the beginning section (far left in the figure) and the right wheelpath towards the end of this section.

Figure 4.34 shows another 175-ft section following the section shown in the first ex-

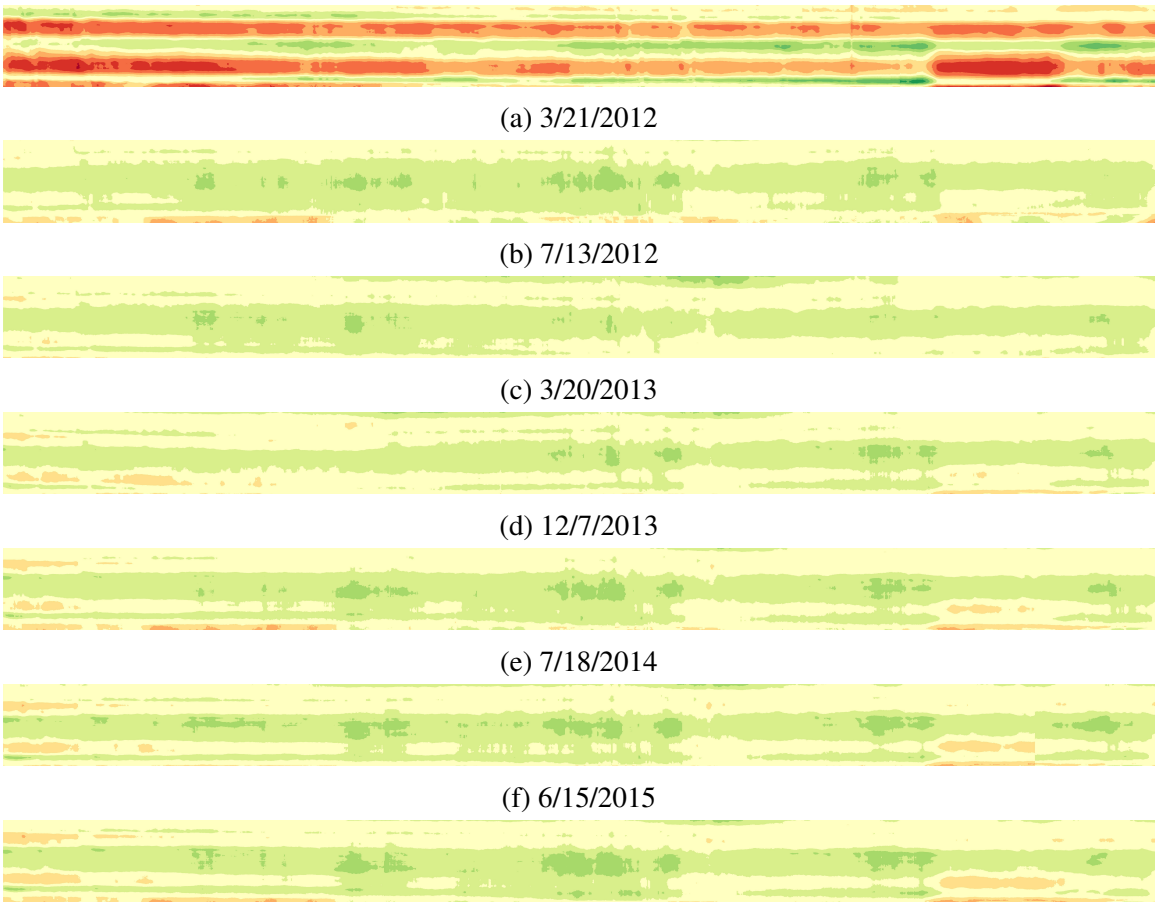

(a) 3/21/2012

(b) 7/13/2012

(c) 3/20/2013

(d) 12/7/2013

(e) 7/18/2014

(f) 6/15/2015

(g) 2/17/2016

Figure 4.33: Visualization of Long-Term 3D Pavement Data Registration: First Example

ample on SR 26. The rehabilitated area, which ended within this example, did not gain as much rutting back as the previous example. By comparing the second half of the section (i.e., the right half images) throughout the 7 timestamps, it is noted that rutting grew and became more severe in the right wheelpath towards the end of this section. The lane center location at around the two-thirds point through the section showed an increase in elevation, indicating that the lane center materials were likely pushed up by plastic flow. Note that in Figure 4.34c, a small area showed elevation that is much deeper (redder) than its surrounding area. This was caused by a sharp elevation change in the transverse direction that appeared close to the right lane marking area. Since the registration method proposed in this chapter relied on the assumption that elevations of lane boundaries would not change

over time, foreign debris or sharp elevation changes (e.g., an edge drop-off) can cause this type of noise in the registered data. Although this type of situation is rare, it is a limitation of the proposed method that can be improved in the future.

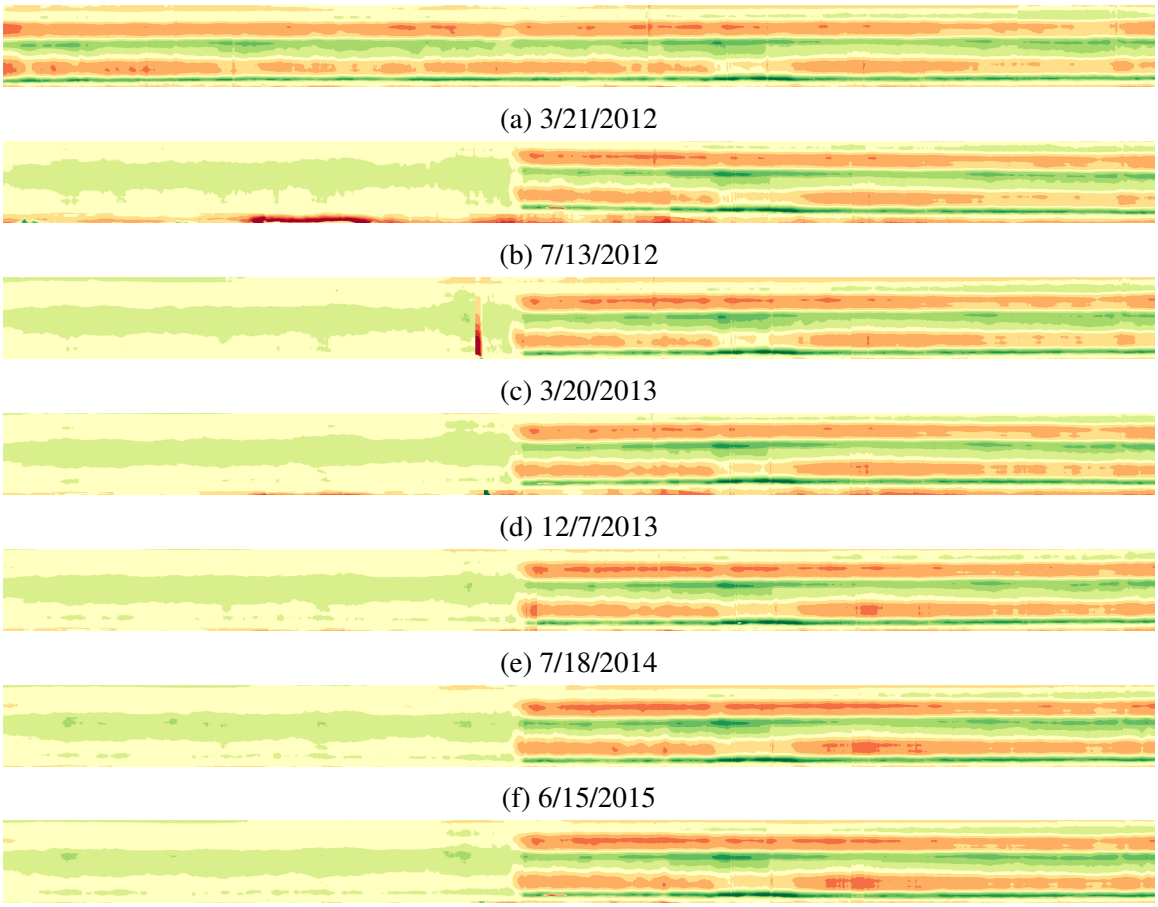

(a) 3/21/2012

(b) 7/13/2012

(c) 3/20/2013

(d) 12/7/2013

(e) 7/18/2014

(f) 6/15/2015

(g) 2/17/2016

Figure 4.34: Visualization of Long-Term 3D Pavement Data Registration: Second Example

4.4.2 Quantifying Deterioration by Image Subtraction

In addition to showing the shape of rutting at each timestamp separately, the exact changes between each pair of temporally sequential 2D images (or 3D models) can be further quantified by subtracting the elevations (z values) of first timestamp data points from the elevations of second timestamp data points at their corresponding x and y coordinates. Image subtraction techniques have been used in other fields, such as medical imaging and mi-

crolensing observations, to detect objects or change of objects through image subtraction between the same image with different kernels, or between two temporally sequentially images (Kano et al., 1999; Alard and Lupton, 1998; Alard, 2000). In our study, we implement a simple image subtraction technique between images collected at two different timestamps. The subtraction results are then used to observe the detailed change of 3D rut shape over time in Chapter 5.

2D Deterioration Maps

As shown in Figures 4.35 and 4.36, a 30-ft section on SR26 westbound was selected to visualize the detailed 3D shapes and their changes among 3 timestamps (i.e., 3/21/2012, 3/20/2013, 2/17/2016). As stated earlier, this section underwent a surface treatment in May, 2012 and this change is reflected in Figure 4.35, as the rutting changed from being severe in 2012 to moderate in 2013. The exact change, including filled wheelpaths and leveled edges, can be clearly seen in Figure 4.35c. Similarly, Figure 4.36 shows 3D rut shapes and their changes between the latter two timestamps. Between these two timestamps, the exact deterioration of ruts, including deformed wheelpaths and pushed-up lane center and edges, is clearly evident in Figure 4.36c.

3D Deterioration

Furthermore, the subtraction results can also be visualized in 3D models. Using the same example, Figures 4.37 and 4.38 show the 3D models of rut shapes at each timestamp and their changes.

4.5 Summary

In this chapter, a 3D data registration method was proposed to place different sets of 3D pavement data in the same spatial reference so that they can directly be compared and used for pavement deterioration analysis. The method was proposed to address possible sys-

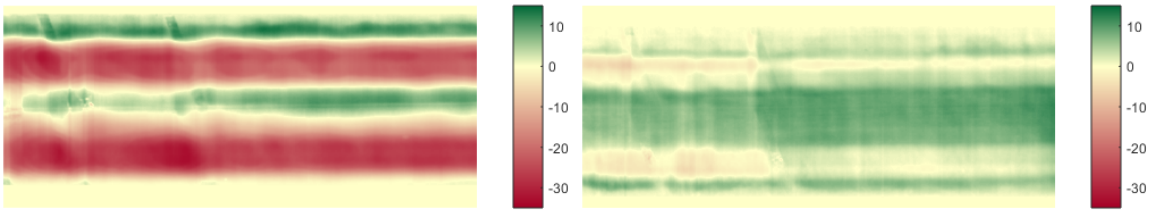

(a) 3/21/2012 (b) 3/20/2013

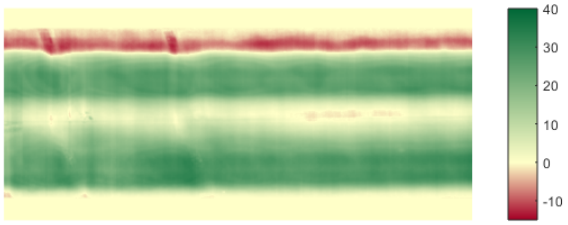

(c) Change between 3/21/2012 and 3/20/2013

Figure 4.35: Visualizing Rut Shapes and Change between 2012 and 2013 in 2D Color Maps

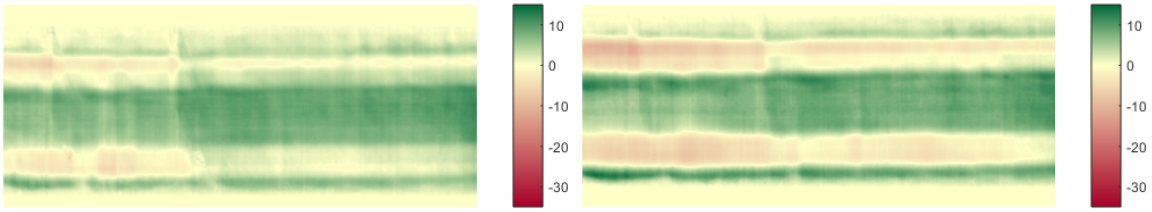

(a) 3/20/2013 (b) 2/17/2016

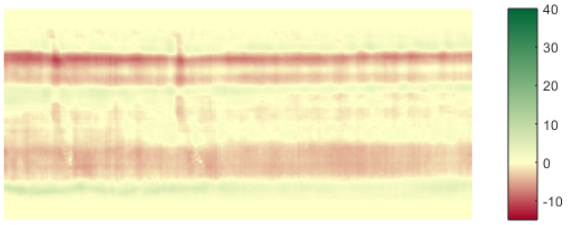

(c) Change between 3/20/2013 and 2/17/2016

Figure 4.36: Visualizing Rut Shapes and Change between 2013 and 2016 in 2D Color Maps

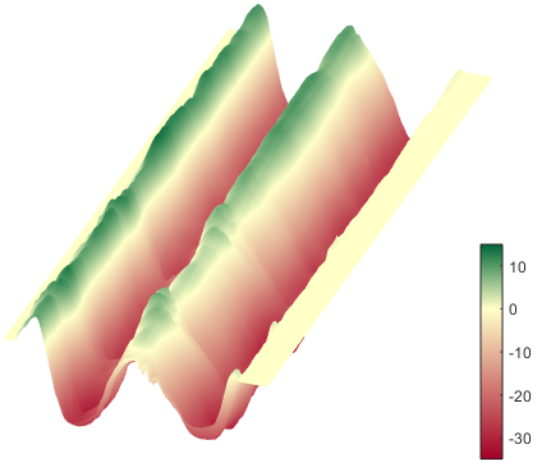

(a) 3/21/2012

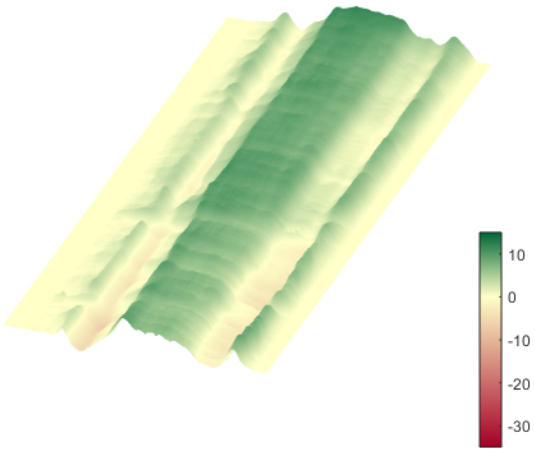

(b) 3/20/2013

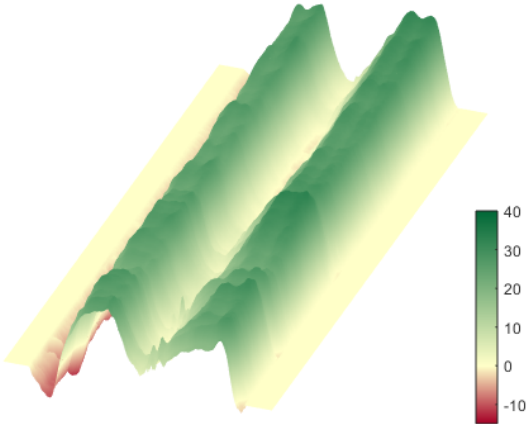

(c) Change between 3/21/2012 and 3/20/2013

Figure 4.37: Visualizing 3D Rut Shapes and Change between 2012 and 2013

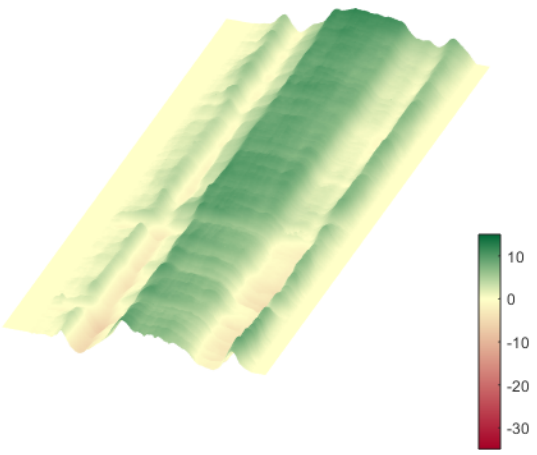

(a) 3/20/2013

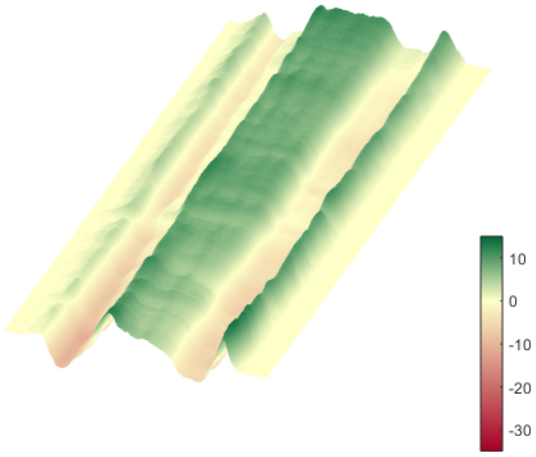

(b) 2/17/2016

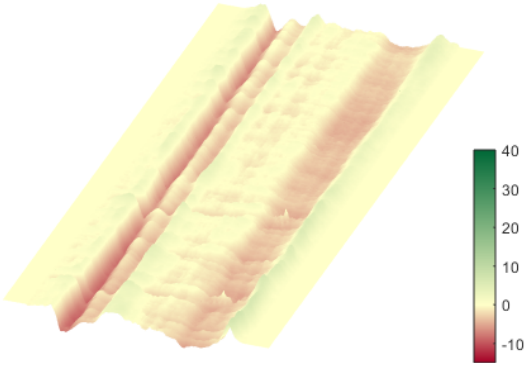

(c) Change between 3/20/2013 and 2/17/2016

Figure 4.38: Visualizing 3D Rut Shapes and Change between 2013 and 2016

tematic and operational noise and errors that are common to all automated data collection techniques. Results of the case study over 6 miles on SR 26 in Georgia showed that the proposed method can significantly reduce the effect of the identified errors and effectively register different sets of 3D pavement data. The registered data, as demonstrated in the examples of (1) two 175-ft sections with 7 timestamps of registered data; and (2) the 2D and 3D visualization of rut shapes of a 30-ft section and their exact change between timestamps, can be further used to quantify the true rut deterioration behaviors that have not been studied before.

Because the identified data variability issues are common to most data collection techniques, the proposed method can be possibly applied to study the deterioration of other types of pavement distresses with some minor modifications that are specific to their special characteristics. The proposed method and procedures can be easily reproduced and implemented by state DOTs and other researchers to evaluate and monitor pavement conditions at a finer level. Extended research developed based on this method can be used to explore and discover new information that has not yet been attained in the past, leading to better understanding of pavement deterioration behaviors and, ultimately, data-driven pavement management decisions.

CHAPTER 5

CHARACTERIZING 3D RUT SHAPE AND ITS DETERIORATION

In this chapter, 3D rut shapes and their deterioration at multiple scales, including project, segment, and individual rut-levels, are analyzed using (1) descriptive statistics of spatial parameters and the proposed temporal parameters; and (2) 2D and 3D visualization and image subtraction. In this study, a pavement project is defined as a section of pavement, typically a few miles long, which has consistent pavement type, design, maintenance activity, etc. A pavement segment is a road section that is typically 1 mile or less in length. Individual rut refers to a road section that is smaller than 1 mile in length.

For project and segment-level deterioration, boxplots are generated to show the distribution of rut parameters at different timestamps. A boxplot is a practical tool that depicts the overall distribution of data (McGill et al., 1978). As depicted in Figure 5.1, a boxplot consists of a box with three horizontal bars and the whiskers (vertical bars). The box represents the middle fifty percentiles of the data (its range is defined as the interquartile range; IQR), and the horizontal bars at the top, middle, and bottom of the box denote the third quartile, the median, and the first quartile, respectively. The top whisker extends from the top of the box to the farthest data point that is within 1.5 times of the IQR from the top of the box (i.e., the upper extreme), and the bottom whisker extends from the bottom of the box in a similar manner. Any data point beyond the extent of the whiskers are considered outliers.

For individual rut level deterioration, 2D and 3D visualization as well as image subtraction techniques that are similar to the ones shown in the previous chapter, are used to show the detailed 3D rut shapes.

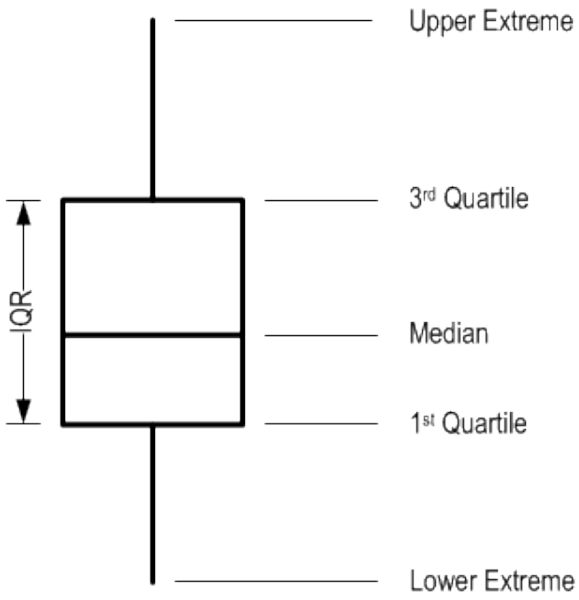

Figure 5.1: Illustration of A Boxplot

5.1 Characterization of 3D Rut Shape and Its Deterioration

In this study, rut parameters defined in the literature as well as some new parameters are used to characterize 3D rut shape and to quantify the change in 3D shape. The following list shows the spatial and temporal rut parameters used in the analysis:

- Profile-based parameters:
  - LRD: PP69 Left rut depth (mm)
  - RRD: PP69 Right rut depth (mm)
  - LRW: PP69 Left rut width (mm)
  - RRW: PP69 Right rut width (mm)
  - LCA: PP69 Left cross-sectional area (mm^2)
  - RCA: PP69 Right cross-sectional area (mm^2)
  - TPA: Total positive area (mm^2)
  - TNA: Total negative area (mm^2)
  - DR: Distortion ratio
  - TD: Total distortion (mm^2)

  - TAD: Total absolute distortion (mm^2)
  - PD: PP69 Percent deformation (%)
- Longitudinal parameters:
  - LRL: Left rut length (m)
  - RRL: Right rut length (m)
  - LRV: Left rut volume (m^3)
  - RRV: Right rut volume (m^3)
- Temporal Parameters:
  - TEA: Total elevated area per year (mm^2/yr)
  - TDA: Total depressed area per year (mm^2/yr)
  - MED: Mean elevated distance per year (mm/yr)
  - MDD: Mean depressed distance per year (mm/yr)

Among these parameters, temporal parameters and TAD are first proposed in this research. The proposed parameters and other parameters that have not been defined in previous chapters are described below.

5.1.1 Profile-based Parameters

Total Absolute Distortion

As discussed in the previous section, current definition of positive and negative areas (Figure 5.2) can be sensitive to the location of the reference line. Therefore, instead of the current use of positive and negative area (i.e., total distortion and distortion ratio), in this study, we propose the total absolute distortion (TAD) as an additional indicator to describe the level of distortion. As defined in Equation 5.1, TAD is the sum of absolute positive areas and absolute negative areas. TAD accounts for the distortion on both sides of the reference line by summation, which naturally makes it less sensitive to the original share

of the pavement surface.

$$TAD = |TPA| + |TNA| \tag{5.1}$$

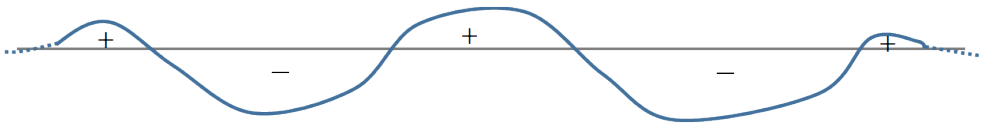

Figure 5.2: Illustration of Positive and Negative Areas

5.1.2 Longitudinal Parameters

Rut Length

Rut length can be defined as the longitudinal extension of an individual rut measured in distance units such as m or ft. Rut length has been used by transportation agencies as a means to identify the percentage or extent of rut within a section length. Some other agencies use rut length as one of the indicators to define and monitor rutting. For example, the Transfund New Zealand measures rut by the length of a wheel path where rut depth exceeds 30 mm (Transfund New Zealand, 1997).

To calculate rut length, the minimum dimensions of a rut needs to be clearly defined. After taking current state DOT practices and AASHTO provisional standards into consideration, in this study, we define the minimum dimensions (i.e., depth, width, and length) of a rut to be 3 mm, 300 mm, and 30 m (1/8 in, 1 ft, and 10ft). In addition, the minimum distance between two ruts needs to be at least 6 m (20 ft), as suggested by Li (2012). If the longitudinal length of the non-rutting area between two ruts is less than 6 m, the two ruts are considered as one, and the total length of this rut is the sum of the lengths of both ruts and the non-rutting area. Any pavement sections failing to meet these requirements, even with measured rutting, are considered localized deformation with a rut length of zero. Rut lengths in the left wheel path (denoted as LRL) are calculated separately from those in the right wheel path (denoted as RRL).

Rut Volume

Rut volume has been explored previously in the literature (Li, 2012); however, it has not yet gained much attention among transportation agencies. Similar to the way rut length is calculated, rut volume is only calculated for ruts that meet the minimum dimensional and spacing requirements stated previously. Rut volume can be defined as the integral of rut areas along the length of the rut, as shown in Equation 5.2. Rut volume in the left wheelpath (denoted as LRV) and the right wheelpath (denoted as RRV) are calculated separately.

$$RV_k = \sum_{i=1}^{n} lA_i, \forall i \in k \tag{5.2}$$

where

RV_k = rut volume of the kth rut;

l = longitudinal distance interval between two consecutive measurements;

A_i = the ith cross-sectional area; and

n = total number of measurements within the boundaries of rut k.

5.1.3 Temporal Parameters

To understand how rut deteriorates, one can compare the rut parameters of the same segment at different timestamp through statistical means (e.g., mean, median, percentiles, boxplot, etc.) With the spatiotemporally registered data, rut deterioration can be further quantified through direct comparison of the 3D rut shapes between different timestamps. In this study, the following temporal parameters are proposed to measure the actual rate of change in 3D rut shapes (transverse profiles) as a more direct means to quantify rut deterioration.

Total Elevated and Depressed Areas Per Year

As depicted in Figure 5.3, the total elevated area per year (TEA) is the elevating rate of the total elevated area per year. Elevated areas are defined as the areas enclosed by two profiles

where the elevation of the second timestamp profile (red profile) exceeds the elevation of the first timestamp profile (blue profile). Total depressed area per year (TDA), on the other hand, is the depressing rate of the sum of depressed areas, where the elevation of the second timestamp profile is lower than the elevation of the first timestamp profile. Equations 5.3 and 5.4 define the total elevated and depressed area mathematically.

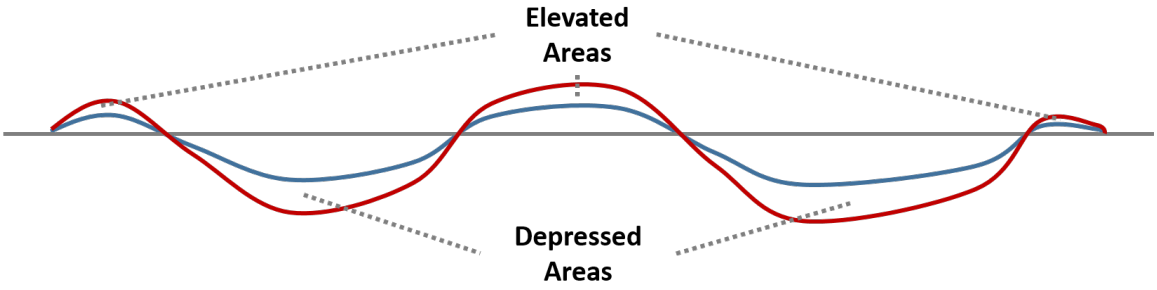

Figure 5.3: Illustration of Temporal Parameters

$$TEA = \frac{365}{t} \sum_{j=1}^{J} d_j, \forall j \in i \tag{5.3}$$

$$TDA = \frac{365}{t} \sum_{k=1}^{K} d_k, \forall k \in i \tag{5.4}$$

$$d_i = \mathbf{z_{2}}_i - \mathbf{z_{1}}_i, i = 1, ..., n \tag{5.5}$$

where

TEA = total elevated area per year (mm^2/yr);

TDA = mean depressed area per year (mm^2/yr);

t = number of days between Timestamps 1 & 2;

d_j = the jth point with positive elevation change;

d_k = the kth point with negative elevation change;

d_i = the signed elevation change of the ith point from profile $\mathbf{z_1}$ to profile $\mathbf{z_2}$;

$\mathbf{z_1}$ = profile elevations at Timestamp 1;

$\mathbf{z_2}$ = profile elevations at Timestamp 2;

J = total number of elevated points;

K = total number of depressed points; and

n = total number of points per profile, $J + K \leq n$.

Mean Elevated and Depressed Distances Per Year

In addition to the change in cross-sectional profile areas, change in elevation can also be calculated. In this study, the mean elevated distance per year (MED) is defined as the annual rate of in the average positive elevation from the first timestamp to the second timestamp. As defined in Equation 5.6, the mean elevated distance is the rate the average elevation changes among all points that have a positive elevation change. Mean depressed distance per year, or MDD, can be calculated in the same manner using Equation 5.7.

$$MED = \frac{TEA}{J} \tag{5.6}$$

$$MDD = \frac{TDA}{K} \tag{5.7}$$

where

MED = mean elevated distance per year (mm/yr); and

MDD = mean depressed distance per year (mm/yr).

5.2 Project-Level Rut Deterioration

For project-level analysis, long-term 3D pavement data collected on Georgia State Route 26 between Mileposts 5.5 and 11.5 were used. This road section consists of two 6-mile projects, one in the eastbound direction and the other in the westbound direction. Long-term 3D pavement data were collected at 7 timestamps between March, 2012 and February, 2016.

5.2.1 Deterioration of Profile-based Parameters

Figure 5.4 shows the boxplots of all profile-based rut parameters of SR26 eastbound Mileposts 5.5 to 11.5 at multiple timestamps. From this figure, it is noticed that rutting within this project slowly became more severe. This result echos GDOT's annual survey results, in which the pavement condition evaluation system (PACES) rating of this project gradually decreased over the analysis period.

Most profile-based parameters did not change dramatically over the course of these 7 timestamps. Several profile-based parameters, including rut depth, rut cross-sectional area, percent deformation, and total absolute distortion, showed similar trends that increased gradually. Interestingly, while these parameters showed positive trends at Timestamps 1, 2, 3, 5, and 6, their trends slowed down or became negative at timestamps 4 and 7. A possible explanation of this observation can be the seasonal variability, i.e., rut deterioration slows or stops in low temperature seasons, as depicted in Figure 5.5 (White et al., 2002). Note that Timestamps 4 and 7 were in December and February, respectively, and Timestamps 1, 2, 3, 5, and 6 were in summer and spring.

Other profile-based parameters, such as total positive area, total negative area, distortion ratio, and total distortion, nevertheless, did not have a clear common trend. Overall, value of the total negative area was larger than that of the positive area, indicating that the majority of this project had larger depression than elevation. Consequently, the total dis-

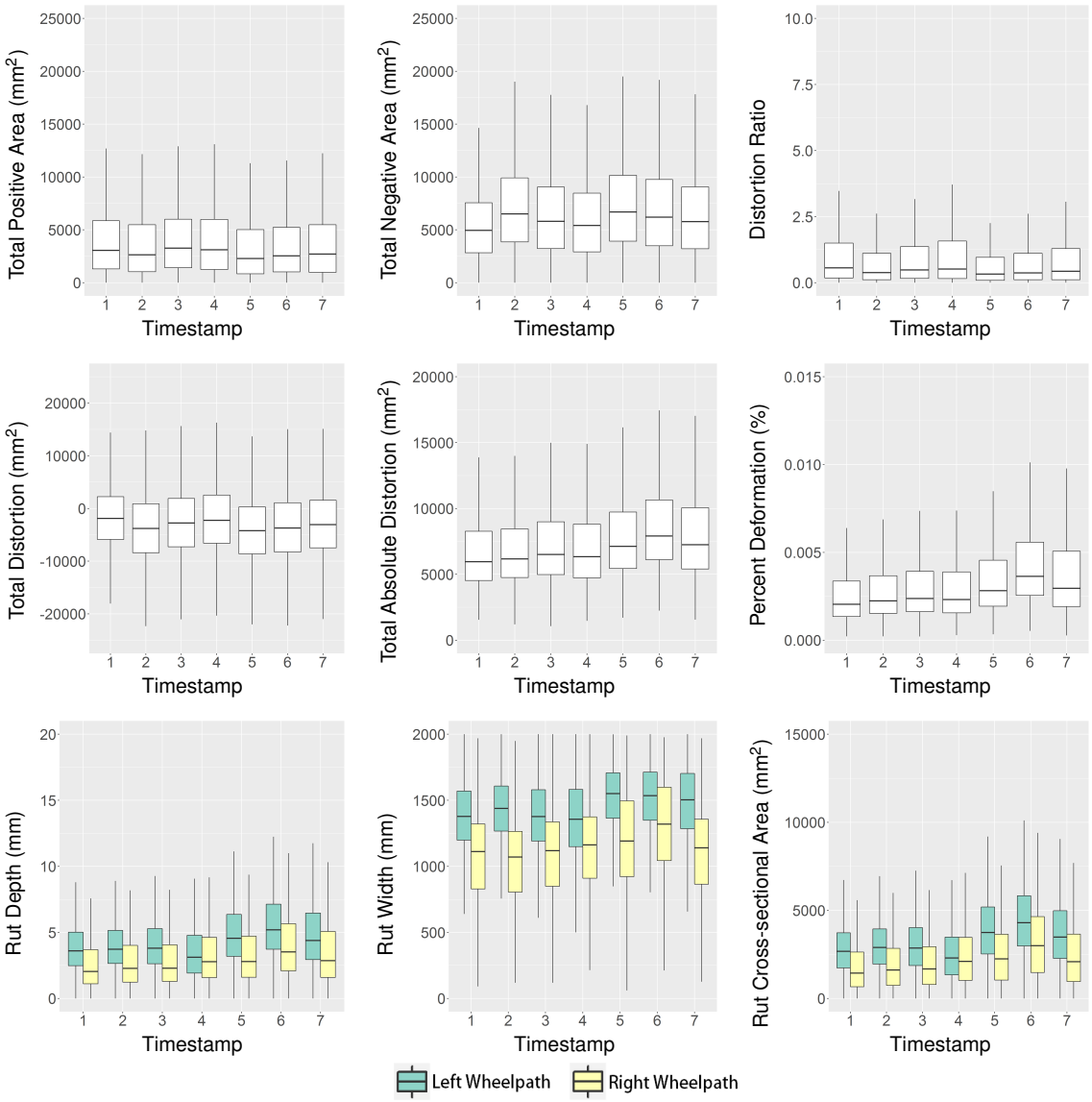

Figure 5.4: Deterioration of Profile-based Parameters at Project-level: SR26 Eastbound MP5.5-11.5

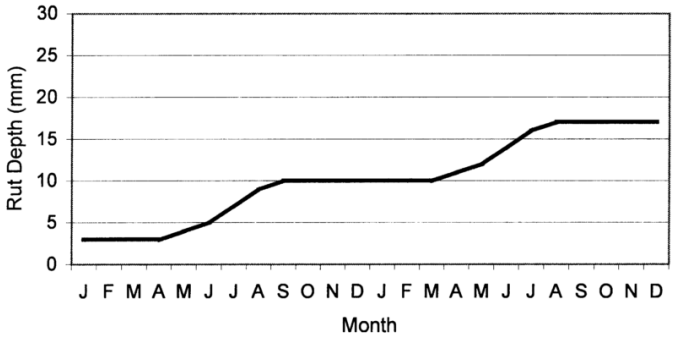

Figure 5.5: Potential Seasonal Effects on Rutting (White et al., 2002)

tortion, which is defined as total positive area minus total negative area, tend to be negative throughout the analysis period.

Similar findings are also observed in the other 6-mile project in the Westbound direction on SR26, which is reasonable because the two projects share very similar, if not the same, pavement design, traffic volume and characteristics, and climates. Overall, the Eastbound direction had more severe rutting than the Westbound direction. Results of the Westbound project are shown in Figure 5.6.

5.2.2 Deterioration of Longitudinal Parameters

Deterioration of project-level longitudinal parameters, including the total length, and volume of ruts, are summarized in this section. As depicted in Figure 5.7, high correlation between rut length and rut volume can be observed. This phenomenon is expected since both rut length and rut volume are only calculated at locations where there is rutting. In addition, these two parameters generally follow similar trends as the ones observed in a few profile-based parameters, including rut depth, rut cross-sectional area, percent deformation, and total absolute distortion. This result indicates that the deterioration of rut shape is multi-dimensional, i.e., rut deteriorates in depth, length, cross-sectional area, and volume. Seasonal variation seems to have an effect on the changes observed in longitudinal parameters, too. While positive trends in length and volume can be observed during spring and summer seasons, growth in rut length and volume became moderate and sometimes

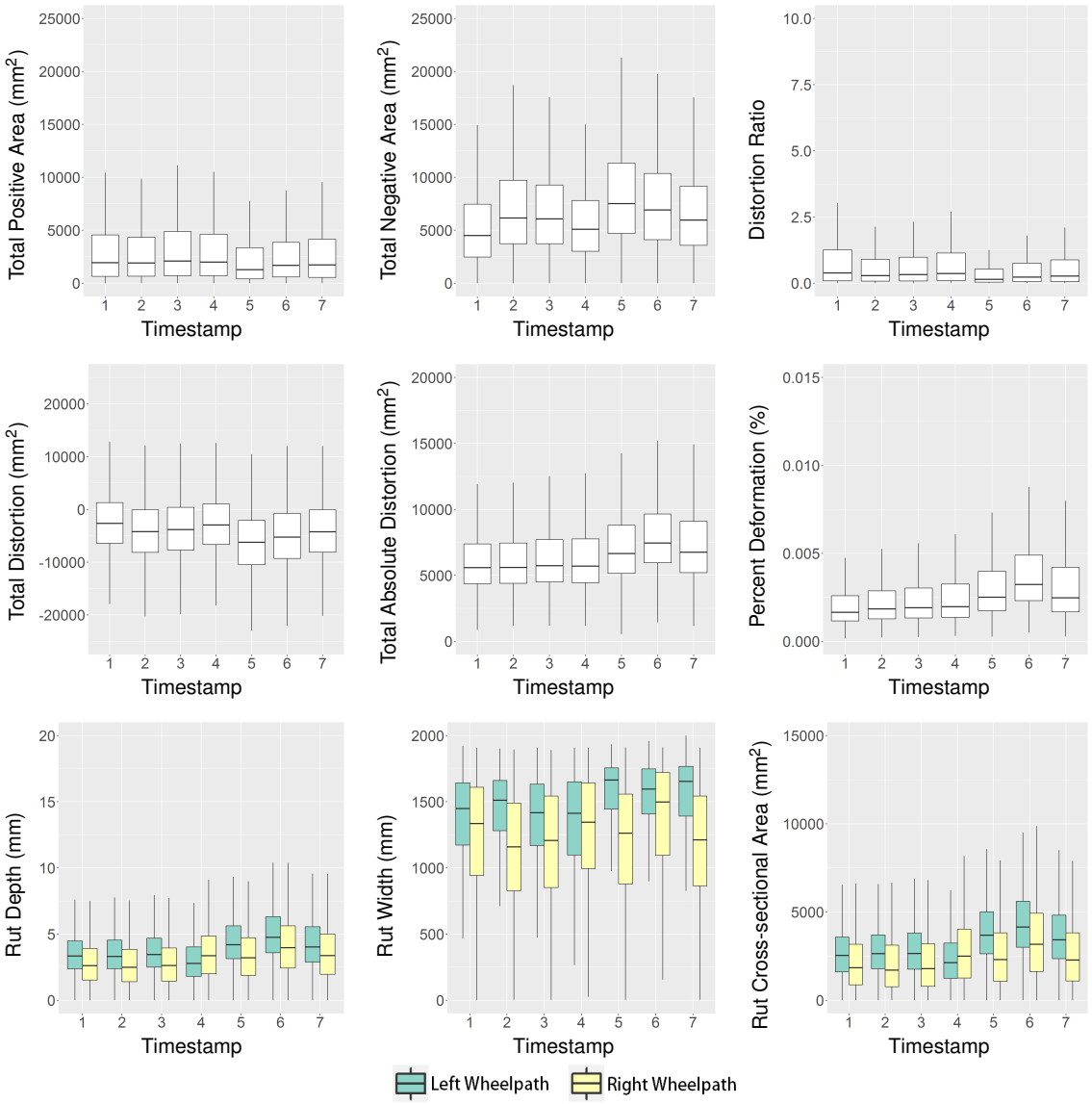

Figure 5.6: Deterioration of Profile-based Parameters at Project-level: SR26 Westbound MP11.5-5.5

negative in winter. Further confirmation of this observed behavior can be performed in the field to verify the effect of seasonal variation on rut shapes.

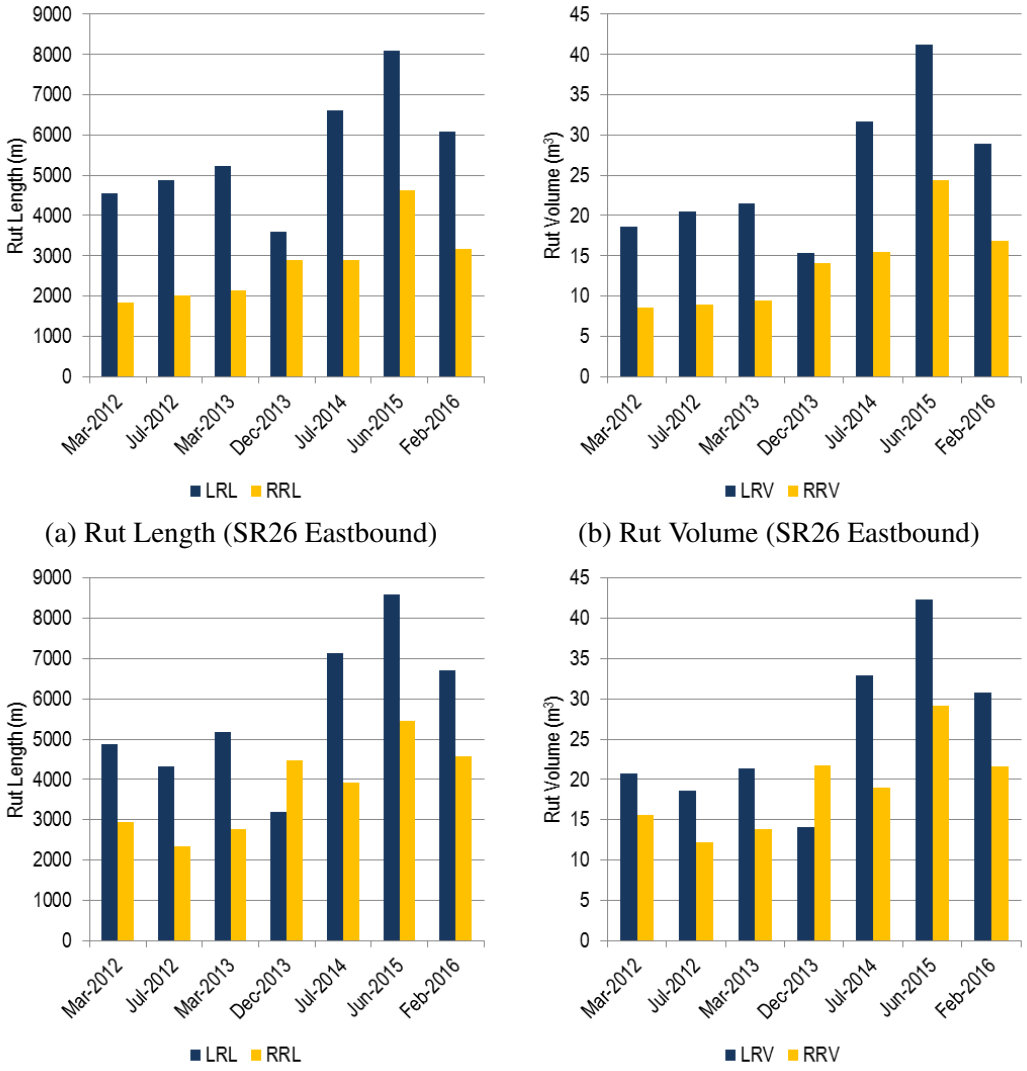

(a) Rut Length (SR26 Eastbound)

(b) Rut Volume (SR26 Eastbound)

(c) Rut Length (SR26 Westbound)

(d) Rut Volume (SR26 Westbound)

Figure 5.7: Deterioration of Longitudinal Parameters at Project-level

5.2.3 Deterioration of Temporal Parameters

Figures 5.8 and 5.9 show the deterioration of ruts in temporal rut parameters, including the mean elevated and depressed distances, and the total elevated and depressed areas. As defined in the previous section, temporal parameters at each timestamp were obtained by calculating their rates of change per year.

These two figures show that the two projects shared similar trends in all four parameters. It is noticeable that while the deterioration rates were temperate (e.g., <1.5 mm/yr) at most timestamps, the depression rates in depth and in area were higher at Timestamps 2 and 5. This finding can be associated with the seasonal variation as discussed above. As depicted in Figure 5.5, the deterioration of rut depth tends to be more rapid in late spring and summer, including April, May, June, July, and August, and it slows down during the late fall and winter season (i.e., October to February).

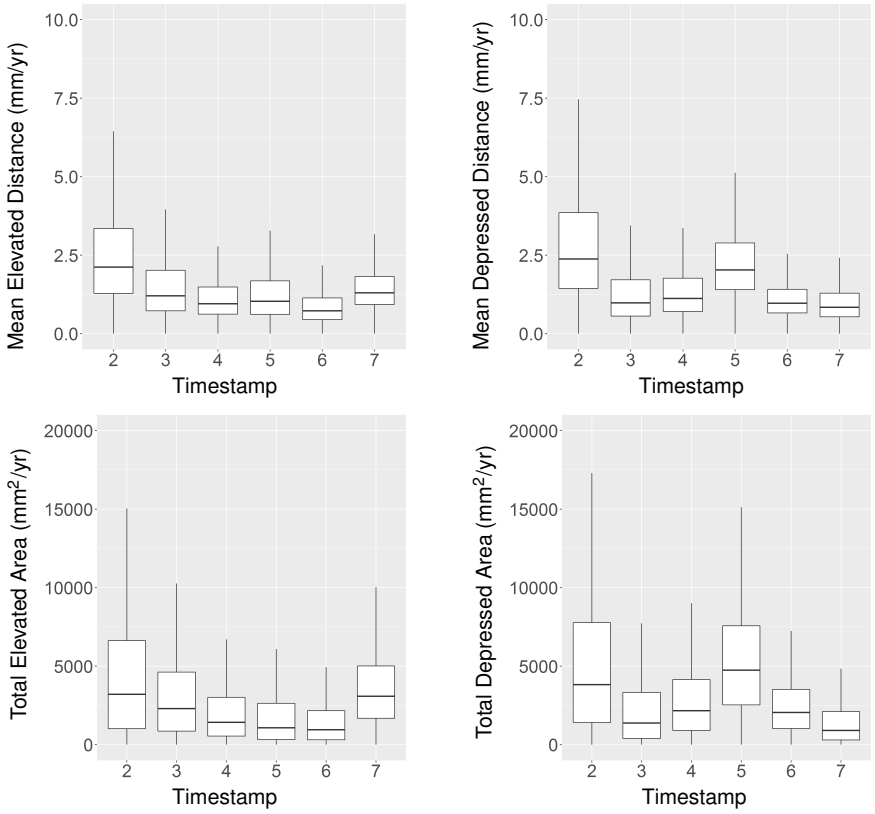

Figure 5.8: Deterioration of Temporal Parameters at Project-level: SR26 Eastbound

By comparing these two timestamps with their respective previous timestamps, it is noted that the season transitioned from winter or early spring to summer. Given the fact that a rut deteriorates more rapidly in spring and summer, these two timestamps are therefore expected to have higher deterioration rates.

Interestingly, although Timestamp 6 was also in summer, deterioration rates at this

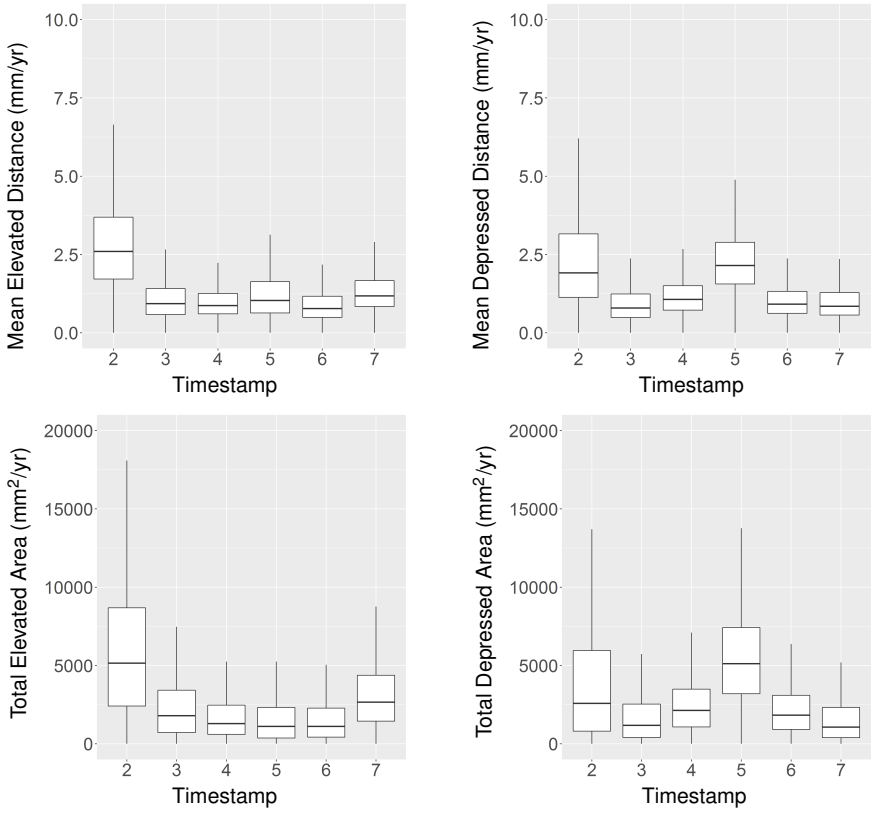

Figure 5.9: Deterioration of Temporal Rut Parameters at Project-level: SR26 Westbound

timestamp were not as pronounced as those at Timestamps 2 and 5. This is because deterioration rates at both Timestamps 2 and 5 were calculated over shorter periods (i.e., 4 months and 7 months) in spring and summer, whereas the rates at Timestamp 6 were calculated over a 11-month period that spanned all seasons. Since the deterioration rate is typically higher in summer, when propagating a rate that is observed over a few summer months to an annual rate, this projected annual rate is expected to be higher. On the contrary, if the period between two timestamps was longer (e.g., close to a year or more than a year), the deterioration rate is more likely to be "balanced out" over the course of the period. As a result, deterioration rates at Timestamp 6 were not as noticeable as those at Timestamps 2 and 5.

5.3 Segment-Level Rut Deterioration

Rut deterioration in the two projects shown in the previous section, together with two other segments (one on SR275 and the other on I95), are further analyzed on a one-mile segment basis. Similar to the project-level analysis, deterioration of rutting in these 14 segments are analyzed using descriptive statistics of various spatial and temporal rut parameters, and the results are summarized below.

5.3.1 Deterioration of Wheelpath-specific Profile-based Parameters

Figures 5.10 to 5.13 show the deterioration of wheelpath-specific rut parameters including rut depth, rut width, and rut cross-sectional area. By comparing the deterioration these rut parameters, several findings that are consistent with the results of project-level analysis can be summarized. First, seasonal variation seems to have effect on all segments, as rut parameters tend to grow slower or negatively at Timestamps 4 and 7 and faster at the other timestamps. Second, it is evident that rut depth and rut cross-sectional area shared similar trends, indicating these two parameters have higher correlation. Rut width, on the other hand, shows large variation between 0 mm and 2,000 mm (which are essentially the possible minimum and maximum width) and does not show clear correlation with other parameters.

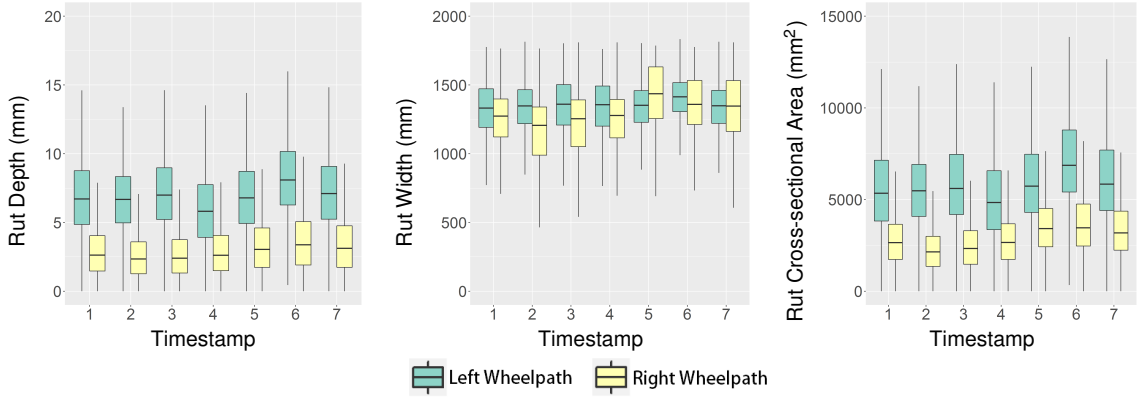

Figure 5.10: Deterioration of Wheelpath-specific Profile-based Parameters at Segment-level: SR275 Northbound MP0-1

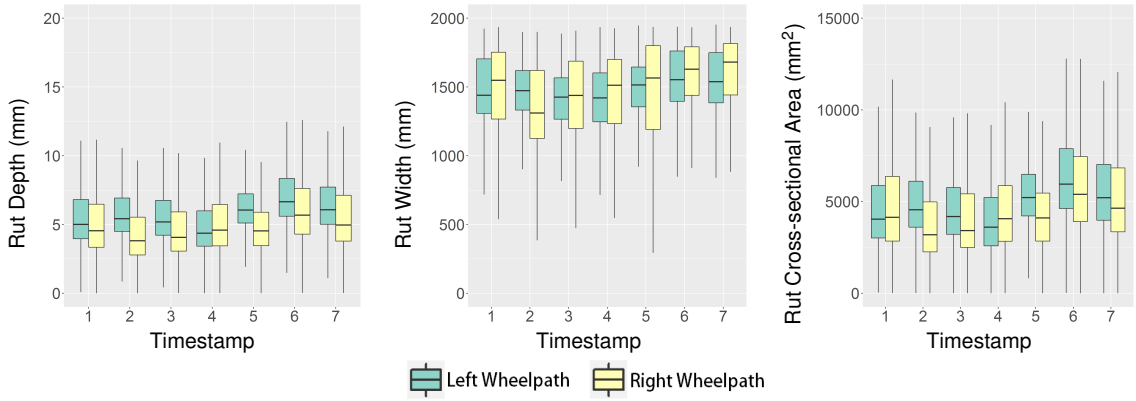

Figure 5.11: Deterioration of Wheelpath-specific Profile-based Parameters at Segment-level: I95 Southbound MP101-100

By comparing consecutive segments on SR26's two projects, as depicted in Figures 5.12 and 5.13, it was noted that rut conditions vary noticeably among these segments. An overall observation is that segments on the Eastbound direction of SR26 had more severe ruts than those on the Westbound direction. Segments between Mileposts 10.5 to 11.5 on both directions showed extremely severe rutting, with the rut depth larger than 1 in. A possible explanation of the severe rutting in these two segments is that it has a lot of truck traffic traveling from and to the Savannah Port. There is an intersection at around Milepost 11.5 that is also at the beginning and ending of a transition slope to a bridge. As a result, excessive stop-and-go heavy truck traffic may be the cause of severe rutting in these two segments.

Furthermore, when comparing the deterioration of rut parameters in segments from different routes, it is observed that the general trend of rut deterioration was slow on SR275 and I95 than several segments on SR26. This finding indicates that rut deterioration can potentially be affected by traffic characteristics and different pavement design.

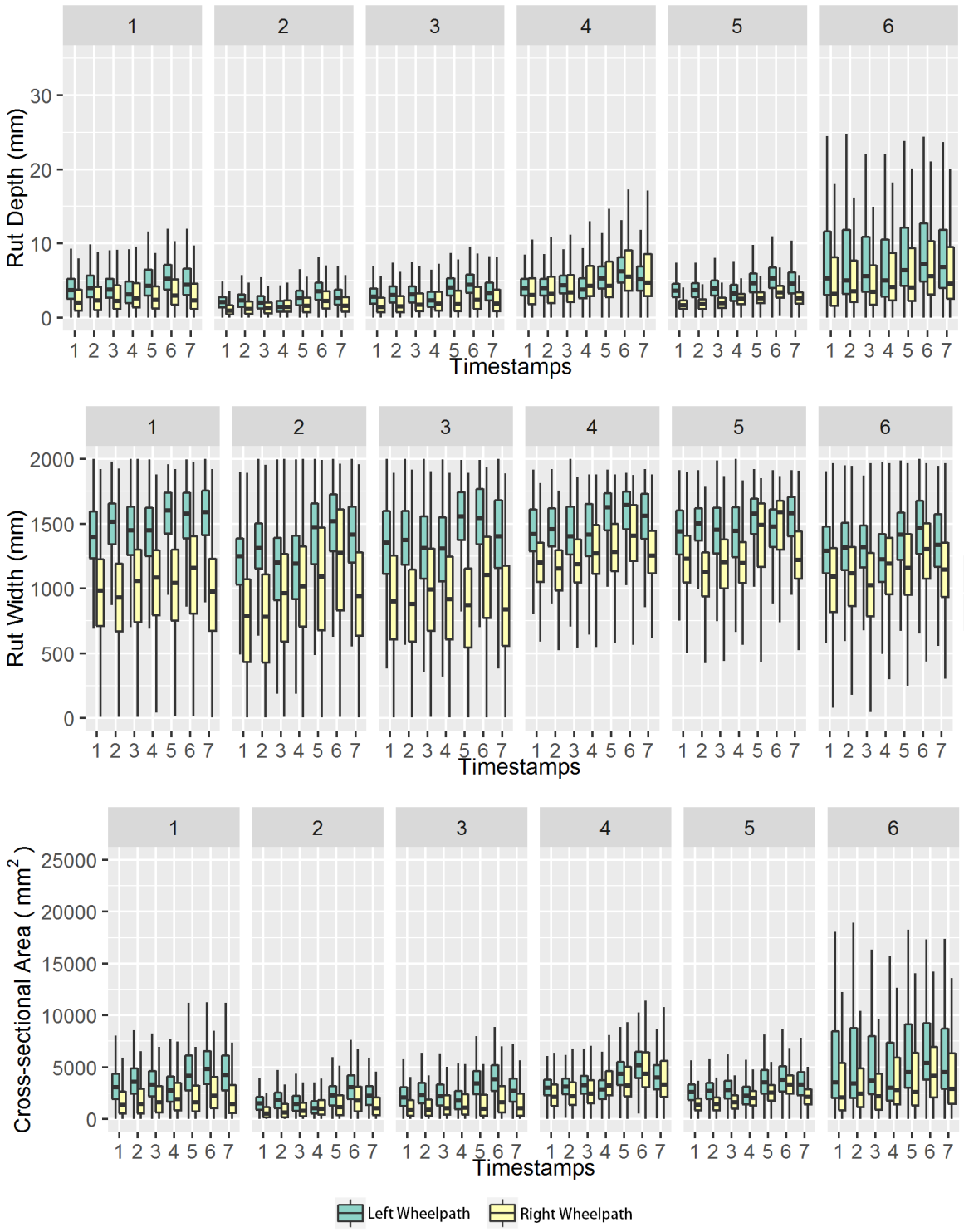

Figure 5.12: Deterioration of Wheelpath-specific Profile-based Parameters at Segment-level: SR26 Eastbound MP5.5-11.5

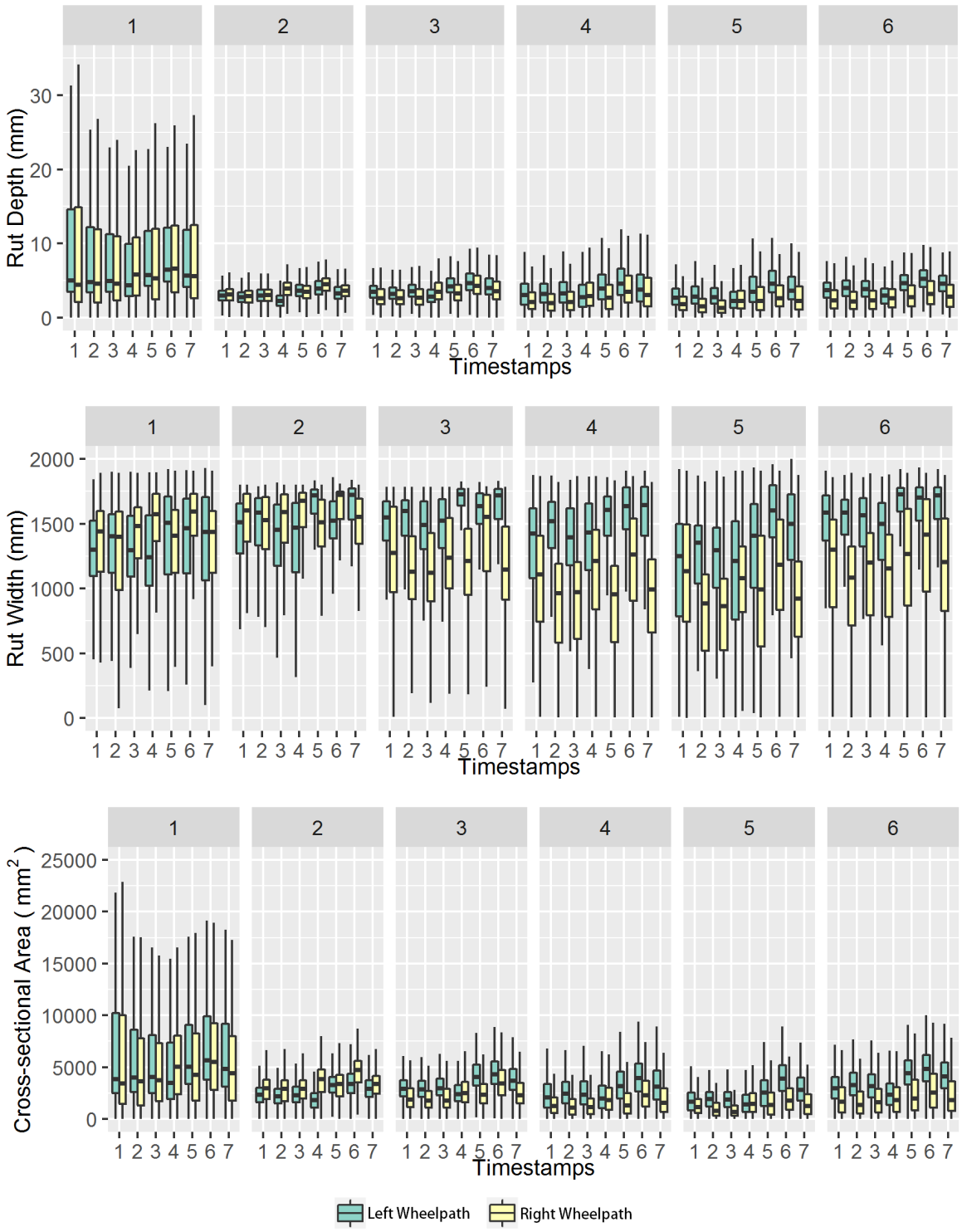

Figure 5.13: Deterioration of Wheelpath-specific Profile-based Parameters at Segment-level: SR26 Westbound MP11.5-5.5

5.3.2 Deterioration of Other Profile-based Parameters

Deterioration of other profile-based rut parameters, including total positive and negative areas, total distortion, total absolute distortion, distortion ratio, and percent deformation, are further analyzed in this section. Results of the deterioration of these parameters are shown in Figures 5.14 to 5.19. In Figure 5.14, it is observed that the deterioration of other profile-based parameters was not noticeable in the SR275 segment throughout the 7 timestamps. In Figure 5.15, on the other hand, a gradual deterioration can be observed in parameters such as TAD and PD.

It is noted that the rut parameters derived based on the positive and negative areas, including TPA, TNA, TD, and DR, show larger variation in their trends over the 7 timestamps in most of the segments, unlike the trends of TAD and PD, which are more consistent and similar to the trends of rut depth and cross-sectional area. Since the positive and negative areas are defined by calculating the areas defined by the transverse profile and an imaginary reference line that connects two edges of the lane, variation can be introduced into these parameters when the geometric relationship between the profile and the reference line slightly changes. Parameters such as TD and DR, therefore, cannot directly reveal true physical shape and conditions of the rut; instead, they represent the relative relationship between TPA and TNA.

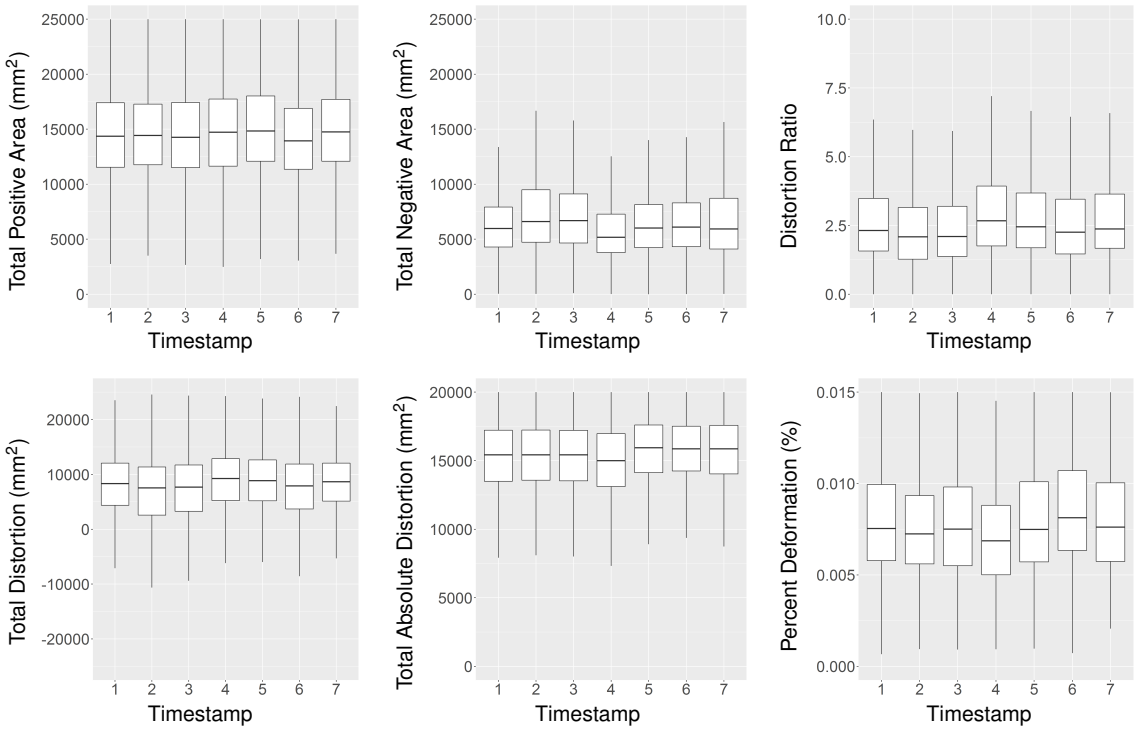

Figure 5.14: Deterioration of Other Profile-based Parameters at Segment-level: SR275 MP0-1

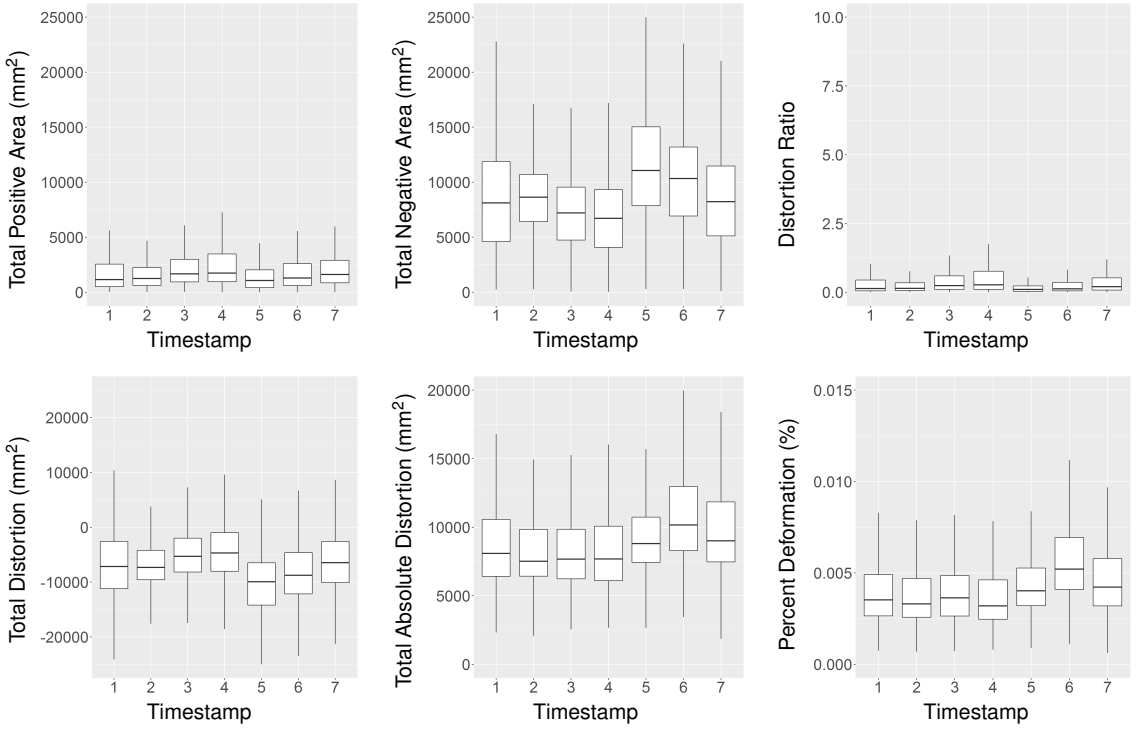

Figure 5.15: Deterioration of Other Profile-based Parameters at Segment-level: I95 MP101-100

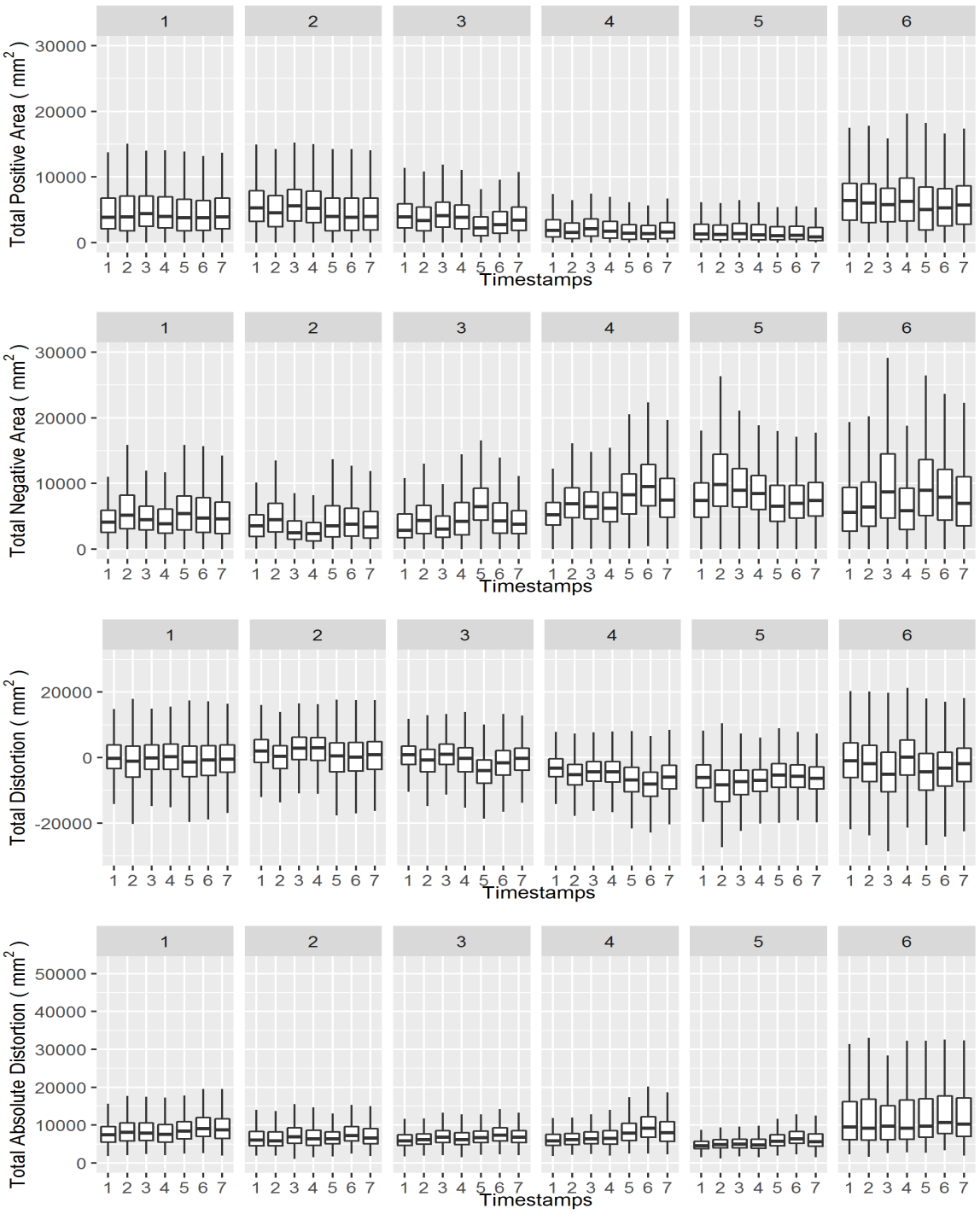

Figure 5.16: Deterioration of Profile-area-based Parameters at Segment-level: SR26 Eastbound MP5.5-11.5

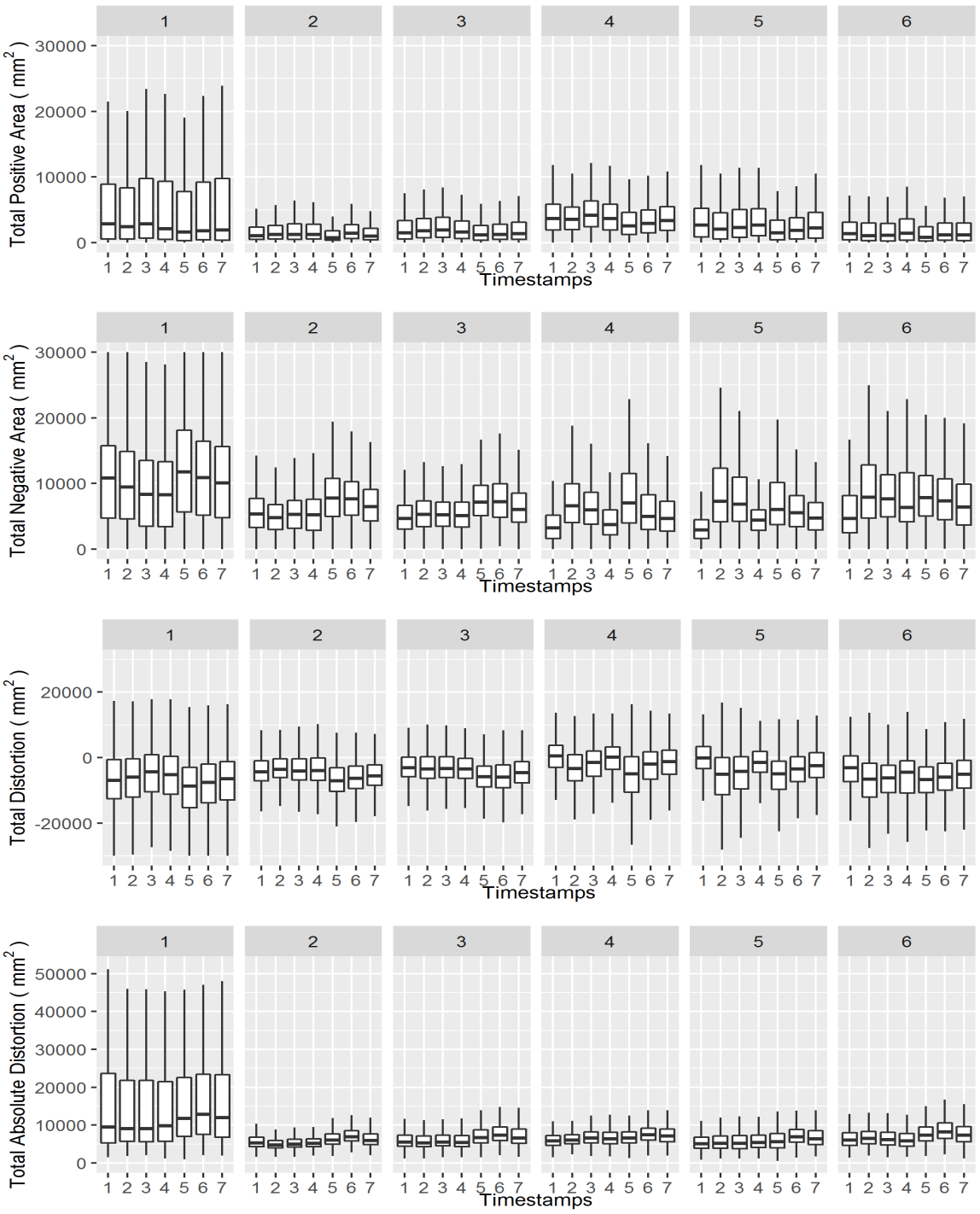

Figure 5.17: Deterioration of Profile-area-based Parameters at Segment-level: SR26 Westbound MP11.5-5.5

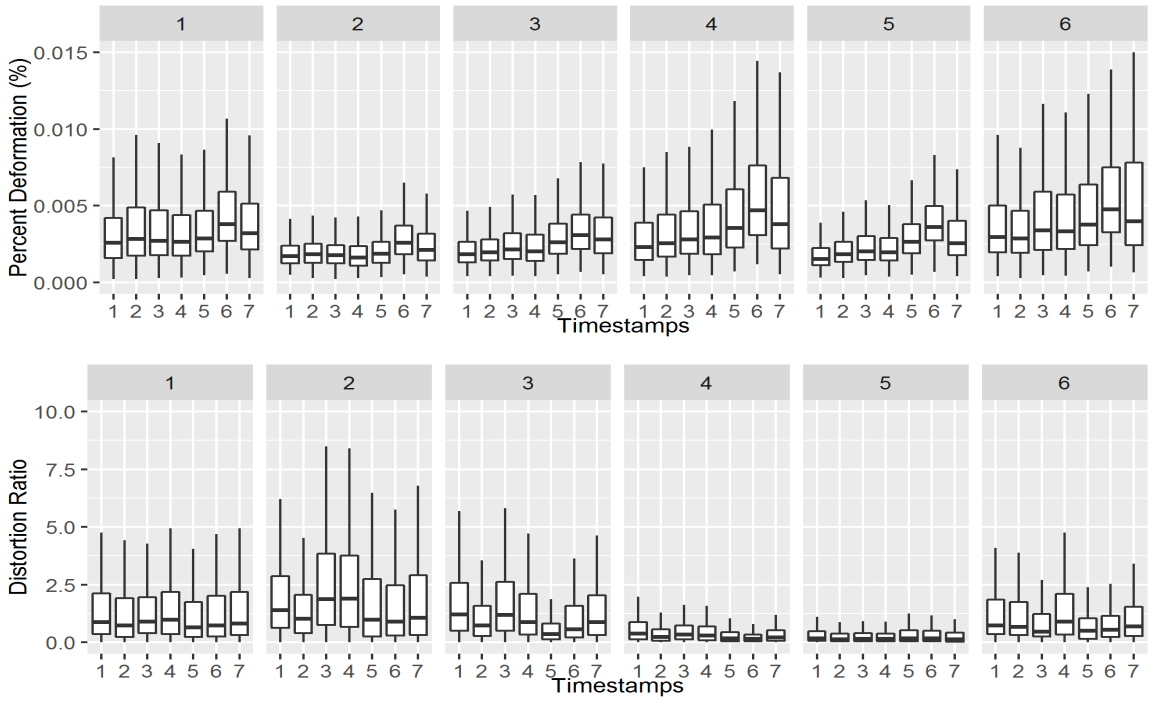

Figure 5.18: Deterioration of Other Profile-based Parameters at Segment-level: SR26 Eastbound MP5.5-11.5

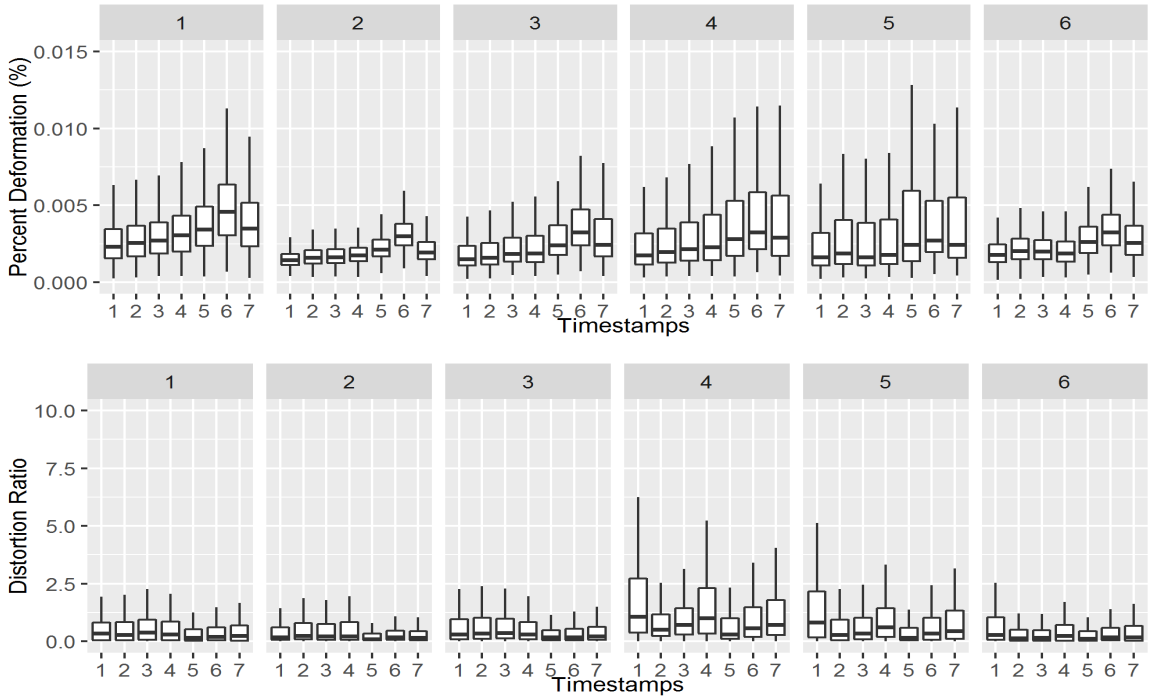

Figure 5.19: Deterioration of Other Profile-based Parameters at Segment-level: SR26 Westbound MP11.5-5.5

5.3.3 Deterioration of Longitudinal Parameters

Figures 5.20 and 5.21 show the deterioration of longitudinal parameters at segment-level. In these figures, each bar represents the length or volume of rutting in a segment at a given timestamp. By comparing the length and volume values of the same segment across multiple timestamps, a positive trend is generally observed. This indicates that most of the segments deteriorates in length and volume. When comparing the parameters between left and right wheelpaths, it is noted that left wheelpath overall had more severe rutting in the left wheelpath. Similar relationship between wheelpaths can also be found in other wheelpath-specific parameters, such as rut depth and cross-sectional area. This finding, however, is inconsistent with the general expectation that rutting in the right wheelpath is typically more severe than the left wheelpath since traffic load is usually higher on the right wheelpath under the effect of cross slope.

5.3.4 Deterioration of Temporal Parameters

Figures 5.22 to 5.25 show the deterioration of temporal rut parameters. The effect of seasonal variation, as discussed in previous sections, is also evident in the trends of temporal parameters at the segment level. Note that when compared to other segments, SR275 has overall smaller temporal parameter values (in Figure 5.22), indicating that rutting in this segment deteriorate slower than the other segments. I95 and SR26 segments, on the other hand, showed fairly similar trends and patterns. It is noted that all segments on SR26 had very similar temporal parameter values at the same timestamp, this result indicates that although segments in the same project may have different severity levels of rutting, they tend to deteriorate at the same rate in this case. One possible explanation of this finding is that since all segments of these two pavement projects share very similar pavement design, age, and traffic characteristics, they deteriorate in the similar manner.

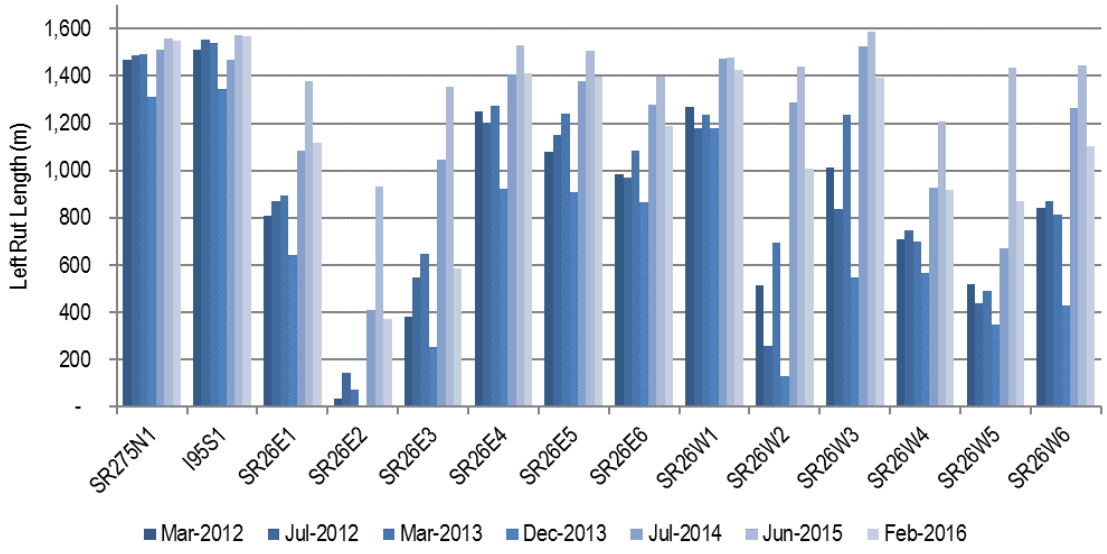

(a) Left Rut Length

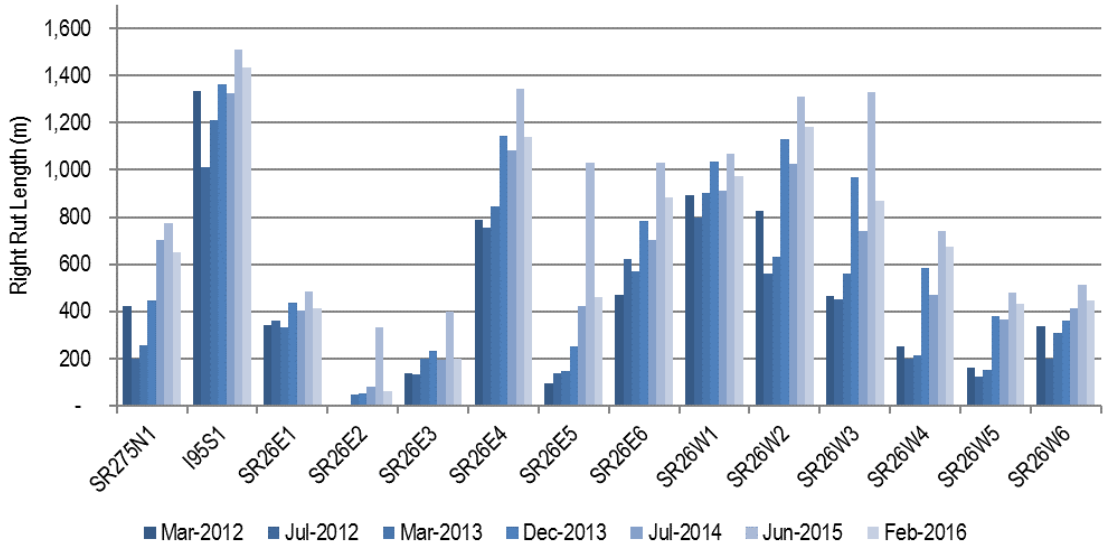

(b) Right Rut Length

Figure 5.20: Deterioration of Rut Length at Segment-level

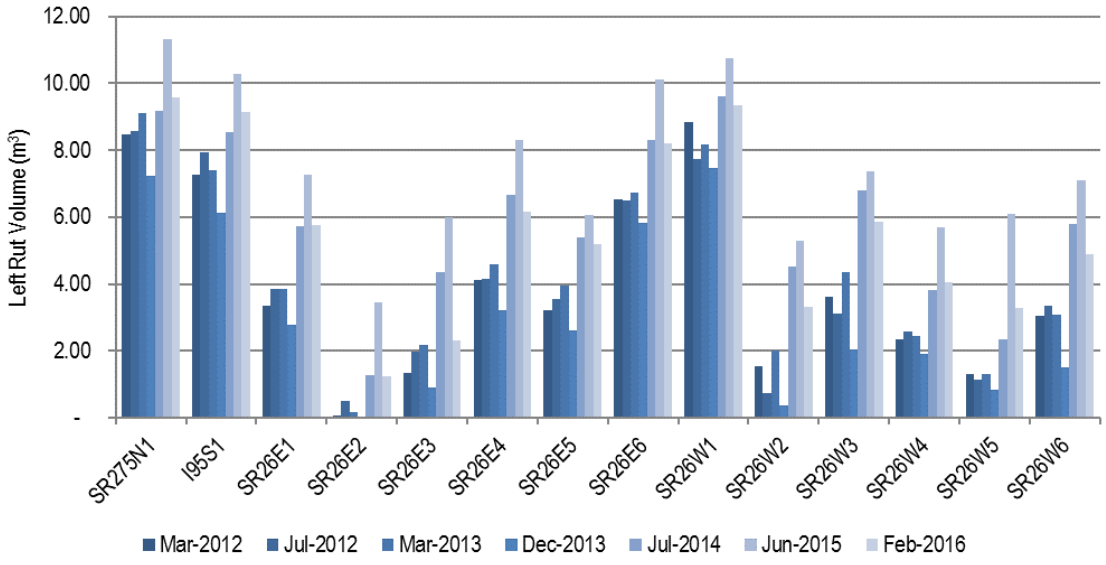

(a) Left Rut Volume

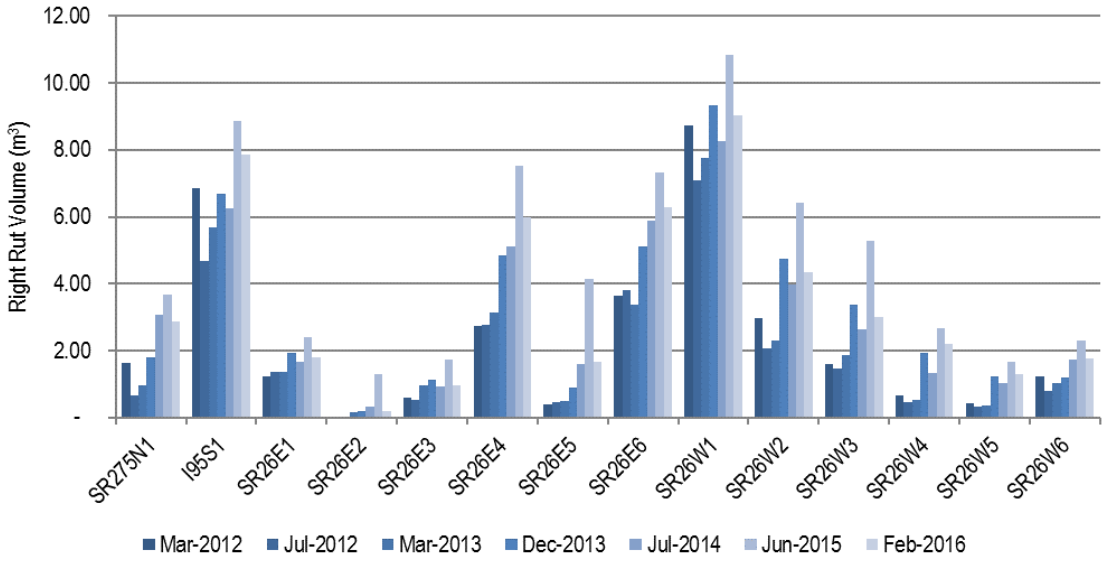

(b) Right Rut Volume

Figure 5.21: Deterioration of Rut Volume at Segment-level

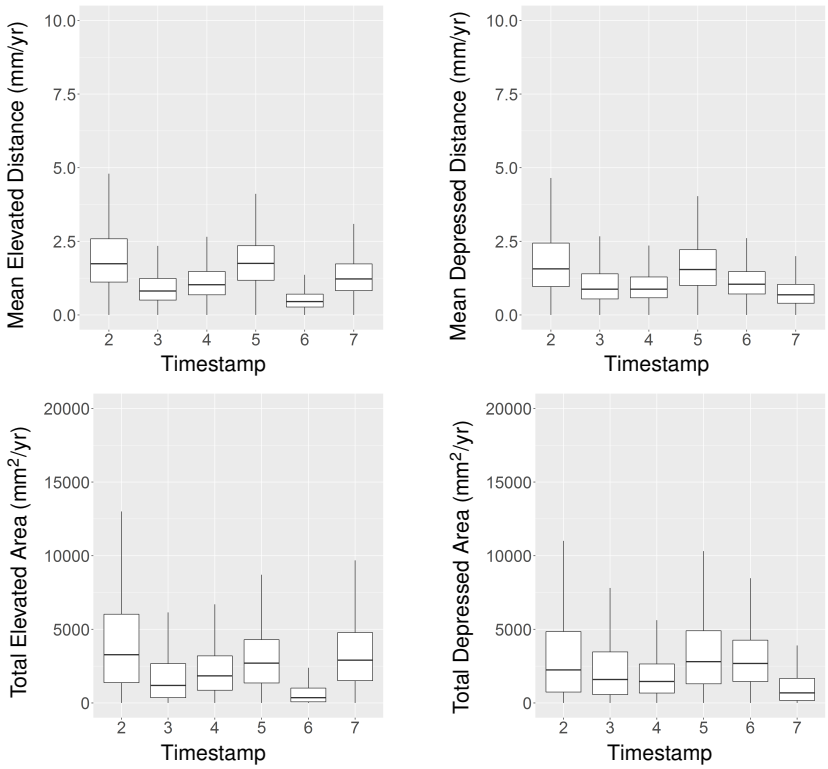

Figure 5.22: Deterioration of Temporal Parameters at Segment-level: SR275

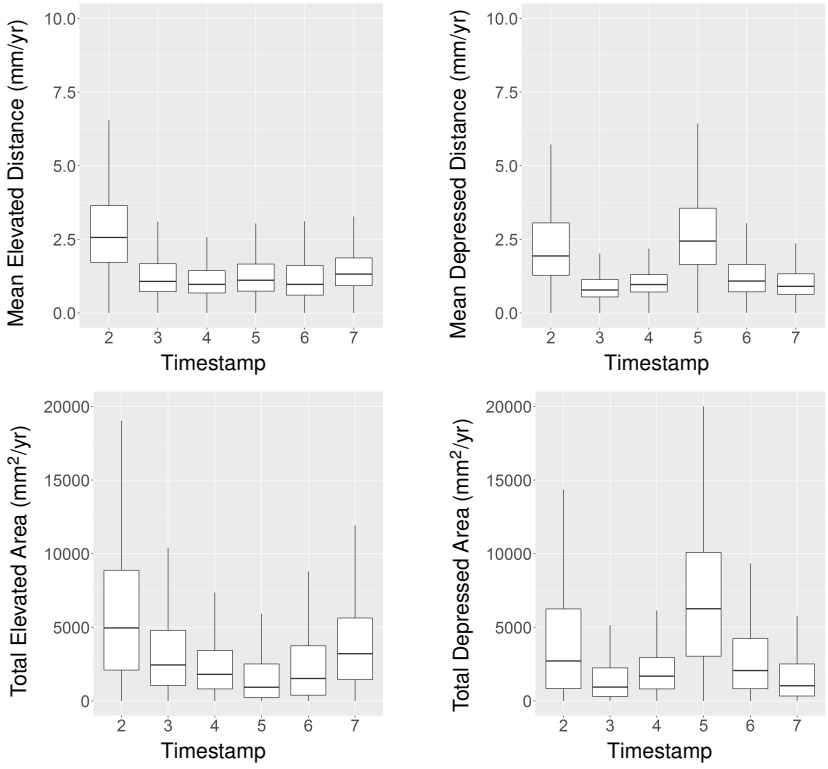

Figure 5.23: Deterioration of Temporal Parameters at Segment-level: I95

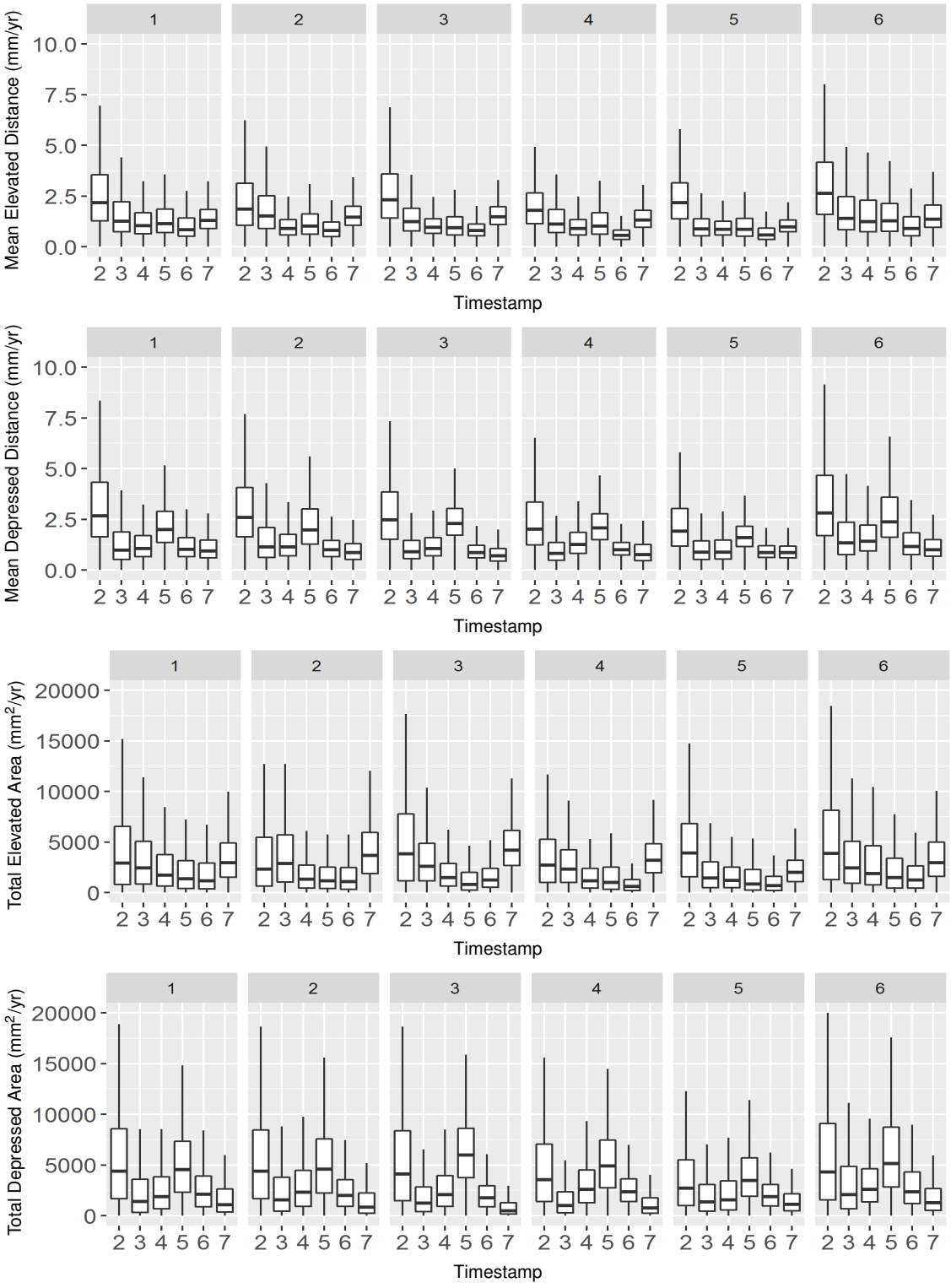

Figure 5.24: Deterioration of Temporal Parameters at Segment-level: SR26 Eastbound MP5.5-11.5

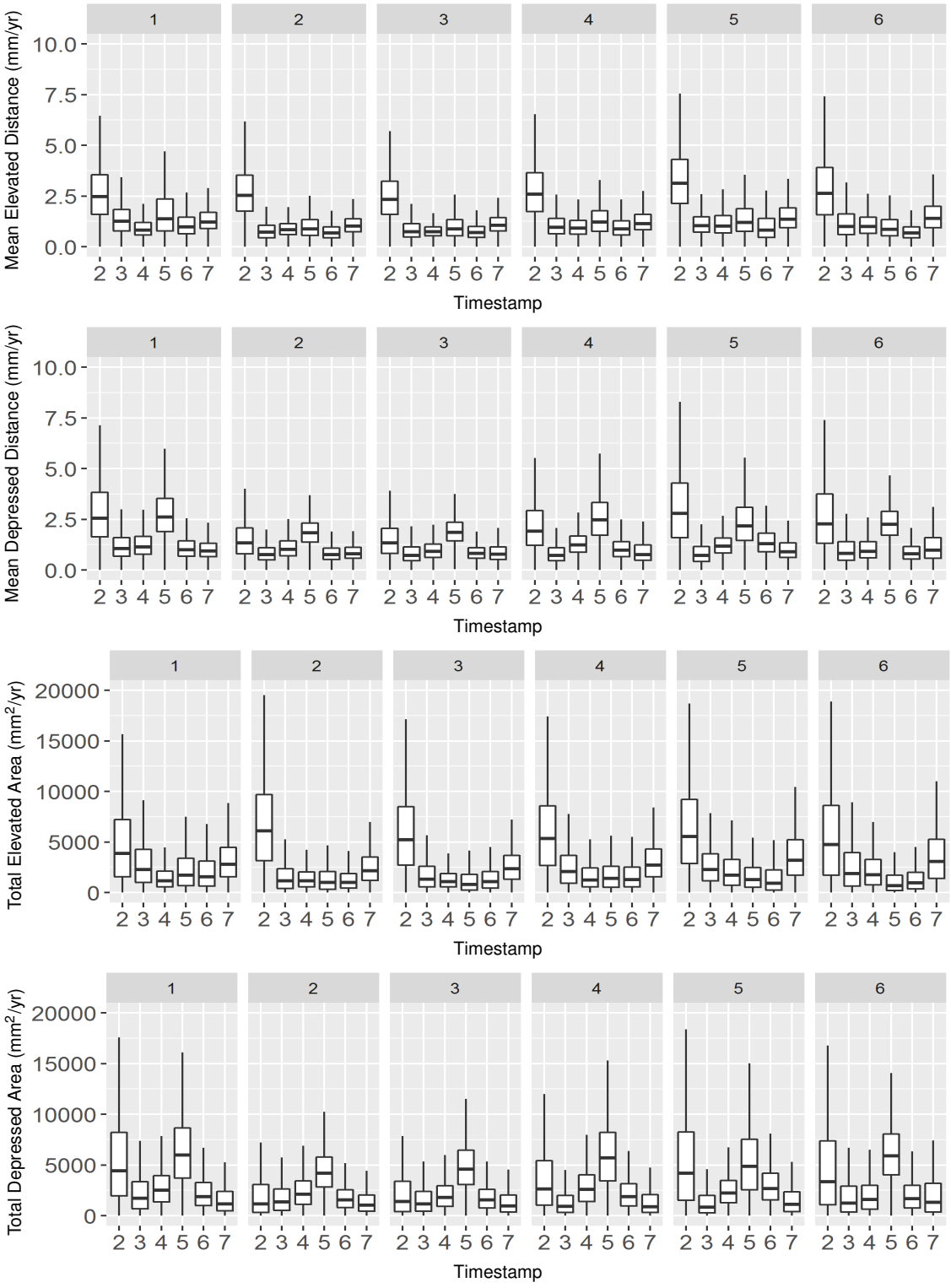

Figure 5.25: Deterioration of Temporal Parameters at Segment-level: SR26 Westbound MP11.5-5.5

5.4 Individual Rut-Level Deterioration Visualization

The above sections demonstrate how 3D sensing technology and the proposed method in Chapter 4 can be used as statistical means that advances the understanding of rut deterioration at larger scales. In fact, the strength of proposed method prevails when used to study the detailed deterioration of rutting at a finer level. In this section, a few examples are selected to demonstrate how the proposed method can be used to quantify rut deterioration at individual rut-level. Acknowledging the possible effect of seasonal variation on the shape of rutting, only summer timestamps (i.e., 7/13/2012, 7/18/2014, and 6/15/2015) were selected for the individual rut-level analysis in this section.

5.4.1 Rut Deterioration of a Selected Section on SR26

Figures 5.26 and 5.27 illustrate the 3D rut shapes of a 25-meter pavement section on SR26 and the exact change in shape between different timestamps. By comparing the 3D shapes of these timestamps, it is clear that ruts in both wheelpaths deteriorated faster close to the beginning section (bottom left of each figure). This finding was also observed in the field at the beginning section, which was at an intersection where heavy truck traffic frequently decelerates and accelerates. From the 3D shape change, as depicted in Figures 5.26d and 5.26e, it is clear that the change was more severe between the first two timestamps. This is reasonable because the first two timestamps were two years apart whereas the last two timestamps were only one year apart. From the 2D deterioration maps in Figures 5.27d and 5.27e, it is evident that the deterioration in this section can be associated with heavy truck traffic because of the dual-wheel shapes observed in both wheelpaths. The exact elevation and cross-sectional area changes can be further calculated and represented using the temporal parameters proposed in this study.

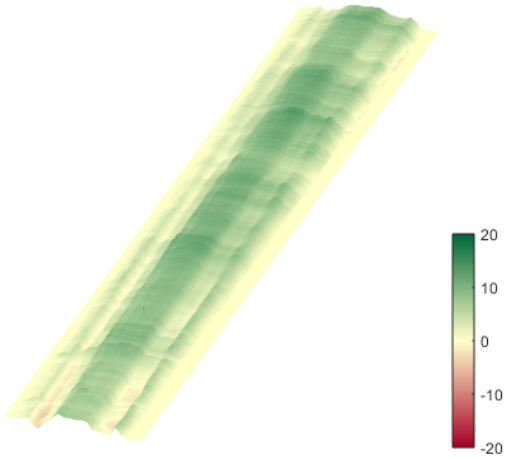

(a) 7/13/2012

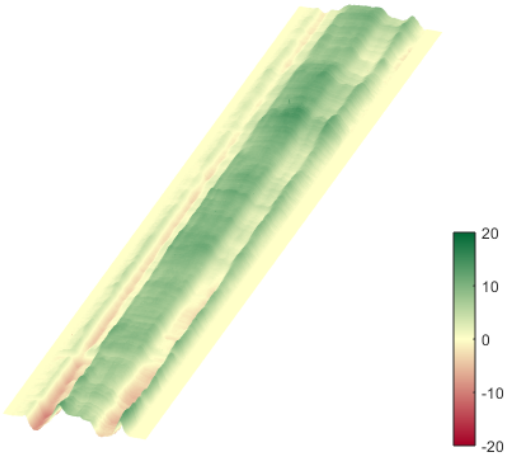

(b) 7/18/2014

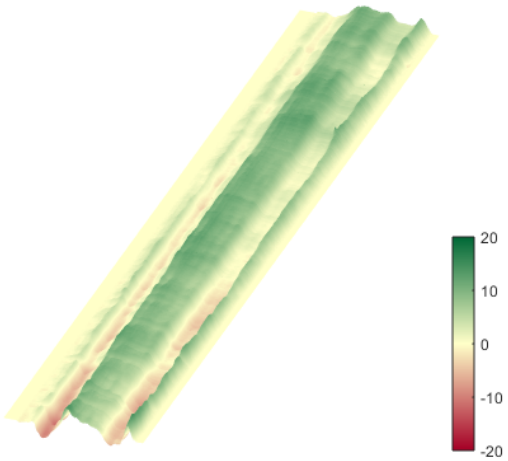

(c) 6/15/2015

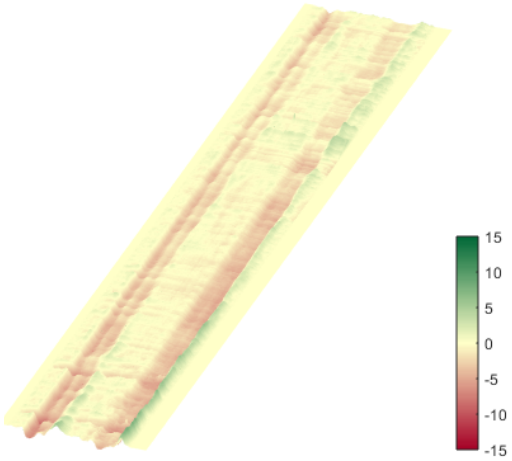

(d) 7/13/2012 to 7/18/2014

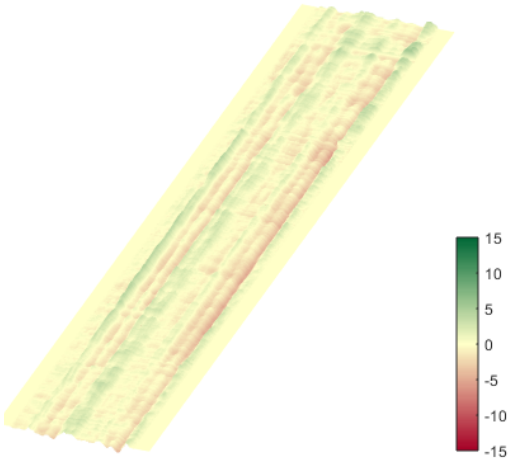

(e) 7/18/2014 to 6/15/2015

Figure 5.26: 3D Visualization of Rut Deterioration on SR26 Westbound

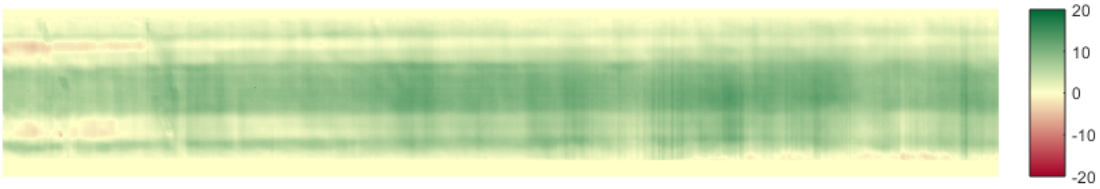

(a) 7/13/2012

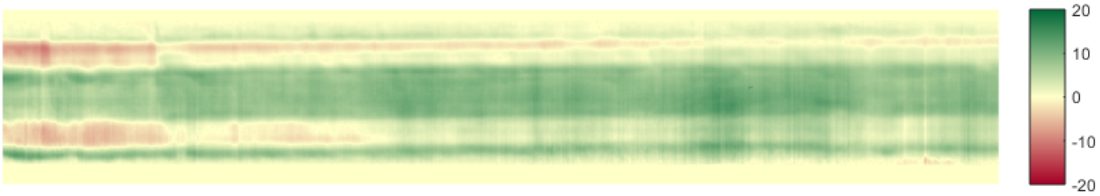

(b) 7/18/2014

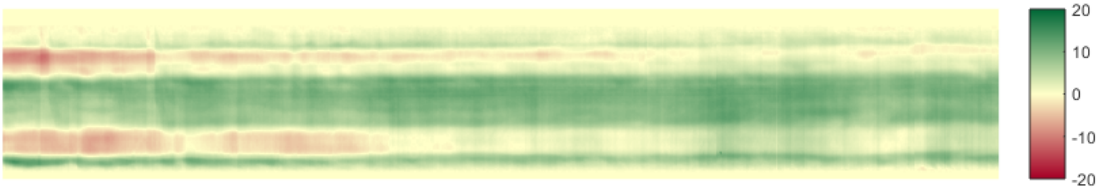

(c) 6/15/2015

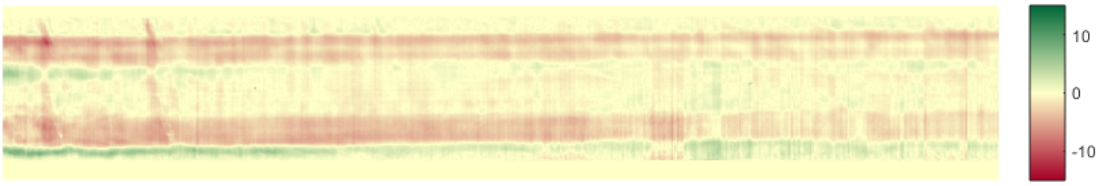

(d) 7/13/2012 to 7/18/2014

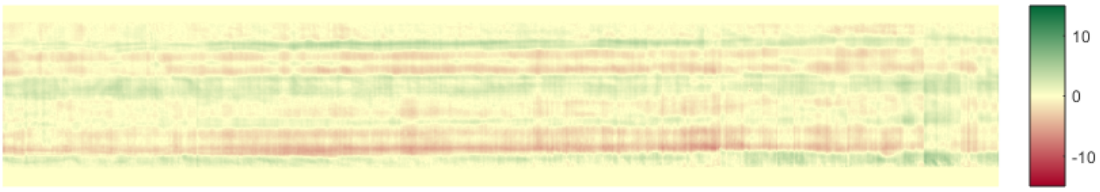

(e) 7/18/2014 to 6/15/2015

Figure 5.27: 2D Visualization of Rut Deterioration on SR26 Westbound

5.4.2 Rut Deterioration of a Selected Section on SR275

A 45-meter section on SR275 Northbound was selected to demonstrate how the proposed method can be used to visualize and quantify the deterioration of rutting. As shown in Figures 5.28 and 5.29, rutting in both wheelpaths grew not only in depth, but also in length and volume. While the deterioration was not as obvious as the previous example on SR26, the change in the longitudinal shape was appreciable. This finding further affirms the importance of the use of longitudinal parameters for rut characterization and deterioration analysis.

5.4.3 Discussion

The two examples shown in this section demonstrated how the proposed boundary-based data registration method can effectively register multi-timestamp 3D pavement data for rut characterization and deterioration analysis at large scales, such as project and segment-levels, it can also support deterioration analysis at individual rut-level.

The examples above also demonstrate two types of data visualization for long-term 3D pavement data. Each of these two types of visualization has its advantages and disadvantages. For example, the 3D models can help engineers evaluate the pavement at a scale and detailed level that cannot be achieved even in the field. Many 3D modeling software can provide interactive functions that allow engineers to examine the pavement section at any desired scale and angle. These 3D graphics, however, are limited by the viewing angle if plotted on a 2D surface (i.e., paper). The 2D visualization, on the other hand, can effectively provide a holistic view of how the section deteriorates using color, even though it does not visually show the 3D shape.

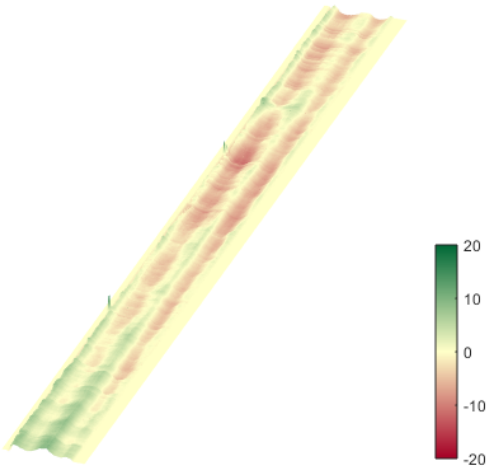

(a) 7/13/2012

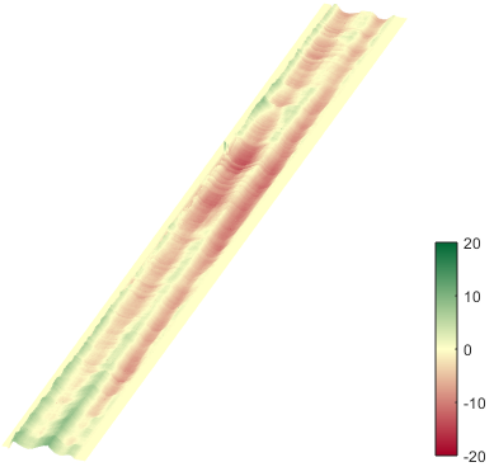

(b) 7/18/2014

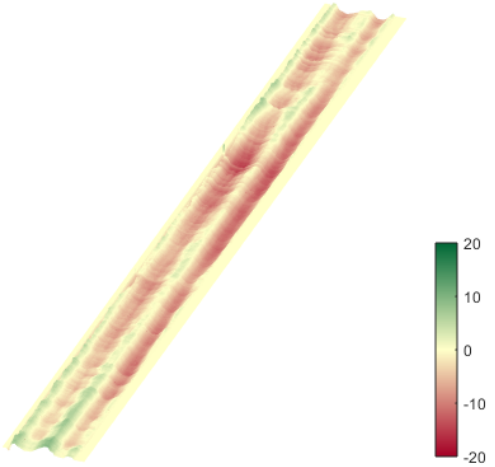

(c) 6/15/2015

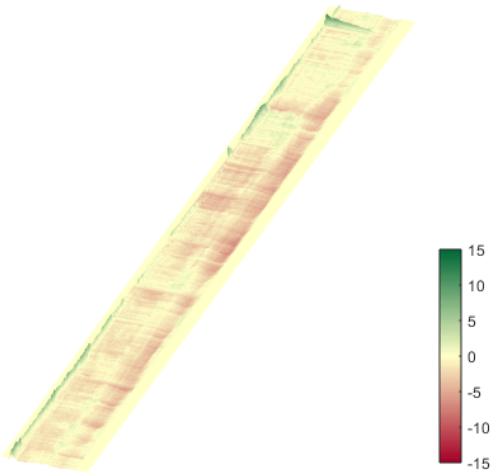

(d) 7/13/2012 to 7/18/2014

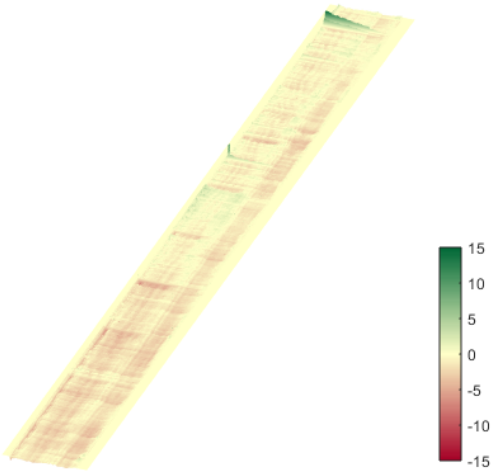

(e) 7/18/2014 to 6/15/2015

Figure 5.28: 3D Visualization of Rut Deterioration on SR275 Northbound

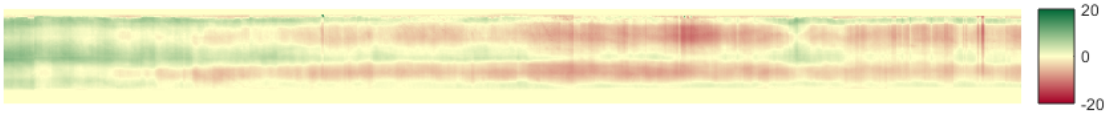

(a) 7/13/2012

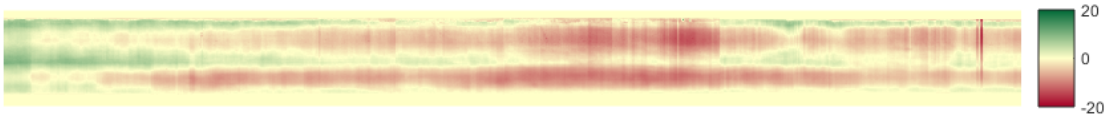

(b) 7/18/2014

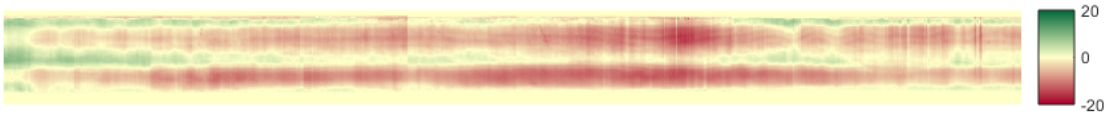

(c) 6/15/2015

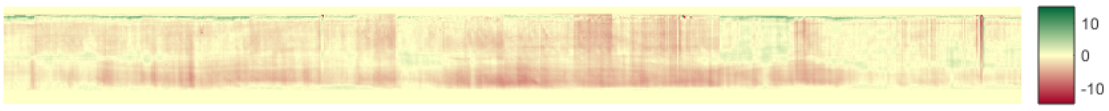

(d) 7/13/2012 to 7/18/2014

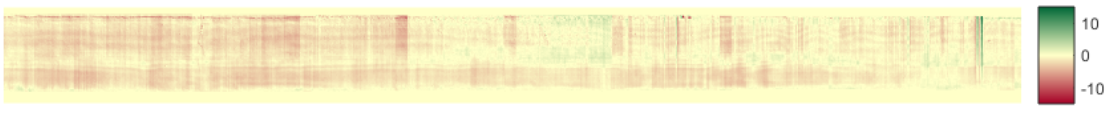

(e) 7/18/2014 to 6/15/2015

Figure 5.29: 2D Visualization of Rut Deterioration on SR275 Northbound

5.5 Preliminary Assessment of Rut Parameters

Fair amount of rut parameters has been defined in the literature to characterize the shape of 3D rutting. While some parameters can provide a fair representation of the severity of rutting, they may not be sufficient to describe the deterioration behavior of ruts. In this section, some preliminary assessment of rut parameters used in this study, in terms of their correlation and some observed issues, are summarized.

5.5.1 Correlation among Rut Parameters

Correlation among rut parameters has been studied in the literature for identifying the potential variation of different data collection techniques. For example, Simpson (1999) examined the correlation between rut depths derived using different methods (e.g., straightedge and stringline). Simpson also explored the correlation among other parameters such as rut width, positive area, negative area, and fill area. Qiu (2013) also conducted correlation analysis to examine rut depth measurements calculated using the AASHTO PP69 provisional standard and the straightedge method.

In this section, correlation among rut parameters used in this study is examined. Figures 5.30 to 5.33 show the correlation matrices among rut parameters on the available routes. From these matrices, several findings in the multi-scale deterioration analysis can be confirmed. For example, it is noted that several rut parameters, including PD, LRD, RRD, LCA, RCA, and TAD, show high correlations. This indicates that these parameters generally reflect the severity of rutting, i.e., the higher these parameters are, the more severe the rutting is. Longitudinal parameters also show high correlations with the aforementioned parameters, especially on SR26, indicating that ruts grow not only in depth and area, they also grow in length and volume. Temporal parameters, share high correlation among themselves; however, they do not well correlate with other spatial parameters. This implies that temporal parameters represent certain rut features (e.g., deterioration) that other spatial pa-

rameters cannot. The correlation matrix of SR275 rut parameters show less correlation among them, which can be caused by the lack of diversity in rut conditions in this dataset.

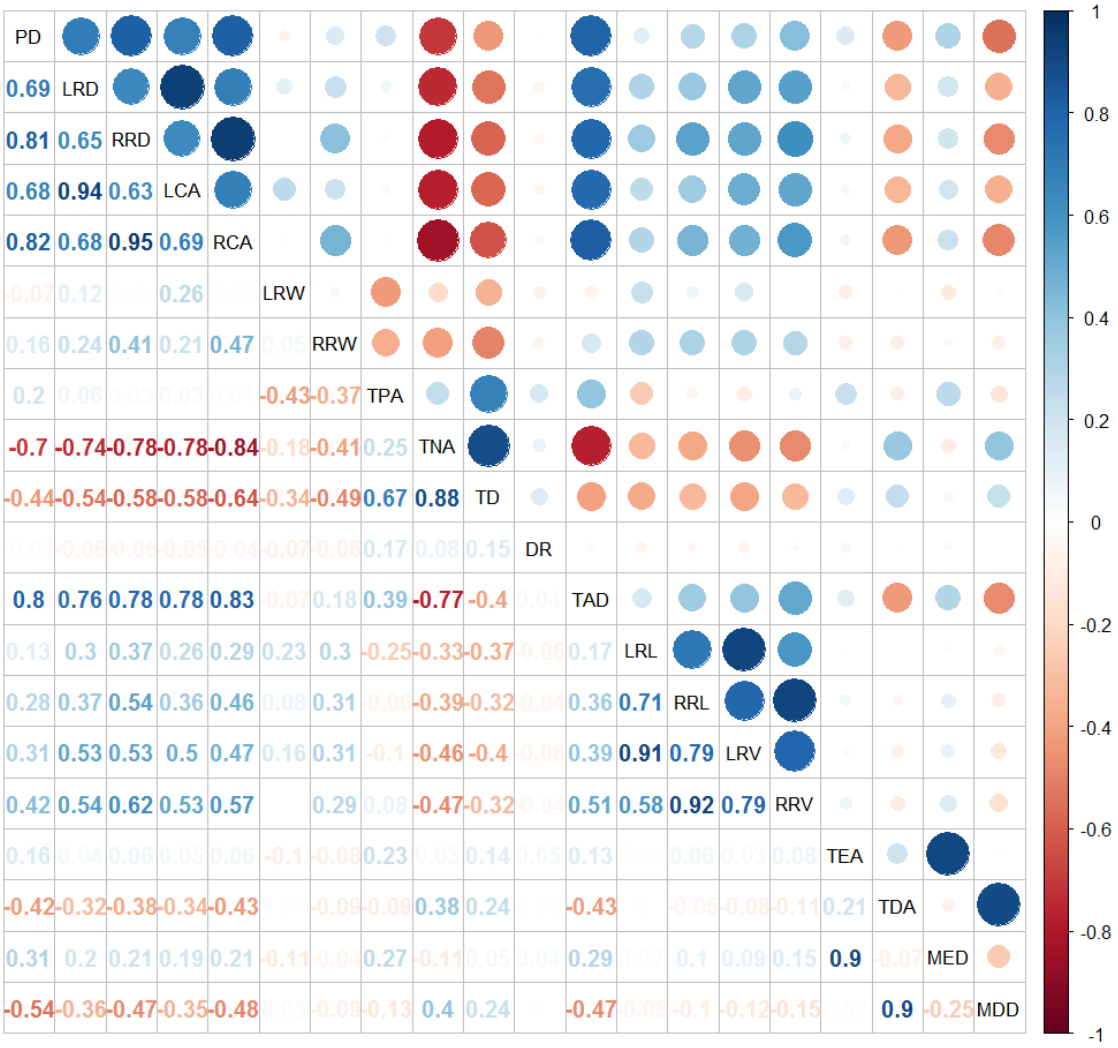

Figure 5.30: Correlation Matrix of Rut Parameters on SR26 Eastbound

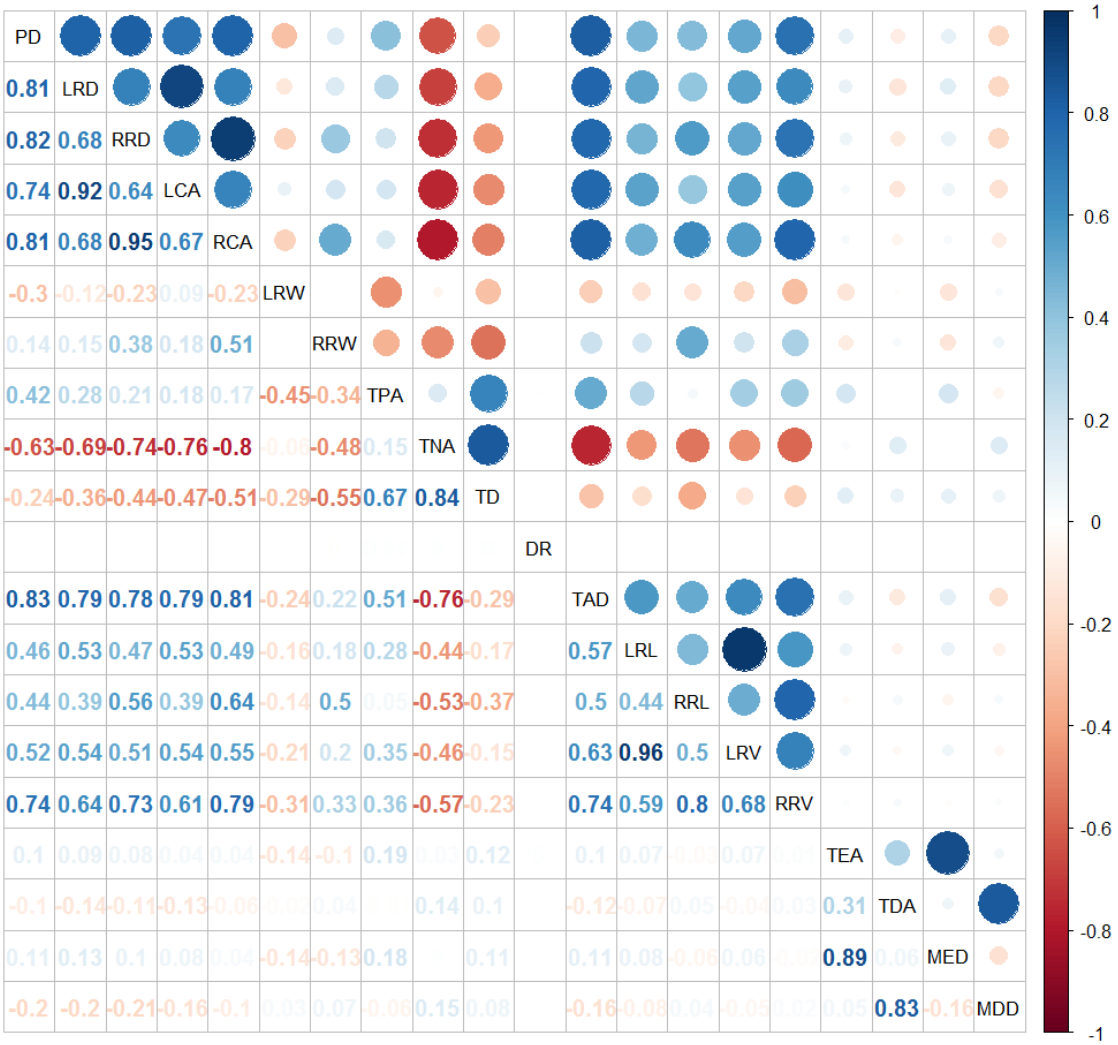

Figure 5.31: Correlation Matrix of Rut Parameters on SR26 Westbound

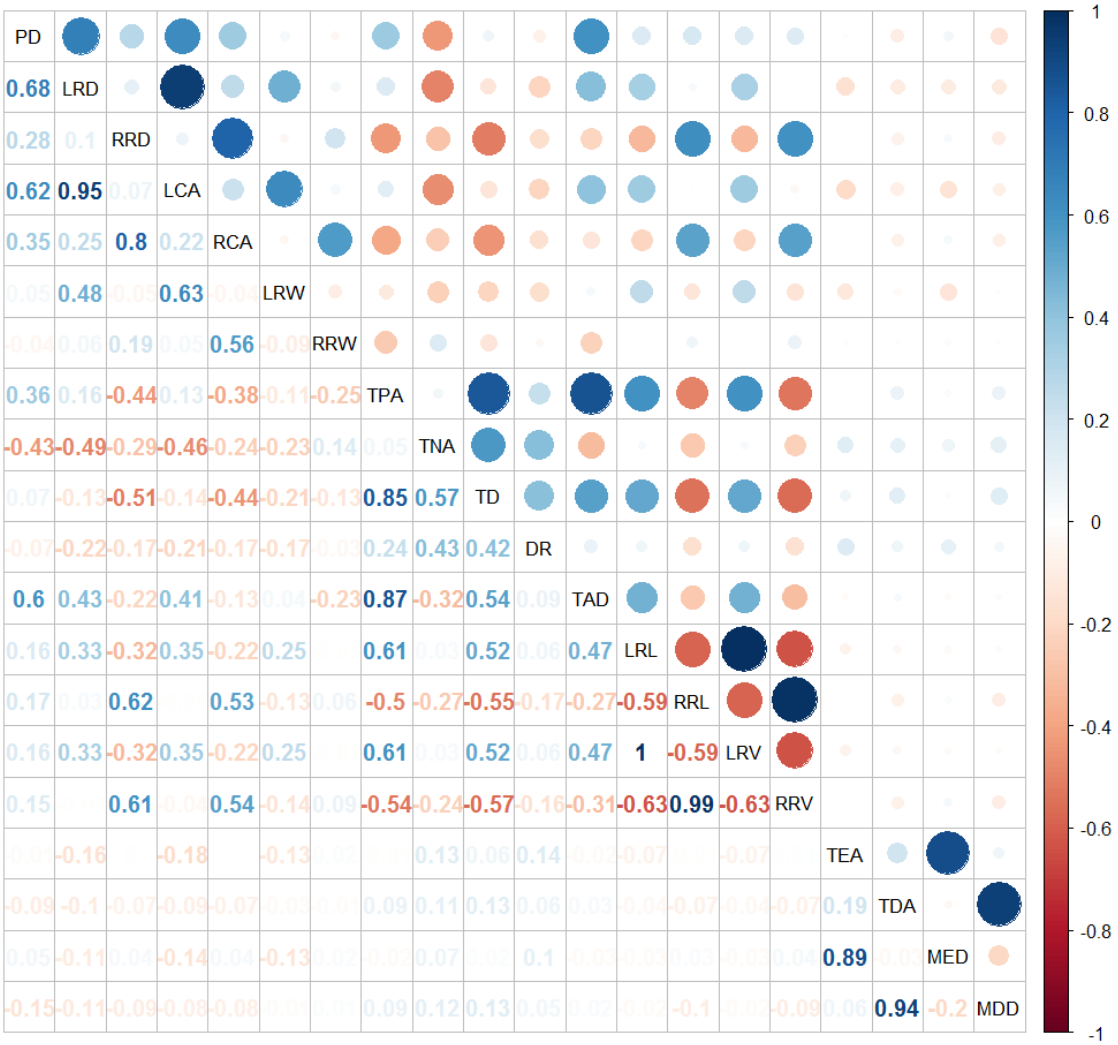

Figure 5.32: Correlation Matrix of Rut Parameters on SR275 Northbound

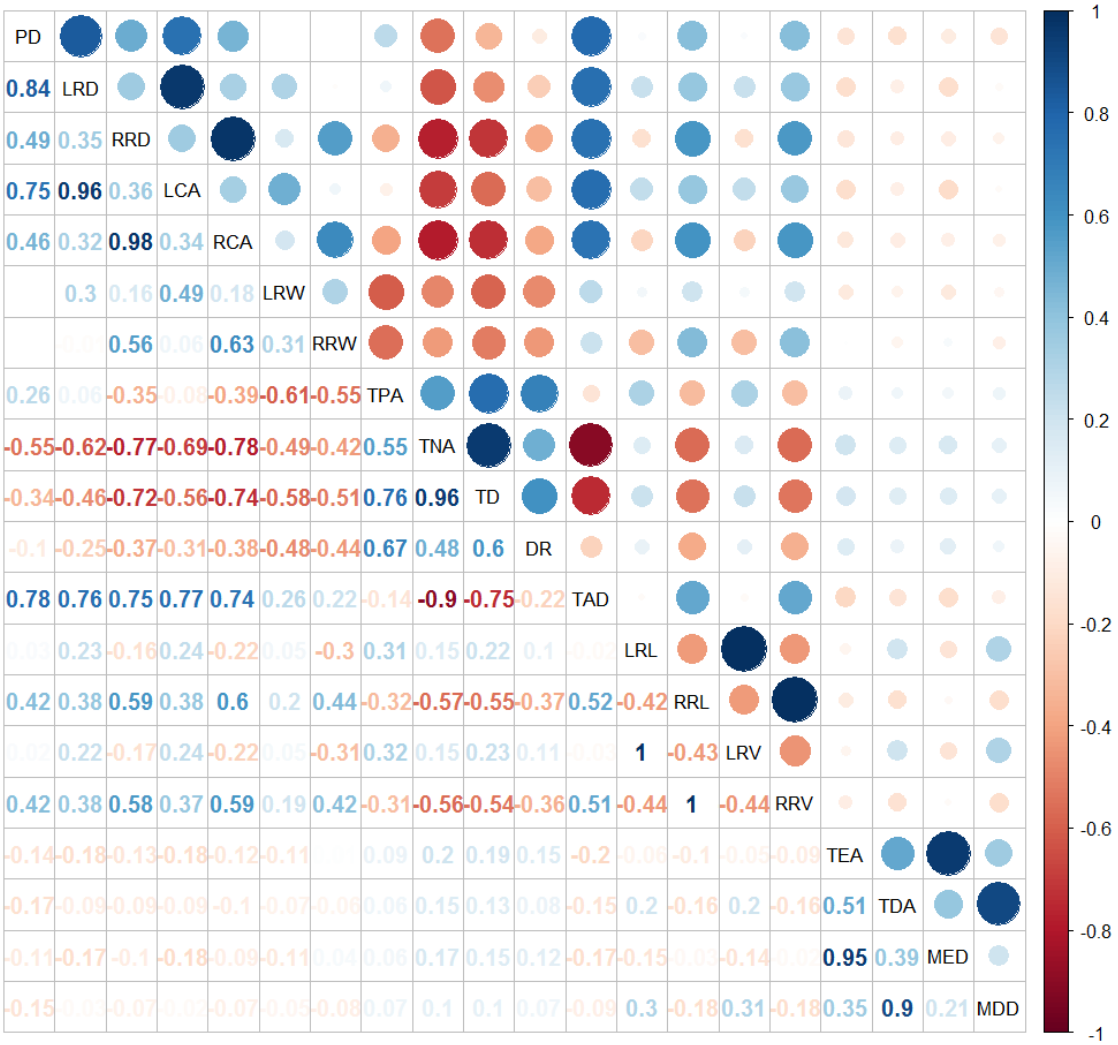

Figure 5.33: Correlation Matrix of Rut Parameters on I95 Southbound

5.5.2 Observed and Potential Issues of Parameters

Partial Lane Profile-based Parameters

Partial profile-based parameters in this study refer to rut parameters that are derived from part of the transverse lane profile. For example, for calculating right wheelpath rut parameters, as depicted in Figure 5.34, AASHTO PP69 rotates the transverse profile so that the elevations at the right edge (Spot 5) and the lane center (Spot 1) are zero. Rut parameters, such as right rut depth, width, and cross-sectional area can be calculated using just the right half of the profile. Moreover, some studies and software for two sensor systems (e.g., LCMS) use profiles collected from the two sensors separately to calculate left and right rut parameters (Li, 2012). For instance, profiles collected by the right sensor of GTSV were used to calculate right rut depths in the study conducted by Li (2012).

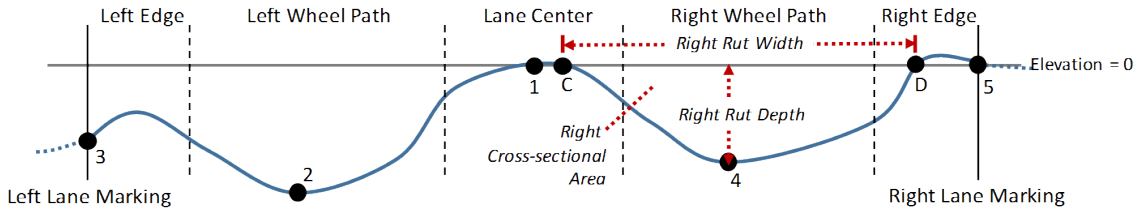

Figure 5.34: Deriving PP69 Right Rut Parameters

A potential issue of calculating rut parameters using partial lane profiles is that these partial profiles may not reveal the entire shape if the rut is not entirely in the wheel path. For instance, Figure 5.35 shows an isolated rut on 11th Street in Atlanta. This rut is wide and its basin exceeds the typical width of the wheelpath (e.g., 1,000 mm). A stitched transverse profile of this rut is shown in Figure 5.36. The straightedge rut depth measured at this location was approximately 38.1 mm (1.5 in). However, if rut depth is calculated using the right half of the rotated profile (Figure 5.37), the calculated rut depth became 32.4 mm. Calculation of other right wheelpath rut parameters, such as rut width and cross-sectional area, would also result in underestimation. Moreover, similar results are expected if only the half profile collected by the right laser unit was used to calculate rut parameters.

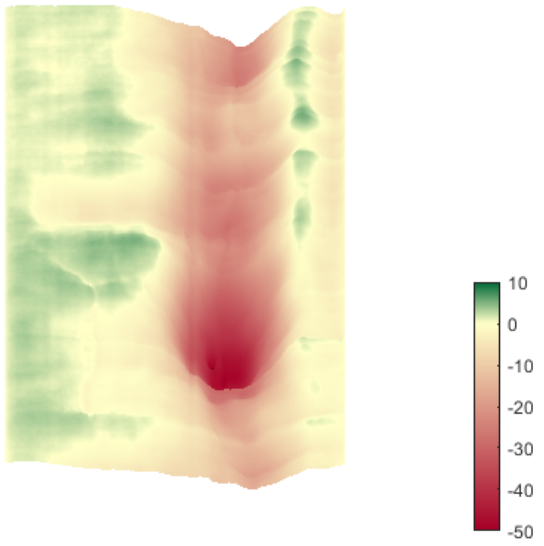

Figure 5.35: An Example of Wide Rutting on 11th Street in Atlanta

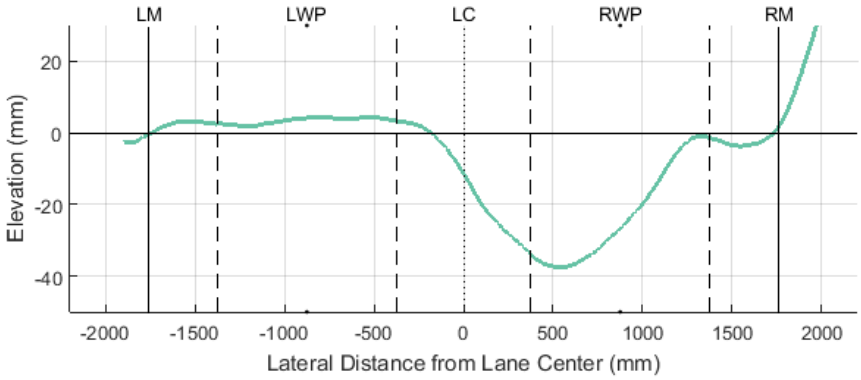

Figure 5.36: Transverse Profile of a Wide Rut in Right Wheelpath

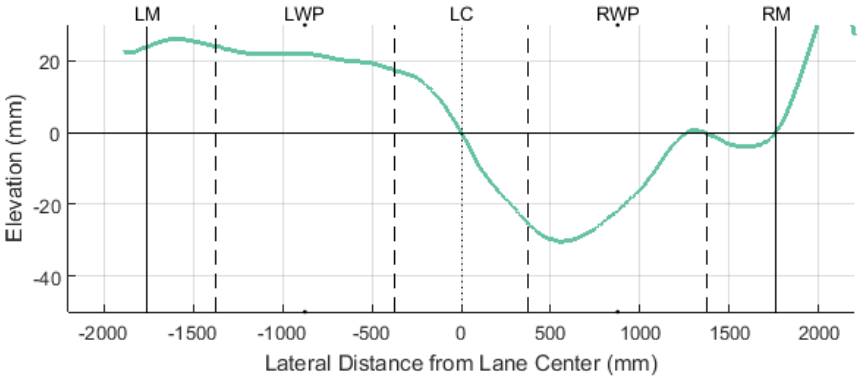

Figure 5.37: Rotated Transverse Profile for Calculating Right Rut Parameters

Another potential issue of calculating rut parameters using partial lane profiles is that the same measurement may be the outcomes of different rut shapes. As depicted in Figure 5.38, the two profiles show two distinct shapes of rutting, however, their left rut parameters (e.g., depth, width, and cross-sectional area) may be the same based on PP69 definition.

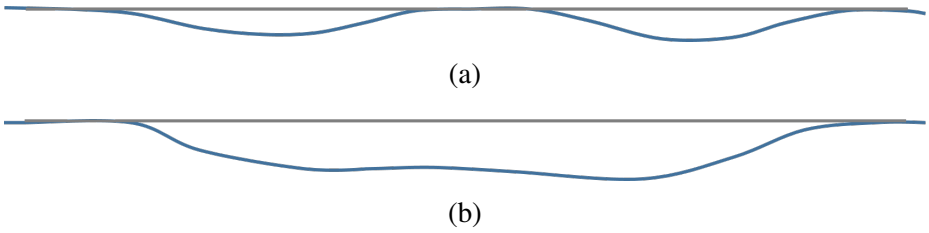

Figure 5.38: Illustration of Different Rut Shapes with Same Left Rut Depth

A possible solution for the above issues with regard to partial lane profile-based parameters is that, instead of rotating the transverse profile, the normalized lane profile can be used to derive wheelpath-based parameters. The following describe the solution in more details.

As depicted in Figure 5.39, the 5 zones defined in PP69 are adapted to determine the lowest point (valley) in each wheelpath zone, and the highest point (peak) in each of the other three zones. Since left rut parameters and right rut parameters can be calculated in the same manner, the following describe how left profile-based parameters are defined and calculated.

- **Left rut depth** is defined as the vertical distance between the left wheelpath valley and either (1) the line connecting left and right peaks (if the center peak is lower than this line, as depicted in Figure 5.39a) or (2) the line connecting left and center peaks (see Figure 5.39b);

- **Left rut width** is determined as the horizontal distance between left and center peaks; and

- **Left rut area** is the area enclosed by the profile and either the line connecting left and

right peaks (Figure 5.39a) or the line connecting left and center peaks (Figure 5.39b). Note that for the either case, left rut area can be calculated as the sum of vertical distances from all profile points between left and center peaks to the corresponding peak connecting line.

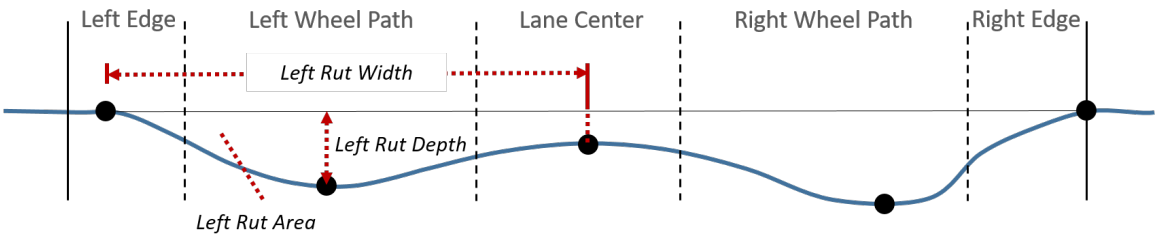

(a) Lower Center Elevation

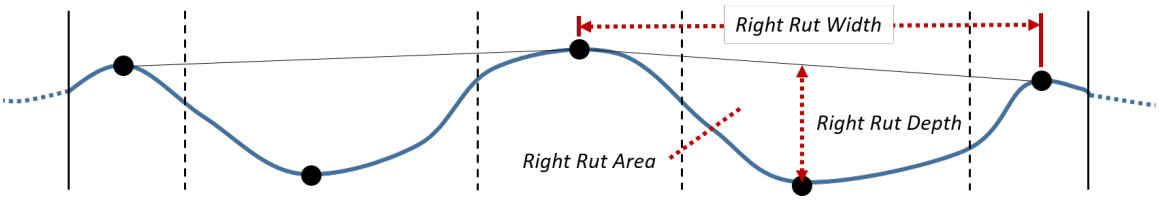

(b) Higher Center Elevation

Figure 5.39: Proposed Definition of Wheelpath-specific Rut Parameters

Reference Surface Plane Assumptions

Positive and negative areas in the literature were determined by connecting both edges of the lane with an imaginary straight line, as depicted in Figure 5.40. However, this reference line does not represent the actual horizon plane or the original pavement surface. Consequently, the derived positive and negative areas and the total distortion and the distortion ratio cannot well represent the severity of rutting, and direct comparison of these parameters may not be meaningful.

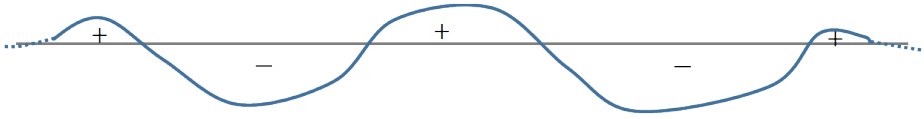

Figure 5.40: Illustration of Positive and Negative Areas

5.6 Summary

In this chapter, 3D rut shape and its deterioration behaviors were characterized and analyzed at multiple scales using long-term 3D pavement data. Rut parameters, including transverse profile-based parameters, longitudinal parameters, and temporal parameters were defined and proposed. Descriptive statistics and 2D and 3D visualizations were used to analyze the deterioration behaviors of rutting. Some key findings of this chapter are summarized as the following:

- Transverse profile-based rut parameters, including rut depth, rut cross-sectional area, percent deformation, and total absolute distortion show good correlation among each other, providing consistent information about the conditions of ruts.
- Longitudinal parameters also showed similar trends as the aforementioned parameters, indicating that ruts not only grow in depth and area, they grow longitudinally in length and volume.
- Temporal parameters provide a direct means to quantify the deterioration of rutting. These parameters can be very useful especially when the rate of deterioration is high.
- The multi-scale analysis results show that seasonal variation can have appreciable effect on the deterioration of ruts. Temporal parameters derived from a shorter period (e.g., a few months), can be affected by the seasonal variation. This finding suggests that, for different deterioration analysis applications, different analysis periods should be applied in order to obtain consistent results.
- The comparison among three different routes showed that traffic and roadway characteristics also play an important role in the deterioration of ruts. Other factors, such as the age and design of the pavement can also contribute to the actual deterioration behavior of ruts.
- 2D and 3D visualization of ruts at individual level shows the importance and

benefits of having registered long-term 3D pavement data. Details of how rut deteriorates, e.g., the development of dual-wheel shape ruts and the growth in rut length and volume, were able to be identified in the selected sections. This information can further support the diagnosis of rutting and inform data-drive maintenance decisions.

- Some parameters, such as PP69's partial lane profile-based parameters, total positive area, total negative area, distortion ratio, and total distortion, can possibly introduce larger variation because they are calculated on a reference that tend to be variable. Future research can be conducted to further analyzed the possible effect of these parameter.

CHAPTER 6

3D RUT CLASSIFICATION - A CASE STUDY ON GEORGIA SR26

In order to make effective and timely treatment decisions, accurate diagnosis of the cause of pavement rutting is vitally important. Inaccurate diagnosis results in ineffective pavement treatment decisions, which not only increase long-term pavement maintenance costs, but also lead to further deterioration of ruts that may cause more safety and rideability issues. In this chapter, a case study was conducted to classify rutting using spatial and temporal features of 3D pavement data.

6.1 Site Description

This case study for rut classification was conducted on SR26 in Chatham County, Georgia, close to the Port of Savannah. Nine 500-ft test sites, including 4 westbound and 5 eastbound locations, were selected (see Figure 6.1). For each site, field testing including falling weight deflectometer (FWD) and coring, were performed (see Figure 6.2), and 3D pavement data were collected using the GTSV as described in Chapter 3.

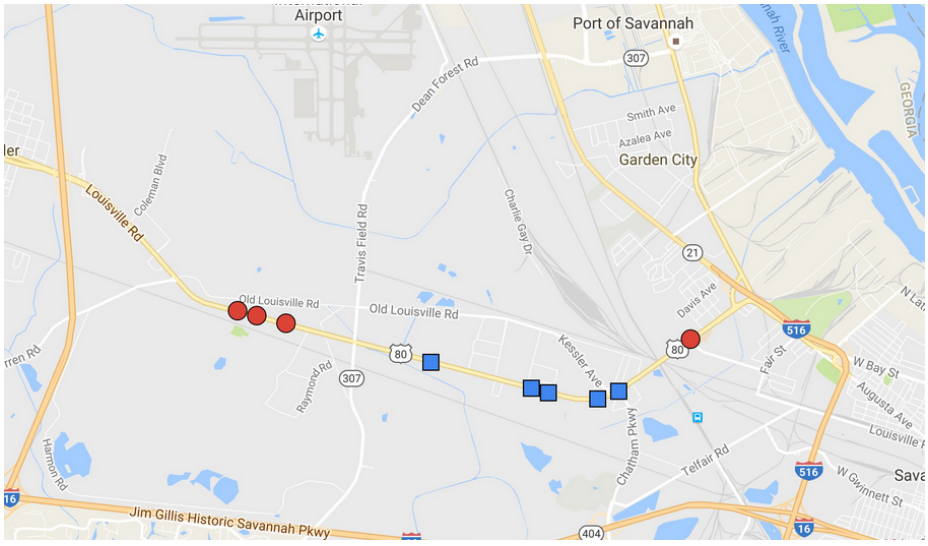

Figure 6.1: Test Site Locations on SR26 Near Savannah Port (Source: Google Map data)

(a) Falling Weight Deflectometer (b) Coring Truck

Figure 6.2: Field Testing Using FWD and Coring

As shown in Table 6.1, these sites represent three typical types of rutting, such as post-construction compaction and minor surface distresses on the asphalt concrete layer (Type I), plastic movement caused by shearing (Type II), and base layer failure (Type III). Note that approximately 250 ft of Site W1 was rehabilitated in 2012, and it was considered to be Type IV (rehabilitated Type II) rutting. The types of rutting were determined using field evaluations of surface conditions, as well as testing results from FWD and coring. Multi-timestamp overlay of typical profiles of each test site is shown in Appendix B.

6.2 Data Preparation

3D pavement data were collected by the GTSV at these nine 500-ft test sites on December 6, 2011, December 7, 2013, and February 17, 2016. These three timestamps formed 2 analysis periods: (1) Dec. 6, 2011 to Dec. 7, 2013; and (2) Dec. 7, 2013 to Feb. 17, 2016. Two sets of rut parameters were calculated as follows: (1) transverse profile-based parameters were derived from the latter timestamp data of each analysis period; and (2) temporal rut parameters were calculated by comparing the latter timestamp data to the former timestamp data. These rut parameters were then used as data entries for the subsequent classification.

Each 500-ft test site originally contained approximately 60,000 data entries. However,

Table 6.1: Test Site Descriptions and Rut Types

Site ID	Surface Conditions	Coring Results	FWD Results	Rut Type
W1	Plastic flow observed, no cracking	Thick AC layer, no cracking	Normal moduli	II / IV*
W2	Severe load cracking with GAB materials pumped to the surface	Deep cracks through AC layer	Weak base layer modulus	III
W3	Severe load cracking with GAB materials pumped to the surface	Deep cracks through AC layer	Weak base layer modulus	III
W4	Moderate load cracking	Shallow cracks in top few inches	Normal moduli	I
E1	Severe load cracking with GAB materials pumped to the surface	Deep cracks through AC layer	Weak AC and base layer moduli	III
E2	Moderate load cracking	Shallow cracks in top few inches	Normal moduli	I
E3	Moderate load cracking	Shallow cracks in top few inches	Normal moduli	I
E4	Severe load cracking with GAB materials pumped to the surface	Deep cracks through AC layer	Weak AC and base layer moduli	III
E5	Plastic flow observed; no cracking	Thick AC layer, no cracking	Weak base layer modulus	II

* Part of this test site was rehabilitated in 2012 and is considered as a separate type

since two consecutive entries are derived from profiles that are merely 5 mm apart, they may likely share very similar features; data entries are sampled at 1-ft intervals. In other words, approximately 1,000 data entries were extracted from each site. Incomplete profiles (e.g., lane marking location was outside of the view of sensors) were further excluded from the subsequent analysis. The final dataset used in the case study contained 7,561 data entries (3,561 Type I; 1,107 Type II; 2,615 Type III; and 278 Type IV), and each data entry consisted of 44 rut parameters, as described in Section 6.2.1.

6.2.1 Rut Parameters

In this study, a total of 44 rut parameters were considered for the classification. The following considerations were applied to determine these 44 parameters:

- **Combine wheelpath-specific rut parameters**: Differences between rut parameters calculated separately for two wheelpaths are often insignificant. In practice, rut parameters (e.g., rut depth) are usually reported based on the average value between two wheelpaths. In this case study, we implemented this practice and used the average values for wheelpath-specific parameters.

- **Exclude longitudinal rut parameters**: Due to the fact that each test site is merely 500 ft long, sample profiles within each test site may very likely belong to the same rut. In other words, these data points may share the same rut length and rut volume, which can make these longitudinal parameters perfect predictors for the rut types. Therefore, in this case study, longitudinal parameters are excluded from the analysis.

- **Include zonal rut parameters**: As shown in the study conducted by White et al. (2002), profile features (i.e., curvature reversal) within the lane canter can be a criterion for classifying rut types. Therefore, in this study, in addition to the aforementioned rut parameters, rut features, such as the average elevation, standard deviation of elevations, maximum elevation, and minimum elevation, within each of the 5 zones depicted in Figure 6.3 are further derived and considered in the classification process. In addition, in order to better describe the shape of the profile within each zone, the profile segment within each zone is fitted with a quadratic function and the corresponding coefficients are included in the classification analysis (see Equation 6.1).

$$\mathbf{z_i} = a_i \mathbf{x_i}^2 + b_i \mathbf{x_i} + c_i, \tag{6.1}$$

where $\mathbf{z_i}$ is the elevation of transverse profile within zone i, $\mathbf{x_i}$ denotes the transverse

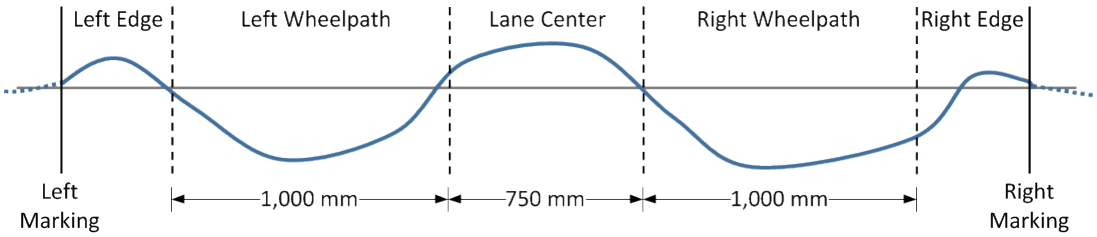

Figure 6.3: Five Zones of a Lane

locations of zone i; a_i, b_i, and c_i are coefficients of the fitted quadratic function that best describe the profile shape within zone i ($i \in 1, ..., 5$).

Each data entry in the subsequent analysis contained these 44 rut parameters (i.e., features) and each data entry was associated with a rut type. A complete list of rut parameters considered in this case study are the following:

- RD: Average rut depth (mm)
- RW: Average rut width (mm)
- CA: Average rut cross-sectional area (mm^2)
- PD: Percent deformation (%)
- TD: Total distortion (mm^2)
- DR: Distortion ratio
- TAD: Total absolute distortion (mm^2)
- TEA: Total elevated area (mm^2/yr)
- TDA: Total depressed area (mm^2/yr)
- AVG_i: Average elevation in zone i (mm)
- STD_i: Standard deviation of elevations in zone i (mm)
- MAX_i: Maximum elevation in zone i (mm)
- MIN_i: Minimum elevation in zone i (mm)
- a_i: Coefficient a of fitted quadratic function in zone i, $i \in 1, ..., 5$
- b_i: Coefficient b of fitted quadratic function in zone i, $i \in 1, ..., 5$
- c_i: Coefficient c of fitted quadratic function in zone i, $i \in 1, ..., 5$

6.3 A Supervised Method for Rut Classification

In this study, a supervised classification model was constructed to predict rut types based on the 3D spatial and temporal features of ruts. Algorithms and experimental procedures are summarized below.

6.3.1 Correlation-based Feature Selection

Many rut parameters can be derived from 3D pavement data; however, these parameters (i.e., features) may be highly correlated with each other. Including all features in the classification process can be computationally expensive and ineffective. In fact, for most statistical learning models, one of the rules of thumb is to find features that are as independent from each other as possible. As a result, in this study, the correlation-based feature selection (CFS) method was applied to select a subset of features that can best differentiate the types. The CFS algorithm was originally proposed by Hall (1999). The fundamental hypothesis behind this algorithm is that "a good feature subset is one that contains features highly correlated with the class, yet uncorrelated with each other" (Hall, 1999).

CFS is basically a filter algorithm that ranks feature subsets according to a heuristic correlation function (see Equation 6.2). Based on the hypothesis stated above, this function selects subsets of features that are highly correlated with the class and uncorrelated with other features within the subset. Irrelevant and redundant features are not selected because a subset containing these features would not be evaluated as the best subset.

$$M_S = \frac{k\overline{r_{cf}}}{\sqrt{k + k(k-1)\overline{r_{ff}}}}, \tag{6.2}$$

where M_S is the heuristic score that measures the "merit" of a feature subset S, k denotes the number of features within subset S, $\overline{r_{cf}}$ is the average correlation between subset features and class, and $\overline{r_{ff}}$ is the average inter-correlation between features (Hall, 1999). The selection process of CFS starts with either none or all features then sequentially adds or

removes features to form a new subset. A subset with higher merit is kept and the search goes on. The search stops when five consecutive, fully-expanded subsets fail to improve the current best subset (Hall, 1999). CFS feature selection in this study was performed in R using the *Biocomb* package (R Core Team, 2016; Natalia Novoselova, 2015; Wang et al., 2005).

6.3.2 Support Vector Machines

Support vector machines (SVMs) are a supervised learning technique that has been widely used for classification and regression analysis. Fundamentally, a support vector machine constructs a hyperplane, i.e., a classifier, that best separates different classes of data. As depicted in Figure 6.4, an optimal linear hyperplane is determined by maximizing the margin between support vectors, as denoted in squares. A variety of techniques has been suggested to improve the applicability of the original maximum-margin hyperplane algorithm, which is based on a linear classifier. Two significant evolutions of the SVMs include (1) the introduction of nonlinearity (Boser et al., 1992), which allows the construction of the hyperplane on a "transformed feature space" (Wikipedia, 2016b) using nonlinear kernel functions; and (2) the soft margin, which softens the original constraint of the linear SVM and introduces a penalty of cost for misclassification. SVMs have been shown to yield accurate classification results (Kotsiantis, 2007). They work well with high dimensional data and have high tolerance toward irrelevant and redundant variables (Wang et al., 2005; Kotsiantis, 2007).

In this study, we used the Gaussian radial basis function, a commonly used kernel in SVM classification (Chang et al., 2010); we implemented a pair of grid searches to find the optimal soft margin parameter among $C = \{0.1, 1, 10, 100\}$, and a kernel parameter among $\gamma = \{0.5, 1, 2\}$.

SVM models used in this study were implemented in R (R Core Team, 2016) using the *e1071* package (Meyer et al., 2015), which was developed based on LIBSVM, a library for

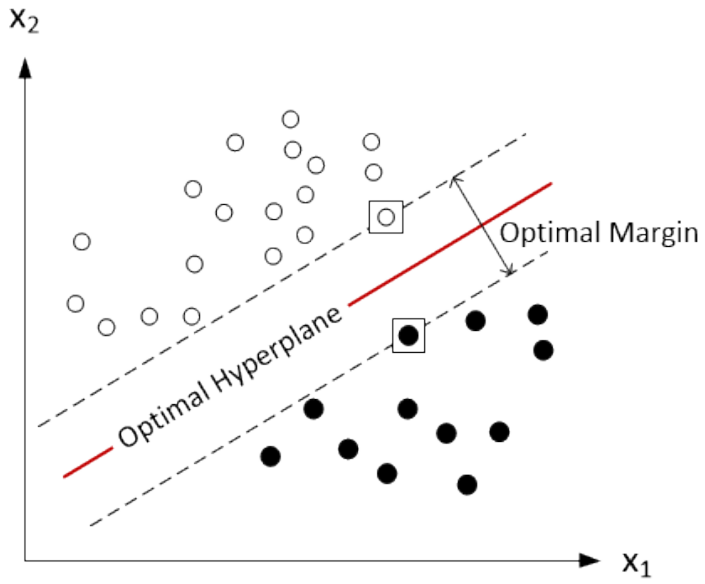

Figure 6.4: Illustration of the Optimal Hyperplane and Margin for SVMs (Adapted from Cortes and Vapnik (1995))

SVMs developed by Chang and Lin (2011). The *cvTools* R package developed by Alfons (2012) was used to generate subsets of data for validating the SVMs using k-fold cross-validation. In this study, we used k=5, indicating that the dataset was randomly and evenly divided into five subsets. Each of these five subsets was used as the testing set to validate SVMs developed using the other four subsets (i.e., the training set).

6.3.3 Experimental Design and Procedure

To assess the ability of the proposed method in predicting rut types, two sets of experiments were designed: (1) classification for all four rut types; and (2) classification for three rut types, excluding the Type IV rutting. Each set of experiments was performed under four scenarios of input features to compare possible combinations of available features, as shown in Table 6.2. The detailed experimental procedure for each experiment includes (1) selecting input features (see Table 6.2); (2) selecting a feature subset using the CFS algorithm; (3) dividing data into a training set (two-thirds of all data entries) and a testing set (remaining one-third data entries); (4) performing SVM classification; and (5) validating

the classification model using the k-fold cross-validation algorithm, with k=5.

Table 6.2: Input Feature Scenarios for Rut Classification Experiments

Scenario	Description	Input Features
1	Features from the literature	RD, TD, DR
2	All features	RD, RW, CA, PD, TD, DR, TAD, TEA, TDA, AVG_i, STD_i, MAX_i, MIN_i, a_i, b_i, c_i
3	All but temporal features	RD, RW, CA, PD, TD, DR, TAD, AVG_i, STD_i, MAX_i, MIN_i, a_i, b_i, c_i
4	All but zonal features	RD, RW, CA, PD, TD, DR, TAD, TEA, TDA

6.4 Results

Using the nine test sites on SR26 as a case study, the proposed method was used to predict rut types according to the designed experimental procedure. Results of the case study, including the selected features, as well as classification accuracy, were summarized in the following sections.

Table 6.3 shows the results of feature selection using CFS. Note that since Scenario 1 was to simulate classification results using rut parameters considered in the literature, CFS was not applied, and the three parameters (RD, TD, and DR) were used for all experiments under Scenario 1.

For Scenarios 2, 3, and 4, the following findings can be summarized from the feature selection results:

- Profile-based rut parameters, including rut depth (RD), distortion ratio (DR), and percent deformation (PD), were selected by CFS for all scenarios in both sets of experiments. This indicates that these parameters had higher correlations with the types of ruts and were less correlated with other parameters. This feature selection results also confirmed that rut depth, although it may not represent the complete 3D rut shape, is an important feature for rut classification.

Table 6.3: Selected Features for Rut Classification Experiments

Scenario	Four-Type Experiments	Three-Type Experiments†
1*	RD, TD, DR	RD, TD, DR
2	RD, PD, DR, TEA, AVG_3, STD_2, STD_3, STD_4, MAX_1, MAX_2, MAX_3, MAX_4, MAX_5, a_2, a_5, b_3, c_2, c_3, c_4, c_5	RD, PD, DR, AVG_1, AVG_3, STD_2, STD_3, STD_4, MAX_1, MAX_2, MAX_3, MAX_5, a_2, a_5, b_3, b_4, b_5, c_2, c_3, c_4, c_5
3	RD, PD, DR, AVG_3, STD_2, STD_3, STD_4, MAX_1, MAX_2, MAX_3, MAX_4, MAX_5, a_2, a_5, b_3, c_2, c_3, c_4, c_5	RD, PD, DR, AVG_1, AVG_3, STD_2, STD_3, STD_4, MAX_1, MAX_2, MAX_3, MAX_5, a_2, a_5, b_3, b_4, b_5, c_2, c_3, c_4, c_5
4	RD, PD, TD, DR, TAD, TEA	RD, PD, DR, TAD

* Feature selection for Scenario 1 was based on the literature, CFS was not applied.

† Type IV ruts were excluded in three-type experiments

- Zonal parameters, especially those representing the features of the wheelpaths and the lane center area (Zones 2, 3, and 4), were key features that should be included in the classification models.
- Temporal features (i.e., TEA) were useful when Type IV ruts were to be identified but they may not be useful features when Type IV ruts were excluded. This is reasonable, since TEA detects the elevated area, which was an important and unique feature for Type IV ruts.
- Total distortion (TD) was not selected in most of the cases, indicating that other features, such as DR, TAD, and zonal parameters were likely better features for classification. In fact, as discussed in Chapter 5, the TD value can be significantly affected by the relative elevation of the profile to the horizon, making it more sensitive to sources of error and variation.
- When zonal parameters were excluded from the pool (i.e., Scenario 4), some profile-based parameters, such as TD and TAD, were selected; however, these profiled-based features were not selected under Scenarios 2 and 3 when zonal parameters were included in the consideration, indicating that zonal parameters provided more distinctive features that made TD and TAD less important.

Rut classification results of this case study are shown in Tables 6.4 and 6.5. For both four- and three-type experiments, it was clear that the inclusion of zonal rut parameters significantly improved the predictability of the SVM models. In fact, a classification accuracy of approximately 95% was achieved when zonal parameters were included (in Scenarios 2 and 3 experiments). For three-type experiments, Scenarios 2 and 3 yielded the same feature selection and classification results, indicating that temporal parameters were unlikely to be important features when there were no maintenance activities.

Table 6.4: Classification Results for Four-Type Experiments

Scenario 1 ($Accuracy = 82.2\%$, $C = 100$, $\gamma = 2$)

	I_{True}	II_{True}	III_{True}	IV_{True}
I_{Pred}	253	39	7	42
II_{Pred}	80	986	71	1
III_{Pred}	21	161	789	0
IV_{Pred}	19	3	4	45

Scenario 2 ($Accuracy = 94.9\%$,$C = 10$, $\gamma = 0.5$)

	I_{True}	II_{True}	III_{True}	IV_{True}
I_{Pred}	368	19	2	7
II_{Pred}	4	1122	47	0
III_{Pred}	1	48	822	0
IV_{Pred}	0	0	0	81

Scenario 3 ($Accuracy = 94.7\%$, $C = 10$, $\gamma = 0.5$)

	I_{True}	II_{True}	III_{True}	IV_{True}
I_{Pred}	366	17	2	8
II_{Pred}	4	1119	46	1
III_{Pred}	2	53	823	0
IV_{Pred}	1	0	0	79

Scenario 4 ($Accuracy = 87.9\%$, $C = 100$, $\gamma = 2$)

	I_{True}	II_{True}	III_{True}	IV_{True}
I_{Pred}	295	36	5	2
II_{Pred}	62	1041	72	0
III_{Pred}	16	112	794	0
IV_{Pred}	0	0	0	86

Table 6.5: Classification Results for Three-Type Experiments

Scenario 1 (84.4%, $C = 100$, $\gamma = 2$)

	I_{True}	II_{True}	III_{True}
I_{Pred}	250	38	10
II_{Pred}	87	974	68
III_{Pred}	23	152	826

Scenarios 2&3 (95.4%, $C = 10$, $\gamma = 0.5$)

	I_{True}	II_{True}	III_{True}
I_{Pred}	350	15	4
II_{Pred}	6	1111	44
III_{Pred}	4	38	856

Scenario 4 (84.2%, $C = 100$, $\gamma = 2$)

	I_{True}	II_{True}	III_{True}
I_{Pred}	273	23	9
II_{Pred}	61	930	53
III_{Pred}	26	211	842

Moreover, by comparing Scenario 1 results with Scenario 4 results in Table 6.4, it is clear that the inclusion of the temporal feature and other new features (e.g., PD and TAD)

provided positive effect on the prediction for all four types of rut. However, a similar comparison of Scenarios 1 and 4 in Table 6.5 revealed that the models based on the CFS method only yield results comparable to the models based on features used in the literature.

When comparing detailed classification results by rut types, it was noticed that rut Types II and III accounted for most misclassified cases in all experiments. In fact, these two types of rutting, as pointed out in the literature, do share similar features (White et al., 2002). As shown in Table 6.6, the TD criteria for differentiating surface and base rut types overlapped between -7,500 mm^2 and 0 mm^2.

These misclassification cases, nevertheless, were significantly improved when zonal parameters were used in the SVMs. Cross-validation results, as shown in Table 6.7, were consistent with those shown in Tables 6.4 and 6.5. The improvement can be attributed to the fact that zonal features, such as the maximum, average, and standard deviation of elevations within each zone, can capture unique features of different rut types that are not found in full-lane profile-based parameters, such as TD and DR.

Table 6.6: Criteria for Determining Rut Types (White et al., 2002)

Type	Total Distortion (mm^2)	Distortion Ratio	Other Conditions
Surface	-7500 $<$x $<$0	0.3 $<$x $<$0.8	Curvature reversal between wheelpaths
Base	-7500 $<$x $<$5000	0.4 $<$x $<$3.0	No curvature reversal between wheelpaths
Subbase/ Subgrade	$<$-2000	$<$0.5	N/A
Heave	$>$5000	0	N/A

Table 6.7: Classification Accuracy Results from Five-fold Cross-Validation

	Four-Type Experiments				Three-Type Experiments		
Scenarios	1	2	3	4	1	2&3	4
Fold 1	80.7%	94.6%	94.5%	87.0%	84.1%	95.3%	83.7%
Fold 2	84.1%	96.3%	96.2%	89.3%	85.4%	94.4%	86.1%
Fold 3	82.1%	95.0%	94.5%	88.6%	82.8%	94.6%	82.4%
Fold 4	83.5%	95.8%	95.9%	88.5%	84.4%	95.1%	84.1%
Fold 5	81.8%	95.6%	94.7%	87.2%	84.1%	95.1%	83.5%

6.5 Summary

In this chapter, a supervised statistical learning method was proposed to classify ruts using rut parameters defined in the literature, as well as some newly proposed features in this study. A case study on Georgia SR 26 was conducted to demonstrate the proposed method. Some key findings of the case study are as follows:

- Using the CFS algorithm for feature selection, a subset of important features can be effectively selected and redundant and irrelevant rut parameters can be excluded. This step provides crucial information for federal and state transportation agencies to select key rut parameters in support of their pavement evaluation and monitoring decisions.

- The proposed zonal rut parameters, including the maximum, mean, and standard deviation of the profile, as well as the quadratic coefficients, significantly improved the accuracy of classification results, indicating that they were able to capture unique features that were more descriptive to the cause of ruts but distinctive from other existing parameters.

- Rut parameters in previous classification literature, such as RD and DR, were also shown to be relevant and important features in this study. Additional important features identified in this study include PD and TAD. This result indicates that the two parameters were effective and can be included in state DOTs' practices for rut evaluation and monitoring.

- The effectiveness of temporal parameters in differentiating other types of ruts was, nevertheless, not significant in this case study. A possible explanation of this result can be the fact that the pavement on the SR 26 project is relatively old, and no significant deformation changes can be observed in most of the test sites. As a result, the use of temporal parameters for capturing a higher rate of change in rut shapes (such

as those of new pavements) was not applicable in this case.

Overall, the proposed method and the case study demonstrated the potential benefits of utilizing 3D rut features that became more readily available with the advancement in 3D sensing technology. Selected feature subsets in this study can serve as a possible direction for state DOTs to start leveraging the information these rut parameters bring. The proposed method, as demonstrated in the case study, can effectively help diagnose possible causes of ruts. With more and more 3D pavement data being collected, the proposed method can be further validated using a more comprehensive dataset to avoid potential overfitting and to further associate causes of ruts with the proposed rut features and other factors, such as pavement design, age, and traffic characterization, which may help describe and differentiate causes. Ultimately, the proposed method can help transportation agencies more accurately and effectively identify the causes of ruts in support of data-driven pavement management decisions.

CHAPTER 7
ASSESSING THE EFFECT OF DIFFERENT SAMPLING INTERVALS ON 3D RUT CHARACTERISTICS

With the advancement in 3D sensing technology, many 3D rut characteristics can now be defined and calculated at 1 mm intervals. The amount of data, nevertheless, can be immense. For example, at 5 mm intervals, one mile of 3D pavement data used in this study consists of approximately 320,000 transverse profiles that require approximately 1 gigabyte of storage. With thousands of miles of roadways to be maintained by state DOTs, it is impractical and ineffective to store and process all transverse profiles. Therefore, there is a need to explore how to accurately calculate rut parameters while minimizing the data storage and processing time needed. In this chapter, a sensitivity analysis is conducted to assess the effect of different sampling intervals on the accuracy of rut parameters, including profile-based, longitudinal, and temporal parameters used in this dissertation. The results of the sensitivity analysis are then used to develop a tier-based dynamic sampling strategy that samples data in multiple tiers in order to reduce the amount of data being processed. Details of the sensitivity analysis and the dynamic sampling strategy are summarized below.

7.1 Effect of Different Data Sampling Intervals on Rut Characterization: A Sensitivity Analysis

In order to identify adequate sampling intervals for reporting accurate rut parameters, a sensitivity analysis is conducted in this section to assess the effect of different data sampling intervals on the accuracy of reported rut parameters that are derived from the sampled data.

7.1.1 Experimental Setup

The 3D pavement data collected on June 15, 2015 on the three 3D long-term pavement data routes described in Chapter 3 are selected for this sensitivity analysis. The data were collected on two 6-mile sections on SR26, one 1-mile section on SR275, and another 1-mile section on I95. The sensitivity analysis described in this section is performed separately for each of these four sections.

Table 7.1 shows the design of the sensitivity analysis, which simulates different data sampling intervals, including 5 mm, 10 mm, 20 mm, 50 mm, 100 mm, 200 mm, 500 mm, 1m, 2m, 5m, 10m, 20m, and 50m. In general, the larger the interval is, the more number of simulations at the same interval are conducted with different starting locations to ensure potential data sampling errors can be reasonably identified. The number of simulations shown in Table 7.1 is determined so that on average, every 100 mm of the road would be sampled once among all the simulations of each interval.

Table 7.1: Design of the Sensitivity Analysis

Sampling Interval	Number of Simulations
5mm	1 (Ground truth)
10mm	1
20mm	1
50mm	1
100mm	1
200mm	2
500mm	5
1m	10
2m	20
5m	50
10m	100
20m	200
50m	500

As depicted in Figure 7.1, for each simulation, a starting location is randomly selected within the first sampling section, which is defined as the starting road section with a length equivalent to the sampling interval (i.e., S_i mm). From this starting location, data are then

sampled at the corresponding interval of that simulation.

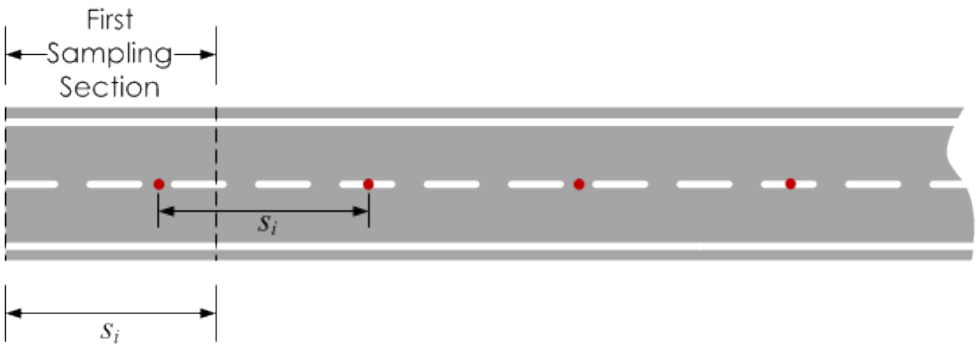

Figure 7.1: Illustration of the Setup of a Sampling Simulation

Each sampled dataset are then used to derive rut parameters. Rut parameters considered in this study include left rut depth (LRD), right rut depth (RRD), left rut width (LRW), right rut width (RRW), left cross-sectional area (LCA), right cross-sectional area (RCA), percent deformation (PD), total absolute distortion (TAD), total distortion (TD), distortion ratio (DR), left rut length (LRL), right rut length (RRL), left rut volume (LRV), right rut volume (RRV), total elevated area per year (TEA), total depressed area per year (TDA), mean elevated distance per year (MED), and mean depressed distance per year (MDD).

To assess the accuracy of rut parameters calculated from sampled data, the following techniques are used. For longitudinal parameters, the percent error in total length or volume between the ground truth and the sample is calculated and reported. For profile-based and temporal rut parameters, the Kolmogorov-Smirnov hypothesis test (Kolmogorov, 1933) is conducted to compare the distributions of rut parameters between the ground truth and the sample. As depicted in Figure 7.2, the Kolmogorov-Smirnov test (K-S test) is a hypothesis test technique that examines the similarity of the cumulative distribution of two samples of data. The null hypothesis is that the two samples have the same distribution. The output of a K-S test is the p-value indicating the significance of the hypothesis testing. A p-value less than 0.05 rejects the null hypothesis at 95% confidence level. In this study, if the K-S test between the ground truth and a sample results in a rejection of the null hypothesis, this sample is considered inaccurate. The K-S test is conducted using the $ks.test$ function in

the base package of R (R Core Team, 2016).

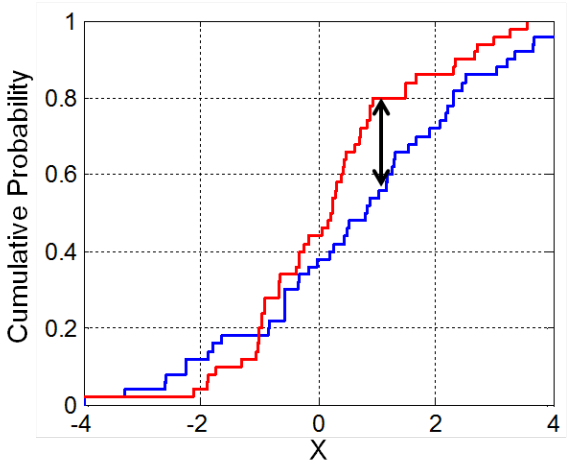

Figure 7.2: Illustration of the two-sample KolmogorovSmirnov statistic (Source: Wikipedia (2016a))

7.1.2 Results

In this study, 3D pavement data collected on June 15, 2015 on SR26, SR275, and I95 are used. Table 7.2 shows the results of K-S test of all profile-based and temporal parameters. The results are shown in terms of the minimum sampling interval that has more than 5% of its simulations that fail the K-S test (i.e., rejected the null hypothesis). As shown in Table 7.2, K-S test results show that most profile-based rut parameters, including LRD, RRD, LRW, RRW, LCA, RCA, PD, TAD, TD, and DR, have the same distribution as the ground truth at 50 m or larger sampling intervals. This result indicates that, for profile-based parameters, state DOTs can sample at larger sampling intervals (e.g., 20 m) and still get an accurate sample that is representative to the ground truth.

Temporal parameters, including TEA, TDA, MED, and MDD, on the other hand, show larger variability at smaller intervals (e.g., 5 m). This suggests that to obtain accurate results for temporal parameters, the sampling interval should not be larger than 5 m. For example, a sampling interval of 2 m would likely produce an accurate sample under the K-S test.

Table 7.2: Minimum Sampling Interval with More than 5% Simulations Fail K-S Test

Rut Parameter	SR275	I95	SR26E	SR26W
LRD	-	-	-	-
RRD	-	-	-	-
LRW	-	-	-	-
RRW	-	-	-	50 m
LCA	-	-	-	50 m
RCA	-	-	-	-
PD	-	-	-	-
TAD	-	-	-	50 m
TD	-	-	-	-
DR	-	-	-	-
TEA	20 m	-	-	5 m
TDA	-	5 m	10 m	5 m
MED	20 m	-	-	-
MDD	-	-	5 m	-

- Minimum interval $>$ 50 m

Figures 7.3 to 7.6 show the results for longitudinal parameters. The accuracy is presented in the percent error between the sample results and the ground truth. Any simulations resulted in an error larger than 5% are shown as the yellow points in these figures. From these figures, it is noted that most longitudinal parameters show comparable results to the ground truth at intervals of 2,000 mm (2 m) or above. This result suggests that for accurately obtain longitudinal rut parameters, the maximum sampling interval should be approximately 2 m.

7.1.3 Discussions

By comparing the minimum intervals suggested by the results shown above, it is noted that the sampling interval for profile-based parameters (20 m) can be much larger than temporal parameters (2 m). This finding is reasonable because temporal parameters are expected to have larger variation along the longitudinal direction than profile-based parameters. Consequently, temporal parameters require a smaller sampling interval to achieve the desired accuracy.

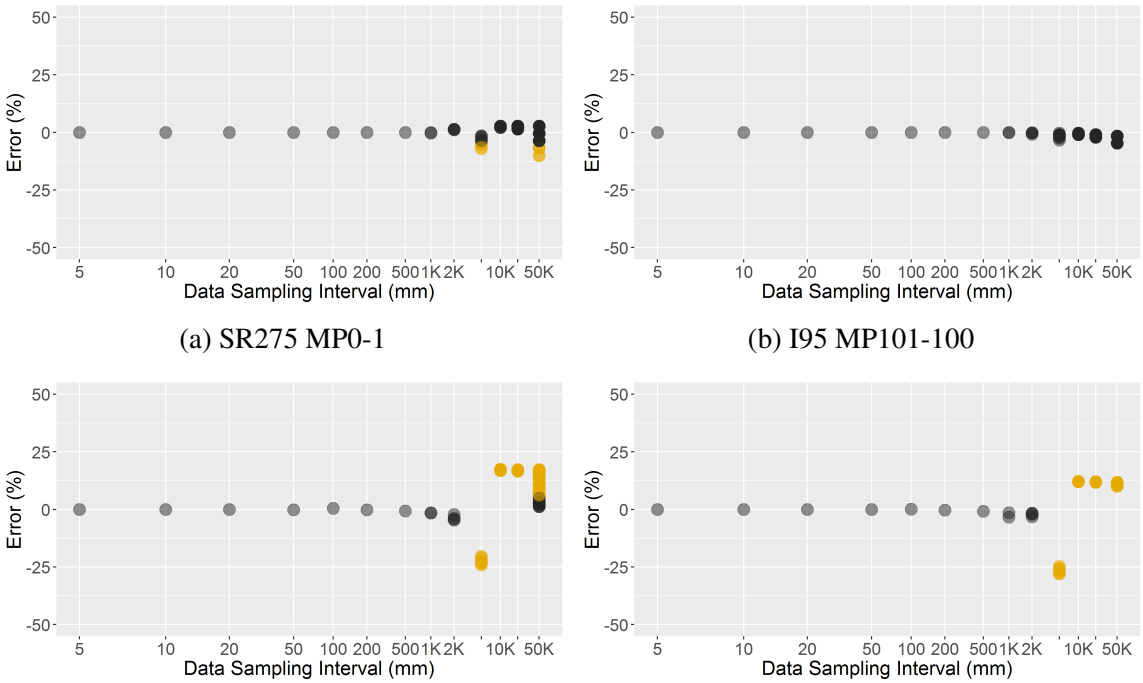

(a) SR275 MP0-1

(b) I95 MP101-100

(c) SR26 MP5.5-11.5

(d) SR26 MP11.5-5.5

Figure 7.3: Sampling Error of Total Left Rut Length

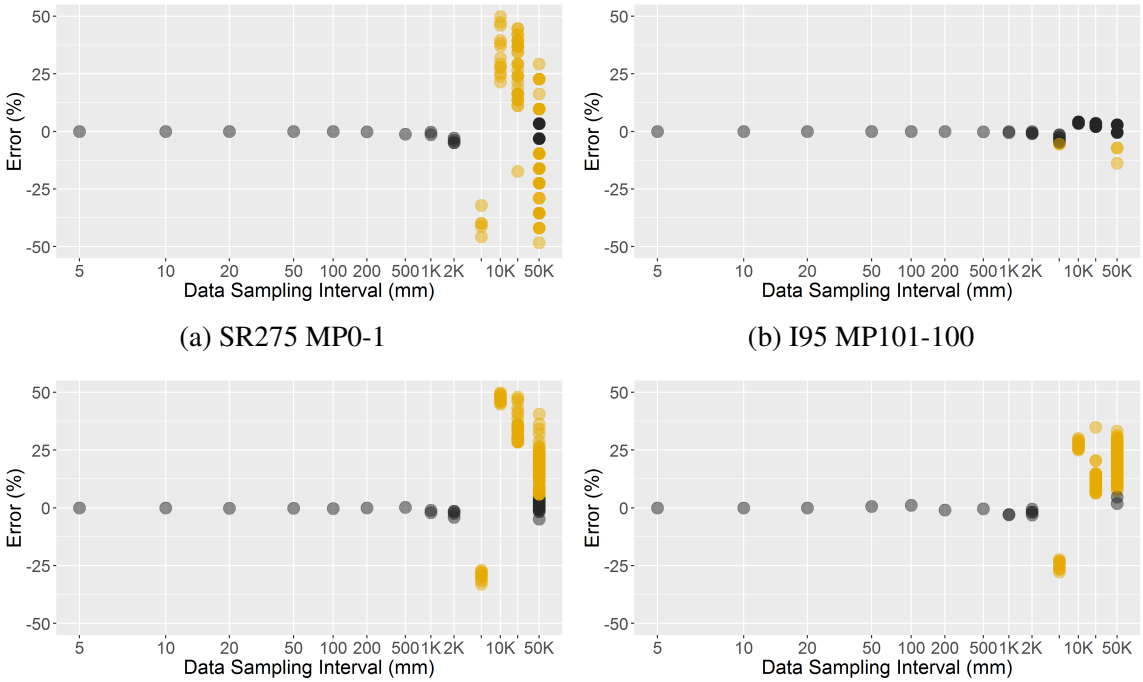

(a) SR275 MP0-1

(b) I95 MP101-100

(c) SR26 MP5.5-11.5

(d) SR26 MP11.5-5.5

Figure 7.4: Sampling Error of Total Right Rut Length

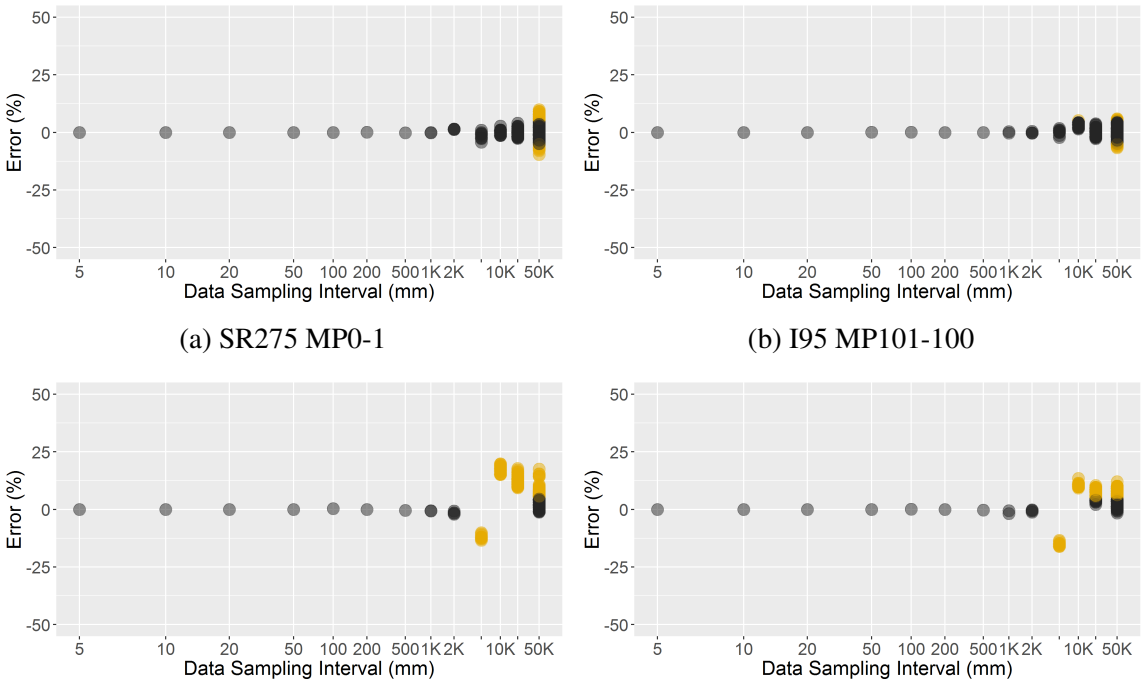

(a) SR275 MP0-1

(b) I95 MP101-100

(c) SR26 MP5.5-11.5

(d) SR26 MP11.5-5.5

Figure 7.5: Sampling Error of Total Left Rut Volume

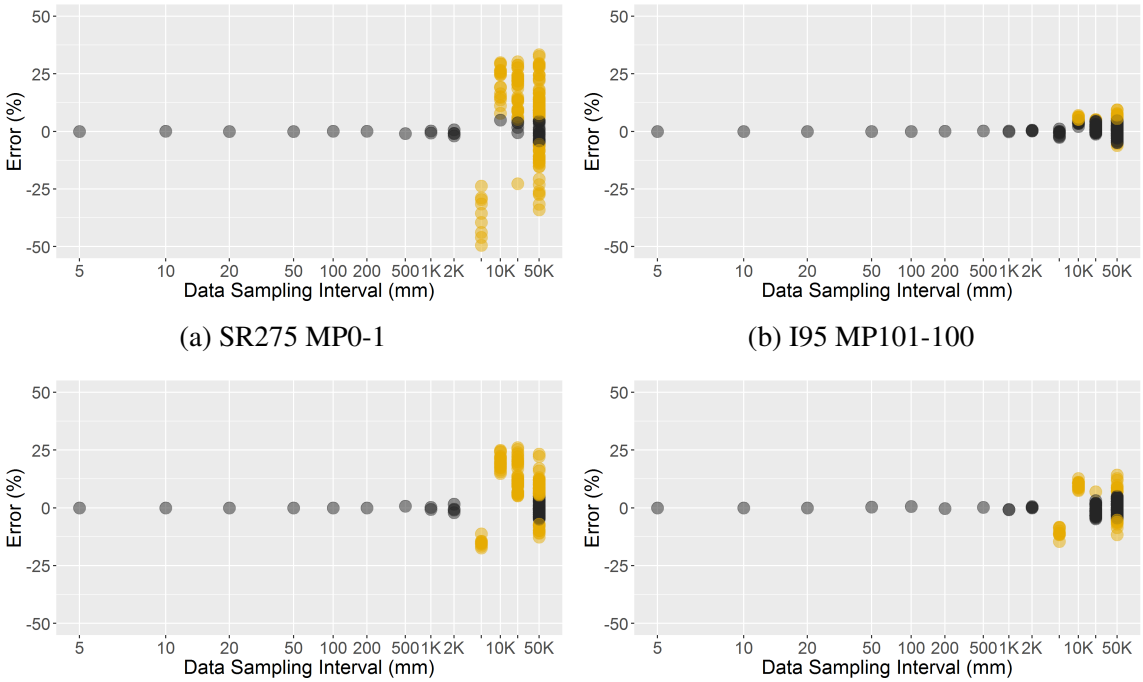

(a) SR275 MP0-1

(b) I95 MP101-100

(c) SR26 MP5.5-11.5

(d) SR26 MP11.5-5.5

Figure 7.6: Sampling Error of Total Right Rut Volume

Similarly, when comparing the results of longitudinal parameters to those of profile-based parameters, it is noted that longitudinal parameters require larger sampling intervals than profile-based parameters. This can be explained by the fact that longitudinal parameters are calculated based on thresholding techniques, i.e., 3 mm in depth, 300 mm in width, and 30 m in length. When sampling at larger intervals, such as 10 m, the distance between two consecutive sampled measurements are very close to the 30 m threshold in length, which tend to introduce much larger errors. To achieve comparable accuracy, therefore, longitudinal parameters require smaller sampling intervals (e.g., 2 m) than profile-based parameters.

It is noted that different sections in the above cases show different results. For example, for longitudinal parameters, while SR26 and SR275 showed large error at a sample interval larger than 5 m, I95 tend to have accurate results at even larger intervals. This is likely caused by the different rut conditions and their spatial distribution throughout different sections. Similar sensitivity analysis can be further conducted to study the effect of different rut conditions and their distribution on the sampling error. These results can be used to determine the best sampling strategy for accurate calculation and reporting of rut parameters on different roads with different rut conditions.

7.2 A Tier-based Dynamic 3D Pavement Data Sampling Strategy for Rut Condition Evaluation and Monitoring

In this section, a tier-based dynamic sampling strategy is proposed to accurately acquire rut parameters, including profile-based and longitudinal parameters, while reducing the amount of data required to be processed. Note that since the proposed temporal parameters are mostly useful when used for analyzing and quantifying deterioration of ruts at individual rut level, they are not considered in this proposed strategy, which is targeted for larger scale reporting purposes.

7.2.1 Proposed Method

Based on the results of the sensitivity analysis shown above, the proposed dynamic sampling strategy consists of five tiers (Figure 7.7). Tier 1 samples data at 16 m intervals, this interval is determined to ensure that accurate profile-based rut parameters can be calculated and reported based on the results of the sensitivity analysis above. All Tier 1 points (Figure 7.7a) that have a rut depth greater than 3 mm and a rut width greater than 300 mm are selected as the input for the next tier (selected points are denoted as the filled markers in Figure 7.7). Note that since the dynamic sampling strategy is proposed to capture accurate longitudinal parameters, the depth and width criteria used here are based on the definition used for calculating rut length in Chapter 5.

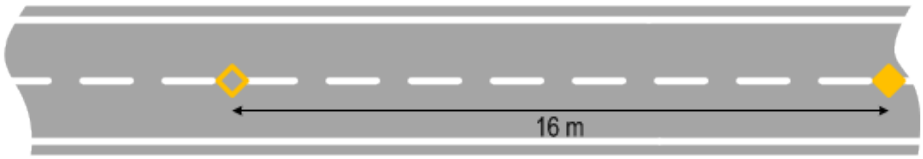

(a) Tier 1

(b) Tier 2

(c) Tier 3

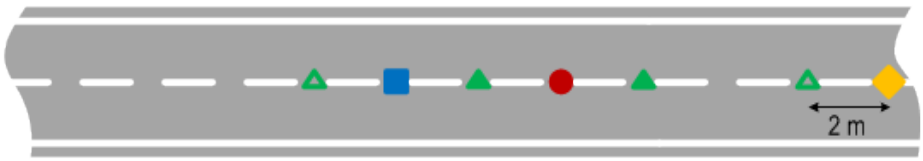

(d) Tier 4

Figure 7.7: A Tier-based Dynamic Sampling Strategy

Tier 2 (Figure 7.7b) samples data 8 m before and after the points selected from Tier 1. Similarly, all sample points in Tier 2 are examined using the rut depth and width criteria. Points with depth and width that meet the criteria, along with any points selected in Tier 1, are then selected as the input for Tier 3. Tiers 3 basically repeats the process in Tier 2, and the only difference among these tiers is that the sampling interval is cut in half in Tier 3 (i.e., 4 m). This iterative process is terminated after Tier 4. The reason the process stops after Tier 4 is because Tier 4's sampling interval reaches 2 m, which is the suggested sampling interval for longitudinal parameters in the previous section.

For reporting profile-based rut parameters, including rut depth, rut width, rut cross-sectional area, etc., all sampled data in Tier 1 can be used. For deriving longitudinal parameters, on the other hand, results from the dynamic sampling strategy are used. Longitudinal parameters are calculated using the same approach as defined in Chapter 5, and their results are shown in the next section.

7.2.2 Results

Tables 7.3 to 7.6 show the values of longitudinal parameters, including total left rut length (LRL), total left rut volume (LRV), total right rut length (RRL), and total right rut volume (RRV), derived from the sampled data using the proposed method. The results of each tier are compared with ground truth results, which are obtained by processing data at 5 mm intervals, and the results of 2-m static sampling. Any result parameters with larger than 5% error from the ground truth are highlighted in these tables.

From these results, several findings can be summarized. First, it can be observed that all dynamic sampling final results (Tier 4) are within 5% error, indicating that the proposed dynamic sampling strategy can accurately capture the attributes of longitudinal parameters. Second, the left wheelpath of the SR275 section and both wheelpaths of I95 section show that all steps of the dynamic and static sampling were able to derive accurate longitudinal parameters. This is because these three wheelpaths have an extensive amount of rutting

Table 7.3: Dynamic Sampling Results Compared (SR275 NB)

Sampling Method (Interval)	LRL (m)	LRV (m^3)	RRL (m)	RRV (m^3)	# Profile Processed
Ground Truth (5 mm)	1557	11313	774	3686	321425
Dynamic Tier 1 (16 m)	1600 *2.8%*	11356 *0.4%*	1088* *40.5%*	4469* *21.3%*	101
Dynamic Tier 2 (8 m)	1536 *-1.3%*	10962 *-3.1%*	632* *-18.4%*	2747* *-25.5%*	201
Dynamic Tier 3 (4 m)	1508 *-3.1%*	11107 *-1.8%*	364* *-53.0%*	1681* *-54.4%*	402
Dynamic Tier 4 (2 m)	1586 *1.9%*	11356 *0.4%*	796 *2.8%*	3541 *3.9%*	804
Static Sampling (2 m)	1574 *1.1%*	11341 *0.2%*	764 *-1.3%*	3495* *-5.2%*	803

* Error larger than 5%

Table 7.4: Dynamic Sampling Results Compared (I95 SB)

Sampling Method (Interval)	LRL (m)	LRV (m^3)	RRL (m)	RRV (m^3)	# Profiles Processed
Ground Truth (5 mm)	1574	10274	1508	8879	314798
Dynamic Tier 1 (16 m)	1568 *-0.4%*	10395 *1.2%*	1568 *4.0%*	9026 *1.7%*	99
Dynamic Tier 2 (8 m)	1568 *-0.4%*	10370 *0.9%*	1520 *0.8%*	8848 *-0.3%*	197
Dynamic Tier 3 (4 m)	1564 *-0.6%*	10260 *-0.1%*	1484 *-1.6%*	8769 *-1.2%*	394
Dynamic Tier 4 (2 m)	1572 *-0.1%*	10287 *0.1%*	1530 *1.5%*	8924 *0.5%*	787
Static Sampling (2 m)	1572 *-0.1%*	10270 *0.0%*	1504 *-0.3%*	8870 *-0.1%*	786

Table 7.5: Dynamic Sampling Results Compared (SR26 EB)

Sampling Method (Interval)	LRL (m)	LRV (m^3)	RRL (m)	RRV (m^3)	# Profile Processed
Ground Truth (5 mm)	8099	41202	4624	24434	1904115
Dynamic Tier 1 (16 m)	9520*	48518*	6720*	29408*	596
	17.5%	*17.8%*	*45.3%*	*20.4%*	
Dynamic Tier 2 (8 m)	7456*	39764	4016*	21487*	1191
	-7.9%	*-3.5%*	*-13.2%*	*-12.1%*	
Dynamic Tier 3 (4 m)	6492*	35927*	3264*	19406*	2381
	-19.8%	*-12.8%*	*-29.4%*	*-20.6%*	
Dynamic Tier 4 (2 m)	7836	40423	4684	24374	4675
	-3.2%	*-1.9%*	*1.3%*	*-0.2%*	
Static Sampling (2 m)	7856	40475	4530	24317	4760
	-3.0%	*-1.8%*	*-2.0%*	*-0.5%*	

* Error larger than 5%

Table 7.6: Dynamic Sampling Results Compared (SR26 WB)

Sampling Method (Interval)	LRL (m)	LRV (m^3)	RRL (m)	RRV (m^3)	# Profile Processed
Ground Truth (5 mm)	8591	42313	5447	29199	1926854
Dynamic Tier 1 (16 m)	9632*	45067*	6576*	29747	603
	12.1%	*6.5%*	*20.7%*	*1.9%*	
Dynamic Tier 2 (8 m)	7952*	39032*	4304*	23085*	1205
	-7.4%	*-7.8%*	*-21.0%*	*-21.0%*	
Dynamic Tier 3 (4 m)	6576*	34665*	3648*	21872*	2409
	-23.4%	*-18.1%*	*-33.0%*	*-25.1%*	
Dynamic Tier 4 (2 m)	8576	41941	5556	28959	4783
	-0.2%	*-0.9%*	*2.0%*	*-0.8%*	
Static Sampling (2 m)	8292	41200	5366	29205	4817
	-3.5%	*-2.6%*	*-1.5%*	*0.0%*	

* Error larger than 5%

that almost extend consistently throughout the entire 1-mile section (approximately 1,600 m), as noted in their corresponding rut lengths (1,557 m, 1,574 m, and 1,508 m). Third, routes with less rutting, such as the right wheelpath on SR275, show higher variation when the number of sample is small. This finding implies that, for routes with fewer ruts, smaller sample intervals may be needed in order to achieve the desired accuracy.

With regard to the data processing need, the rightmost column of Tables 7.3 to 7.6 shows the number of profiles being processed. It is noted that, although first few tiers of the dynamic sampling strategy show significant reduction in the number of profiles to be processed, they generally do not yield accurate results. The number of profiles being processed in Tier 4 shows that the proposed method can significantly reduce the number to be processed while maintaining desired accuracy. For example, out of the 1,926,854 profiles collected on SR26 westbound between Mileposts 11.5 and 5.5, the dynamic sampling only processed 4,783 profile, which is equivalent to 0.25% of the total. This result indicates that, in comparsion with processing data at 5 mm intervals, state DOTs can save up to 99.75% of their 3D pavement data processing time by applying the proposed dynamic sampling strategy.

The dynamic sampling strategy also shows results that are comparable to the static sampling results in terms of accuracy and number of sample profiles. For both 1-mile section (i.e., SR275 and I95) since rutting was observed throughout the section in at least one wheelpath, the dynamic sampling picked up pretty much the exact same number of samples to be processed. For the two 6-mile sections, the dynamic sampling strategy shows slight reduction in the number of profiles to be processed.

7.3 Summary

In this chapter, a sensitivity analysis was conducted to assess the effect of different sampling intervals on rut parameter accuracy. Results indicate that for profile-based rut parameters, including rut depth, rut width, rut cross-sectional area, percent deformation, total distortion,

distortion ratio, and total absolute distortion, can be sampled at larger intervals (e.g., 20 m) and still accurately represent the ground truth population. For temporal parameters, such as the mean elevated and depressed distance and the total elevated and depressed areas, a finer interval (e.g., 2 m) is required to achieve the desired accuracy. Similarly, longitudinal parameters, including rut length and rut width, should also be sampled at 2 m intervals to ensure the sampled data produce results that are within 5% deviation from the ground truth.

A tier-based dynamic sampling strategy was proposed to explore the effectiveness of dynamically adjusting sampling intervals according to rut characteristics, such as rut depth and width. Results indicate that the proposed dynamic sampling strategy was able to produce accurate estimation of longitudinal profiles while significantly reducing the number of profiles being processed. Results of the dynamic sampling strategy indicate that state DOTs can reduce data processing need up to 99% or more.

To apply the findings of this chapter, state DOTs can apply the proposed tier-based dynamic sampling strategy for multiple purposes. For example, for reporting purposes, e.g., HPMS, a state DOT can use Tier 1 sample points to generate and report measurements such as rut depth and cross-sectional area. For identifying local problematic areas or estimating the length and volume of ruts, on the other hand, sample data from Tier 4 can be used.

Based on the sensitivity analysis results, it is noted that different pavement rut conditions and their spatial distribution may result in different optimal sampling intervals. Future research can be conducted to further examine the effect of different rut conditions and their spatial distribution on the optimal sampling. The results can be used to determine the starting sampling interval (at Tier 1) and the number of tiers to be used in the proposed dynamic sampling strategy for different routes under different rut conditions.

CHAPTER 8
CONCLUSIONS AND RECOMMENDATIONS

Pavement rutting is one of the most common pavement surface distresses; ruts are caused by insufficient compaction during construction, excessive asphalt in the pavement surface layer, and insufficient structural support. State DOTs monitor and report rutting as part of their routine pavement condition evaluation efforts under the requirement of the HPMS and the MAP-21 Act. Traditionally, rut depth has been the primary indicator that measures the performance and severity of ruts. However, rut depth is insufficient to characterize the actual 3D rut shape and its deterioration behavior, which are essential for identifying causes and determining adequate treatment methods and timing.

Although 3D rut characteristics, such as rut depth, rut width, rut cross-sectional area, positive and negative areas, total distortion, and distortion ratio, etc., have been proposed and studied, it is difficult to accurately and reliably obtain large amount of these 3D characteristics using the current 3-point and 5-point rut bar systems that are commonly used by state DOTs. Sensing technology, which is capable of collecting 3D pavement surfaces at 1-mm resolution (equivalent to more than 4,000 points, continuous full-lane width coverage, instead of 3 or 5 points), provides a great opportunity for characterizing 3D rut shape and its deterioration behaviors in the real-world environment. There is a need, therefore, to develop a methodology to utilize 3D sensing technology and long-term 3D pavement data for 3D rut characterization and deterioration analysis.

This study proposed a spatiotemporal methodology that utilizes sensing technology to characterize 3D rut shapes and analyze their deterioration behaviors. The primary focus of this research is to develop a method that can accurately and effectively register 3D pavement data collected at different timestamps so that they can directly be compared and contrasted. This chapter summarizes the key contributions and findings of this dissertation

and recommends directions for future research.

8.1 Contributions

The primary contributions of this dissertation are as follows:

- **A boundary-based registration method was proposed to spatially and temporally register 3D pavement data for characterizing 3D rut shapes and quantifying their deterioration behaviors.**
  - The data registration method, to the best of the author's knowledge, is the first attempt to register multi-timestamp 3D pavement data for studying rut deterioration.
  - The proposed method is capable of accurately registering and aligning multi-timestamp 3D pavement data in 3D space for direct comparison, which is an essential step for the subsequent rut deterioration analysis.
  - The segment boundary identification procedure of the proposed method identifies lane boundary features, including lane markings and milepost locations, which are essential elements that can be easily identified in most 2D/3D data. Consequently, the proposed method is generally applicable to registering 3D pavement data in support of the study of other pavement surface distresses, such as cracking and raveling.
  - The proposed method contains key procedures that identify and correct possible data noise and errors caused by inter-sensor and vehicle-pavement geometries. These procedures can serve as a data preprocessing step that is necessary to ensure the reliability and accuracy of data analysis using 3D sensing technology.
- **Visualization of 3D rut shapes and their deterioration using registered data was implemented in 2D color maps and 3D models.**

- The 2D and 3D visualization is capable of objectively and accurately presenting the 3D shapes of ruts, which can be a useful means for engineers to evaluate rut conditions. The accurate 3D shape can also provide useful information for accurate estimation of materials and resources needed to perform maintenance and rehabilitation work, such as leveling.
- The direct subtraction between two 2D images or two 3D models visualizes the exact change of the 3D rut shape between the two corresponding timestamps. This direct subtraction provides detailed information about how exactly ruts deteriorate in 3D space, which otherwise cannot be quantified using individual rut parameters, such as rut depth, rut width, cross-sectional area, or rut length. Moreover, instead of treating the entire mile with the same treatment, the visualized deterioration can provide a quick and accurate means for identifying problematic locations on the road and lead to adequate and cost-effective treatment decisions.

- **The registration method was used to register multi-timestamp 3D pavement data as case studies to characterize 3D rut shapes and their deterioration.**
  - This multi-timestamp 3D pavement dataset contains data collected in 14-mile road segments at 7 timestamps, which is equivalent to 98 miles of data. This is the first attempt to register 3D pavement data collected in the real-world environment on a large scale.
  - Spatial and temporal parameters, such as total absolute distortion, mean elevated and depressed distances, and total elevated and depressed areas were proposed. Among the proposed parameters, temporal parameters provide a direct means to quantify the deterioration of rutting, which cannot be achieved without first registering the data.
  - Case studies using data collected on SR26, SR275, and I95 in Georgia showed

that the proposed parameters are capable of characterizing rut shapes and quantifying their deterioration behaviors under different traffic and roadway characteristics.

- **A rut classification study was conducted to classify causes of rutting using spatial and temporal characteristics of 3D pavement data.**
  - Zonal rut parameters (e.g., the mean, standard deviation, maximum, and minimum elevations, as well as the coefficients of a fitted quadratic function for each zone) were first proposed to characterize rut shapes within each zone (i.e., the left edge, the left wheelpath, the lane center, the right wheelpath, or the right edge zone).
  - The correlation-based feature selection algorithm (Hall, 1999) was applied to identify a subset of key rut parameters that can best describe rut types. Support vector machines (Cortes and Vapnik, 1995) were further constructed to classify rut types. The selected key parameters and the classification models can provide new information for state DOTs to identify possible causes of rutting and derive adequate and effective maintenance decisions.
- **A dynamic sampling strategy was proposed based on the results of sensitivity analysis on the effect of different data sampling strategies on data error.**
  - A sensitivity analysis was performed to identify possible errors introduced by different data sampling strategies and their effect on the accuracy of different rut parameters. Results of the sensitivity analysis were then used to propose a dynamic sampling strategy to reduce the data processing needs while maintaining the accuracy of the information derived.

8.2 Summary of Findings

8.2.1 Findings of the Proposed Data Registration Method

Findings of the proposed data registration method are as follows:

- **The proposed data registration method can accurately register 3D pavement data collected at different timestamps.**

  A case study was conducted using 2 runs of 3D pavement data collected on a 6-mile section on Georgia SR26, 3 days apart. Results of the case study show that raw 3D pavement data, if not processed, can have significant discrepancies between the two timestamps, with the root-mean-square error (RMSE) up to 11.74 mm. After the proposed method was applied to process and register the two sets of data, the RMSE was significantly reduced to 1.49 mm. This result indicates that the proposed boundary-based registration method can accurately and effectively register 3D pavement data collected at different timestamps.

- **Inter-sensor geometries, including the difference between sensor roll angles and altitudes, can have significant impact on the accuracy of measurements.**

  Preliminary assessment of the effect of inter-sensor geometries indicates that a slight difference in geometries between the two sensors can result in a large difference in the measurement. Specifically, with a simulated 0.3° (i.e., 0.5% slope) difference in sensor roll angles, the range measurement in the lane center area can differ approximately 10 mm. Moreover, with a 10 mm difference in sensor altitudes, the profile can result in approximately 2,000 mm^2 difference in an area covered by the profile. Both inter-sensor geometries were corrected using the proposed inter-sensor geometry correction procedure, which is a key step of the proposed method.

- **The proposed method can effectively correct vehicle-pavement geometries, including the roll angle and the lateral displacement.**

Vehicle-pavement geometries, in terms of the roll angle and lateral displacement, can vary between timestamps, resulting in appreciable differences in the cross slope and location of the collected profile at different timestamps. The registration method corrected the roll angle issue with the proposed lane marking-based profile normalization procedure and it corrected the lateral displacement issue with the proposed lane center-based spatial mapping procedure. Results of the case study showed that the proposed normalization process significantly reduced the RMSE from 12.02 mm to 2.98 mm. The spatial mapping procedure further reduced the RMSE from 2.98 mm to 1.49 mm.

8.2.2 Findings of 3D Rut Characterization and Deterioration Analysis

Spatial and temporal parameters were utilized and proposed in this study to characterize 3D rut shapes and analyze their deterioration over time. Findings of the multi-scale deterioration analysis are as follows:

- **The proposed spatial and temporal parameters can effectively capture and quantify seasonal variations in the deterioration of ruts.**

  The proposed parameters, including total absolute deformation (TAD), mean elevated and depressed distances (MED & MDD), and total elevated and depressed areas (TEA & TDA), were able to not only capture seasonal variations in rut deterioration, but also quantify them. Descriptive statistics, i.e., boxplots that show the distribution, quartiles, and range of the proposed spatial parameters, along with other parameters, such as rut depth, rut cross-sectional area, and percent deformation, show clear and consistent trends of rut deterioration, and the proposed temporal parameters were able to quantify the rate of change between different timestamps. Results of the analysis show that, in the summer season, higher deterioration rates are observed (approximately twice the rate of the winter season); a more consistent rate can be observed when the analysis period was over the course of multiple seasons. This

finding further suggests that the routine data collection should be conducted on an annual or biannual basis in one or multiple seasons consistently instead of changing the season of data collection from year to year.

- **The 2D and 3D visualization is effective in visualizing 3D rut shapes and identifying the exact change in rut shapes at the individual rut level.**

  The developed 2D images and 3D models are able to visualize the exact 3D shapes of rutting, providing an effective and holistic means for engineers to grasp information that is otherwise difficult to see in the field. The implemented image subtraction technique was able to visualize and quantify the exact change of 3D rut shape and can be used to accurately identify problematic locations (e.g., locations with more rapid deterioration) and diagnose the causes of rutting. An example in this study showed that rutting in the wheelpath grew in a dual-wheel shape, indicating that the cause of rut deterioration in this area was primarily caused by heavy truck traffic.

8.2.3 Findings of the Applications

- **The proposed spatial parameters (TAD and zonal parameters) can significantly improve rut classification accuracy.**

  The proposed parameters, including the TAD and zonal parameters (e.g., maximum, mean, standard deviation, and quadratic coefficients), were identified as part of the key features through the correlation-based feature selection (CFS) process. The rut classification study using support vector machines (SVMs) shows that the inclusion of the proposed parameters (especially the zonal parameters) significantly improved the accuracy of classification. When compared with classification models that use traditional parameters, the new models improved the accuracy from approximately 82% to 95%. This result indicates that the proposed parameters provide unique features that can better describe and differentiate the causes of rutting among plastic

movement, base layer failure, and surface compaction.

- **The sensitivity analysis on data sampling intervals and the proposed dynamic sampling strategy can effectively reduce the data processing efforts required by state DOTs.**

  The sensitivity analysis on different data sampling intervals showed that although profile-based rut parameters can be accurately reported at a sampling interval of 20,000 mm or more, temporal and longitudinal parameters require a denser data sampling interval (e.g., 2,000 mm) in order to be accurately derived. In the case study, the proposed dynamic sampling strategy was able to reduce the number of profile to be processed from 4,467,192 to 11,049 (i.e., 0.25% of the data) while maintaining 95% accuracy of the reported rut parameters. This result suggests that the proposed dynamic sampling strategy can be implemented by state DOTs to effectively process 3D pavement data and derive useful information without the fear of "drowning in data."

8.3 Recommendations for Future Research

Results of this dissertation present promising outcomes that can be used to better understand the 3D characteristics and deterioration behaviors of pavement rutting. The following are a summary of recommendations for research that can be extended from this dissertation:

- Additional tests can be performed to examine the robustness of the proposed method under different roadway characteristics. For example:
  - The effect of different surface textures, such as dense-graded asphalt, open-graded friction course (OGFC), unpaved roads, etc., on the performance of the registration method can be assessed. The results of these tests can be used to identify potential enhancement of the proposed methodology in terms of (1) the

coefficients used for automatic lane marking detection; and (2) the window size for smoothing, under different surface conditions.

  - The limitation of the proposed method under different lane widths and lateral displacements can also be examined. The current system covers approximately 4 m in the transverse direction of the lane. However, with the lateral displacement due to the actual driving trajectory, the exact coverage of the lane may be narrower. The effect of different lane widths, lateral displacements, and the measurement error introduced by these factors can be further assessed to identify the limitations of the proposed method for possible improvement.
  - One of the key assumptions of the proposed method is that the elevation of the pavement at lane marking locations does not change over time. This assumption can be further examined by observing the actual elevation change of the pavement surface using static devices. Similarly, field observations can also be performed in the same manner to verify the findings, such as seasonal variation and changes of 3D rut shapes, in the data. The results of these evaluations can be used to further identity the limitation of the proposed method and enhance its accuracy.

- The proposed method assumes certain inter-sensor and vehicle-pavement geometries would not have significant effect on the accuracy of data registration. This assumption can be further verified using simulations. For instance:

  - The effect of inter-sensor yaw and pitch angles was assumed to be negligible. A sensitivity study can be conducted to examine the effect of different combinations of inter-sensor yaw and pitch angles on the actual measurements. This study can be done by simulating the measurements of the laser scanners with a variety of inter-sensor yaw and pitch angles on a surface with known geometries. Surfaces with different severity levels of ruts can also be examined.

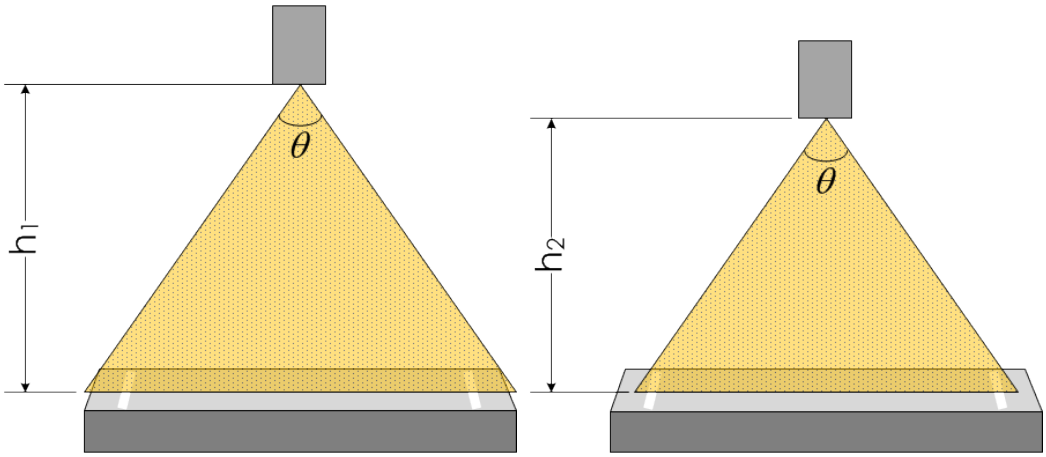

Figure 8.1: Illustration of Potential Effect of Different Sensor Heights

  - The height of the sensor above the ground can affect the assumed 1-mm transverse resolution in this study. As depicted in Figure 8.1, with a sensor farther from the surface (8.1a), the actual measurement between two consecutive measurements in the transverse direction can be larger than the respective interval with a sensor closer to the surface (Figure 8.1b). This effect can be simulated and examined in a similar manner. Additional profile scaling in the transverse direction may be added to the proposed method to address this effect if it is deemed not negligible.

- Automation of the data registration method can be a valuable future research topic. The current method is a semi-automatic process that requires users to verify and identify the boundaries of a pavement segment. In other words, the proposed method can be fully automated if the boundaries can be automatically identified. Additional features of the pavement surface, including the shape and texture in the spatial and frequency domains, can be explored and possibly used as additional control points to automate the registration process.

- Since tens or hundreds of rut parameters can now be derived using 3D pavement data, the effectiveness of existing and proposed rut parameters, and their potential use

can be further studied and designed for state DOTs to effectively utilize 3D sensing technology. For example:

  - As identified in the characterization and deterioration analysis, some rut parameters, such as rut depth, cross-sectional area, percent deformation, and total absolute distortion, show more consistent deterioration trends than other parameters, including rut width, total distortion, and distortion ratio. The former parameters may be better features that better describe the overall conditions of rutting and support the development of accurate performance models. These parameters can be included as part of the routine pavement data collection practices for performance evaluation and monitoring purposes.
  - As shown in the classification case study, some rut characteristics, such as the proposed zonal parameters, the proposed total absolute distortion, rut depth, percent deformation, and distortion ratio can be useful for identifying and differentiating causes of rutting. These parameters can be used on a case-by-case basis to identify the causes individual rutting and derive the proper timing, methods, and urgency of treatment.

- Derived rut parameters and observed deterioration behaviors can be further associated with the theoretical mechanisms of pavement materials. The scope of this dissertation was primarily on utilizing 3D sensing technology to derive and quantify 3D rut characteristics and their deterioration behaviors. There is a lack of association between the derived information and the mechanism of pavements. Future research can be conducted to associate the observed 3D characteristics and behaviors with pavement mechanisms to advance the comprehensive understanding of pavement characteristics and deterioration behaviors.

- Additional rut parameters can be used to improve the performance modeling of rutting. Existing rut performance models use rut depth as the sole dependent variable;

however, appreciable errors have been identified. With more rut parameters identified as good indicators of the trend of rut deterioration, these parameters can be used to develop and possibly improve the existing rut deterioration forecasting practices.

- With the results of the rut classification case study, it is possible to utilize the comprehensive rut parameters to further identify and classify types of rutting through unsupervised statistical learning on a more diverse and comprehensive dataset. This can help advance the understanding of the causes of rutting and better differentiate their types through statistical means.

- The proposed methods and results of the case studies can be useful information for state DOTs to drive adequate maintenance decisions. Future research can be conducted to incorporate and implement the proposed methods and procedures into the existing pavement management systems to streamline the process for data-driven and cost-effective maintenance decisions.

Appendices

APPENDIX A

ASSESSING THE EFFECT OF SENSOR GEOMETRIES ON RUT MEASUREMENTS

Sensor angles, i.e., roll, pitch, and yaw angles, can affect the accuracy of the measurements collected by the sensor. As depicted in Figure A.1, for a two-sensor system, different sensor angles can result in different measurements of the pavement surface, which then lead to inaccurate characterization of ruts. In this study, a synthetic pavement rutting with known ground-truth shape is created and different sensor angles are simulated to assess the effect of different sensor angles on rut measurements.

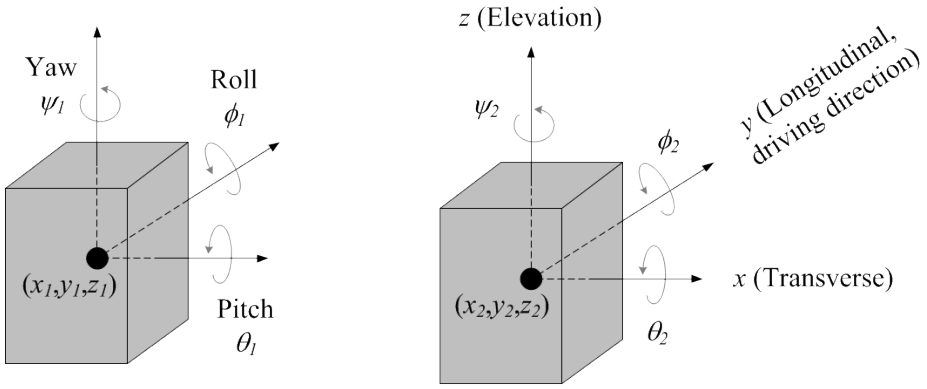

Figure A.1: Geometries of Two Sensors

A.1 Synthetic Rutting

In order to assess the effect of different sensor angles on rut measurements, a synthetic rutting was developed. As depicted in Figures A.2 and A.3, the synthetic rutting consists of five quadratic functions that depict the shape of rutting. The five quadratic functions are bounded by the zones (e.g., left edge, left wheelpath, lane center, right wheelpath, and right edge). This synthetic rutting is designed to be symmetric on both sides the lane center and its shape is assumed to be the same along the longitudinal direction.

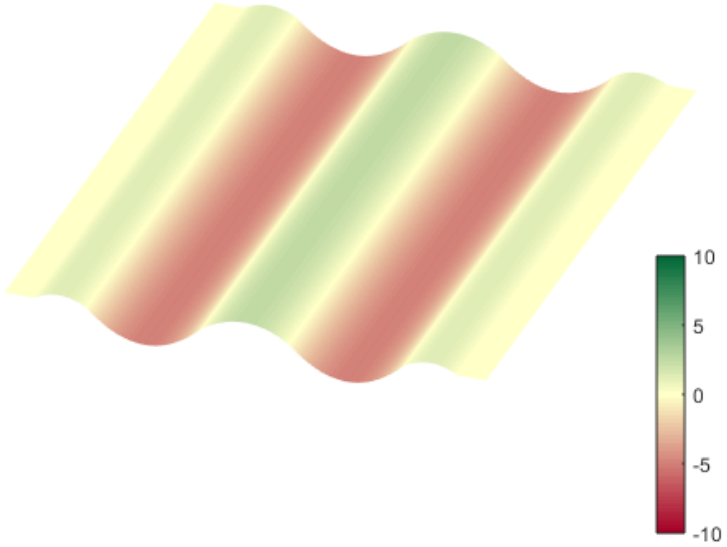

Figure A.2: 3D View of the Synthetic Rutting

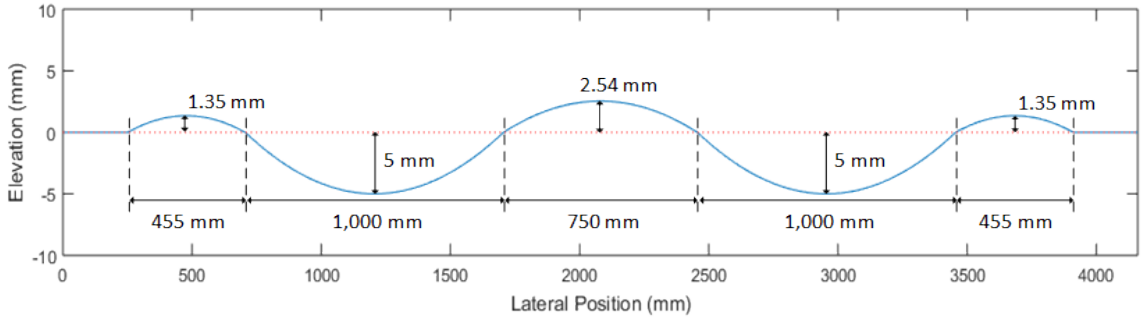

Figure A.3: The Transverse Profile of the Synthetic Rutting

A.2 Simulating Different Sensor Angles

In this study, different sensor angles, including different yaw and roll angles, are simulated, and the resulting profiles and rut parameters derived from them are compared with the ground truth profile (as depicted in Figure A.3) and rut parameters derived from it. Both sensors are assumed to be 2.25 meters above the ground.

Two scenarios, each with different testing sensor angles, are simulated. The first scenario simulates different sensor yaw angles. As depicted in Figure A.4b, both sensors are rotated about the z-axis for a certain degree and the resulting profiles collected are compared with the ground truth. The yaw angles tested are 5°, 10°, 15°, 20°, 25°, and 30°.

The second scenario simulates different sensor roll angles. As depicted in Figure A.4c, both sensors are rotated about the y-axis (i.e., along the driving direction) for a certain degree but in different directions (one clockwise and the other counterclockwise). In other words, the inter-sensor roll angle would be twice of the tested roll angle. The roll angles tested include 0.05°, 0.1°, 0.15°, 0.2°, 0.25° and 0.3°.

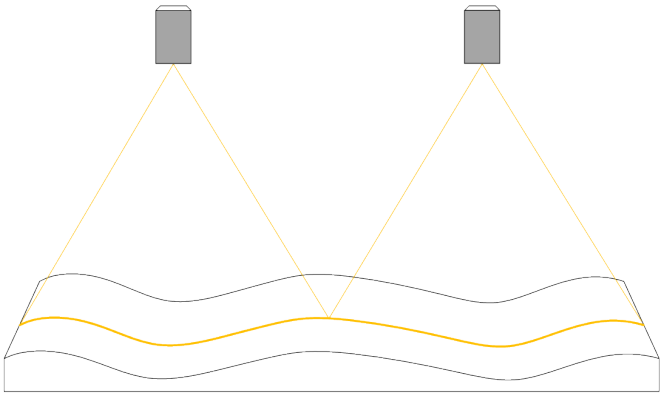

(a) Original

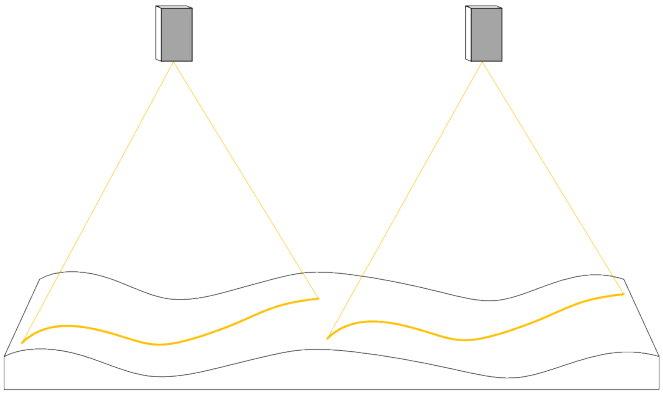

(b) Change in Yaw Angle

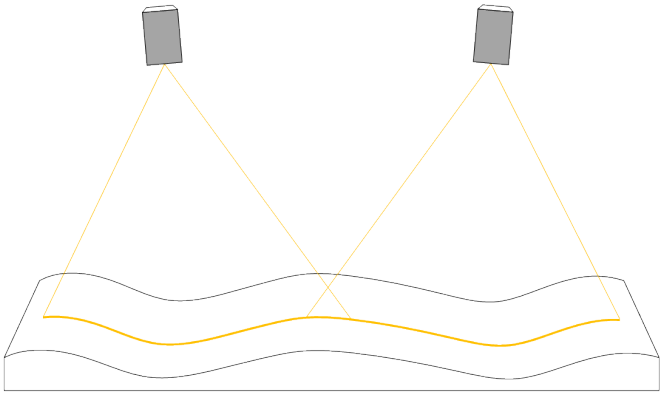

(c) Change in Roll Angles

Figure A.4: Illustration of the Scanned Profile with Different Sensor Angles

A.3 Results

Transverse profiles collected from the above simulations are then further used to calculate rut parameters, including rut depth (RD), rut width (RW), cross-sectional area (CA), total positive area (TPA), total negative area (TNA), total absolute distortion (TAD), and percent deformation (PD). Results of the two scenarios are summarized below.

Figure A.5 shows the transverse profile outcomes from different sensor yaw angles. It is noted that the larger the yaw angle is, the less similar the profile is from the original profile. Figure A.6 shows the results of different sensor roll angles. Similarly, the larger the roll angle is, the larger the difference between the original and simulated profiles is.

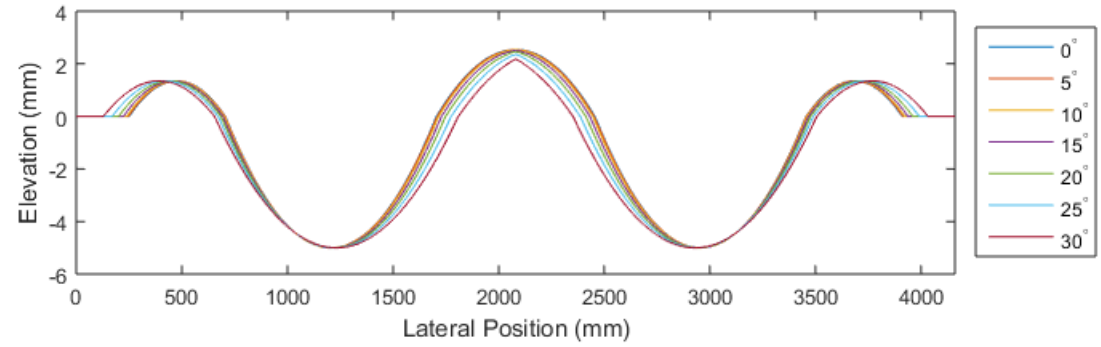

Figure A.5: Transverse Profiles from Different Sensor Yaw Angles

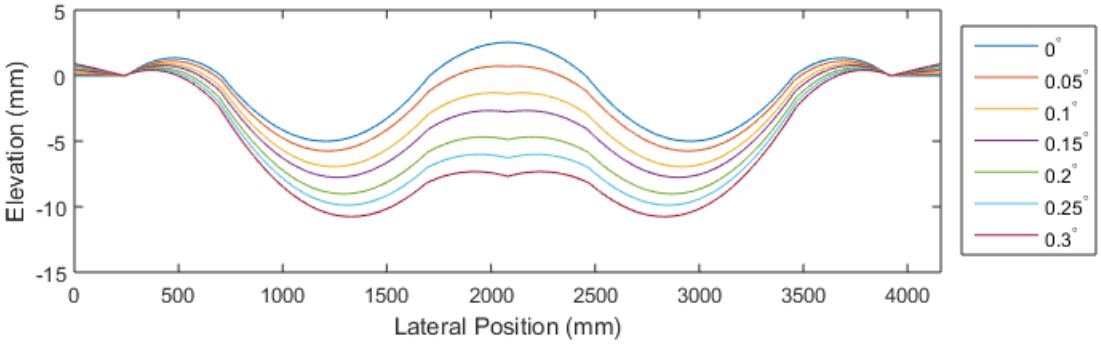

Figure A.6: Transverse Profiles from Different Sensor Roll Angles

From the above two figures, noticeable differences can be observed between the original profile and the simulated ones. This finding indicates that sensor angles should be accounted for in order to obtain accurate 3D rut shape. Moreover, by comparing the pro-

files in Figures A.5 and A.6, it is noted that the error introduced by sensor roll angles is much larger. This result indicates that sensor roll angle tends to introduce larger error and should be addressed.

The above observations are also reflected in the root-mean-square-error (RMSE) as well as rut parameters shown in Tables A.1 and A.2. One interesting finding is that while the 3D rut shape may change noticeably, as shown in the RMSE, TPA, TNA, TAD, and PD, the derived RDs, RWs, and CAs tend to be closes to the ground truth. RD, RW, and CA were calculated based on the AASHTO PP69 provisional standard, which rotates the profile for these types of wheelpath-specific parameters. Rotating the profiles, in this case, counters the distortion sensor angles introduces. This finding, nevertheless, is alarming because it implies that these wheelpath-specific parameters tend to neglect and does not represent the complete shape of the profile well.

Table A.1: Effect of Different Sensor Yaw Angles on Rut Measurements

Yaw Angle	RMSE	LRD	LRW	LCA	TPA	TNA	TAD	PD
0°	–	6.4	1390	4968	1584	7191	8775	0.0044
5°	0.018	6.3	1393	4981	1587	7193	8780	0.0044
10°	0.072	6.3	1403	5026	1575	7234	8809	0.0043
15°	0.162	6.3	1416	5093	1545	7317	8861	0.0042
20°	0.289	6.3	1434	5176	1496	7453	8949	0.0040
25°	0.459	6.2	1453	5265	1416	7671	9087	0.0038
30°	0.672	6.1	1475	5338	1302	7994	9296	0.0035

Table A.2: Effect of Different Sensor Roll Angles on Rut Measurements

Roll Angle	RMSE	LRD	LRW	LCA	TPA	TNA	TAD	PD
0°	–	6.3	1390	4968	1584	7191	8775	0.0044
0.05°	0.834	6.2	1423	4723	526	8817	9343	0.0041
0.1°	2.003	6.3	1455	4849	247	12504	12751	0.0042
0.15°	2.788	6.3	1457	4933	191	15083	15274	0.0044
0.2°	3.969	6.4	1461	5062	148	18978	19126	0.0047
0.25°	4.760	6.4	1463	5149	141	21586	21727	0.0050
0.3°	5.552	6.4	1466	5237	149	24201	24350	0.0054

The results indicate that for state DOTs only using sensing technology for rut depth calculation, addressing sensor angle issues may not be necessary given the negligible error being introduced. However, for state DOTs interested in using sensing technology to compute and compare 3D rut characteristics, sensor angles, especially sensor roll angles, should be accounted for to ensure the accuracy of pavement rut measurements.

APPENDIX B

RUT CLASSIFICATION TEST SITES – ADDITIONAL INFORMATION

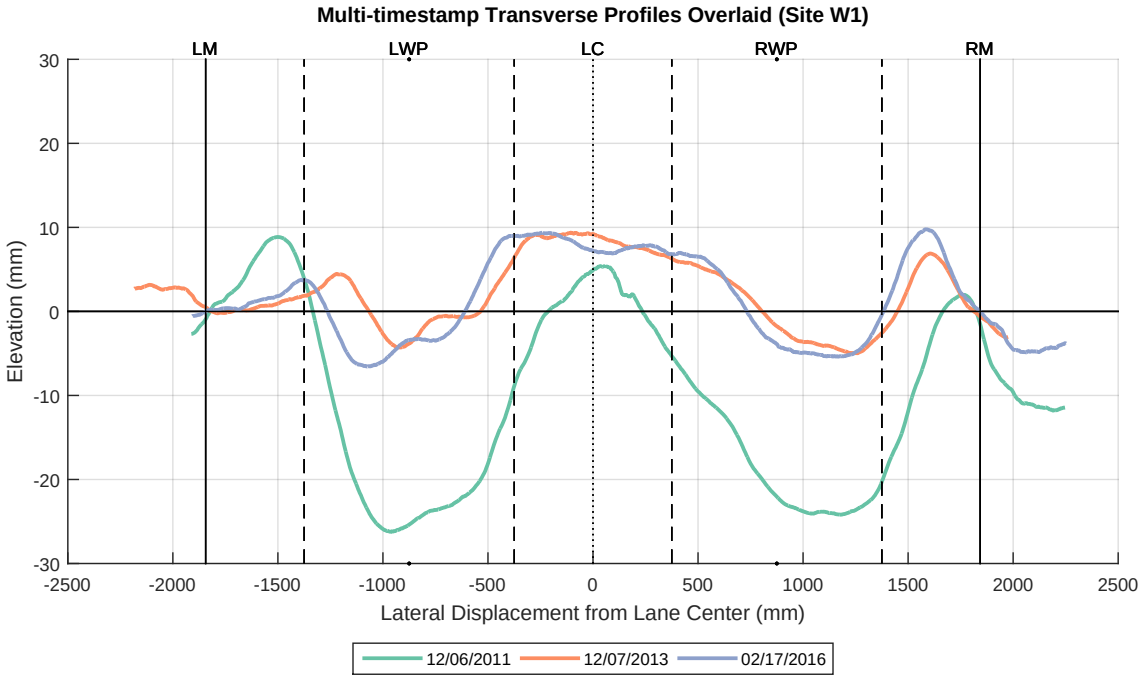

Figure B.1: Transverse Profiles Overlay at Test Site W1

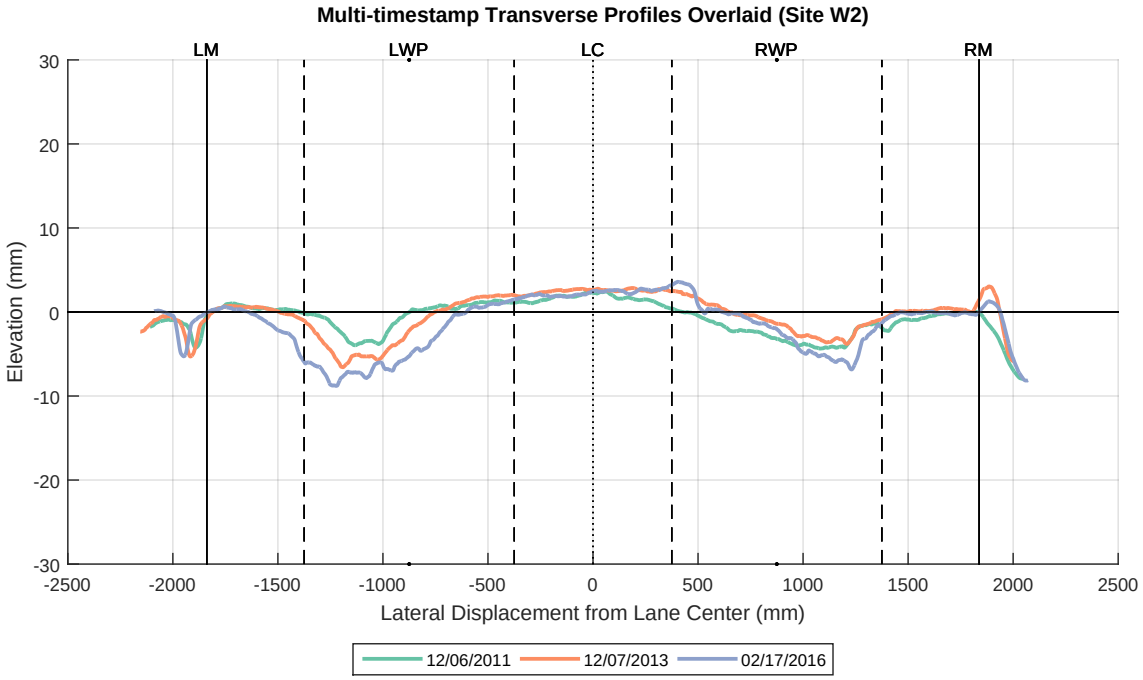

Figure B.2: Transverse Profiles Overlay at Test Site W2

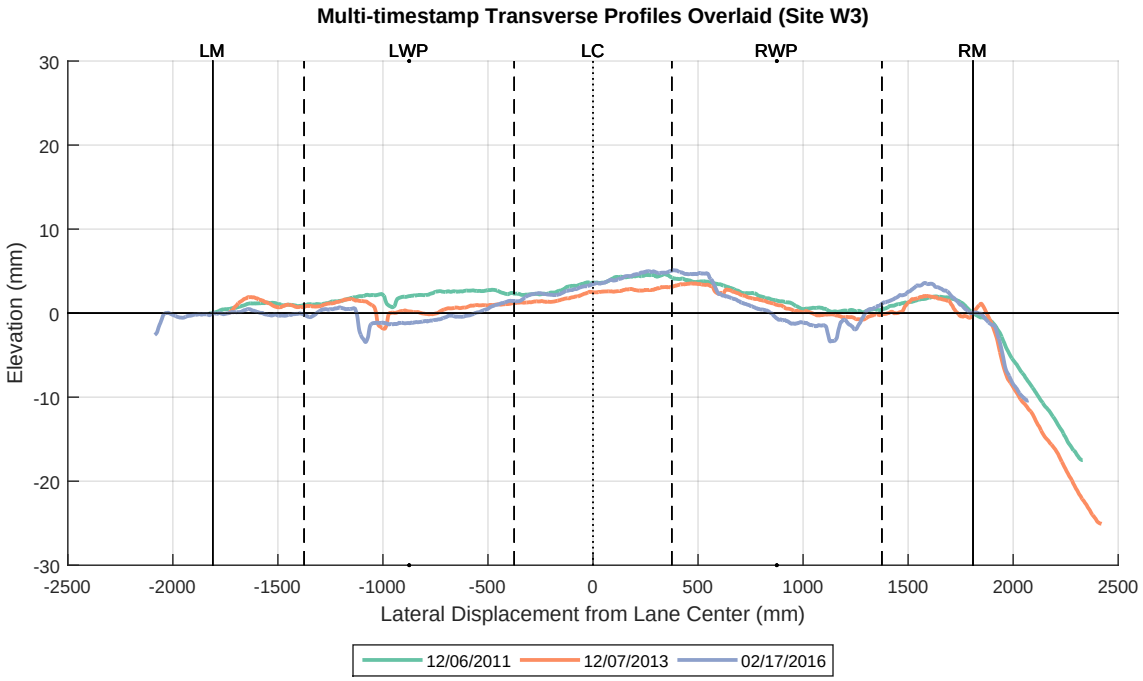

Figure B.3: Transverse Profiles Overlay at Test Site W3

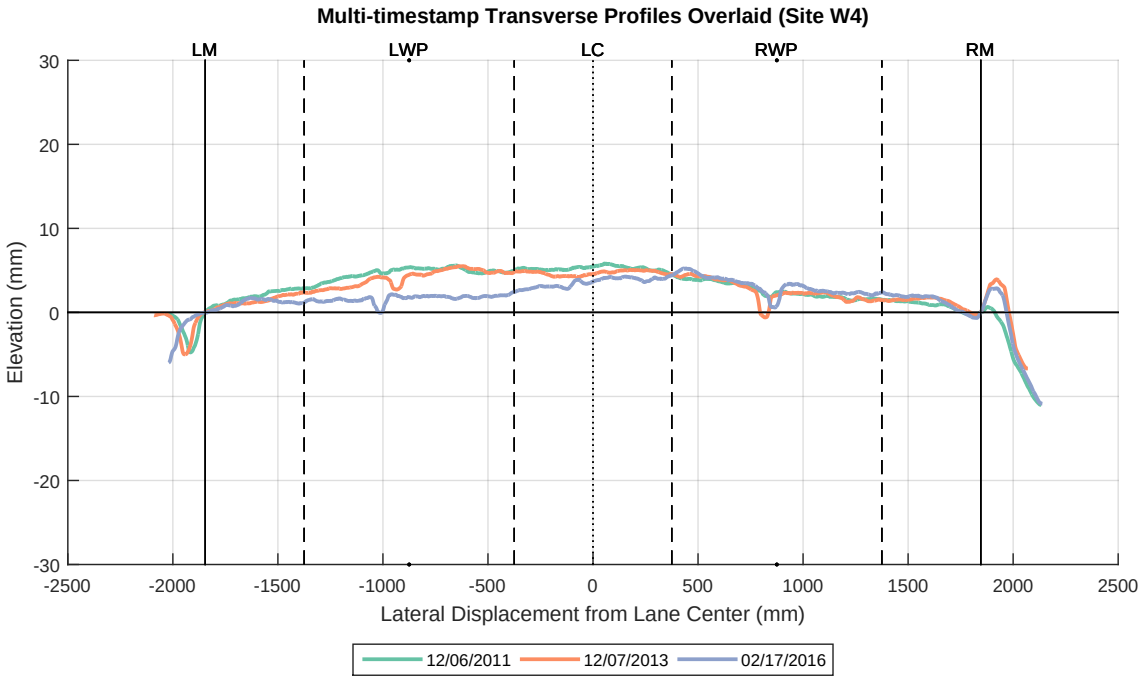

Figure B.4: Transverse Profiles Overlay at Test Site W4

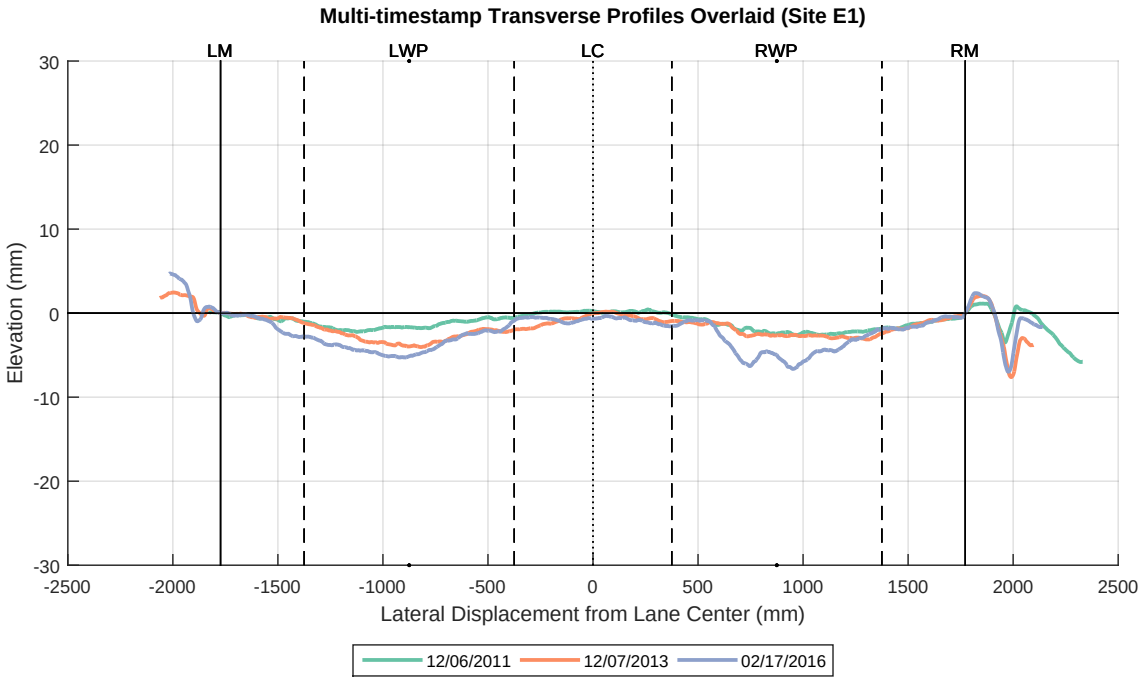

Figure B.5: Transverse Profiles Overlay at Test Site E1

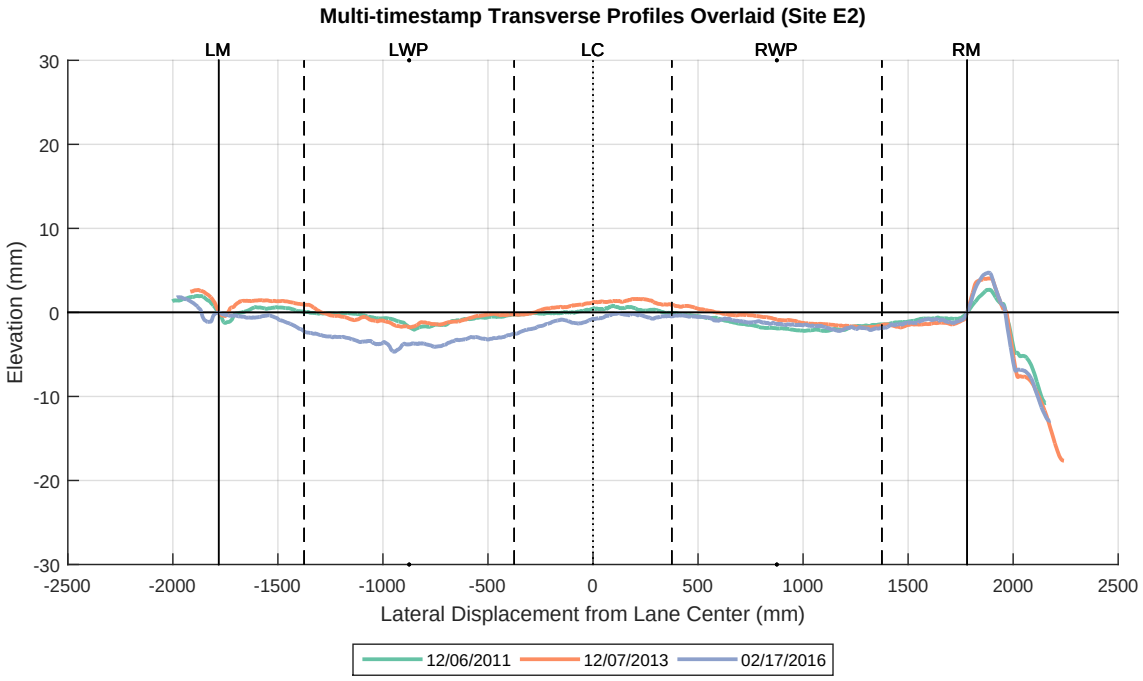

Figure B.6: Transverse Profiles Overlay at Test Site E2

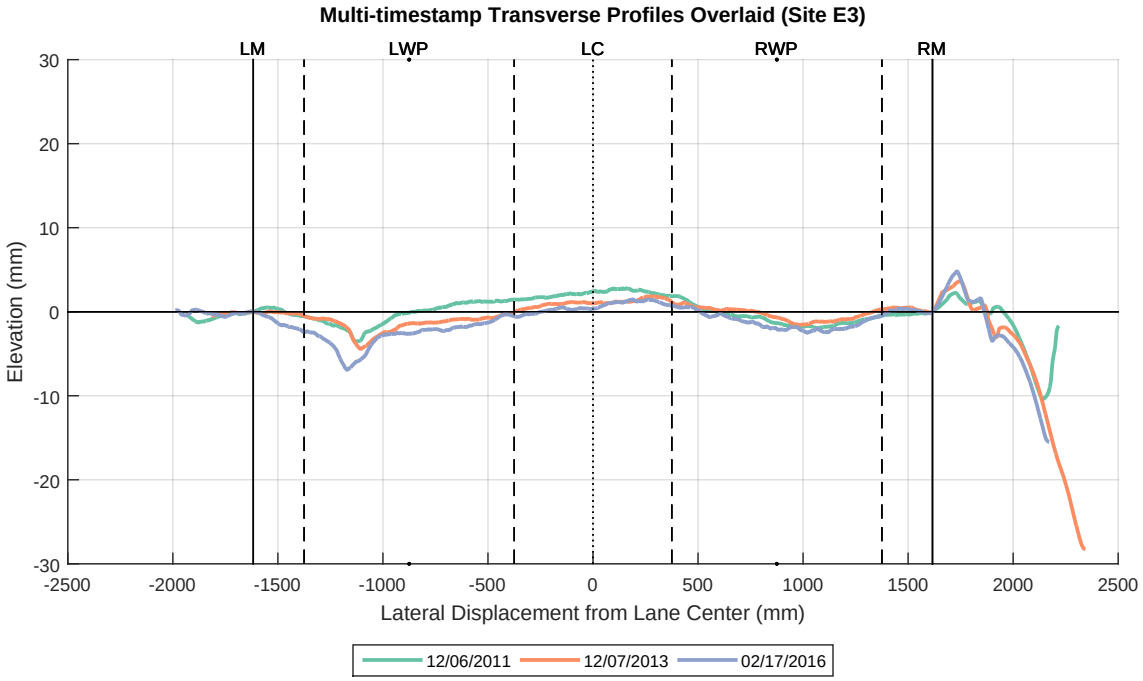

Figure B.7: Transverse Profiles Overlay at Test Site E3

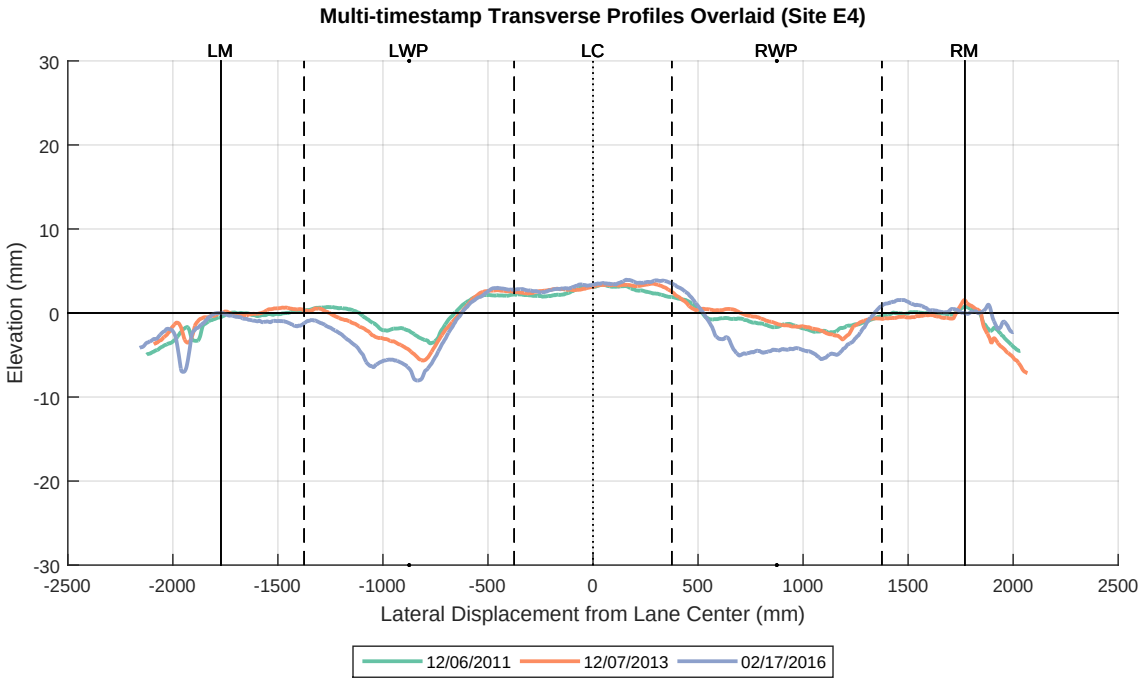

Figure B.8: Transverse Profiles Overlay at Test Site E4

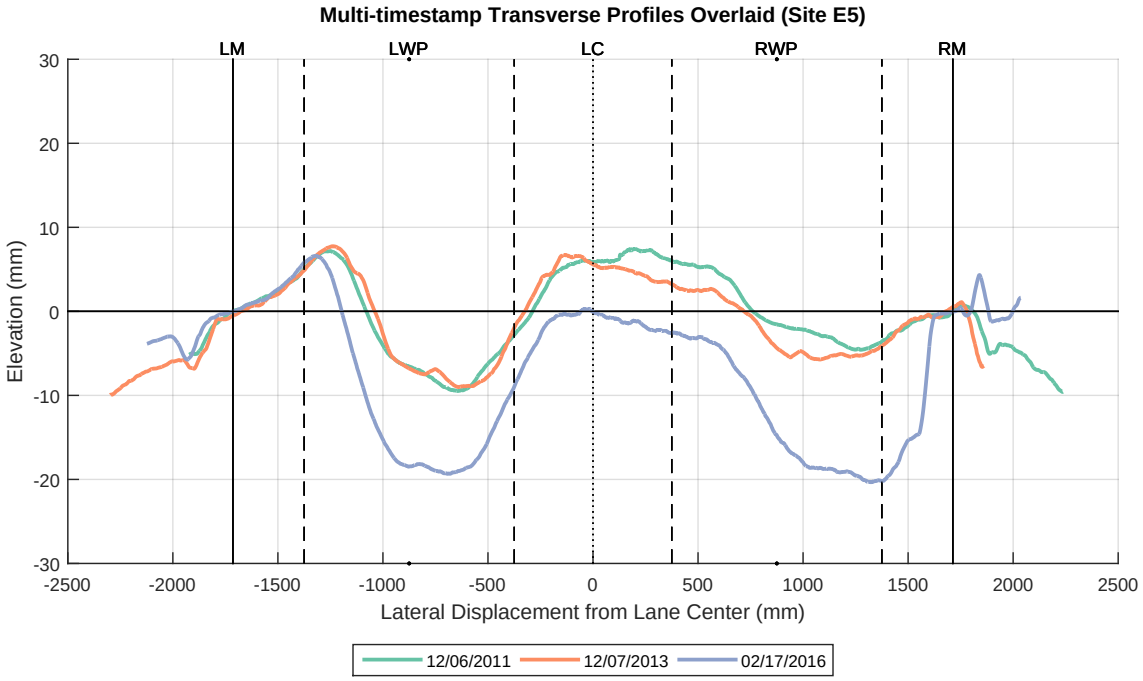

Figure B.9: Transverse Profiles Overlay at Test Site E5

REFERENCES

Alard, C. (2000). "Image subtraction using a space-varying kernel". In: *Astronomy and Astrophysics Supplement Series* 144.2, pp. 363–370.

Alard, C. and Robert H. Lupton (1998). "A Method for Optimal Image Subtraction". In: *The Astrophysical Journal* 503.1, pp. 325–331.

Alfons, Andreas (2012). *cvTools: Cross-validation tools for regression models*. R package version 0.3.2. URL: https://CRAN.R-project.org/package=cvTools (visited on 09/30/2016).

American Association of State Highway and Transportation Officials (2014a). *AASHTO PP69-14 Standard Practice for Determining Pavement Deformation Parameters and Cross Slope from Collected Transverse Profiles*. American Association of State and Highway Transportation Officials.

American Association of State Highway and Transportation Officials (2014b). *AASHTO PP70-14 Standard Practice for Collecting the Transverse Pavement Profile*. American Association of State and Highway Transportation Officials.

American Association of State Highway and Transportation Officials (2014c). *AASHTO R48-10 Standard Practice for Determing Rut Depth in Pavements*. American Association of State Highway and Transportation Officials.

AMES Engineering (2016). *3D Laser Image & Measurement System*. URL: https://amesengineering.com/products/3d-laser-image-measurement-system/ (visited on 11/23/2016).

ARA, Inc., ERES Consultants Division (2004). *Guide for Mechanistic-Empirical Design of New and Rehabilitated Pavement Structures*. Washington D. C.: Transportation Research Board of the National Academies.

ASTM International (2011). *ASTM E1703/E1703M-10 Standard Test Method for Measuring Rut-Depth of Pavement Surfaces Using a Straightedge*. ASTM International.

ASTM International (2015). *ASTM E1778-98a - Standard Terminology Relating to Pavement Distress*. ASTM International.

Austroads (2011). *Test Method AG:AM/T009 - Pavement Rutting Measurement with a Multi-Laser Profilometer*. Austroads.

Bandini, Paola and Hung V. Pham (2010). *Transition from manual to automatic rutting measurements: effect on pavement serviceability index values*. New Mexico Department of Transportation.

Bertozzi, Massimo and Alberto Broggi (1998). "GOLD: A parallel real-time stereo vision system for generic obstacle and lane detection". In: *IEEE transactions on image processing* 7.1, pp. 62–81.

Bianchini, Alessandra, Paola Bandini, and David W. Smith (2010). "Interrater Reliability of Manual Pavement Distress Evaluations". In: *Journal of Transportation Engineering* 136 (2), pp. 165–172.

Bogus, Susan M., Giovanni Migliaccio, and Arturo Cordova (2010). "Assessment of Data Quality for Evaluations of Manual Pavement Distress". In: *Transportation Research Record: Journal of the Transportation Research Board* 2170, pp. 1–8.

Boser, Bernhard E., Isabelle M. Guyon, and Vladimir N. Vapnik (1992). "A Training Algorithm for Optimal Margin Classifiers". In: *Proceedings of the Fifth Annual Workshop on Computational Learning Theory*. COLT '92. Pittsburgh, Pennsylvania: ACM, pp. 144–152.

Brown, Lisa Gottesfeld (1992). "A Survey of Image Registration Techniques". In: *ACM Comput. Surv.* 24.4, pp. 325–376.

Capuruço, Renato A. C., Susan L. Tighe, Li Ningyuan, and Tom Kazmierowski (2006). "Performance Evaluation of Sensor- and Image-Based Technologies for Automated Pavement Condition Surveys". In: *Transportation Research Record: Journal of the Transportation Research Board* 1968, pp. 47–52.

Chang, Chih-Chung and Chih-Jen Lin (2011). "LIBSVM: A library for support vector machines". In: *ACM Transactions on Intelligent Systems and Technology* 2 (3), 27:1–27:27.

Chang, Tang-Hsien, Chih-Sheng Hsu, Chieh Wang, and Li-Kai Yang (2008). "Onboard Measurement and Warning Module for Irregular Vehicle Behavior". In: *IEEE Transactions on Intelligent Transportation Systems* 9 (3), pp. 501–513.

Chang, Yin-Wen, Cho-Jui Hsieh, Kai-Wei Chang, Michael Ringgaard, and Chih-Jen Lin (2010). "Training and Testing Low-degree Polynomial Data Mappings via Linear SVM". In: *J. Mach. Learn. Res.* 11, pp. 1471–1490.

Chang-Albitres, Carlos M., Roger E. Smith, and Olga J. Pendleton (2007). "Comparison of Automated Pavement Distress Data Collection Procedures for Local Agencies in San Francisco Bay Area, California". In: *Transportation Research Record: Journal of the Transportation Research Board2* 1990, pp. 119–126.

Chen, Dar Hao and Zheng Li (2008). "Comparisons of Five Computational Methods for Transverse Profiles". In: *Journal of Testing and Evaluation* 36.5, pp. 1–8.

Chen, Dar-Hao, John Bilyeu, Deborah Walker, and Mike Murphy (2001). "Study of Rut-Depth Measurements". In: *Transportation Research Record: Journal of the Transportation Research Board* 1764, pp. 78–88.

Cortes, Corinna and Vladimir Vapnik (1995). "Support-vector networks". In: *Machine Learning* 20.3, pp. 273–297.

Dawn, Suma, Vikas Saxena, and Bhudev Sharma (2010). "Remote Sensing Image Registration Techniques: A Survey". In: *Proceedings of the 4th International Conference on Image and Signal Processing*. ICISP'10. Berlin, Heidelberg: Springer-Verlag, pp. 103–112.

Deacon, John, John Harvey, Irwin Guada, Lorina Popescu, and Carl Monismith (2002). "Analytically Based Approach to Rutting Prediction". In: *Transportation Research Record: Journal of the Transportation Research Board* 1806, pp. 9–18.

Fang, Hongbing, John E. Haddock, Thomas D. White, and Adam J. Hand (2004). "On the characterization of flexible pavement rutting using creep model-based finite element analysis". In: *Finite Elements in Analysis and Design* 41.1, pp. 49–73.

Flintsch, Gerardo and Kevin K. McGhee (2009). *NCHRP Synthesis 401: Quality Management of Pavement Condition Data Collection*. National Cooperative Highway Research Program, Transportation Research Board of the National Academies.

Fonseca, L. M. G. and B. S. Manjunath (1996). "Registration Techniques for Multisensor Remotely Sensed Imagery". In: *Journal of Photogrammetry Engineering and Remote Sensing* 62.9, pp. 1049–1056.

Freeborough, Peter A, Roger P Woods, and Nick C Fox (1996). "Accurate registration of serial 3D MR brain images and its application to visualizing change in neurodegenerative disorders". In: *Journal of computer assisted tomography* 20.6, pp. 1012–1022.

Friston, Karl. J., J. Ashburner, C. D. Frith, J.-B. Poline, J. D. Heather, and R. S. J. Frackowiak (1995). "Spatial registration and normalization of images". In: *Human Brain Mapping* 3.3, pp. 165–189.

Fwa, T. F., H. R. Pasindu, and G. P. Ong (2012). "Critical Rut Depth for Pavement Maintenance Based on Vehicle Skidding and Hydroplaning Consideration". In: *Journal of Transportation Engineering* 138 (4), pp. 423–429.

Gramling, Wade L, John E Hunt, and George S Suzuki (1991). "Rational Approach to Cross-profile and Rut Depth Analysis". In: *Transportation Research Record* 1311, pp. 173–179.

Haas, R., W. R. Hudson, and J. P. Zaniewski (1994). *Modern Pavement Management*. Malabar, Florida: Krieger Publishing Company.

Hall, Mark A. (1999). "Correlation-based Feature Selection for Machine Learning". PhD thesis. Department of Computer Science, University of Waikato.

Huang, Yaxiong (Robin), Todd Copenhaver, and Phillip Hempel (2011). "Texas Department of Transportation 3D Transverse Profiling System for High-Speed Rut Measurement". In: *Journal of Infrastructure Systems* 19 (2), pp. 221–230.

INO, Pavemetrics Systems Inc. (2010). *LCMS Data Processing Library: User Manual (Rev 1.3)*. Quebec City, Quebec, Canada.

Jiang, Chenglong (2015). "A Crack Detection and Diagnosis Methodology for Automated Pavement Condition Evaluation". PhD thesis. Georgia Institute of Technology.

Jiang, Chenglong and Yichang James Tsai (2016). "Enhanced Crack Segmentation Algorithm Using 3D Pavement Data". In: *Journal of Computing in Civil Engineering* 30.3, p. 04015050.

Jiang, Chenglong, Yichang (James) Tsai, and Zhaohua Wang (2016). "Use of Three-Dimensional Pavement Surface Data to Analyze Crack Deterioration". In: *Transportation Research Record: Journal of the Transportation Research Board* 2589, pp. 154–161.

Kandhal, Prithvi S. and L. Allen Cooley (2003). *NCHRP Report 508: Accelerated Laboratory Rutting Tests: Evaluation of the Asphalt Pavement Analyzer*. National Cooperative Highway Research Program, Transportation Research Board of the National Academies, p. 73.

Kano, Akiko, Kunio Doi, Heber MacMahon, Dayne D. Hassell, and Maryellen L. Giger (1999). "Digital image subtraction of temporally sequential chest images for detection of interval change". In: *Medical Physics* 21.3, p. 453.

Kolmogorov, A. N. (1933). "Sulla Determinazione Empirica di una Legge di Distribuzione". In: *Giornale dell'Istituto Italiano degli Attuari* 4, pp. 83–91.

Kotsiantis, SB (2007). "Supervised Machine Learning: A Review of Classification Techniques". In: *Informatica* 31, pp. 249–268.

Laurent, J., M. Talbot, and M. Doucet (1997). "Road surface inspection using laser scanners adapted for the high precision 3D measurements of large flat surfaces". In: *Proceedings. International Conference on Recent Advances in 3-D Digital Imaging and Modeling (Cat. No.97TB100134)*. IEEE Comput. Soc. Press, pp. 303–310.

Lee, Hosin and Jungyong Kim (2006). "Analysis of Error in Pavement Ground Truth Indicators for Evaluating the Accuracy of Automated Image Collection and Analysis System". In: *Journal of ASTM International* 3 (5), pp. 1–15.

Lenngren, C. A. (1988). "Some Approaches in Treating Automatically Collected Data on Rutting". In: *Transportation Research Record: Journal of the Transportation Research Board* 1196, pp. 20–26.

Li, Feng (2012). "A Methodology for Characterizing Pavement Rutting Condition using Emerging 3D Line Laser Imaging Technology". Ph.D. Dissertation. Georgia Institute of Technology.

Li, Tian-tian, Xue Wang, and Hui-qi Liu (2015). In: *Advances in Image and Graphics Technologies - 10th Chinese Conference, IGTA 2015*. Vol. 525. Beijing, China: Springer Berlin Heidelberg, pp. 234–242.

Lowe, D. G. (1999). "Object recognition from local scale-invariant features". In: *The Seventh IEEE International Conference on Computer Vision*. Vol. 2, 1150–1157 vol.2.

Lucas, Bruce D and Takeo Kanade (1981). "An iterative image registration technique with an application to stereo vision". In: *International Joint Conference on Artificial Intelligence, IJCAI*. Vol. 81. 1, pp. 674–679.

McCall, J. C. and M. M. Trivedi (2004). "An integrated, robust approach to lane marking detection and lane tracking". In: *Intelligent Vehicles Symposium, 2004 IEEE*, pp. 533–537.

McGhee, Kenneth H. (2004). *NCHRP Synthesis 334: Automated Pavement Distress Collection Techniques*. National Cooperative Highway Research Program, Transportation Research Board of the National Academies.

McGill, Robert, John W. Tukey, and Wayne A. Larsen (1978). "Variations of Box Plots". In: *The American Statistician* 32.1, pp. 12–16.

McQueen, Jason and David Timm (2005). "Statistical Analysis of Automated Versus Manual Pavement Condition Surveys". In: *Transportation Research Record* 1940, pp. 53–62.

Mehta, Yusuf, Reynaldo Roque, George Lopp, and Claude Villiers (2001). "Evaluation of Road Surface Profiler and Transverse Profilograph for Determination of Rut Depths".

In: *Transportation Research Record: Journal of the Transportation Research Board* 1764, pp. 157–163.

Meyer, David, Evgenia Dimitriadou, Kurt Hornik, Andreas Weingessel, and Friedrich Leisch (2015). *e1071: Misc Functions of the Department of Statistics, Probability Theory Group (Formerly: E1071), TU Wien*. R package version 1.6-7. URL: https://CRAN.R-project.org/package=e1071 (visited on 09/30/2016).

Morosiuk, Greg, Mike J. Riley, and J B Odoki (2004). *The Highway Development and Management Series: Volume 6 Modelling Road Deterioration and Works Effects*. 2nd.

Mraz, Alexander, Manjriker Gunaratne, Abdenour Nazef, and Bouzid Choubane (2006). "Experimental Evaluation of a Pavement Imaging System: Florida Department of Transportation's Multipurpose Survey Vehicle". In: *Transportation Research Record: Journal of the Transportation Research Board* 1974, pp. 97–106.

Natalia Novoselova Junxi Wang, Frank Pessler Frank Klawonn (2015). *Biocomb: Feature Selection and Classification with the Embedded Validation Procedures for Biomedical Data Analysis*. R package version 0.2. URL: https://CRAN.R-project.org/package=Biocomb (visited on 09/28/2016).

Onyango, Mbakisya A. (2009). "Verification of mechanistic prediction models for permanent deformation in asphalt mixes using accelerated pavement testing". PhD thesis. Kansas State University.

Oteng-Seifah, Samuel and Phillip Manke G (1976). "Study of Rutting in Flexible Pavements in Oklahoma". In: *Transportation Research Record* 602, pp 97–99.

Otsu, Nobuyuki (1979). "A Threshold Selection Method from Gray-Level Histograms". In: *IEEE Transactions on Systems, Man, and Cybernetics* 9 (1), pp. 62–66.

Paterson, William D. O. (1987). *Road deterioration and maintenance effects : models for planning and management*, pp. 1–472.

Pathway Services Inc. (2016). *Pathway 3D*. URL: http://pathwayservices.com/3D_imaging.shtml (visited on 11/23/2016).

Pavemetrics Systems Inc. (2016). *Laser Crack Measurement System (LCMS)*. URL: http://www.pavemetrics.com/applications/road-inspection/laser-crack-measurement-system/ (visited on 01/03/2016).

Perera, R. W., S. D. Kohn, and G. R. Rada (2008). *LTPP Manual for Profile Measurements and Processing*. Pavement Performance Division, Federal Highway Administration.

Phoenix Scientific Inc. (2016). *Phoenix Scientific Inc.* URL: http://www.phnx-sci.com/PPS/Home.html (visited on 02/01/2016).

Qiu, Shi (2013). "Measurement of Pavement Permanent Deformation based on 1mm 3D Pavement Surface Model". PhD Dissertation. Oklahoma State University.

Qiu, Shi, Kelvin C. P. Wang, Wenjuan Wang, Qiang Li, and Allen Zhang (2015). "Reducing the Effect of Inaccurate Lane Identification on PP69-10-Based Rut Characterization". In: *Journal of Infrastructure Systems* 22 (1).

Quintus, Harold L. Von, Jagannath Mallela, Ramon Bonaquist, Charles W. Schwartz, and Regis L. Carvalho (2012). *NCHRP Report 719: Calibration of Rutting Models for Structural and Mix Design*. Washington D.C.: National Cooperative Highway Research Program, Transportation Research Board of the National Academies.

R Core Team (2016). *R: A Language and Environment for Statistical Computing*. Vienna, Austria: R Foundation for Statistical Computing. URL: https://www.R-project.org/ (visited on 09/21/2016).

Serigos, Pedro A., Jorge A. Prozzi, Boo H. Nam, and Mike R. Murphy (2012). *Field Evaluation of Automated Rutting Measuring Equipment*. Center for Transportation Research at The University of Texas at Austin.

Serigos, Pedro A., Michael Murphy, and Jorge A. Prozzi (2015). "Evaluation of Rut-Depth Accuracy and Precision Using Different Automated Measurement Systems". In: *Journal of Testing and Evaluation* 43 (1), pp. 149–158.

Simpson, Amy (1999). "Characterization of Transverse Profile". In: *Transportation Research Record: Journal of the Transportation Research Board* 1655, pp. 185–191.

Simpson, Amy L. (2001a). *Characterization of Transverse Profiles*. Office of Infrastructure Research and Development, Federal Highway Administration.

Simpson, Amy L. (2001b). "Measurement of Rutting in Asphalt Pavements". Ph.D. Dissertation. The University of Texas at Austin.

Simpson, Amy L, Jerome F Daleiden, and William O Hadley (1995). "Rutting Analysis from a Different Perspective". In: *Transportation Research Record: Journal of the Transportation Research Board* 1473, pp. 9–16.

Start, Marc, Jeong Kim, and William Berg (2015). "Potential Safety Cost-Effectiveness of Treating Rutted Pavements". In: *Transportation Research Record: Journal of the Transportation Research Board*.

Suh, Young-Chan and Nam-Hyun Cho (2013). "Development of a rutting performance model for asphalt concrete pavement based on test road and accelerated pavement test data". In: *KSCE Journal of Civil Engineering* 18 (1), pp. 165–171.

Transfund New Zealand (1997). *RAMM - Road Condition Rating and Roughness Manual*. Wellington: Transfund New Zealand.

Tsai, James Yi-Chang, Feng Li, and Yi-Ching Wu (2013). "A New Rutting Measurement Method Using Emerging 3D Line-Laser-Imaging System". In: *International Journal of Pavement Research and Technology* 6.5, pp. 667–672.

Tsai, Yi-Chang James and Feng Li (2012). "Critical Assessment of Detecting Asphalt Pavement Cracks under Different Lighting and Low Intensity Contrast Conditions Using Emerging 3D Laser Technology". In: *Journal of Transportation Engineering* 138.5, pp. 649–656.

Tsai, Yi-Chang James and Zhaohua Wang (2014). *A Remote Sensing and GIS-enabled Asset Management System (RS-GAMS)*. Research, Innovative Technology Administration Office of Research, Development, and Technology, USDOT.

Tsai, Yi-Chang (James), Chenglong Jiang, and Yuchun Huang (2014a). "Multiscale Crack Fundamental Element Model for Real-World Pavement Crack Classification". In: *Journal of Computing in Civil Engineering* 28.4, p. 04014012.

Tsai, Yichang, Chenglong Jiang, and Zhaohua Wang (2012a). "Pavement Crack Detection Using High-Resolution 3D Line Laser Imaging Technology". In: *7th RILEM International Conference on Cracking in Pavements*. Dordrecht: Springer Netherlands, pp. 169–178.

Tsai, Yichang, Yiching Wu, James Lai, and Georgene Geary (2012b). "Ridge-to-Valley Depth Measured with Road Profiler to Control Micromilled Pavement Textures for Super-Thin Resurfacing on I-95". In: *Transportation Research Record: Journal of the Transportation Research Board* 2306, pp. 144–150.

Tsai, Yichang, Yiching Wu, and Zachary Lewis (2014b). "Full-Lane Coverage Micromilling Pavement-Surface Quality Control Using Emerging 3D Line Laser Imaging Technology". In: *Journal of Transportation Engineering* 140.2, p. 04013006.

Tsai, Yichang (James) and Zhaohua Wang (2015a). *Development of an Asphalt Pavement Raveling Detection Algorithm Using Emerging 3D Laser Technology and Macrotexture Analysis*.

Tsai, Yichang (James) and Zhaohua Wang (2015b). *Technology Overview on Validating 3D Transverse Profile Data and Measurement of Pavement Surface Distresses*. URL:

https://collaboration.fhwa.dot.gov/dot/fhwa/tpf5299/DocumentLibrary/3D_Laser_Validation_Review_2015-3-9.pdf.

Tsai, Yichang (James), Zhaozheng Hu, and Chris Alberti (2010). "Detection of Roadway Sign Condition Changes using Multi-Scale Sign Image Matching (M-SIM)". In: *Photogrammetric Engineering & Remote Sensing* 76.4, pp. 391–405.

Tsai, Yichang (James), Zhaohua Wang, and Feng Li (2011). "Assessment of Rut Depth Measurement Using Emerging 3D Continuous Laser Profiling Technology". In: *Transportation Research Board 90th Annual Meeting*. Washington D.C.

Tsai, Yichang (James), Yiching Wu, Chengbo Ai, and Eric Pitts (2012c). "Critical Assessment of Measuring Concrete Joint Faulting Using 3D Continuous Pavement Profile Data". In: *Journal of Transportation Engineering* 138.11, pp. 1291–1296.

Tsai, Yichang James, Chenglong Jiang, and Zhaohua Wang (2014c). "Implementation of automatic crack evaluation using Crack Fundamental Element". In: *2014 IEEE International Conference on Image Processing (ICIP)*. IEEE, pp. 773–777.

Tsai, Yichang (James), Zhaohua Wang, and Feng Li (2015). "Assessment of Rut Depth Measurement Accuracy of Point-Based Rut Bar Systems Using Emerging 3D Line Laser Imaging Technology". In: *Journal of Marine Science and Technology* 23 (3), pp. 322–330.

Villiers, Claude, Reynaldo Roque, and Bruce Dietrich (2006). "Interpretation of Transverse Profiles to Determine the Source of Rutting Within an Asphalt Pavement System". In: *Transportation Research Record: Journal of the Transportation Research Board*.

Wang, Chieh (Ross) and Yichang James Tsai (2017a). "A Spatiotemporal Methodology for Pavement Rut Classification Using 3D Pavement Data". In: *World Conference on Pavement and Asset Management, WCPAM2017*. Abstract accepted. Milan, Italy.

Wang, Chieh (Ross) and Yichang James Tsai (2017b). "Characterizing Rut Deterioration Using 3D Pavement Data: A Pilot Study on Georgia State Route 26". In: *Transportation Research Board 96th Annual Meeting*. Forthcoming. Washington, D.C.

Wang, Chieh (Ross) and Yichang (James) Tsai (2017c). "Registration of 3D Pavement Data over Multiple Timestamps for Rut Deterioration Analysis: A Quasi-automated Method". In: *Transportation Research Board 96th Annual Meeting*. Forthcoming. Washington D.C.

Wang, I-Lin, Yi-Chang James Tsai, and Feng Li (2011). "A network flow model for clustering segments and minimizing total maintenance and rehabilitation cost". In: *Computers & Industrial Engineering* 60 (4), pp. 593–601.

Wang, Kelvin C.P., Qiang Joshua Li, Guangwei Yang, You Zhan, and Yanjun Qiu (2015). "Network level pavement evaluation with 1mm 3D survey system". In: *Journal of Traffic and Transportation Engineering (English Edition)* 2.6, pp. 391–398.

Wang, Yu, Igor V. Tetko, Mark A. Hall, Eibe Frank, Axel Facius, Klaus F.X. Mayer, and Hans W. Mewes (2005). "Gene selection from microarray data for cancer classificationa machine learning approach". In: *Computational Biology and Chemistry* 29 (1), pp. 37–46.

White, Thomas D., John E. Haddock, Adam J. T. Hand, and Hongbing Fang (2002). *NCHRP Report 468: Contributions of Pavement Structural Layers to Rutting of Hot-Mix Asphalt Pavements*. Washington D.C.: National Cooperative Highway Research Program, Transportation Research Board of the National Academies.

Wikipedia (2016a). *KolmogorovSmirnov test — Wikipedia, The Free Encyclopedia*. URL: https://en.wikipedia.org/wiki/Kolmogorov%E2%80%93Smirnov_test (visited on 09/15/2016).

Wikipedia (2016b). *Support vector machine — Wikipedia, The Free Encyclopedia*. URL: https://en.wikipedia.org/wiki/Support_vector_machine (visited on 10/10/2016).

Wu, Y. J., F. L. Lian, and T. H. Chang (2006). "Traffic Monitoring and Vehicle Tracking using Roadside Cameras". In: *2006 IEEE International Conference on Systems, Man and Cybernetics*. Vol. 6, pp. 4631–4636.

VITA

Chieh (Ross) Wang is a native of Taipei, Taiwan, and an alumnus of National Taiwan University (Civil Engineering BS '05 and MS '07). His research revolves around, but is not limited to, the development of intelligent applications and data-driven solutions for the evaluation, monitoring, management, and safety of the sustainable transportation system.